OFDM Based Air Interfaces for Future Mobile Satellite Systems

Sundarampillai Janaaththanan

Submitted for the Degree of
Doctor of Philosophy
from the
University of Surrey

Centre for Communication Systems Research
Faculty of Engineering and Physical Sciences
University of Surrey
Guildford, Surrey GU2 7XH, UK

December 2008

© S. Janaaththanan 2008

Dedicated to my loving parents, Sundarampillai and Sacidevi

Summary

This thesis considers the performance of OFDM in a non-linear satellite channel and mechanisms for overcoming the degradations resulting from the high PAPR in the OFDM signal in the specific satellite architecture. It was motivated by new S-DMB applications but its results are applicable to any OFDM system via satellites. Despite many advantages of OFDM, higher PAPR is a major drawback. OFDM signals are therefore very sensitive to non-linear distortion introduced by the power amplifiers and thus, significantly reduce the power efficiency of the system, which is already crucial to satellite system economics. Simple power amplifier back-off to cope with high OFDM PAPR is not possible. Two transmitter based techniques have been considered: PAPR reduction and amplifier linearization.

The thesis proposes a novel gradient based PAPR reduction algorithm using a Tone Reservation technique. The algorithm is shown to have significantly reduced complexity and improved PAPR reduction performance when compared with the most efficient existing algorithms. Moreover, it is also shown that the proposed algorithm is effective when it is combined with pre-distortion technique.

The performance of polynomial based and LUT based pre-distortion techniques are evaluated and compared, in terms of adaptation speed, accuracy and complexity, in the remote adaptation scenario, assuming the feedback signal from the satellite is degraded by AWGN noise. The polynomial based pre-distortion technique shows more robustness to the noise whereas the LUT pre-distorter is more sensitive. For the LUT pre-distorter, a modified Secant algorithm is proposed and an adaptive strategy using the Secant and modified Secant algorithm based on an approximate threshold SNR is also proposed.

Finally, the performance of OFDM based and HSPA based air interfaces are evaluated and compared in the return and forward links of future mobile satellite system. HSPA based air interfaces employing advanced rake receivers can outperform OFDM based air interfaces in the multipath channel. A CAZAC sequence is investigated for estimating the channel in the presence of amplifier non-linearity in SC-FDMA systems, shown to perform well. SC-FDE is proposed for S-DMB type systems as an alternative approach to OFDM and demonstrates approximately a 3dB gain compared to OFDM in the ideally linearized amplifier. Furthermore, SC-FDE has the same overall complexity and can easily be configured to co-exist with OFDM receiver.

Key words: Mobile Satellite, OFDM, PAPR, Pre-distortion, HSPA, SC-FDE, SC-FDMA.

Email: S.Janaaththanan@surrey.ac.uk

Acknowledgments

I would like to express my profound gratitude to my supervisors Professor Barry G. Evans and Dr. Christos Kasparis for their support and guidance throughout my research work. I appreciate their patience and faith in me, particularly in the early part of my PhD, when a lot of time had to be spent in developing my fundamental understanding of the OFDM systems. This work would not have been possible without their valuable guidance and constant support.

There are number of other CCSR members who must be thanked. In particular, I am thankful to Dr. Atta Quddus for his constant support, especially when working with the HSDPA simulator. I am also thankful to Azizul Azizan for the productive technical discussions.

I am very much grateful for the financial support from Overseas Research Studentship (ORS) and the European Union's 6th framework project Satellite Communications Network of Excellence (SatNEx).

Through it all, I owe my greatest debt to my family –my parents, my brother and my sisters. I am most grateful to their love, encouragement, and support throughout my life.

Contents

List of Figures

List of Tables

Glossary of Terms

List of Abbreviations

3G	Third Generation
ACE	Active Channel Extension
BER	Bit Error Rate
BLER	Block Error Rate (One OFDM Block with channel coding)
CF	Crest Factor
CP	Cyclic Prefix
DFT	Discrete Fourier Transform
FER	Frame Error Rate
FFT	Fast Fourier Transform
GI	Guard Interval
GMR	GEO Mobile Radio
HPA	High Power Amplifier
HSDPA	High Speed Downlink Packet Access
HSUPA	High Speed Uplink Packet Access
IBI	Inter-Block Interference
IBO	Input Back-Off
ICI	Inter-Carrier Interference
IDFT	Inverse Discrete Fourier Transform
IFFT	Inverse Fast Fourier Transform
IMR	Intermediate Module Repeater
INMARSAT	International Maritime Satellite Organization
ISI	Inter-Symbol Interference
LTWTA	Linearized Travelling Wave Tube Amplifier
LUT	Look Up Table

MAESTRO	Mobile Applications & sErvices based on Satellite & Terrestrial inteRwOrking
MBMS	Multimedia Broadcast Multicast Services
MoDiS	Mobile Digital Broadcast Satellite
MSE	Mean Square Error
NMAE	Normalized Maximum Absolute Error
NMSE	Normalized Mean Square Error
OBO	Output Back-off
OFDM	Orthogonal Frequency Division Multiplexing
PAPR	Peak-to-Average Power Ratio
PD	Pre-distorter
PTS	Partial Transmit Sequence
QPSK	Quadrature Phase Shift Keying
RMAE	Relative Maximum Absolute Error
RMSE	Relative Mean Square Error
SATIN	Satellite-UMTS IP-based Network
SC-FDE	Single Carrier Frequency Domain Equalization
SC-FDMA	Single Carrier Frequency Division Multiple Access
S-DMB	Satellite Digital Multimedia Broadcasting
SLM	Selected Mapping
S-UMTS	Satellite-UMTS
TI	Tone Injection
TR	Tone Reservation
TTI	Transmission Time Interval
TWTA	Travelling Wave Tube Amplifier
UMTS	Universal Mobile Telecommunication System
WCDMA	Wideband Code Division Multiple Access

List of Mathematical Symbols

a, α	Scalar Constant
$x(t)$	Function, parameter is t
$x[n]$	Sequence, parameter is n
$\mathbf{x}$	vector
$\mathbf{X}$	matrix
$\Re\{y\}$	Real part of y
$\Im\{y\}$	Imaginary part of y
$\|\cdot\|$	Norm
$\|\cdot\|_2$	l_2-norm
$\|\cdot\|_p$	l_p-norm
$\|\cdot\|_\infty$	l_∞-norm
f	Frequency
$J(\cdot)$	Cost function
E_b/N_0	Signal Energy per bit divided by the noise spectral density
E_c/I_{or}	Ratio of the average transmit energy per PN chip of the physical channels to the total transmit power spectral density
I_{or}	Total transmit power spectral density of the downlink signal at the Node B antenna
I_{oc}	Power spectral density of a band-limited white noise source (modelling interference from other cells) as measured at the UE antenna
I_{or}/I_{oc}	Geometry Facto, i.e. power received from the serving cell divided by the power received from surrounding cells plus the thermal noise

Chapter One

1 Introduction

1.1 Introduction

The spectacular growth of video and data communication over the internet and the pervasion of mobile telephony, brings with it great expectations for mobile multimedia communications. Multimedia services have received impetus from the emergence of third generation (3G) mobile communication systems and therefore, mobile operators are under pressure to assure that the capacity of the wireless networks is available to satisfy these growing demands [HOLM02]. Consequently, the WCDMA based 3G system has continuously evolved over the past few years with new features being added to further enhance multimedia service delivery. For example, High Speed Packet Access (HSPA) is the high data rate versions of the WCDMA based UMTS standard; in which High Speed Downlink Packet Access (HSDPA), defined in 3GPP Release 5, and High Speed Uplink Packet Access (HSUPA), defined in3GPP Release 6, were introduced in the forward and return links, respectively. A further standard, evolved HSPA (HSPA+) was proposed and defined in 3GPP Release 7 [3GPP08]. The next major step in the evolution of the radio transmission scheme is the 3GPP Long Term Evolution (LTE), defined in the 3GPP Release 8 standard. In the latter, OFDM based interfaces, OFDMA in the forward link and SC-FDMA in the return link, are considered as suitable candidates for the next generation air interface with the objective of achieving enhanced user experience, low latency, higher throughput and improved spectral efficiency [3GPP814].

Satellite systems have traditionally been successful in providing both broadcasting services and services to niche geographical areas [EVAN99]. Standards have progressed in a rather different way from mobile satellite systems. The air interface standardization work jointly carried out by European Telecommunications Standards Institute (ETSI) and Telecommunications Industry Association (TIA) for the Thurya Mobile Satellite System called the GEO Mobile Radio (GMR)-1 showed close resemblance to the terrestrial based GSM standard. This allowed the integration of standard GSM services into the system by using as much as possible, off-the-shelf components such as the mobile switching center (MSC), the visitor location register (VLR), short message service center (SMSC), etc [THUR08]. In addition INMARSAT have used the GSM network

architecture for their BGAN system but have chosen a different and proprietary air interface [EVAN04]. These strategies suggested an evolutionary path towards satellite based UMTS building on T-UMTS.

The system definition and development of the Satellite UMTS (S-UMTS) system have largely been pursued within the context of the European Union (EU) projects SATIN, MODIS and MAESTRO, which champion a satellite WCDMA air interface to maximize the synergy with terrestrial UMTS (T-UMTS) [KARA04]. Intermediate Module Repeaters (IMRs) are incorporated in order to enhance the signal coverage in the urban and indoor environments where the signal is often shadowed by large buildings as proposed in EU FP5 SATIN project [SATI06]. The validation and demonstration of this innovative concept with field trials in Europe was realized in the follow-on EU MoDiS Project. The latter concentrated on S-DMB – a broadcast system to mobiles, but was closely allied to S-UMTS [MODI06]. The S-UTMS standard was developed by the ETSI MSS group with an emphasis on the provision of services which are best delivered via satellite while keeping close synergy with their terrestrial counterparts. The S-UMTS standard has thus far not been adopted by any commercial system. Furthermore, the working group, also called ETSI-SES, has recently extended its focus towards investigating OFDM in the forward link of the mobile satellite system in order to improve capacity over WCDMA [ETRI07].

In addition, by considering the most important aspect of the future mobile satellite system, keeping maximum commonality with the terrestrial mobile system, the Working Party (WP) 4C of the Radio-Communication part of International Telecommunication Union (ITU-R) has recently called attention for investigation into new satellite radio transmission technologies (RTTs) based on multicarrier transmission technologies for the satellite component of IMT-2000 and IMT-Advanced, taking into account the compatibility with the new RTTs for the terrestrial component [ITUE8]. Derived from involvement in the EU projects and in ETSI by the satellite group at Surrey the objective of the work in this thesis was to investigate OFDM in its role as a component of future air-interface standards. The work has been based on the S-DMB system but is applicable to all satellite systems with OFDM air interfaces and in some cases to OFDM based in terrestrial systems. Results provided in the thesis have also formed part of the following projects;

- European Union's FP6 IST Projects - Mobile Applications & sErvices based on Satellite and Terrestrial inteRwOrking (MAESTRO) [MAES06]
- Collaborative research project with Electronic Telecommunication Research Institute (ETRI) of Korea to investigate OFDM in satellite systems [ETRI07]

1.2 Motivation

The principal task of this thesis is to investigate the physical layer performance on the OFDM based air interfaces in a non-linear wideband mobile satellite channel. The main factor that motivates us to embark in this investigation is the notion that the S-UMTS system should be developed with maximum commonalities with the continuous evolution of the T-UMTS radio access scheme within the 3GPP air interface standardization; OFDM based air interfaces are considered as attractive candidates for all next generation terrestrial air interfaces. For example, Orthogonal Frequency Division Multiple Access (OFDMA) and Single Carrier Frequency Division Multiple Access (SC-FDMA) schemes are presently being investigated under 3GPP Long Term Evolution (LTE), also called 3GPP Release 8 [3GPP814].

An additional factor which motivates the investigation is the wider excess delay spread characterisation of the wideband mobile satellite channel defined in the S-UMTS system. This is due to the incorporation of terrestrial repeaters in the urban and indoor environment, which generate increased "artificial" multipath components with larger number of delayed signal components than in T-UMTS. Therefore, considering the OFDM based air interface in such systems was needed and further motivates the investigation.

The current research literature in the area of satellite based air interfaces has not given much attention to the implementation of OFDM. The OFDM system needs to be adapted in a continuous evolution of the S-UMTS research. We investigate this adaptation via satellite HSPA to OFDM in S-UMTS and S-DMB to SC-FDE for long term evolution satellite systems.

1.3 Thesis Aim

The main aim of the thesis is to investigate the Physical layer performance of OFDM based air interfaces for future mobile satellite systems with maximum commonalities with the terrestrial based air interfaces based on the extension of 3GPP standards. In the 3GPP LTE, there are two different air interfaces used in the return and the forward links. We therefore divide the aim into two individual components as given by:

- To investigate the **OFDM** air interface in the non-linear mobile satellite channel and to evaluate the physical layer performances of the **OFDM** air interface based on **3GPP 25.892** standards in the forward link of the non-linear mobile satellite system.
- To evaluate the physical layer performances of the **SC-FDMA** based on **3GPP 25.814** standards air interface in the return link of the non-linear wideband mobile satellite system.

1.4 Thesis Objectives

In order to accomplish the aims set in section 1.3, the objectives are as follows:

a) To conduct a survey of transmitter based compensation approaches available for mitigating the non-linear distortion introduced by the on-board satellite power amplifier.
b) To identify the suitable compensation techniques from the existing literature.
c) To propose an efficient algorithm in terms of performance and complexity for TR based PAPR reduction technique.
d) To investigate the impact in the performance when the proposed algorithm and the amplifier linearization technique are combined.
e) To identify the problem in implementing pre-distortion technique at the gateway of the satellite systems and to assess the applicability of the existing digital pre-distortion techniques in the context of remote adaptation scenario.
f) To propose an adaptive strategy by improving the performance of the algorithm in realistic scenario.
g) To evaluate and compare the link-level performance of OFDM based and HSPA based systems in the forward and return links of the non-linear wideband mobile satellite system.
h) To investigate the CAZAC sequence for SC-FDMA channel estimation in the presence of non-linear TWTA and evaluate and compare the performance of SC-FDE as an alternative approach to OFDM.

1.5 Original Achievements

The original achievements detailed in this thesis can be summarized as follows:

a) The proposal of a novel **low complexity Tone Reservation (TR) algorithm for reducing the PAPR of the OFDM signal**. The algorithm provides improved PAPR reduction performance. The performance of the algorithm was further evaluated for different pilot locations and in combination with DFT-precoding based PAPR reduction technique.

b) The effective improvement of the spectral re-growth reduction **when the amplifier linearization technique and the TR based PAPR reduction technique are combined**.

c) The comparison between the **polynomial based and LUT based pre-distorters with realistic assumptions in remotely adapting the pre-distorter's coefficients**. The polynomial pre-distorter showed robustness to noisy feedback channel. Moreover, **an adaptive strategy based on an approximate threshold SNR is proposed**. This is based on the proposed modified Secant algorithm which can be used when the SNR in the feedback

channel is below an approximate threshold SNR and the conventional Secant algorithm can otherwise be used.

d) **First evaluation of comparison between OFDM and HSDPA, SC-FDMA and HSUPA over wideband mobile satellite channel**. (The C++ based HSDPA simulator [ATTA05] was extended to include the OFDM transmitter and receiver based signal processing units based on 3GPP 25.892 standard)

e) **First proposal to use SC-FDE for Satellite Digital Multimedia Broadcasting systems** and evaluations which demonstrated it outperforms OFDM in the presence of ideally linearized power amplifier. The investigation of the **Constant Amplitude Zero Auto Correlation (CAZAC) sequence for channel estimation in the presence of non-linear TWTA** for SC-FDMA system.

1.6 Organization of the Thesis

The thesis is organized in seven chapters as depicted in Figure 1-1:

Chapter 2 starts with a brief description of the historical developments in mobile satellite systems. Subsequently, Satellite UMTS and Satellite DMB systems are introduced, including key EU projects leading to standards developments. The chapter also describes the gap filler IMR channel, gap filler and the architecture of the integrated Satellite /Terrestrial S-DMB systems.

Chapter 3 first introduces basic concepts in OFDM and also provides the mathematical modelling of signals, with reference to a generic OFDM system. The major advantages and drawbacks of OFDM systems are then discussed, giving special consideration to non-linear distortion introduced by the non-linear amplifiers. The rest of the chapter is dedicated to the specific characterisation of the non-linear distortion effects caused by the satellite TWTA, and possible transmitter based compensation techniques. A literature survey of these mitigation techniques is given, which covers power back-off, PAPR reduction techniques and amplifier linearization techniques.

Chapter 4 provides an introduction to the Tone Reservation method as one of the appropriate compensation technique for mitigating the non-linear distortion encountered in mobile satellite systems. A review of the previous research work in the TR technique is provided. A low complexity gradient based proposed algorithm is elaborated along with the corresponding analytical derivations. Moreover, the complexity of the proposed algorithm is compared with the most efficient existing algorithm. The performance of the proposed algorithm is also evaluated in the presence of the non-linear on-board power amplifier.

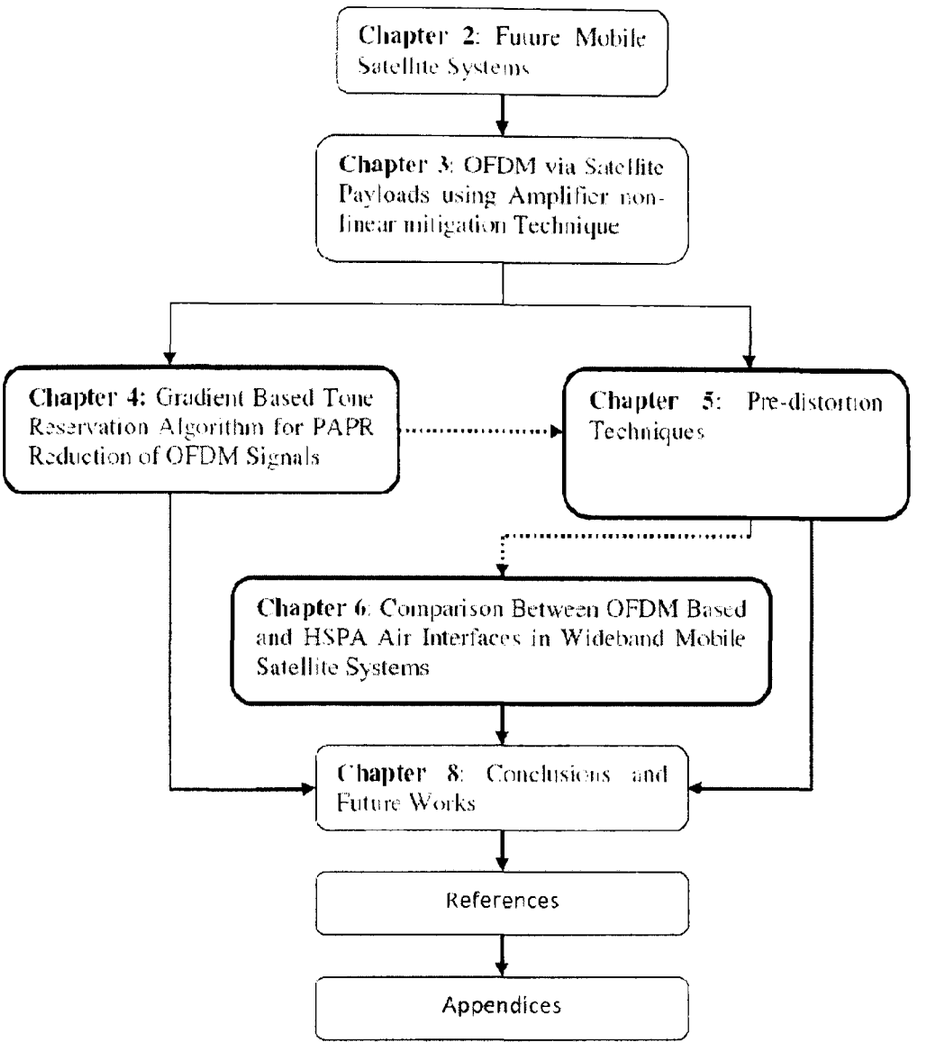

Figure 1-1: The relationship between different chapters of the thesis: an arrow indicates the flow of some of the information from one chapter to another.

Chapter 5 introduces a complete mathematical description of the non-linear power amplifier and an ideal linearizer model. The performance of the TR algorithm is evaluated in the combined "ideal linearizer + amplifier" scenario. In this chapter, we further evaluate and compare the two well known digital pre-distortion techniques, LUT based and Polynomial based, in the forward link of the wideband mobile satellite system, with realistic assumptions in remotely adapting the pre-distorters' coefficients. The computational complexity of the two algorithms is also provided. Moreover, a modified Secant algorithm is proposed and the performance of the algorithm shown based on some metrics defined in this chapter.

Chapter 6 evaluates the performance of both the OFDM and the SC-FDMA air interfaces in the forward and return links, respectively. The performance evaluation is performed using the

multipath profiles which are representative of the future wideband mobile satellite system. The evaluated performances are then used to provide a fair comparison between the OFDM based and HSPA based air interfaces in the wideband mobile satellite system. The forward link performance is compared between HSDPA and OFDM whereas the return link performance comparison is based on the HSUPA and SC-FDMA. The performance is also evaluated in the presence of the non-linear TWTA. Moreover, the performance of the both polynomial and LUT based pre-distorters are also evaluated in OFDM and SC-FDMA system. In the return link, a realistic channel estimation based on the CAZAC sequence is also investigated in the non-linear channel. In the forward link, the performance of the OFDM based system for extended cyclic prefix is also provided. Finally, the chapter also proposes SC-FDE, as an alternative approach to OFDM in the forward link of the mobile satellite broadcasting systems with low impact on the OFDM based receivers.

Chapter 7 concludes the thesis by highlighting impacts of its major findings and suggesting directions for future work. This is followed by the reference section which has comprehensive details of all the references used herein. The final part of the thesis contains the appendices.

Chapter Two

2 Future Mobile Satellite Systems

2.1 Introduction

Satellite systems were traditionally used for one-way (broadcast) services such as television broadcasting and relaying of trans-oceanic telephone signals. Mobile satellite systems (MSS) have been around since the 1980s, in a similar time frame to terrestrial cellular communications, and the technology applied to them is forever growing in sophistication. Similarly, Terrestrial cellular development has also seen major advances in technology, and offer a more cost-effective, better QoS solution in many situations. However, mobile satellite communication systems offer some key advantages bringing communications to sparsely populated or barren areas, in addition to maritime and aeronautical services [EVAN05]. Satellites also offer key advantage in multicast and broadcast services to mobile devices due to efficient delivery, and can complement well terrestrial cellular communications in this respect via an integrated terrestrial-satellite network approach [KARA04].

The delivery of broadcasting services to handheld devices via hybrid satellite-terrestrial networks is already a commercial reality in the far-east [SANG07]. Satellite Digital Multimedia Broadcasting (S-DMB) in Korea via the Mobile Broadcasting Satellite (MBSAT) has attracted around 1 million subscribers but recently suffered from terrestrial Digital Multimedia Broadcasting (T-DMB) being operated on a free basis for network television. In Japan the system did not take off at all. However there was a surge of interest recently due to two reasons; the offered discounted promotion (approximately 50% discount) and the 2008 Beijing Olympics [MOBI08].

There is great interest in implementing a similar broadcasting system based on hybrid satellite-terrestrial networks in Europe in the near future [MAES06]. The efficiency of such networks in supporting high-speed links even in urban environments is an important motivation in considering an upgrade of the hybrid system in supporting bi-directional data services. Among other issues, such an extension would require choice of a new physical layer/multiple access technology. A crucial factor in making this choice is compatibility with T-UMTS, where presently WCDMA based air interfaces are used [KARA04], [EVAN05].

Moreover, the integrated terrestrial-satellite channel or Intermediate Module Repeater (IMR) channel has more multipath components and wider excess delay spread than for T-UMTS systems. The integrated system should have low cost and complexity impact in order to address the mass consumer market. Thus, it closely follows the terrestrial based air interface standards [EVAN05].

In this chapter, we first summarize some of the historical developments taken in mobile satellite systems. This is followed by the introduction of Satellite UMTS and Satellite DMB systems. Finally, the chapter describes the IMR channel with the illustration of IMR configuration.

2.2 Brief History of Mobile Satellite Systems

In 1945 Arthur C. Clarke proposed that a man-made Earth satellite can be used for communication by radio microwaves between distant locations on Earth. Moreover, if the satellite is positioned at an altitude of about 35 790 km its speed of revolution around the Earth will be the same as the speed of the Earth's rotation and therefore, appear in the same place in the sky. In 1962, the world's first true communication satellite Telstar was launched by the American telecommunication giant AT & T [EVAN99]. Since then, countless communications satellites have been placed into earth orbit, and the technology applied to them was forever growing in sophistication.

The first mobile satellite system, Maritime Communications Satellite (MARISAT), was launched in February of 1976 by the Communication Satellite Corporation (COMSAT), which was used to provide mobile services to the US Navy and other maritime customers. The European mobile satellite system was established when the Maritime European Communication Satellite (MARECS) was launched in the early 1980s by the International Maritime Satellite Organization (INMARSAT) which was set up as an establishment in 1979 by UN International Maritime Organization [WHAL07]. At around the same time as the first cellular operators providing 1G analogue services, INMARSAT provided analogue speech and low data rate services mainly to the maritime market of larger ships in L-band using global beam coverage. In 1990/91, aeronautical services (INMARSAT II) were added to passenger aircraft and to some land vehicles by introducing higher power spot beam satellites. Later in 1997/98, new services such as, paging and navigation were introduced (INAMARSAT III) and higher rate digital services to desktop sized terminals using worldwide spot beam coverage. Whilst INMARSAT concentrated on the use of Geostationary Earth Orbit (GEO) satellites in providing all these services, there were also several regional GEO systems that came into operation for example, OMNITRACS, EUTELTRACS, AMSC and OPTUS targeting land vehicles both in L and Ku bands. Moreover,

they were only moderately successful whilst INMARSAT increased its number of customers to circa 400, 000 today [EVAN04].

Meanwhile, inspired by the research work in the late 80's and early 90's, the Low Earth Orbit (LEO) and Medium Earth Orbit (MEO) constellation satellite systems became attractive and in turn, encouraged the development of IRIDIUM and GLOBALSTAR commercial systems. However, they were too late to compete with the already widely spread terrestrial 2G GSM and therefore, went into temporary bankruptcy by the early 2000's. Despite their early failure, they are still in existence today with fewer customers than initially predicted but niche markets in military and disaster/emergence communication. The commercial 'failure' of the above systems and , more generally, the experience with the 2G satellite personal communication network (S-PCN) systems proved that satellite systems cannot capture the predominant voice market and furthermore, acquire a position in the mass market as stand-alone systems [EVAN04].

On the other hand, in the mid 1990's, several super GEO mobile satellites were proposed with 100-200 spot beams with THURYA operating from the early 2000's based on the ETSI GEO Mobile Radio-1 (GMR-1) standard and providing GSM like services covering Asia and much of Europe [MATO02]. This system also provides 'always-on' high speed GPRS packet data communications up to 144 kbps [THUR08]. Although it was considered to be successful in the early days, it has only sustained a niche market; areas where terrestrial mobile is expensive to deploy [EVAN04].

Meanwhile, INMARSAT continues to thrive providing digital services from 64 kbps up to 432 kbps using its own super-GEO's (INMARSAT IV) targeting the Global Area Network (GAN) to broadband GAN (BGAN). Despite the move taken by the terrestrial operators to WCDMA, INMARSAT has continued to develop its proprietary TDMA based system to deliver 3G equivalent packet based services. The INMARSAT BGAN system can be considered as the only 3G equivalent satellite system to date [EVAN04].

2.3 Satellite UMTS

Third generation (3G) mobile communication systems, or better known as Universal Mobile Telecommunication Systems (UMTS), have now been deployed to deliver a more extensive range of applications such as wireless web browsing, voice, video telephony and streaming multimedia with higher data rates up to 2Mbps. A major aim of UMTS is that the end user can perform applications independent of the actual environment and location, which means he/she can access the same type of services anywhere at any time [HOLM02]. Moreover, in order to provide a seamless – anytime, anywhere – communication, a satellite component has been identified in UMTS due to its fundamental role in providing coverage over scarcely populated regions for true

global roaming and its efficient multicasting service provision. In this way, Satellite-UMTS (S-UMTS) is expected to play a complementary role to the terrestrial-UMTS (TUMTS), rather than as a stand-alone system as in the 2nd generation mobile global satellite systems (Iridium, Globalstar, ICO), whereby the terrestrial and satellite mobile systems were developed independently [TAAG99]. Thus, the S-UMTS standard provides services to mobile users in different scenarios, such as: (i) back up coverage for areas already covered by terrestrial cellular systems; (ii) areas where terrestrial coverage is not available.

The International Telecommunication Union (ITU) defined the global requirements for 3G wireless communication in IMT-2000 standard and several standardization bodies proposed Radio Transmission Technique s (RTT) which can satisfy the IMT-2000 requirements. Among them the WCDMA based RTT proposed by ETSI was eventually approved as the 3G wireless communication standard and the UMTS specification work was then carried out by 3GPP [HOLM02], [TAAG99]. In 3GPP, the research activities in terrestrial systems beyond IMT-2000 are mainly focused on the WCDMA based radio access schemes augmented by HSDPA (high Speed Downlink Packet Access) systems to provide higher data rate requirements [EVAN05].

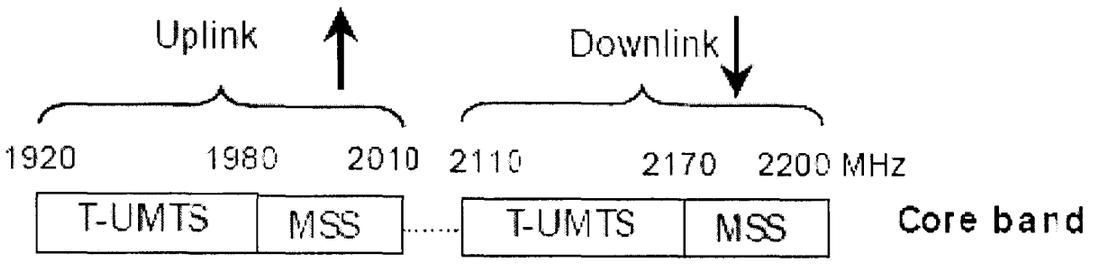

Figure 2-1: IMT-2000 spectrum allocation

The S-UMTS system is proposed to operate in the IMT-2000 Mobile Satellite System (MSS) frequency band which is directly adjacent to the T-UMTS frequency band, as depicted in Figure 2-1. Moreover, the air interface definition has to be performed with particular attention to the on-going T-UMTS standardization activities performed in the Third-Generation Partnership Program (3GPP), in order to maximize commonality. Thus, convergence of a dual-mode receiver, which is lower in complexity, size, and weight, greatly reduces the cost impact on the user terminal. Due to this fact, S-UMTS will boost the commercial opportunities of satellites by addressing mass market. ETSI has adjusted a SWCDMA system for S-UMTS with minimum modifications to the 3GPP standard but as yet no commercial satellite has been launched that uses this system [KARA04], [NARE04], [EVAN05].

2.4 Satellite Digital Multimedia Broadcasting (S-DMB)

Following definition of the IMT-2000 family of technologies for 3G mobile services, including delivery by both satellite and terrestrial transmission, defined by International Telecommunication Union (ITU), there has been an increased demand for push type multimedia services or content delivery over the air to mobile terminals. Moreover, the rapid advancement of memory devices and their significant reduction in cost facilitated the mobile terminal to store and play back large content volumes. Consequently, different technological approaches were considered. These technologies have typically built upon both 3G cellular/PCS and digital terrestrial TV broadcast technologies [KARA04].

Delivering the content based on radio access networks (RAN) such as GPRS, UMTS, HSDPA or CDMA-2000 are well adapted for uni-casting (one-to-one communication) but are not viable for multicast/broadcast, since they severely reduce the capacity of the basic services [EVAN04]. Thus, introducing a multicast/broadcast layer on top of the existing 3G networks was considered to be an alternative way to efficiently deliver the multimedia content to mobile users and this work was standardized within the 3GPP Multimedia Broadcast Multicast Services (MBMS) framework which defines the unidirectional point-to-multipoint provision of multimedia services while optimizing the available capacity in cellular networks. But excessive multicast/broadcast is arguably not efficiently delivered in a cellular structure [KARA04].

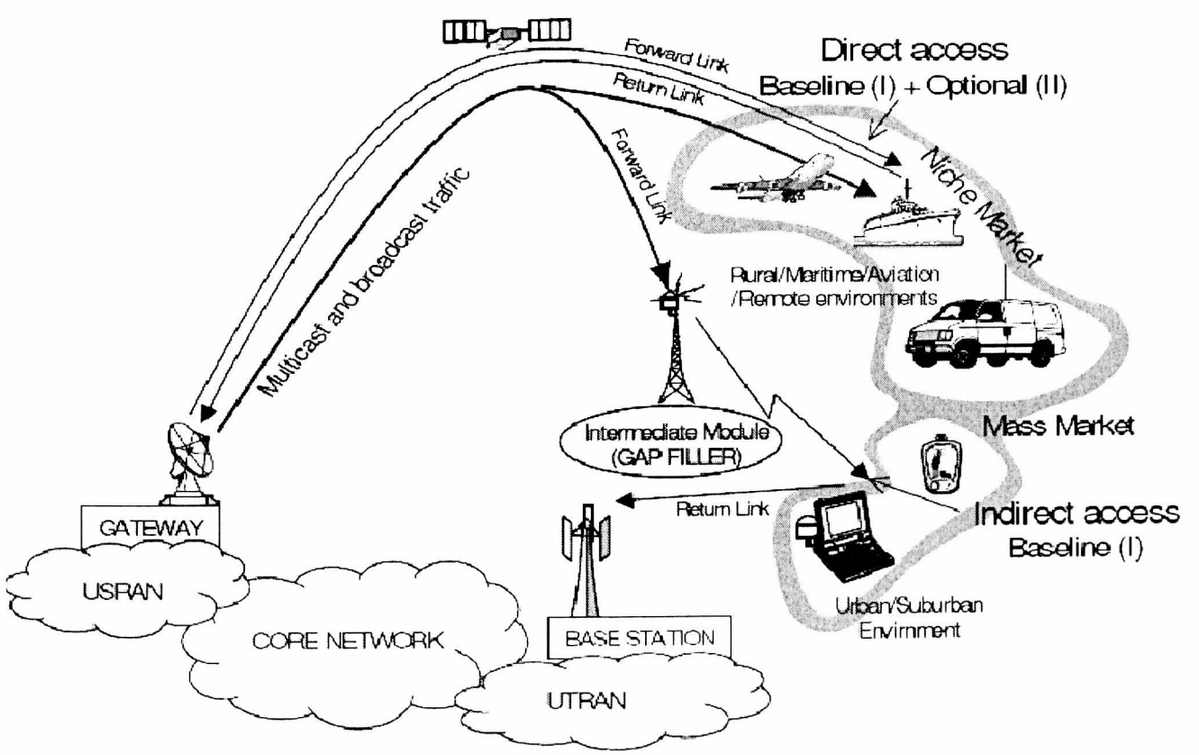

Figure 2-2: S-DMB Concept [SATI06]

However, the inherent broadcast capabilities of satellites render them an attractive candidate for the provision of point-to-multipoint services. Thus, the content delivery capacity can be increased by implementing a satellite based broadcast/multicast layer, which is complementary to the 3G mobile networks. This prompted the EU FP5 Satellite-UMTS IP based Network (SATIN) project to propose a new way forward for mobile satellites in the form of an integrated satellite/terrestrial UMTS system. In this way, the so called S-DMB system, operating in the MSS band, which is directly adjacent to the IMT-2000 allocated to the terrestrial mobile network, has been realized and the basic architecture is shown in Figure 2-2. The system makes use of the 3GPP UTRA FDD WCDMA standardized technology preventing additional cost impact on the 3GPP standardized handset. Thus, the 3G mass market can be addressed by implementing S-DMB features in a 3G handset and incorporates multicast/broadcast via the satellite and all other services via terrestrial [MAES06],[SATI06].

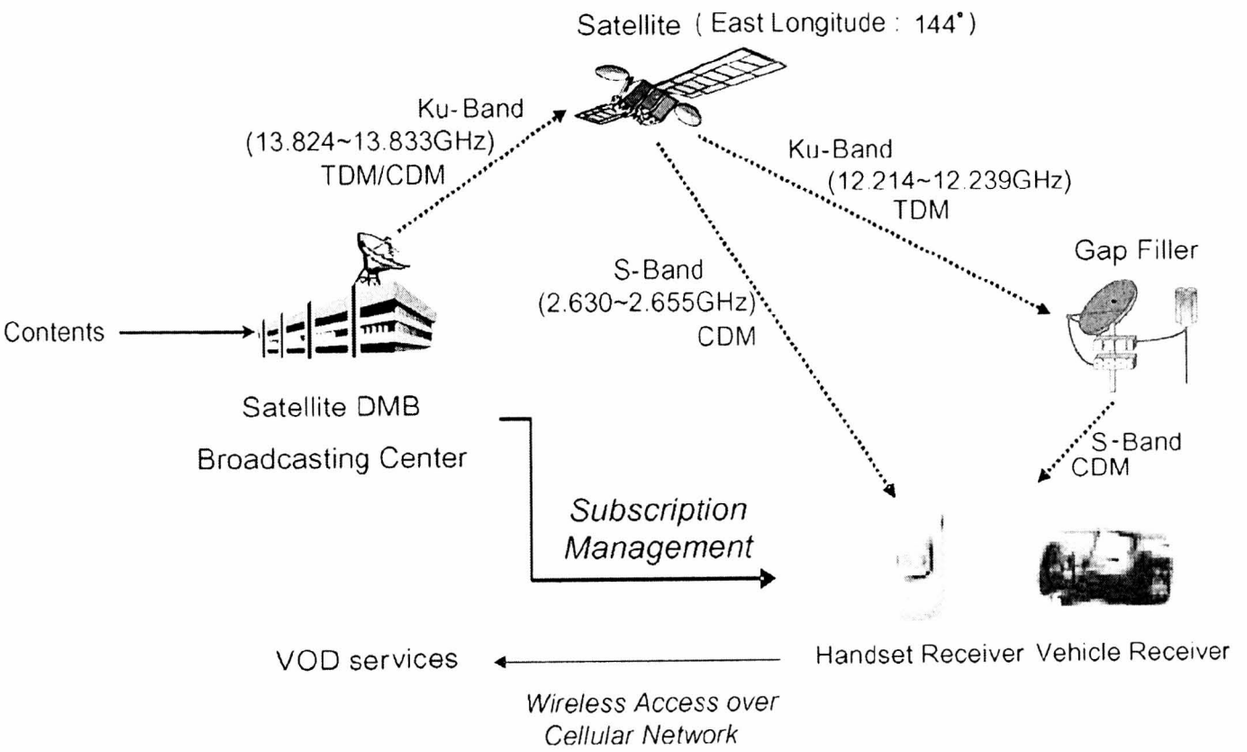

Figure 2-3: The system architecture of Korean S-DMB [SANG07]

Traditionally, satellite systems have been very successful in fixed broadcasting applications where there is no mobility presence and the signal from the satellite can be received by various powerful fixed antennas. On the other hand, in a mobile satellite system, the signals from satellites are heavily shadowed and therefore, result in a poor indoor and urban coverage. In order to rectify this problem, Intermediate Module Repeaters (IMRs) (gap-fillers) were proposed in the EU FP5 SATIN project. The IMR simply retransmits the amplified signal received from the satellite and thereby, improves the coverage of the S-DMB system [SATI06]. The terrestrial integrated components have subsequently been named Auxiliary Transmission Component (ATC) in the US

and Complementary Ground Component (CGC) in Europe [EVAN07]. Subsequent to this, two Satellite Digital Audio Radio Services (S-DARS) systems have been launched into commercial operation, Xm radio (GEO) and SIRIUS radio (HEO), incorporating the same idea of terrestrial repeaters for providing improved coverage in shadowed areas [EVAN05], [DAVA02]. Also in Asia the MBSAT, a commercial S-DMB system, was launched in May 2005 and operated by TU media in Korea which also uses terrestrial repeaters to provide seamless and high quality services to shadowed reception areas [SANG07], [MBCO08].

Note that circa 1 million users of S-DMB have built up in Korea but since the recent introduction of free services via T-DMB they only operate in remote areas and for niche programs. The MBSAT also covers Japan but the S-DMB service never succeeded there.

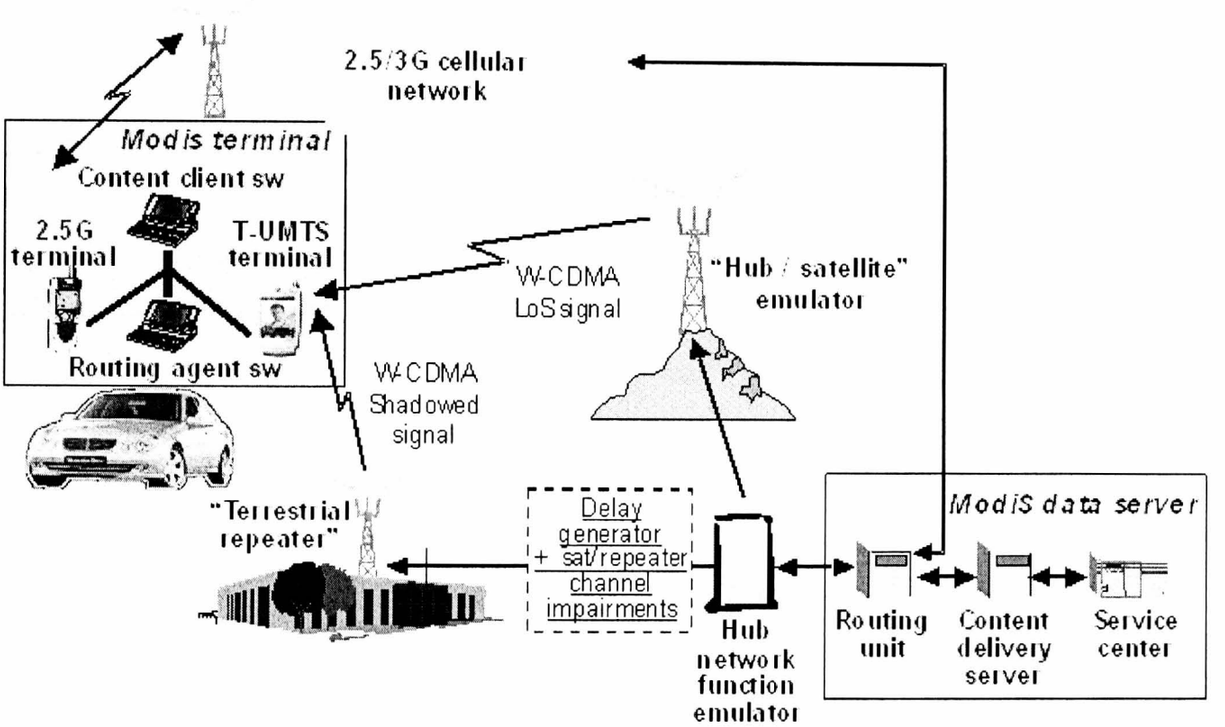

Figure 2-4: MoDiS Experimental Platform [MODI06]

The first validation and demonstration of the S-DMB innovative system concept with field trials in Europe was realized in the follow on EU project Mobile Digital Broadcast Satellite (MoDiS) [MODI06]. An experimental platform representative of the integrated satellite and terrestrial cellular network system architecture of the S-DMB was developed on the Monaco 3G network as shown in Figure 2-4. An EU FP6 project Mobile Applications and sErvices Satellite Terrestrial InteRwOrking (MAESTRO) 2004/06 addressed the whole range of issues pertinent to S-DMB from system design and demonstration to regulation and standardization [ANDR05]. In particular, it was realised that WCDMA would not provide sufficient capacity and thus Orthogonal

Frequency Division Multiplexing (OFDM) was investigated as an alternative air interface [MAES06].

Today a commercial system called SOLARIS is proposed in Europe from 2009 via a 2GHz payload (transponder) on the EUTELSAT W2A satellite. It is a joint venture between EUTELSAT and SES. In the US, ICO have launched a GEO satellite (2008) and are conducting trials using the newly standardised DVB-SH standard based on OFDM [EVAN07].

2.5 Mobile Fading Channel

2.5.1 Fundamental of Mobile channel Characteristics

When the signal travels from the transmitter to the receiver in the channels of interest, the signal suffers from different effects, which are characterised as follows:

Multipath propagation occurs as a consequence of reflections, scattering, and diffraction of the transmitted signal at man-made or natural objects. Thus, at the receiver, a multitude of waves arrives from different directions with different delays, attenuations and phases. The superposition of these waves result in amplitude and phase variations of the composite received signal.

Doppler spread is caused by relative motion between the transmitter and the receiver in the wireless channel. This in turn changes the phases and amplitudes of the signal components arriving at the receiver, resulting in a time-variant multipath propagation. This time-varying signal strength due to time-variant multipath propagation is referred to as fast fading.

Shadowing occurs due to the obstruction of the transmitted signal by e.g. building, trees and hills, which results in attenuation of the signal strength. The varying signal strength by shadowing is called slow fading and can be efficiently counteracted by power control.

Multipath fading is usually classified as slow/fast and frequency-flat/selective fading. The former is related to the rate of change or rapidity of the fading while the latter is related to the time spreading of the signal or signal dispersion. Their formal definitions are given below:

2.5.1.1 Slow or Fast Fading

The notion of slow or fast fading is related to the coherence time (T_O) of the channel that is an expected time interval over which the fading process is correlated. Moreover, the coherence time is inversely proportional to the *Doppler spread* or *fading rate*, (f_d) of the channel, i.e.

$$T_O \approx \frac{1}{f_d} \tag{2.1}$$

A channel is said to be slowly fading if the symbol interval T_S is smaller than the channel's coherence time T_O, otherwise it is considered to be fast. In slow fading, a deep fade affects many symbols leading to a burst of errors whereas in fast fading, the fade levels are essentially de-correlated from symbol to symbol [PROA95].

2.5.1.2 Frequency-Flat and Frequency-Selective Fading

The concept of frequency-flat/selective fading is related to the coherence bandwidth (f_O) of the channel that is a range of frequencies over which the fading process is correlated. Moreover, the coherence bandwidth is inversely related to the *maximum excess delay spread* (τ_{max}), which is the difference between the arrival time of the first and the last resolvable multipath.

$$f_O \approx \frac{1}{\tau_{max}} \tag{2.2}$$

Fading is said to be frequency flat if the signal's bandwidth ($1/T_S$) is much smaller than the coherence bandwidth f_O, or alternatively, when the symbol interval T_S is much larger than the maximum excess delay spread, otherwise the fading is said to be frequency-selective. In frequency-selective fading, the spectral components of the transmitted signal are affected by different amplitude gains and phase shifts whereas in frequency-flat fading, all the spectral components are affected in a similar manner [PROA95]. Those systems that experience frequency-flat fading are also called *narrowband* systems and those that experience frequency-selective fading as *wideband* systems.

In flat fading, the transmitted signal is multiplied by the complex valued fading coefficient whereas in frequency-selective fading channels, the transmitted signal gets convolved with the channel impulse response that can be represented as:

$$h(t) = \sum_{l=0}^{L-1} \alpha_l e^{-j\theta_l} \delta(t - \tau_l) \tag{2.3}$$

where α_l, θ_l, and τ_l are the amplitude, phase and delay associated with the l^{th} path and $\delta(\cdot)$ is the Dirac delta function. The amplitude of the fading α_l is usually treated as a random variable following some distribution (mostly *Rayleigh* in terrestrial radio channels). The mean square value of the fading amplitude $\overline{\alpha_l^2}$ also represents its mean power and it is customary to represent the power of each multipath along with a associated delay in a tabular format, which is called the *power delay profile* (PDP) or *multipath intensity profile* (MIP). The PDPs or MIPs of some of the integrated terrestrial-satellite channel are described in the next section.

2.5.2 Integrated Terrestrial/Satellite Channel

Satellite signals are often blocked and shadowed by trees and buildings in urban and suburban areas. However, the effect can be easily eliminated in case of fixed satellite services, for example satellite television broadcasting applications, by using a large dish antenna mounted on roof top with line of sight (LOS) connection between the satellite and the receiving antenna. On the other hand, this shadowing effect can result in significant coverage loss, even if the satellite has high elevation angle, when the satellite's signal is received by mobile terminals [DAVA02]. In order to address this problem and also to provide sufficient fade margin to the satellite–mobile terminal link, Intermediate Module Repeaters (IMR) are incorporated in the urban and suburban areas; proposed in EU FP5 SATIN project [SATI06]. A similar approach has already been considered in Xm and SIRIUS satellite radio systems in US to provide seamless radio coverage for both urban and suburban areas [DAVA02], as well as in Korea for S-DMB [SANG07].

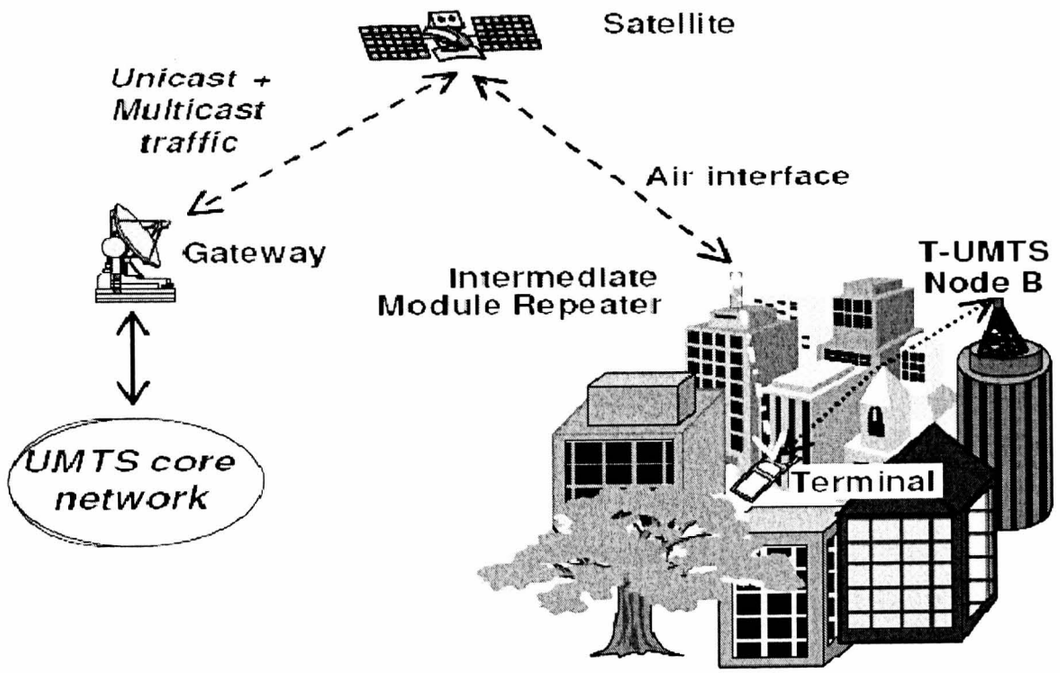

Figure 2-5: IMR concept proposed in SATIN [SEVE02]

Each IMR can be collocated with a T-UMTS Node B as shown in Figure 2-5 and simply re-transmits a replica of the transmitted satellite signal via the MSS band. Thus, it does not necessitate standards modifications and thereby, minimizes the module cost and complexity. Figure 2-6 illustrates a typical IMR configuration in the urban area where the mobile is in the proximity of the ref-IMR and the replica of the satellite signal is re-transmitted after amplification and frequency shift. Moreover, the re-transmitted signals from other IMRs will be received with different time intervals depending on the path lengths, therefore, creating 'artificial' multipath interference with a larger number of signal components and wider excess delay spread than in typical T-UMTS cellular environments [KARA04]. The resulting power delay profile (PDP) of

the channel depends on the type of environment in which the mobile receiver is located. The EU FP6 MAESTRO project investigated different Power Delay Profile (PDP) and these are tabulated in Appendix A, and are used for investigation in the remainder of this thesis [MAES06].

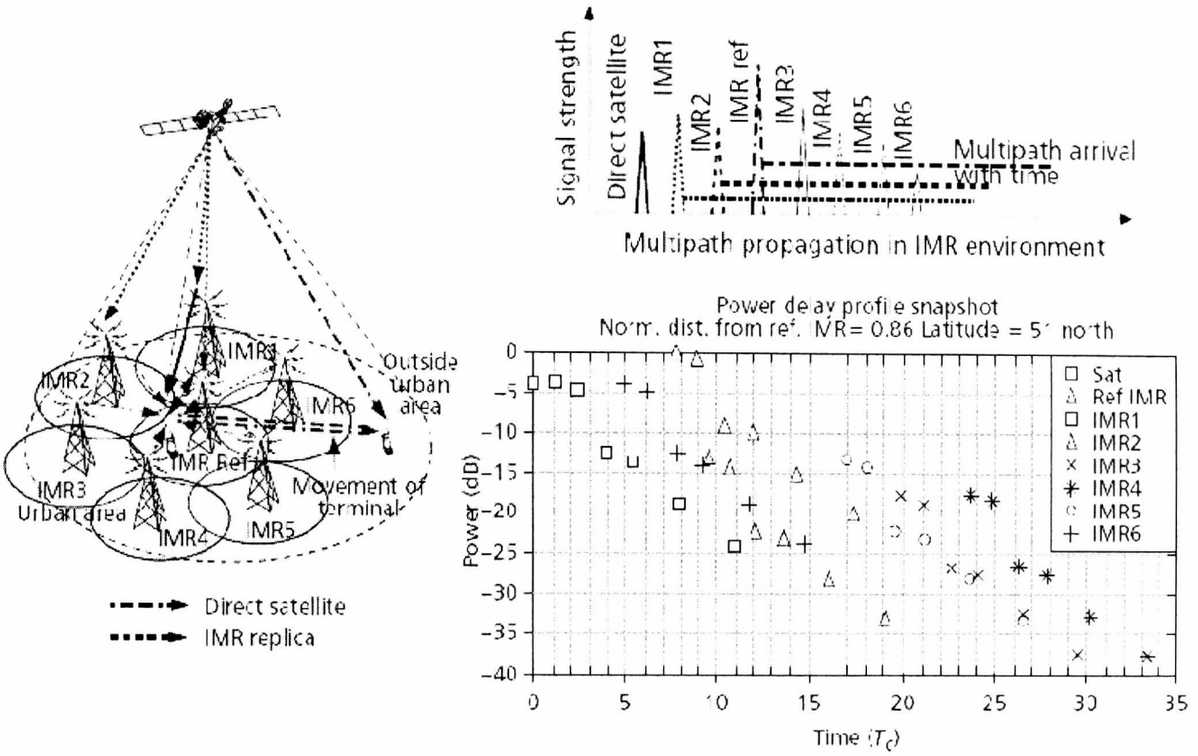

Figure 2-6: IMR layout and artificial multipath due to the introduction of IMRs. The excess delay spread, normalized in chip duration in time units (T_c), is much larger than in T-UMTS [KARA04].

In order to further reduce the cost and complexity impact of the integrated system, a reconfigurable receiver which could utilize the existing hardware available in the T-UMTS is desired. Thus, the satellite radio interface specifications must be as close as possible to the T-UMTS standard [KARA04], [SEVE02]. As already mentioned, OFDM provides greater capacity for satellite based wideband applications and this is in line with the future migration of terrestrial systems towards OFDM based air interfaces [EVAN05]. For example the EU FP6 project MAESTRO was initially focused on the use of 3GPP defined WCDMA radio interface technology for both satellite and terrestrial component. However, the project also investigated the use of OFDM for a satellite multimedia broadcasting system [CION05].

Recently OFDM has found its first application in satellite broadcasting standards, within the DVB-SH standard [DVBS08] and the ETSI-SDR standard [EVAN07], with its ability to provide reliable reception over hybrid satellite-terrestrial channels, which arise due to the use of terrestrial repeaters that facilitate coverage in urban environments [CION06]. Following the example of evolved UTRA (EUTRA) or 3GPP Long Term Evolution (LTE) in T-UMTS the next generation wireless communication systems designed as a step towards the 4G systems [3GPP08], OFDM is

currently being investigated within the ETSI Mobile Satellite Systems (MSS) group[1] as a possible upgrade of the present release of S-UMTS, and in order to ensure compatibility with its terrestrial counterparts [CION05], [LING00].

In the present standardization work on 3GPP LTE, Single Carrier Frequency Division Multiple Access (SC-FDMA), a multiple access technique similar to OFDMA, features as a strong candidate in the return link of the LTE of T-UMTS, achieving better robustness with respect to amplifier non-linearity, relative to OFDMA [3GPP814]. Thus, evaluating the performance of SC-FDMA in the return link of the satellite based system is of high relevance, if the satellite networks are to assume complementary services to the terrestrial ones. A performance evaluation study in the return link of the hybrid terrestrial-satellite channel is investigated in chapter 7 of this thesis.

2.6 Summary

We have provided a brief resume of the developments in mobile satellite communication systems in which 2G compatible GSM/GPRS systems are now in existence. No 3G comparable system apart from INMARSAT BGAN exits. It has been realised that the role of satellite is in delivery of multicast/broadcast services and these so called S-DMB systems exist in Asia using terrestrial gap fillers and are proposed for Europe and the US in 2009. It has been shown that a 3G type WCDMA air interface cannot produce significant capacity and that OFDM is a better bet. OFDM has been incorporated in a new DVB-SH standard which will be used in the new S-DMB systems. OFDM is also likely to be used in some combination of LTE, WiMax which will form the next generation of Terrestrial and Satellite standards and thus the work of this thesis investigating the transition to OFDM over satellite is extremely relevant.

[1] Known as ESTI S-UMTS until recently

Chapter Three

3 OFDM via Satellite Payloads using Amplifier Non-linearity Mitigation Techniques

3.1 Introduction

Over the past few years, Orthogonal Frequency Division Multiplexing (OFDM) has been adopted by many high-rate wireless communication systems and standards, mainly because of its cost-effectiveness in compensating the distortion introduced by the frequency selective radio channels. In particular, in the terrestrial arena OFDM is specified in Digital Video Broadcasting (DVB) standards for fixed and mobile digital multimedia broadcasting: DVB-T and DVB-H, in the Digital Audio Broadcasting (DAB) standard for digital audio broadcasting, wireless LAN and MAN standards IEEE 802.11a/g, IEEE 802.16 [ROHL99]. OFDM is also due to replace W-CDMA within the Long Term Evolution (LTE) of UMTS [3GPP814], and all indications show that OFDM will continue its domination as an air-interface option within the coming years.

As described in chapter 2, OFDM is vastly considered as a possible future upgrade in the satellite based applications. Moreover, OFDM is currently being investigated within the ETSI Mobile Satellite System (MSS) group as a possible upgrade of the present release of S-UMTS, and in order to ensure compatibility with its terrestrial counterpart [CION05], [LING00]. In the performance evaluation of OFDM over satellite links within [ETS443], emphasis is given on the impact of the non-linear response of the on-board Travelling Wave Tube Amplifier (TWTA). This becomes an important issue because of the high PAPR characteristics of OFDM signals, which lead to increased sensitivity to non-linear effects and this in turn is translated to degraded link performance and more severe out-of-band emission levels, relative to the traditional TDM transmission.

This chapter first introduces the basic concepts in OFDM and also provides the mathematical modelling of signals, with reference to a generic OFDM system. The major advantages and drawbacks of OFDM systems are then discussed, giving special consideration to non-linear distortion introduced by the non-linear on-board TWTA. From this point, the rest of the chapter is dedicated to the specific characterisation of the non-linear distortion effects caused by the

TWTA, and possible transmitter based compensation techniques. A literature survey of these mitigation techniques is given, which covers power back-off, PAPR reduction techniques and amplifier linearization techniques.

3.2 Principle of OFDM

3.2.1 Multicarrier Modulation

The concept of using parallel data transmission and frequency division multiplexing (FDM) (i.e. multicarrier transmission) was first proposed in 1960s. In such a system, as shown in Figure 3-1, the total signal bandwidth, W, is divided equally into a number of, N,non-overlapping frequency sub-channels. Each sub-channel is modulated with independently generated narrow-band signals and then these sub-channels are frequency multiplexed. Guard bands are used in order to avoid spectral overlapping and thus eliminate the inter-channel interference. At the receiver, filters are used to separate the signals arriving from different sub-channels [RAMJ00], [HARA03].

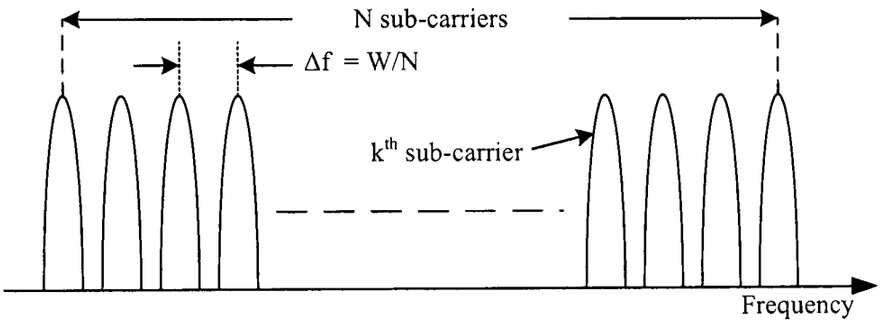

Figure 3-1: Sub-division of Bandwidth W into N Sub-channels of equal bandwidth

The process of generating the traditional multicarrier signal is demonstrated in Figure 3-2. Furthermore, the traditional multicarrier signal can be mathematically represented as a combination of modulated sub-carriers using the following equation [HARA03]:

$$s(t) = \sum_{k=0}^{N-1} a_k \varphi_k(t) \tag{3.1}$$

Where

a_k - data symbol modulating the k^{th} sub-carrier

$\varphi_k(t)$ - modulation signal at the k^{th} sub-carrier

$s(t)$ - multicarrier modulated signal

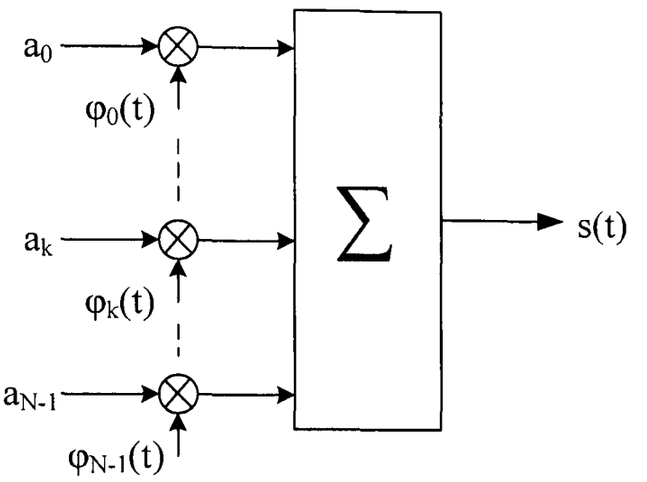

Figure 3-2: Process of Generating the Multicarrier Modulation

In a multicarrier system, a deep fade in the channel can only affect a small percentage of the sub-carriers and these erroneous sub-carriers can be corrected by using a powerful error control coding. On the other hand, in the conventional single carrier system, the symbols are sequentially transmitted with each data symbol occupying the entire bandwidth available for transmission. Thus, a deep fade in the channel can cause the entire link of a single carrier system to fail [HARA03]. Moreover, the multicarrier transmission makes the resulting symbol duration relatively larger than the multipath excess delay spread and this solves the inherent Inter Symbol Interference problem encountered in high-rate single carrier systems. Using the non-overlapping sub-carriers in frequency domain (frequency limited pulse) leads to poor spectral efficiency and thus, it is not attractive to use multi-carrier transmission as a solution to the multipath self-interference problem This is solved by OFDM, where the orthogonality of sub-carriers allows overlapping sub-channels without causing harmful Inter-Channel Interference (ICI) [RAMJ00].

3.2.2 OFDM Characteristics

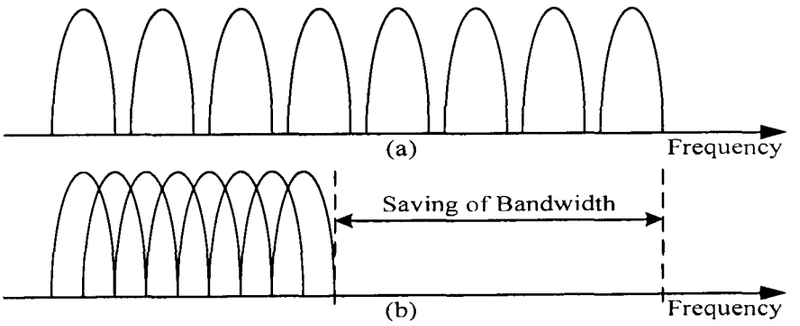

Figure 3-3: Concept of OFDM signal: (a) Conventional multicarrier technique, and (b) orthogonal multicarrier technique

As explained in section 3.2.1, OFDM is a special form of the multicarrier modulation technique which employs spectrally overlapping sub-carriers in the frequency domain. Figure 3-3 illustrates an OFDM system which uses spectrally overlapping sub-carriers and thus, saves almost 50 % of bandwidth.

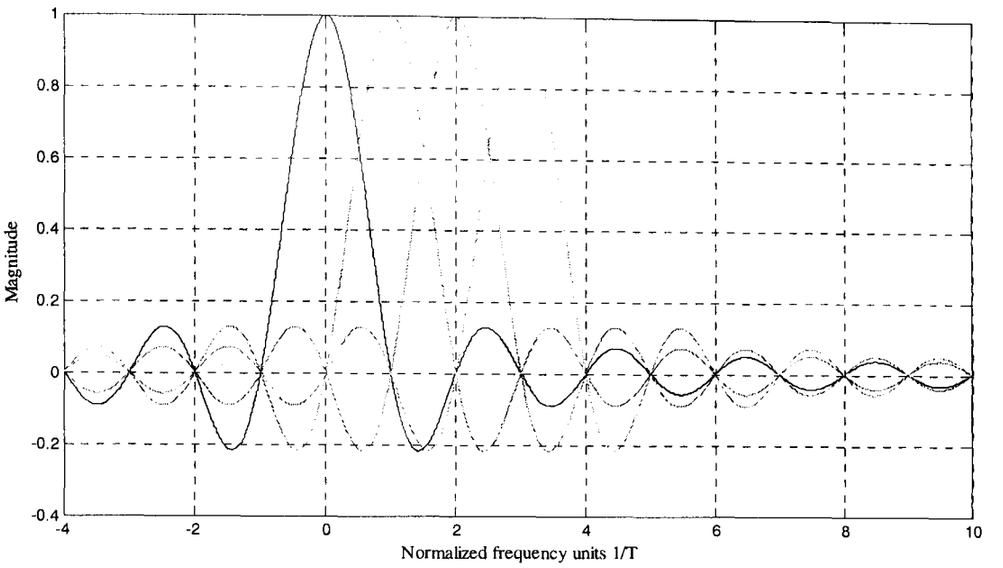

Figure 3-4: Overlapping spectrum of an OFDM signal for Number of Sub-carriers = 4

Since the sub-carrier waveforms are restricted in the time domain, the spectrum of individual sub-carriers is a 'sinc' function in the frequency domain, illustrated in Figure 3-4. Moreover, the spectrum does not cause any interference at the carrier locations due to its orthogonal nature. Figure 3-4 also demonstrates how frequency synchronization is crucial for OFDM systems. In the absence of very accurate carrier synchronization, sub-carriers will not be sampled at their peak energy points and this will lead both to collecting interfering energy from adjacent sub-channels, and degrading useful signal energies.

According to [3GPP892], [MUQU02], [ZHEN00], there are several flavours of OFDM system available, however, this thesis focuses on the Cyclic Prefix (CP) based OFDM, as this has been adopted by most OFDM-based terrestrial and satellite standards : IEEE 802.11a/g/n, IEEE 802.16, DVB-T/H/SH, DAB, Asynchronous Digital ADSL, among others.

Before describing the complete OFDM signal model, it is necessary to introduce some of the terminologies related to OFDM, which we do by following [3GPP892].

3.2.3 Useful OFDM Symbol Signal Generation

The OFDM signal without the CP insertion is called the 'Useful OFDM signal'. The OFDM signal is made up of a sum of N complex orthogonal sub-carriers (indexed with $k = \{0,1,2, \ldots \ldots, N-1\}$) , each one independently modulated by using complex modulation

symbol $X_{m,k}$, where m is the time index and k is the sub-carrier index. Thus, within the symbol duration T the following signal of the m^{th} OFDM block is formed [JAYA02]:

$$x_m(t) = \frac{1}{\sqrt{N}} \sum_{k=0}^{N-1} X_{m,k} e^{j2\pi n \Delta f t} g_n(t - mT) \tag{3.2}$$

where $g_n(t)$ is a rectangular pulse applied to each sub-carrier [ROHL99]. The total continuous time signal $x(t)$ consisting of all OFDM blocks is given by:

$$x(t) = \frac{1}{\sqrt{N}} \sum_{m=0}^{\infty} \sum_{k=0}^{N-1} X_{m,k} e^{j2\pi n \Delta f t} g_n(t - mT) \tag{3.3}$$

As consecutive OFDM symbols do not overlap, we can consider a single OFDM symbol $x(t)$ where $(m = 0)$, without loss of generality. Moreover, the corresponding discrete time representation of the OFDM symbol $x(t)$ can be obtained by appropriate sampling. Since the bandwidth of an OFDM signal is $B = N\Delta f$, the signal can be completely determined by its samples if the sampling time $\Delta t = \frac{1}{B} = \frac{1}{N\Delta f}$. The samples of the signal are written as

$$x_n = \frac{1}{\sqrt{N}} \sum_{k=0}^{N-1} X_k e^{j2\pi nk/N}, \qquad n = 0,1,2,\dots,N-1. \tag{3.4}$$

Furthermore, equation (3.4) describes exactly the N-point Inverse Discrete Fourier Transform (IDFT) of the input data X_k, $k = 0,1,2,\dots,N-1$. Thus, the useful OFDM signal can be generated easily by applying the Inverse Fast Fourier Transform (IFFT) to the length-N modulated symbols and this will be used in Sections 3.2.5 of the chapter to describe the OFDM system model.

Similar to the explanation in Section 3.2.1, the multicarrier nature of OFDM provides robustness to multipath interference incurred by the frequency selective channel. The Guard Interval (GI), in the form of CP, which is inserted in between the consecutive OFDM symbols at the transmitter, plays a key role in facilitating this robustness. In the next Section, it is elaborated how the CP helps to eliminate the Inter-Symbol Interference (ISI) or Inter-Block Interference (IBI) and Inter-Carrier Interference (ICI).

3.2.4 Guard Time and Cyclic Prefix

One of the main properties that makes OFDM an appealing solution is its computational efficiency; low complexity equalization especially for high data rate transmissions [ZHEN00]. In most OFDM applications, a GI is inserted between consecutive OFDM base-band signal blocks to prevent Inter-Symbol Interference (ISI). This guard time is normally chosen larger than the excess delay spread so that multipath components from one symbol do not interfere with the next one.

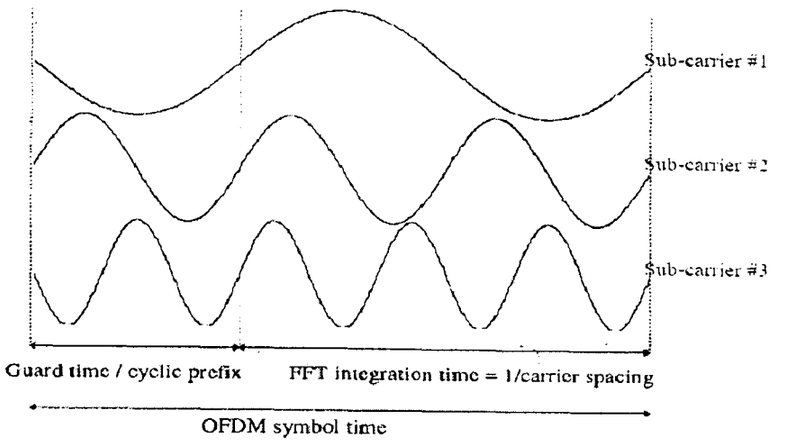

Figure 3-5: Demonstration of Cyclic Extension for OFDM with three sub-carriers [RAMJ00]

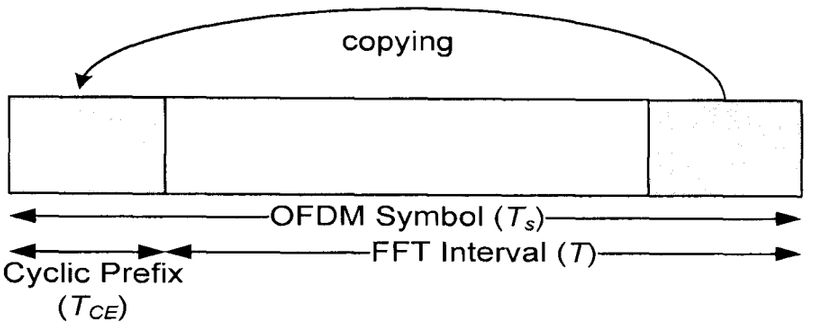

Figure 3-6: Cyclic Prefix Insertion

If the guard interval is composed of a 'silent period' in the time-domain, the system will be free from ISI due to the sufficient inter-symbol distances. However, the system may suffer from inter-carrier interference (ICI) causing the sub-carriers to lose orthogonality. Hence, to overcome the ICI problem, the OFDM symbol is cyclically extended in the time-domain, so that any sub-carrier coming from direct or delayed replicas of the signal will continue to have an integer number of cycles within an FFT interval of duration T. This ensures orthogonality among the different sub-channels as long as the delay remains smaller than the selected guard time [RAMJ00]. In general, this cyclic extension (CE) is implemented in the form of a cyclic prefix (CP) as shown in Figure 3-5, where the extended OFDM symbol interval $T_s = T + T_{CE}$ is represented for only three separate sub-carriers.

In baseband processing terms, the CP is attached by copying the N_p samples at the end of the useful OFDM symbol according to the operation illustrated in Figure 3-6.

3.2.5 OFDM Signal Model

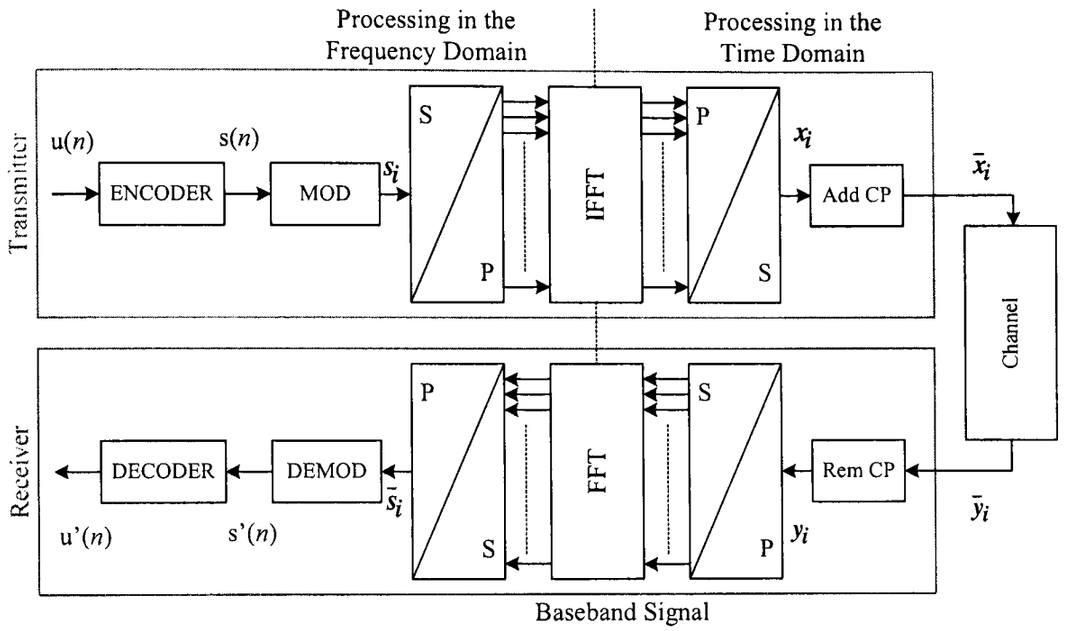

Figure 3-7: OFDM Baseband System Model

In order to describe the OFDM signal model, a discrete-time baseband signal model, shown in Figure 3-7, is used. In the model, it is assumed that the frequency offset estimation and timing is recovered perfectly at the receiver.

In OFDM transmission, a serial data stream $u(n)$ of information bit is first passed through an error control encoder and then modulated to generate information symbols denoted as $s(n)$. The sequence $s(n)$ is then grouped into blocks of size K, $\mathbf{s}_i = [s_i(1), s_i(2), \ldots\ldots, s_i(K)]$, which are subsequently processed by an Inverse Fast Fourier Transform (IFFT):

$$\mathbf{x}_i = \mathbf{F}^H \mathbf{s}_i \tag{3.5}$$

Where $\mathbf{F}$ is the $K \times K$ Fast Fourier Transform (FFT) matrix with $[F]_{p,q} = K^{-1/2} exp(-j2\pi pq/K)$.

A cyclic prefix (CP) of length L is then inserted in $\mathbf{x}_i$to yield $\bar{\mathbf{x}}_i = \mathbf{T}_{CP}\mathbf{x}_i$ of length $(K + L)$, where $\mathbf{T}_{CP} = [\mathbf{0}_{L\times(K-L)}, \mathbf{I}_{L\times L}; \mathbf{I}_{K\times K}]$ describes the CP insertion by concatenating the last L rows of an $K \times K$ identity matrix $\mathbf{I}_{K\times K}$. Thus, the resulting signal following the IFFT and CP insertion can be expressed as:

$$\bar{\mathbf{x}}_i = \mathbf{T}_{CP}\mathbf{F}^H \mathbf{s}_i \tag{3.6}$$

Assuming perfect symbol and block synchronization at the receiver, the received signal can be expressed as:

$$\bar{\mathbf{y}}_i = \mathbf{H}_0\bar{\mathbf{x}}_i + \mathbf{H}_1\bar{\mathbf{x}}_{i-1} + \mathbf{v}_i \tag{3.7}$$

Where $\mathbf{v}_i$ is additive white Gaussian noise (AWGN) with power σ^2 and matrices $\mathbf{H}_0$and $\mathbf{H}_1$are $(K+L)\times(K+L)$ in size with the following structures:

$$\mathbf{H}_0 = \begin{bmatrix} h_0 & 0 & 0 & \cdots & 0 \\ \vdots & h_0 & 0 & \ldots & \vdots \\ h_l & \cdots & \ddots & \cdots & \vdots \\ \vdots & \ddots & \vdots & \ddots & 0 \\ 0 & \cdots & h_l & \cdots & h_0 \end{bmatrix} \quad and \quad \mathbf{H}_1 = \begin{bmatrix} 0 & \cdots & h_l & \cdots & h_1 \\ \vdots & \ddots & 0 & \vdots & \vdots \\ 0 & \cdots & \ddots & \cdots & h_l \\ \vdots & \vdots & \vdots & \ddots & \vdots \\ 0 & \cdots & 0 & \cdots & 0 \end{bmatrix}$$

and $\mathbf{h}$ is the channel impulse response with taps values $[h_0, h_1, \ldots\ldots, h_l]$, $l+1 \le L$.

At the receiver, the CP is removed prior to FFT processing and this can be expressed by a linear transformation matrix: $\bar{\mathbf{R}}_{CP} = [\mathbf{0}_{K\times L}, \mathbf{I}_{K\times K}]$. Hence, the received signal at the receiver:

$$\bar{\mathbf{s}}_i = \mathbf{F}\bar{\mathbf{R}}_{CP}\bar{\mathbf{y}}_i \tag{3.8}$$

Expanding equation (3.8), we have:

$$\begin{aligned} \bar{\mathbf{s}}_i &= \mathbf{F}\bar{\mathbf{R}}_{CP}\mathbf{H}_0\mathbf{T}_{CP}\mathbf{F}^H\mathbf{s}_i + \mathbf{F}\bar{\mathbf{R}}_{CP}\mathbf{v}_i \\ &= \mathbf{F}\tilde{\mathbf{H}}\mathbf{F}^H\mathbf{s}_i + \boldsymbol{\eta}_i \end{aligned} \tag{3.9}$$

Where $\tilde{\mathbf{H}}$ is a circulant-matrix which is defined only by the first row; the rest of the rows are determined by cyclically shifting the previous ones to the right. In particular, the first row of $\tilde{\mathbf{H}}$ is $[h_0, 0,0, \ldots\ldots, 0,0, h_l, h_{l-1}, \ldots\ldots, h_1]$. Using the algebraic property of circulant matrices, that they are diagonalized by pre-multiplication with the DFT and IDFT matrices, respectively, the overall system input-output relationship reduces to:

$$\bar{\mathbf{s}}_i = \boldsymbol{\Lambda}\mathbf{s}_i + \boldsymbol{\eta}_i \tag{3.10}$$

Where $\boldsymbol{\Lambda} = \mathbf{F}\tilde{\mathbf{H}}\mathbf{F}^H$, is a $K\times K$diagonal matrix whose diagonal elements are channel responses at corresponding sub-carrier frequencies. It is noted that due to the orthogonality of $\mathbf{F}$ the statistics of Gaussian noise terms do not change. Equalization can be performed in the frequency domain simply by multiplying each element of $\bar{\mathbf{s}}_i$ by a correction term which can be determined based on the zero-forcing or MMSE criteria, yielding: $\hat{\mathrm{s}}_i(n) = \bar{\mathrm{s}}_i(n)/\Lambda_{nn}$ and $\hat{\mathrm{s}}_i(n) = {\bar{\mathrm{s}}_i(n)conj(\Lambda_{nn})}\big/{|\Lambda_{nn}|^2 + \sigma^2}$, respectively. The selection of the design parameters and their corresponding impact on the system are addressed in the next section.

3.2.6 Impact of OFDM parameters

In this sub-section, the design criteria on some of the OFDM parameters are briefly exposed, such as: Guard Interval, Number of Sub-carriers, and OFDM symbols duration.

Impact of Guard Interval

The length of the CP must be designed so that it absorbs the signal energy dispersed by the multipath channel. Thus by choosing the CP-length to be greater than the maximum multipath excess delay spread of the channel, the ISI and ICI problems are avoided .Thus the design condition is,

$$T_{CE} \geq \tau_{max} \tag{3.11}$$

where τ_{max} is the maximum delay spread which in practice is characterised through channel measurement campaigns within the operating physical environment.

Impact of Symbol Duration

As stated in the previous Section, the length of the CP should be larger than the delay spread of the channel. However the CP introduces information and energy utilisation overheads and thus it should be much smaller than the symbol duration in order to obtain the maximum possible throughput. Thus,

$$T_s \gg T_{CE} \tag{3.12}$$

On the other hand, the larger the symbol duration is the more sensitive to fast temporal fading, especially if the symbol period is larger than the channel coherence time. Therefore, the inter-carrier orthogonality is not maintained and the performance in the fast temporal fading will be degraded [3GPP892]. In other words, the symbol duration has direct connection with the selection of suitable number of sub-carriers. But, the number of sub-carriers, on the other hand, is limited by the coherence bandwidth of the channel.

Impact of Inter-carrier Spacing

Sub-dividing the bandwidth into a large number of individual sub-bands makes the bandwidth of these sub-channels smaller relative to the overall bandwidth. With sufficient number of sub-carriers, the inter-carrier spacing can be made much narrower than the coherence bandwidth of the channel. Due to the inverse proportional relationship between the coherence bandwidth and the excess delay spread of the channel, the inter-carrier spacing is generally designed such that:

$$\Delta f \ll \frac{1}{\tau} \tag{3.13}$$

In this case, the channel is converted into a number of flat fading channels and the individual fading on each sub-carrier is modelled as a constant complex gain. Furthermore, the channel equalization is performed simply by dividing received data with the corresponding fading coefficients of the particular FFT grid [3GPP892], [FAZE03].

Therefore, for any realization a trade-off between the number of FFT points, the sensitivity to the Doppler and the rate losses due to the CP has to be found [FAZE03].

Having provided a short description of the principles of OFDM, the next sub-section will discuss the advantages and drawbacks of OFDM when employed in real communication systems.

3.2.7 Advantages and Drawbacks of OFDM

According to [FAZE03], [RAMJ00], [HARA03], some of the strong motivations behind OFDM for its increasing popularity, especially in high data rate systems, are as follows:

- Simple digital implementation is possible by using the FFT operations. However, OFDM was not used some time due to the high complexity associated in realizing it in practical systems. Due to subsequent advances in digital signal processing, the implementation of OFDM systems has now become a very easy task.
- By providing sufficiently large CP and thereby avoiding the ISI and ICI, a low complexity receiver is possible. This feature of OFDM is significant in comparison with the other candidates especially for high data rate systems.
- High spectral efficiency due to nearly rectangular spectrum for large number of sub-carriers and due to the overlapped nature in the frequency domain.
- Having the Channel State Information at the transmitter, individual sub-carriers can be adaptively employed via differently modulated symbols according to the transmission conditions.

In spite of the aforementioned attractive features of OFDM, it also has some drawbacks which are briefly listed below:

- OFDM systems exhibit high Peak-to-Average Power Ratio (PAPR), as a consequence of independently modulated sub-carriers, and therefore, require highly linear power amplifier at the analogue front end of the transmitter.
- Although the guard interval plays the main role in realizing a low complexity receiver for OFDM systems, it causes loss in spectral efficiency.
- Due to the multicarrier nature of OFDM, it is more sensitive to Doppler offsets than the single carrier modulated systems. Thus, very accurate frequency synchronization is required.

- Timing synchronization is important to locate the FFT windowing operation.
- Coding techniques are extremely important for OFDM to realize the frequency diversity of OFDM systems. Otherwise, the system performance will be dictated by the deeply faded sub-carriers in the OFDM system [ZHEN00].

All of the aforementioned disadvantages of OFDM are common to both terrestrial-based and satellite-based systems. There are several approaches to be found in the literature which mitigate these effects for terrestrial systems. However, these approaches are not directly applicable to satellite- based systems due, in particular, to its architectural differences. For example, the onboard high power amplifier and the modulator are not physically co-located, as in terrestrial system architecture. This introduces a complication, for instance, in the design of digital amplifier linearization techniques, which need to have access to the amplifier's output in order to train their linearization parameters.

This thesis mainly focuses on the first drawback and deals with the possible compensation approaches when employing OFDM in the satellite environment with a non-linear on-board amplifier. The rest of the thesis assumes that the considered satellite system is ideally compensated against the other drawbacks listed above.

3.3 Non-Linearity Effects of Power Amplifiers and compensation techniques

3.3.1 Power Amplifiers (PA)

Power Amplifiers (PA) are a crucial component, particularly in satellite communication systems, which are power-limited and every dB of amplifier gain can have a large impact on the system's capacity. However, due to their non-linear characteristics, they cause severe non-linear distortions to signals; particularly those whose instantaneous power fluctuations come close to the PA's saturation power level. Even a small amount of non-linear distortion can lead to undesirable spectral re-growth and in-band distortion. The spectral re-growth causes Adjacent Channel Interference (ACI), whereas the in-band distortion increases the Bit Error Rate (BER) performance of the system. In order to keep the ACI within acceptable limits, the regulatory bodies impose stringent spectral masks on the transmitted signals [DANI08], [CHEN99].

In general, the PA's instantaneous nonlinearity characteristics are represented using amplitude distortion (AM-AM characteristics) and phase distortion (AM-PM characteristics). Figure 3-8 and

3-9 illustrate the measured AM-AM and AM-PM characteristics[2] respectively of an S-band on-board TWTA. There are three different PA operation regions which can be seen from these figures: a linear region where the output signal is simply a scaled version of the input signal, a non-linear region or compression region where the PA's gain decreases, and a saturation region where the output signal reaches maximum [CHEN99]. Operating the HPA in the saturation region provides highest power efficiency [COST99], [CION06], but has other disadvantages.

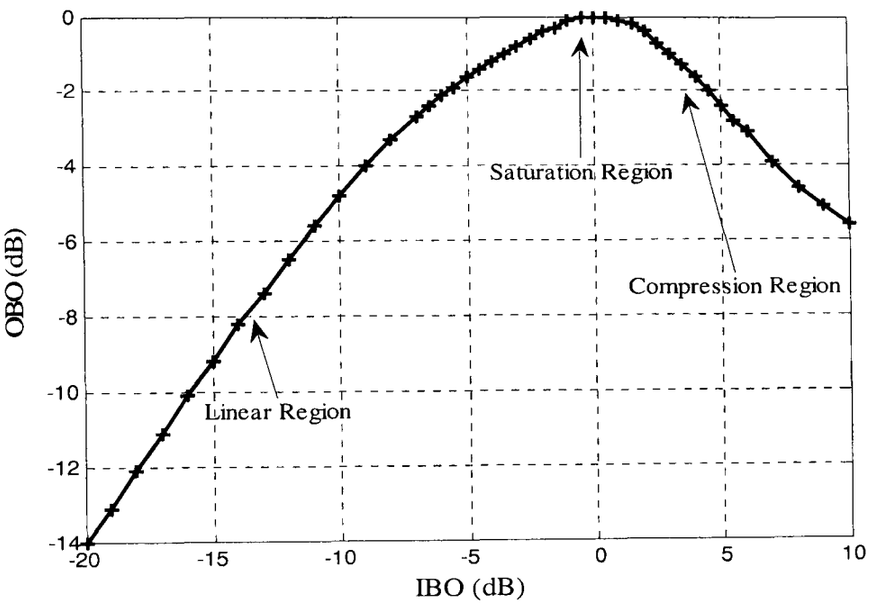

Figure 3-8: S-band TWTA AM-AM Characteristics [CION06]

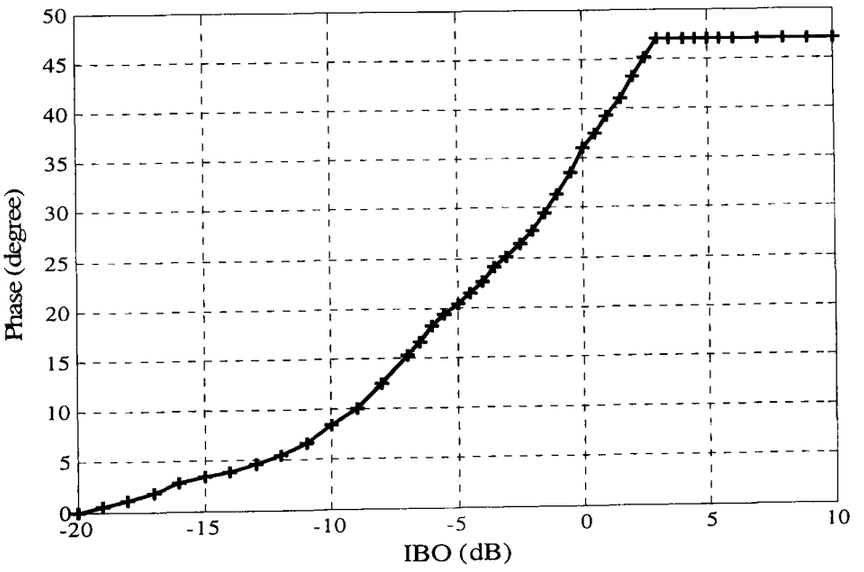

Figure 3-9: S-band TWTA AM-PM Characteristics [CION06]

[2] The TWTA characteristics were obtained within the EU FP6 MAESTRO project (see [CION05])

Furthermore, in literature, the PAs are often assumed to have no memory effects on the input signal. In other words, it is assumed that the PA's output only depends on the PA's present input, exhibiting static nonlinear characteristics (both AM-AM and AM-PM) and therefore, it is generally termed as a memory-less PA.

However, this assumption tends to be unrealistic for signals with wider bandwidth. The PA begins to exhibit memory effects, which can be explained both from a time-domain and frequency domain perspective. In the time domain, the PA's output will not only be decided by the PA's present input signal but also by the PA's past input signals depending on the memory level. While in the frequency domain, the memory effect will be reflected by frequency dependency on the non-linear characteristics of the PA. There are several system models that have been considered in the literature for investigating the memory effects of PA's eg: Volterra series model [CHAN95], Hammerstein model [DING04], memory-polynomial model [DING04], [KIMJ01]. The symptoms of the memory effect in the non-linear PA include: (i) scattering or hysteresis of the AM-AM and AM-PM curves, (ii) asymmetry in the inter-modulation distortion (IMD) products; (iii) IMD variation as a function of tone spacing in a two-tone test [HYUN03].

According to [MOHA04], the amplifiers with relatively wide modulation bandwidth (baseband), such as applications requiring more than 20 MHz, start to heavily suffer from memory effects. Due to this fact, the thesis concentrates on the memory-less power amplifier models, as shown in Figure 3-8 and 3-9, for investigating the non-linear distortion of OFDM signals.

3.3.2 Non-Linear Distortion on OFDM signals

As discussed in section 3.2.7, an important drawback of OFDM is its high envelope fluctuation due to the IFFT processing at the transmitter; resulting from a large number of independently modulated sub-carriers [LIUW99]. The random distribution of the OFDM signal's envelope results in the amplifier being driven in an uncontrolled way in all of its operating regions, including the compression region, which is highly non-linear. Consequently, OFDM signals are more vulnerable to amplifier non-linear distortions, relative to more traditional single carrier transmission systems.

Due to this multicarrier nature of the OFDM signal, the TWTA introduces severe inter-modulation distortion (IMD). The inter-modulation frequency components falling in-and out-of-bands are then associated with signal error probability degradation and signal spreading, respectively [COST99], [SANT98]. Figure 3-10 shows a typical example for the spectral spreading effect of the OFDM signal with 64 sub-carriers, when it is passed through the non-linear TWTA characteristics represented by Figure 3-8 and Figure 3-9. In addition to the spectral

spreading effect, there will also be in-band distortion which will increase the BER performance of the system.

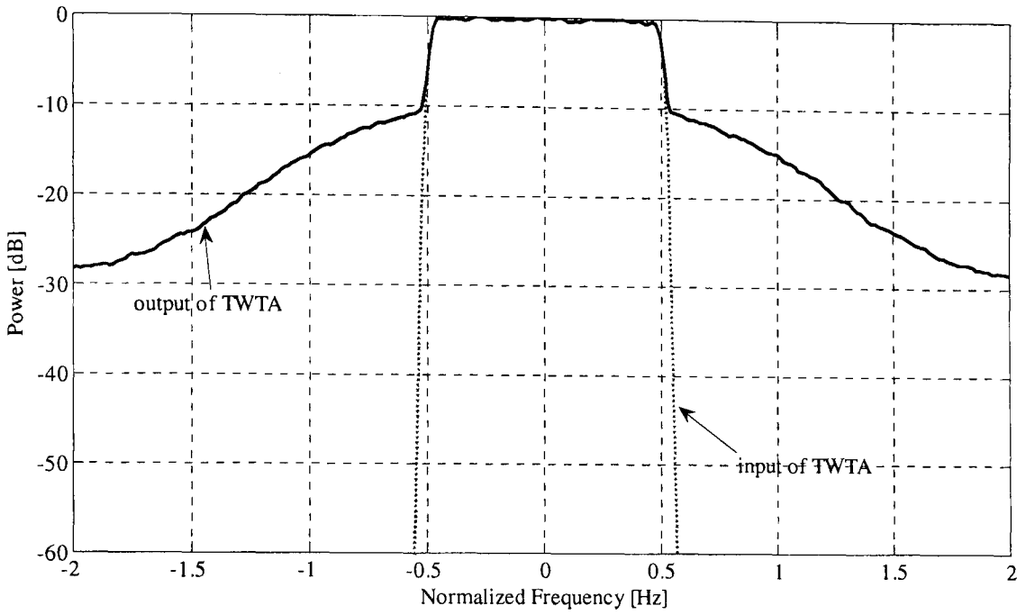

Figure 3-10: Spectral Growth caused by the TWTA

In order to avoid these degradations, a straight forward option would be to incorporate a TWTA with larger linear range or higher maximum output rating in systems employing OFDM modulations. However, such an amplifier leads to a less power efficient communication system. Furthermore, building such a TWTA with maximum power rating is very expensive and therefore, the cost of the system can rise sharply which is affected not only by the TWTA itself but also by some TWTA associated components such as heat sinks, fans etc. [DANI08].

Therefore, it is essential to consider alternative approaches for compensating the non-linear distortion introduced by the TWTA on OFDM signals. The next sub-section introduces various techniques, in particular for OFDM systems, for compensating the non-linear distortion.

3.3.3 Compensation Techniques

In order to obtain a power efficient system with tolerable level of BER and out-of band emissions, the non-linear distortion of the TWTA must be mitigated in some manner and thus allow the TWTA to be operated close to saturation. To achieve this goal, there are different approaches available in the literature which provides compensation at the transmitter [KENI02], [KATZ01], [SEUN05] or at the receiver [QUAC93], [CHEN03]. For the case of transmitter based compensation, the signal to be transmitted is modified prior to its transmission through the TWTA and therefore, mitigates the effect of both in-band distortion and out-of band distortion. On the other hand, in the receiver based compensation, only the in-band distortion can be mitigated and it is still necessary to operate the power amplifier in a region which creates interference falling

within acceptable spectral mask requirements imposed by regulation. Therefore, only the transmitter based approaches are investigated in this thesis.

In the literature, several transmitter-based mitigation techniques have been proposed for OFDM based systems and they can be further grouped into three different main classes, namely: Power back-off method [KENI02], PAPR Reduction Methods [SEUN05], [MULL97], [XIAO98] and Amplifier Linearization Methods [KATZ01], [KENI02].

In the following sections Power back-off method, PAPR Reduction Method and Amplifier Linearization Methods are introduced, and the related literature is also reviewed.

3.4 Power Back-Off

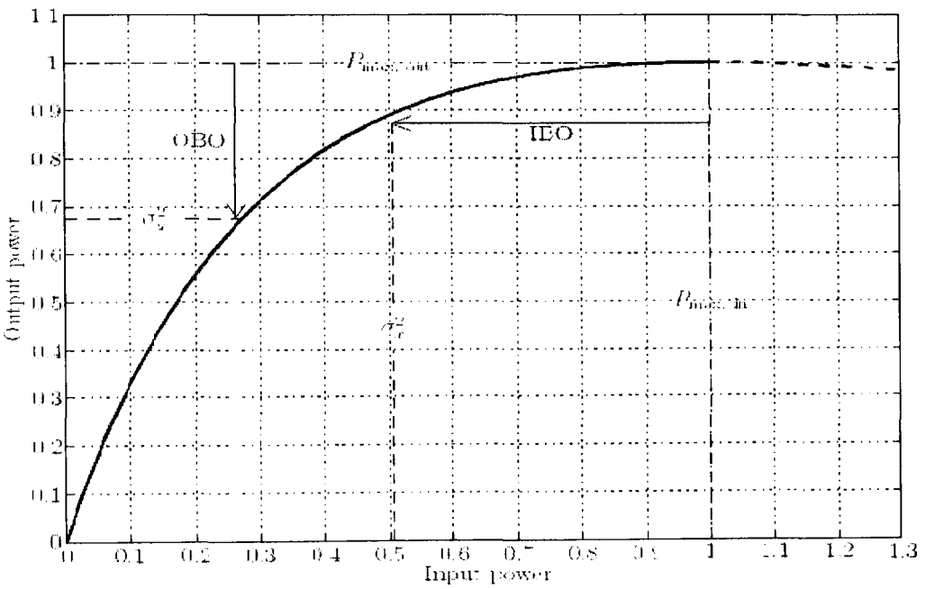

Figure 3-11: Definition of IBO and OBO

According to this approach, the input signal is attenuated ('backed-off') to ensure the amplifier operates in the linear region and therefore, the non-linear distortion of the HPA will be reduced by the amount of back-off level which is measured using the two quantities such as: Input Back-Off (IBO) and Output Back-Off (OBO). They are defined as [COST99]:

$$IBO = 10\log_{10}\frac{P_{max,in}}{\sigma_x^2}\ [\text{dB}] \quad \text{and} \quad OBO = 10\log_{10}\frac{P_{max,out}}{\sigma_y^2}\ [\text{dB}] \tag{3.14}$$

where $P_{max,in}$ and $P_{max,out}$ are the input and output saturation powers and σ_x^2 and σ_y^2 are the average power of the input and output signals. Either IBO or OBO can be used to specify the PA operating point. OBO is useful to quantify how much output power the amplifier generates compared with the maximum available power. Figure 3-11 illustrates the definition of IBO and OBO parameters.

On the other hand, using back-off to mitigate the non-linear distortion comes at the expense of decreased power efficiency. Traditionally the optimal back-off level is obtained at the point where the Carrier over Noise plus Inter-modulation power (C/(N+Intermodulation)) is maximised, as shown in Figure 3-12, although this optimal point needs also to satisfy the out-of-band emission constraints.

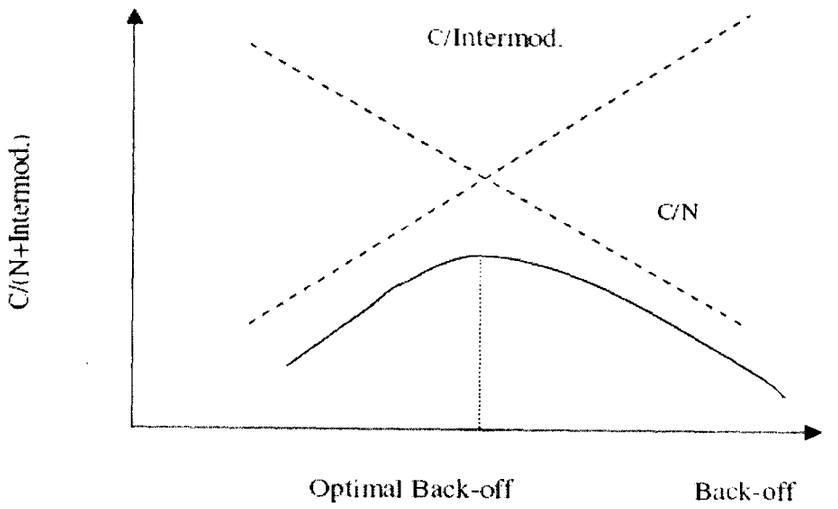

Figure 3-12: Design of optimal Back-off point

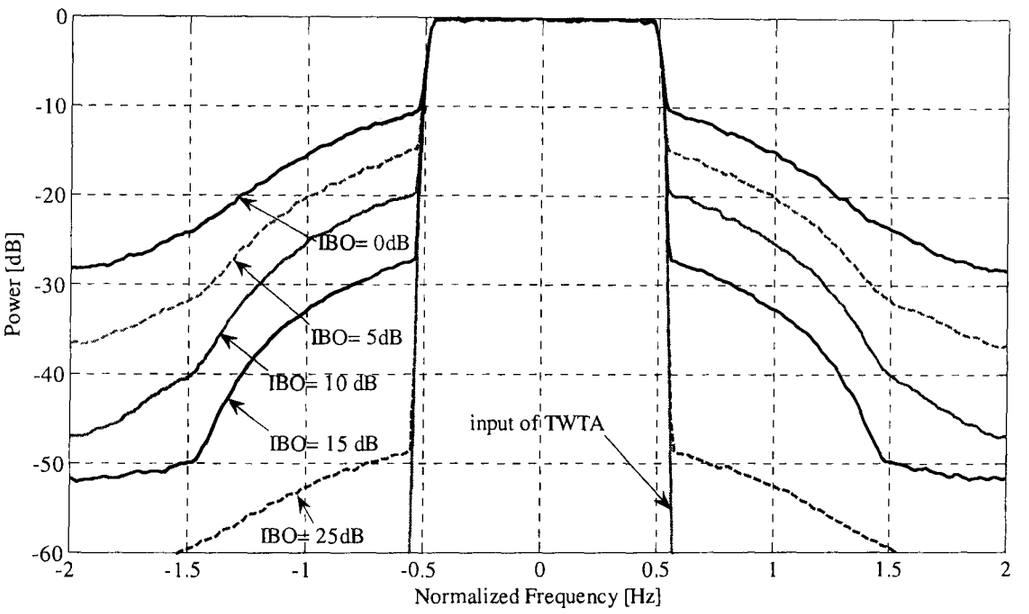

Figure 3-13: Effect different input back-off (IBO) on the spectral re-growth of the output signal

Figure 3-13 shows the spectral spreading of the OFDM signal, with 64 subcarriers, for different *IBO* level. It is observed that larger *IBO* levels are required to reduce the spectral spreading of the output signal. As explained in Figure 3-11, the larger *IBO* level will reduce the output power at

the TWTA output and thereby, cause a significant reduction in the power efficiency of the system. Due to these reasons, the larger IBO is not an attractive option for satellite based systems due to its inherent power limitation by the on-board power sources [SANT98].

In order to minimise the required back-off level, in order to achieve reasonable power efficiency, and at the same time satisfy the spectral mask constraints, other compensation approaches must be incorporated with the system design. The next section describes the different schemes proposed in the literature for PAPR reduction method and amplifier linearization technique.

3.5 PAPR Reduction Method

As already explained a significant disadvantage associated with the OFDM signal is its large envelope fluctuation, and this is usually measured using the Peak-to-Average Power Ratio (PAPR) of the signal. Looking at the IFFT operation at the transmitter, we see that $\boldsymbol{x}^m$ is generated as :

$$\mathbf{x}^m = \mathrm{F}^H \mathbf{X}^m \tag{3.15}$$

where F is the N × N Fast Fourier Transform (FFT) matrix with $[F]_{p,q} = \left(\frac{1}{\sqrt{N}}\right) exp(-j2\pi pq/N)$.

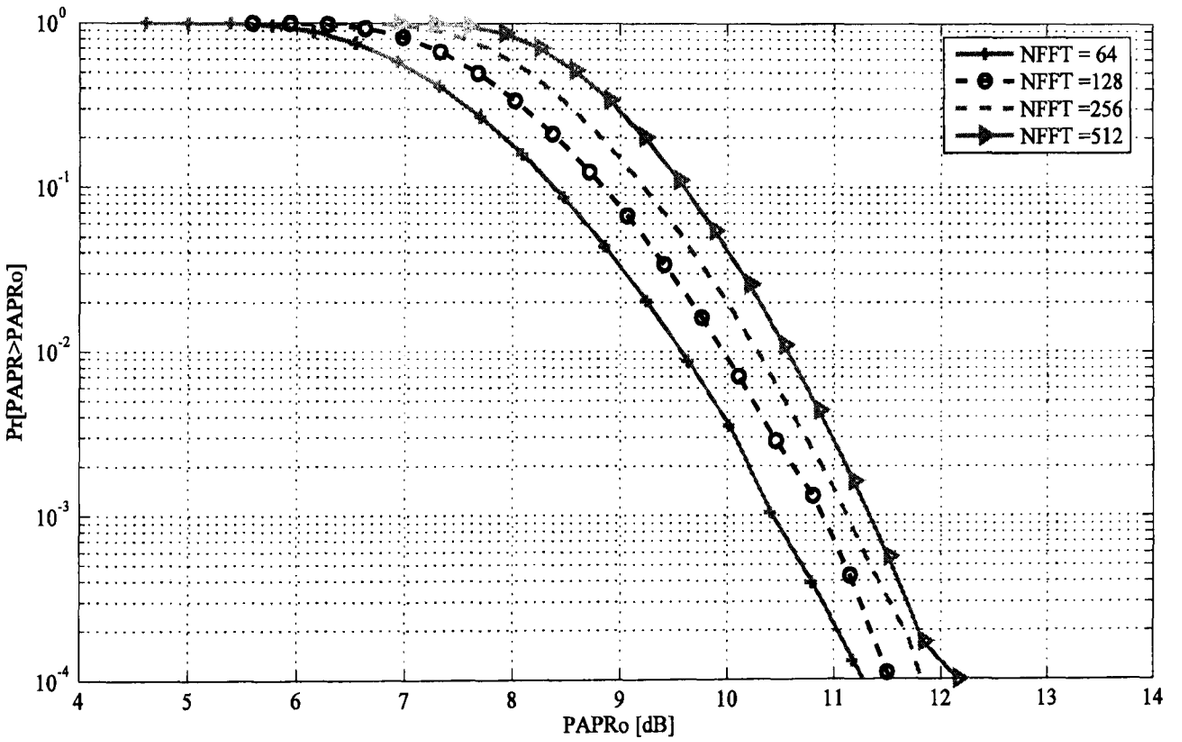

Figure 3-14: PAPR CCDFs for Number of Sub-carriers= 64, 128, 256, 512.

The elements of $\mathbf{X}^m$ are independently generated random variable resulting from the information data modulated into QPSK or other constellations. The IFFT operation is simply a linear combination of N- frequency domain samples, which form N time domain samples. From the

Central-Limit Theorem (CLT), a linear combination of independent zero-mean random variables can be approximated to a zero mean Gaussian distribution as the number of random variable goes to infinity. Similarly, with the large number of N in typical OFDM systems, the magnitudes of the complex time-domain samples can be approximately modelled as Rayleigh random variables. Consequently, with some non-negligible probability the magnitudes of the time-domain samples will be 'entering' the saturation and compression region of the amplifier. Figure 3-14 shows the PAPR distribution of OFDM signal for different number of sub-carriers [TELL99].

3.5.1.1 Mathematical Definition of PAPR

In order to quantify the envelope fluctuation of an OFDM signal, the most popular envelope variation metric, Peak-to-Average Power Ratio (PAPR), is used throughout this thesis. This is evaluated from the ratio between the maximum instantaneous power and the average power of the signal. In some literature, PAPR is related to another parameter called Crest Factor (CF) according to the following relationship [SEUN05]:

$$CF = \sqrt{PAPR} \tag{3.16}$$

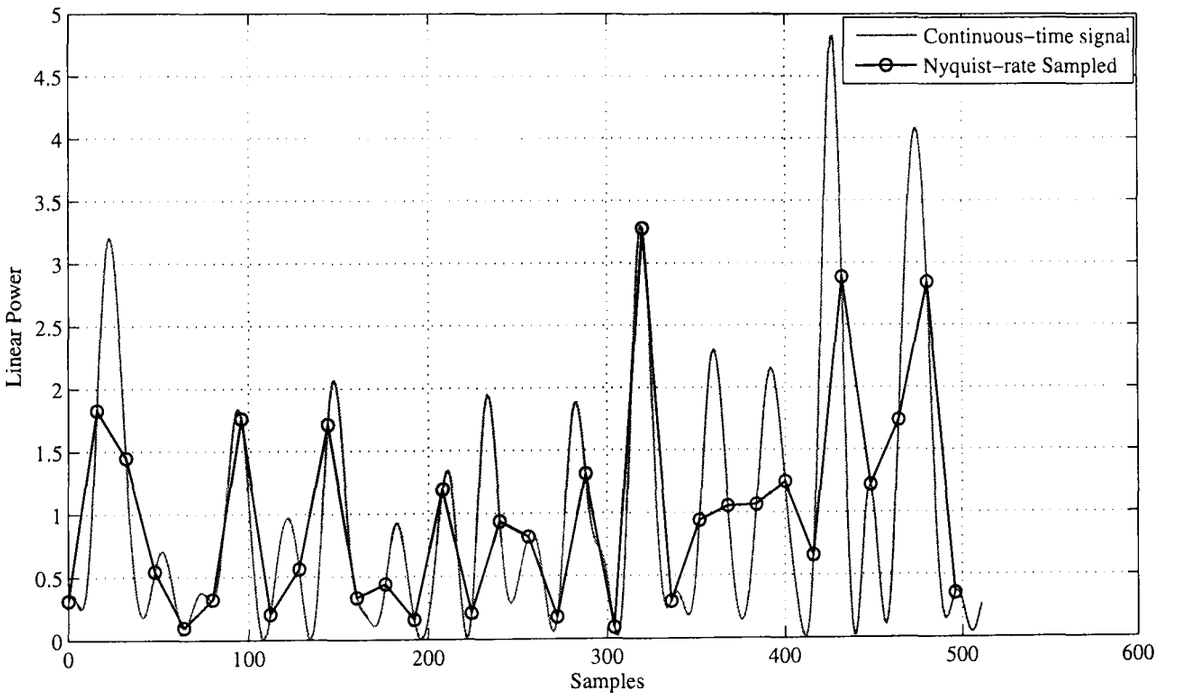

Figure 3-15: Oversampled (L=4) time domain signal and nyquist-rate sampled signal

The PAPR of a discrete-time signal $x(n)$, similar to signal x_n in equation (3.4), where n is discrete-time index, is defined as:

$$PAPR\big(x(n)\big) = \frac{max_{0\le i\le N-1}(|x_i|^2)}{E[|x_i|^2]} \tag{3.17}$$

Correspondingly, PAPR of a continuous-time signal $x(t)$ over $t \in \mathcal{T}$ is defined as:

$$PAPR(x(t)) = \frac{max_{t\in\mathcal{T}}(|x(t)|^2)}{E\left[\frac{1}{\mathcal{T}}\int_{t\in\mathcal{T}}|x(t)|^2 dt\right]} \tag{3.18}$$

where we assume that $x(t)$ is an ideal analog reconstruction of $x[n]$. In general $PAPR(x(t)) \geq PAPR(x[n])$,because analog reconstruction of a signal will result in a peak at least as large as the nyquist-rate sampled discrete-time signals, while its average power remains constant [TELL01]. This fact is demonstrated in Figure 3-15, where the linear power of the nyquist-rate sampled signal and that of the continuous-time signal are compared and the peak-missing of the nyquist sampled signal become obvious.

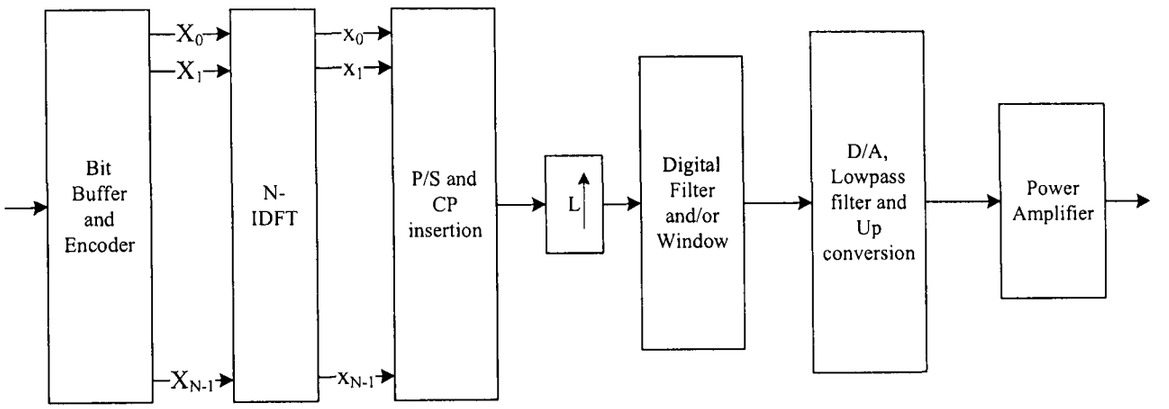

Figure 3-16: Block Diagram of OFDM Transmitter

On the other hand, the signal that passes through the High Power Amplifier (HPA) is a continuous-time (analog) signal and computing this requires a continuous-time Fourier transform (CTFT). This is hard to implement with analog components and can only be approximated with available digital hardware. Due to this fact, in practice, complex base-band OFDM signals are typically generated by using an IDFT as described by the block diagram in Figure 3-16 [TELL99]. Thus, it approximates the $PAPR(x(t))$ by using an oversampled version of $x[n]$ so that for sufficiently large L, $PAPR(x[n/L]) \approx PAPR(x(t))$, where $x[n/L]$ denotes the L-times oversampling of signal $x[n]$.

Although for large values of L the discrete-time signal will approach to the continuous-time signal, an oversampling factor of four is adequate to approximate the continuous-time signal with negligible differences [TELL01]. Figure 3-17 shows the deviation of the PAPR of $x[n/L]$ from the PAPR of x(t) for different values of L, $L \in \{1,2,4,8\}$.

In practice, it is the PAPR of the pass-band signal that determines the non-linear distortion of the PA. Thus, if we assume that the complex baseband signal $x(t)$ is transmitted by modulating the signal onto a carrier frequency f_c. The resulting pass-band signal is given by [PROA95]:

$$x_{PB}(t) = \Re\{x(t)e^{j2\pi f_c t}\} = x_I(t)cos(2\pi f_c t) - x_Q(t)sin(2\pi f_c t) \quad (3.19)$$

Where $x_I(t)$ and $x_Q(t)$ represents the in-phase and quadrature components of $x(t)$.

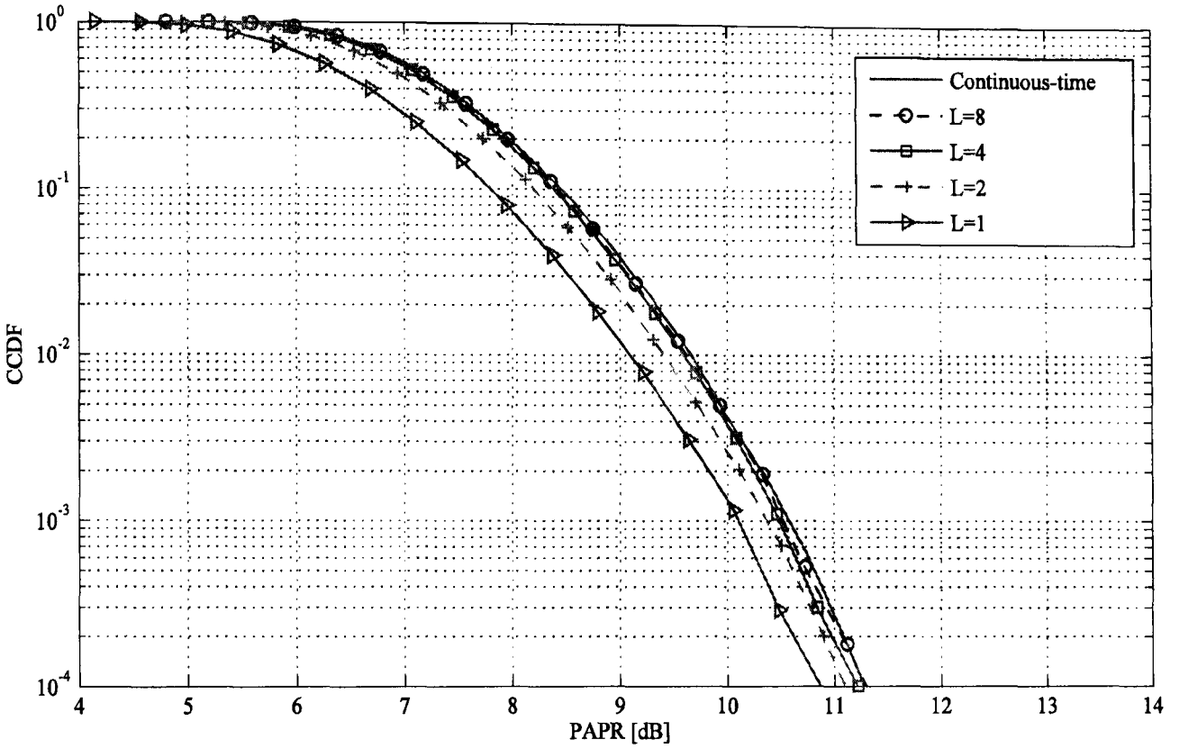

Figure 3-17: CCDF of PAPR for $L \in \{1, 2, 4, 8\}$, N=64 sub-carrier OFDM signal

When the carrier frequency f_c is much greater than the signal bandwidth (i.e. $f_c \gg BW$), which is the case in most practical systems, the peak magnitudes of the complex-baseband and pass-band signals are approximately the same [TELL99],[JAYA02]:

$$max|x_{PB}(t)| \approx max|x(t)| \quad (3.20)$$

The average power of the $x_{PB}(t)$ is written as (assuming equal average in-phase and quadrature phase components of $x(t)$) [TELL99],[JAYA02]:

$$E[|x_{PB}(t)|^2] = E\left[\left|\Re\{x(t)e^{j2\pi f_c t}\}\right|^2\right]$$

$$= E\left[\{x_I(t)\}^2 cos^2 2\pi f_c t + \{x_Q(t)\}^2 sin^2 2\pi f_c t\right]$$

$$= \frac{1}{2}E[|x_I(t)|^2] + \frac{1}{2}E\left[|x_Q(t)|^2\right]$$

$$= \frac{E[|x(t)|^2]}{2}$$

Combining this result with equation (3.20) and the definition of PAPR, the relationship between the complex-baseband PAPR and the pass-band PAPR is:

$$PAPR(x_{PB}(t)) \cong 2PAPR(x(t)) \tag{3.21}$$

Therefore, the pass-band PAPR is roughly 3 dB higher than that of the complex-baseband signal. We can therefore gauge the PAPR of a pass-band signal by simply analyzing it in the complex base band domain.

3.5.2 PAPR Reduction Technique

There have been a number of methods proposed for reducing the PAPR in OFDM system and the literature on them is already quite large. In all of these schemes, the PAPR reduction is achieved from the trade-off among the bit-error rate increase, transmit signal power increase, data rate loss, computation complexity increase [SEUN05]. In the following section, each of these popular schemes will be reviewed.

3.5.2.1 Amplitude Clipping and Filtering

The amplitude clipping belongs to the simplest technique for reducing the PAPR of OFDM signal. According to this approach, the peak envelope of the input signal samples is deliberately limited by a pre-determined value, according to the following threshold:

$$\check{x}(t) = \begin{cases} x, & |x| \leq A \\ Ae^{j\emptyset(x)}, & |x| > A \end{cases} \tag{3.22}$$

where $\emptyset(x)$ is the phase of x. Since larger peaks occur with low probability, clipping could be an effective technique for PAPR reduction. However, clipping is a non-linear process and can cause significant in-band and out-of-band distortion. The in-band distortion degrades the bit-error rate (BER) performance of the system whereas the out-of-band distortion reduces the spectral efficiency by producing spectral re-growth. Filtering after clipping can reduce the out-of-band distortion but may tend to cause some peak re-growth so that the resulting signal after clipping and filtering will exceed the clipping level at some points [XIAO98]. The repeated clipping and filtering approach was proposed in [ARMS02] in order to reduce the overall peak re-growth. But, in general, this approach takes many iterations to reach a desired amplitude level [SEUN05].

Due to the adverse effects introduced on the signal spectrum, the clipping technique (also known as distortion technique) is not generally favoured and the search for distortion-less techniques to reduce the PAPR was needed.

3.5.2.2 Selected Mapping (SLM)

In the SLM technique, the transmitter produces a set of sufficiently different candidate data blocks, all representing the same information as the original data block. Among these candidate

blocks, the most favourable block, in terms of PAPR, is selected for transmission. Figure 3-18 shows the block diagram of SLM technique [BAUM96].

As shown in Figure 3-18, each data block is multiplied by U different phase sequences, each of length N, $B^{(u)} = [b_{u,0}, b_{u,1}, \ldots\ldots\ldots, b_{u,N-1}]$, $u = 1,2, \ldots\ldots\ldots, U$. This results in U modified data blocks. The modified data block for the u^{th} phase sequence is given by:

$$X^{(u)} = [X_0 b_{u,0}, X_1 b_{u,1}, \ldots\ldots\ldots\ldots\ldots, X_{N-1} b_{u,N-1}]^T \text{ where } u = 1,2, \ldots\ldots\ldots, U \qquad (3.23)$$

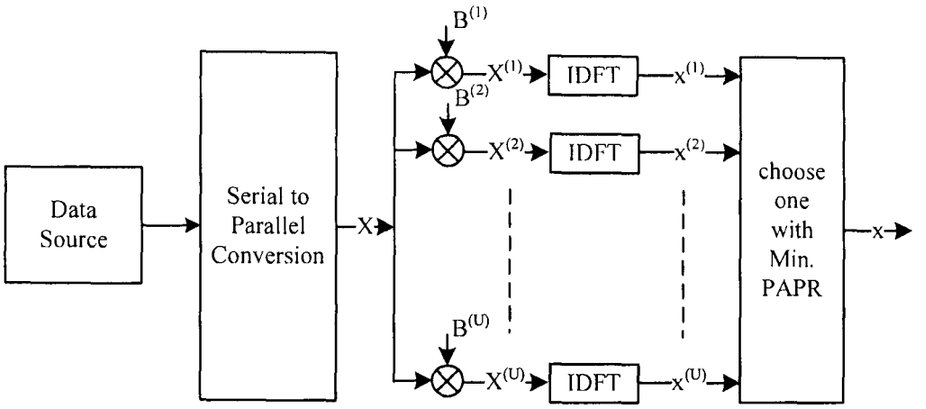

Figure 3-18: A block diagram of the SLM technique [SEUN05]

Having modified the data block using the sequence, the multicarrier signal becomes [SEUN05]:

$$x^{(u)}(t) = \frac{1}{\sqrt{N}} \sum_{n=0}^{N-1} X_n b_{u,n} e^{j2\pi n \Delta f t}, \qquad 0 \le t < NT, u = 1,2, \ldots\ldots, U \qquad (3.24)$$

Finally, the data block which shows lowest PAPR will be selected for transmission. The technique requires a bank of IFFTs at the transmitter and therefore introduces U- times more complexity when compared with the conventional OFDM system [BAUM96].

At the receiver, the information about the selected phase sequence must be available in order to correctly recover the transmitted data. This is achieved simply by transmitting this information as side information to the receiver. Using this knowledge, a return operation is performed at the receiver to recover the original information. Thus, the conventional OFDM receiver needs to be modified in order to accommodate SLM into the system and is therefore not advisable for systems which strongly restrict further modification to the available receivers [BAUM96], [SEUN05].

3.5.2.3 Partial Transmit Sequence (PTS)

In the PTS technique, an input data block of length N symbols is partitioned into several disjoint sub-blocks. The subcarriers within a sub-block are weighted by a phase factor, which is specific to this particular sub-block and they are, in practice, chosen to take discrete values. These phase

factors should be optimised in order to minimize the PAPR of the combined signal. Figure 3-19 depicts the block diagram of the PTS technique [MULL97].

In the conventional PTS technique, the input block $\mathbf{X}$ is partitioned into M disjoint sub-blocks $\mathbf{X}_m = [X_{m,0}, X_{m,1}, \ldots\ldots\ldots, X_{m,N-1}]^T, m = 1,2, \ldots\ldots, M$, such that $\sum_{m=1}^{M} \mathbf{X}_m = \mathbf{X}$. These are called partial transmit sequences (PTS). They are multiplied by a set of complex phase factors, $b_m = e^{j\varphi_m}$,

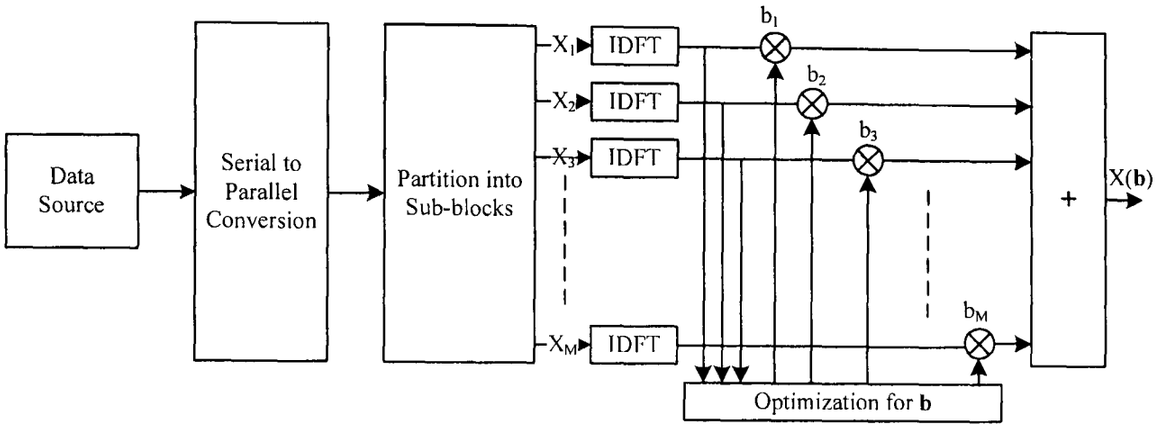

Figure 3-19: A block diagram of PTS technique [SEUN05]

$m = 1,2, \ldots\ldots\ldots, M$ and then the resulting sequences are combined. The set of phase factors are denoted by $\mathbf{b} = [b_1, b_2, \ldots\ldots\ldots, b_M]^T$. The combined time domain signal is given by:

$$\mathbf{x}(\mathbf{b}) = \sum_{m=1}^{M} b_m \cdot \mathbf{x}_m \tag{3.25}$$

where $\mathbf{x}(\mathbf{b}) = [\mathbf{x}_0(\mathbf{b}), \mathbf{x}_1(\mathbf{b}), \ldots\ldots\ldots, \mathbf{x}_{NL-1}(\mathbf{b})]^T$. The optimization problem is to find the set of phase factors which minimizes the PAPR, which can be formulated as [SEUN05]:

$$max_{0 \le k \le NL-1} |x_k(\mathbf{b})| \tag{3.26}$$

Moreover, the PAPR reduction performance can be further increased with greater number of sub-blocks; however, the complexity of the exhaustive search in determining the phase factors producing lowest PAPR is higher. In addition, similar to the SLM technique, the PTS technique also requires the transmission of transmitter side information to the receiver in order to correctly recover the original information. Consequently, conventional OFDM receivers must undergo modifications [MULL97], [SEUN05].

3.5.2.4 Coding

Coding schemes are another distortion-less approach for reducing the PAPR of OFDM signals, and some coding techniques are similar to the phase optimization methods mentioned above. In a more general sense, all distortion-less PAPR reduction methods could be classified as coding

schemes, where some 'codeword' of reduced PAPR is transmitted for any given symbol vector $\mathbf{X}^m$ [SEUN05]. In [JONE94], the block codes were used to reduce the PAPR of OFDM systems. According to this approach, the original data sequence is mapped onto a longer sequence with lower PAPR in the corresponding OFDM signal. In addition, it can also provide additional advantage in terms of Bit Error Rate (BER) performance due to the error correction capability of the codes. However, the main problem is that the data rate is vastly reduced in order to get good PAPR reduction. Furthermore, the trade-off of PAPR, data rate, and coding gain are not very attractive. On the other hand, the usefulness of this technique is rather restricted to OFDM symbols with higher number of sub-carriers due to the requirement of larger look-up tables.

More generally, error control coding is used in virtually all OFDM-based communication systems, and plays a key role in compensating the performance degradation effects caused by non-linear effects (as well as other noise effects). However, classical coding is a receiver-based compensation technique, and is thus unsuitable for preventing out-of-band emissions.

3.5.2.5 Interleaving

In [JAYA00], an interleaver based approach was proposed for reducing the PAPR of OFDM signal. Since highly correlated data blocks have large PAPR, interleaving helps to 'break' this correlation. Similar to SLM different interleaving patterns can be applied in parallel and the interleaved sequence with the lowest PAPR will be selected for transmission, and the information about the selected sequence has to be transmitted to the receiver in order to correctly recover the original information signal. As this approach also depends on the transmission of side information to the receiver, incorrectly received side information can cause severe system degradation [SEUN05].

Interleaving is less complex when compared with the original PTS technique, but achieves comparable results. Notably, there is no practical limitation to use this technique in conjunction with the other PAPR reduction technique. In this way, the combined scheme will further improve the PAPR reduction performance [JAYA00].

3.5.2.6 Tone Reservation (TR)

Tone Reservation (TR) was independently proposed by Gatherer and Polley [GATH98] and Tellado and Cioffi [TELL99]. In this technique, certain subcarriers are reserved for reducing the PAPR of OFDM signal, and as such they do not convey any useful information. Figure 3-20 illustrates the basic operation of TR technique.

At the transmitter, a peak-cancelling signal $c[n]$ is added with the information carrying signal $x[n]$ to reduce the PAPR:

$$\bar{x}[n] = x[n] + c[n] \tag{3.27}$$

Since the sub-carriers in an OFDM signal are mutually orthogonal, these reserved tones do not cause any interference to other sub-carriers, which are exploited for data transmission; thus it is a distortion-free technique. i.e. if the indices of the sub-carriers reserved for PAPR reduction belongs to $\mathcal{B}$, then the indices of the sub-carriers used for data transmission will be $\mathcal{B}^{\perp}$.

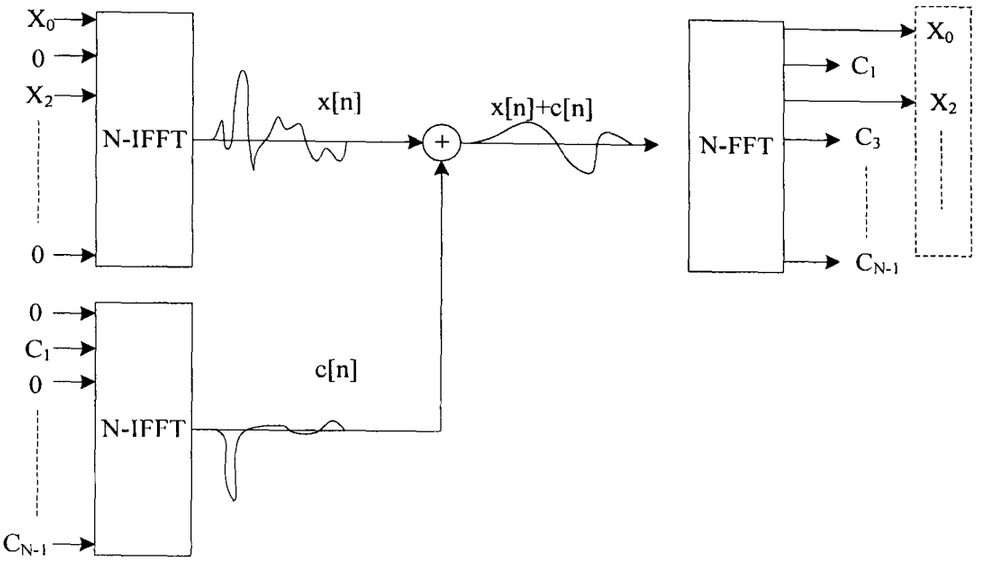

Figure 3-20: Basic operation of Tone Reservation (TR) Method

$$\bar{X}[k] = \begin{cases} X[k], & k \in \mathcal{B}^{\perp} \\ C[k], & k \in \mathcal{B} \end{cases} \tag{3.28}$$

The objective of the TR algorithms is to find the optimum peak-cancelling signal $C[k]$, satisfying the condition in equation (3.28) , which is dependent on the OFDM symbol. This can be formulated as:

$$C[k] = \underset{\tilde{C}[k]\ k\in\mathcal{B}}{\operatorname{argmin}} \left[max\left(\left| x[n] + IFFT\left(\tilde{C}[k]\right) \right|^2 \right) \right] \tag{3.29}$$

Unlike PTS and SLM techniques, TR technique does not need the transmitter side information at the receiver. Despite its many advantages, it slightly reduces the data rate of the system with respect to the number of sub-carriers are assigned for PAPR reduction purpose [SEUN05].

3.5.2.7 Tone Injection (TI)

The Tone Injection (TI) technique was originally proposed by Tellado [TELL99] and according to this approach the original constellation space is expanded to include S-times as many constellation points as the original constellation points. The extra constellation points are generated by shifting copies of the original constellation. The basic idea is that a number of tones

in the OFDM symbol are modified to reduce PAPR by adding a complex constant C and furthermore, receiver will be able to correctly decode the modified tones.

Assuming M-QAM is used as a modulation scheme and the minimum distance between constellation points is d. Then the real and imaginary parts can take values $\{\pm d/2, \pm 3d/2, \ldots, \pm(\sqrt{M}-1)d/2\}$ where $\sqrt{M}$ is equal to the number per dimension. For example, consider the symbols $X_n = d/2 + j\,3d/2$. Transforming X_n by adding the complex constant C:

$$\bar{X}_n = X_n + C_n = X_n + p_n D + jq_n D \tag{3.30}$$

where p_n and q_n are any integer values and selected to reduce the PAPR, while D is a positive real number known at the receiver [SEUN05], [WATT05].

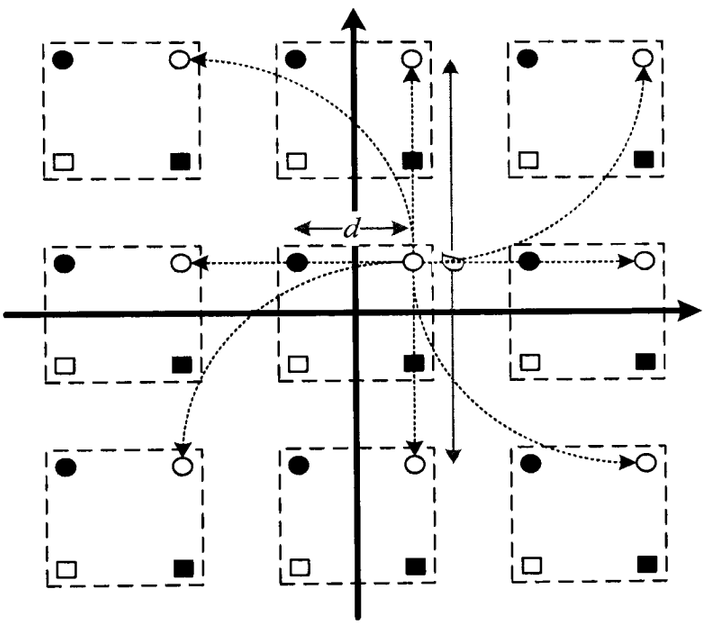

Figure 3-21: QPSK ($M = 4$) constellation extended for Tone Injection (TI) [WATT05]

The transmitted signal after adding the constant C is:

$$\bar{x}_k = \sum_{n=0}^{N-1} (X_n + p_n D + jq_n D) e^{\frac{j2\pi nk}{N}} \tag{3.31}$$

Figure 3-21 illustrates the possible constellation extension for QPSK modulation for applying TI method. In Figure 3-21, the constellation points marked by white circles carry the same information and the TI algorithm selects the constellation point that minimizes the PAPR of the resulting OFDM signal. Generally these equivalent constellation points are spaced by $D = \rho d\sqrt{M}$ with $\rho \geq 1$. Thus, the peak values can be reduced by choosing appropriate p_n, q_n and n [SEUN05].

At the receiver, the complex constant C can be simply removed by performing a modulo-D operation on the real and imaginary part of the output of the Frequency Equaliser (FEQ). Thus, the only addition to the standard receiver is a modulo-D block to correctly decode the received signal and therefore avoid the requirement of transmission of additional information bits as in the SLM and PTS techniques [WATT05].

Although there is no loss in the data rate of the system, the TI approach is more problematic than the Tone Reservation approach since the injected signal occupies the same frequency band as the information bearing signal. In addition to this, the TI technique also increases the average power of the transmitter signal very much due to the newly injected signal [SEUN05].

3.5.2.8 Active Constellation Extension (ACE)

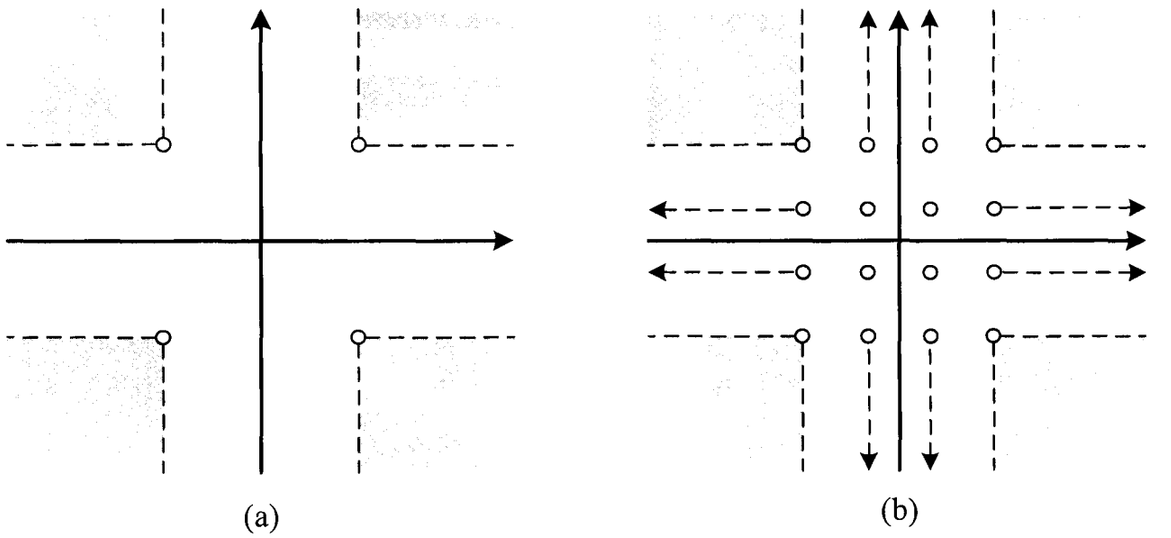

Figure 3-22: Constellation extensions possible in ACE. Plot a) is for QPSK and b) is for 16-QAM.

Active Constellation Extension (ACE) is similar to the Tone Injection method described in section 3.5.2.7 but the difference is to how the constellation is expanded. In ACE, some of the outer constellation points are dynamically extended towards the outside of the original constellation such that the PAPR of the OFDM symbols is reduced. Figure 3-22 illustrates the constellation extension possible in ACE for QPSK and 16-QAM constellation plane. Extending only the outer constellation points without altering the maximum likelihood region increases the noise margin between the constellation points and thereby, tends to slightly decrease the BER performance of the system [KRON03]. Moreover, these modifications increase the transmit signal power of the data block and the usefulness of the scheme is rather restricted to modulation with larger constellation size [SEUN05].

Amongst the reviewed techniques, Tone Reservation (TR) was identified as the most suitable class of PAPR reduction technique, for mitigating the effects of the TWTA in the mobile satellite environment. This selection was based on the following competitive features of this technique:

- In the TR technique, the inserted pilot symbols in the transmitter are simply discarded at the receiver. In other words, no side information is required at the receiver. Thus, it leads a minimum impact on the receiver side.
- It requires minimal modifications to existing standards and systems, since the PAPR reducing pilots can simply substitute a small number of the tail-zero sub-carriers that are typically specified in practical OFDM systems.
- It is also suitable for a SC-FDMA system which has recently been proposed in the 3GPP Long Term Evolution (LTE) as an attractive return link candidate.

3.6 Amplifier Linearization Techniques

This section provides an overview of the different types of linearization approaches that have been proposed in the literature. Main emphasis is given to digital linearization techniques, and in particular digital pre-distortion, since they offer a more cost-effective solution relative to analogue ones, mainly due to their efficient baseband implementation, and also their higher flexibility in adapting to drifts in the amplifier's characteristics, over time, temperature and frequency (channel) [ANDR96], [QIUJ05], [WOOY07].

3.6.1 Feed-forward Linearizer

Feed-forward amplifier linearization [COSK03] is an RF-level technique, whose principle is illustrated in Figure 3-23. A typical feed-forward system involves two cancellation loops: signal cancellation loop and error cancellation loop. The purpose of the signal cancellation loop is to suppress the reference signal form the main power amplifier output signal, leaving only the amplifier distortion, both linear and non-linear, in the error signal. The error signal is then amplified by an auxiliary amplifier and subtracted from the delayed distorted output of the amplifier. The resulting signal is (in principle) distortion free. The auxiliary amplifier only needs to amplify the distortion products and it can therefore be operated at the more linear regions of the device. Furthermore, the feed-forward configuration makes the scheme unconditionally stable, and it is also effective over large signal bandwidths. Disadvantages of the feed-forward linearizer are such as poor overall power efficiency and complex implementation for adaptive tracking when component behaviour changes [BOUM04].

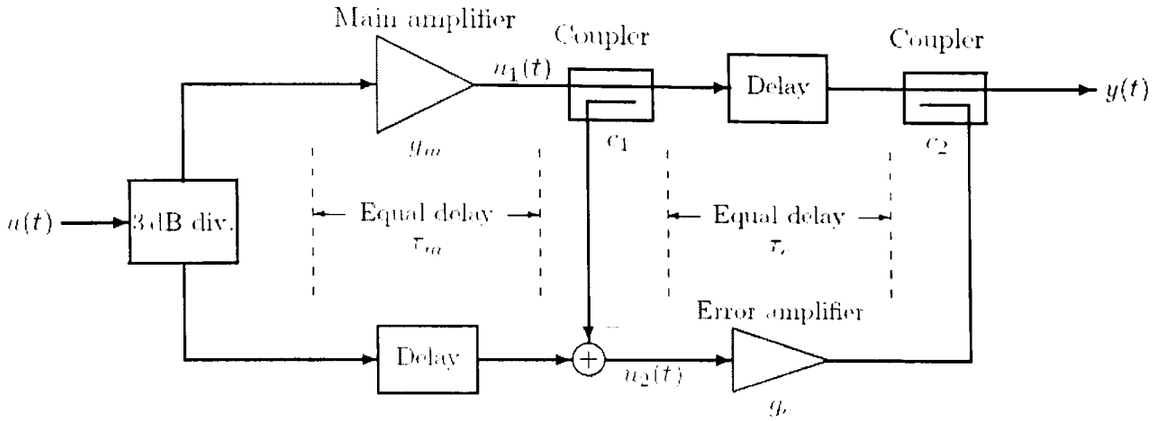

Figure 3-23: Feed-forward Linearizer

As far as the linearization of the onboard amplifier is concerned, the feed-forward structure does not appear to offer an attractive option, since it would have to be part of the payload (leading to higher complexity, mass and power consumption).

3.6.2 Other (two amplifier based) RF Linearization Techniques

3.6.2.1 Envelope Elimination and Restoration (EER)

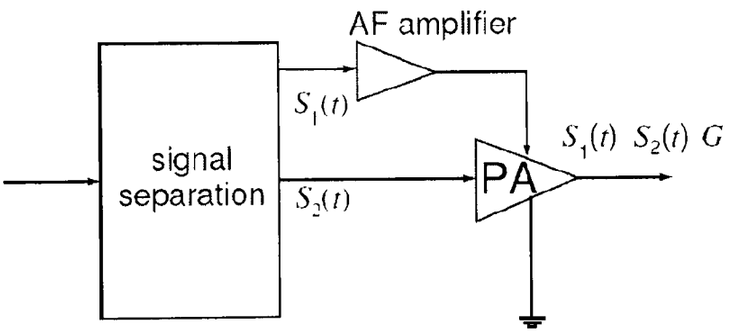

Figure 3-24: EER principle

The principle of the EER technique [YANG02], [QIUJ05] is illustrated in Figure 3-24. The modulated signal: $s(t) = A(t)\cos(\omega_c t + \emptyset(t))$ is split into two components: the baseband envelope component $s_1(t) = A(t)$ and a constant envelope phase modulated RF component $s_2(t) = \cos(\omega_c t + \emptyset(t))$. The constant envelope RF component is then amplified by the non-linear amplifier, whose power supply is modulated with the baseband signal $s_1(t)$, amplified by an efficient low frequency amplifier.

The EER technique is characterized by good linearity and efficiency, and also simplicity of implementation. On the other hand it is sensitive to timing mismatching between the amplitude and phase component.

3.6.2.2 Linear amplification using Nonlinear Components (LINC)

The LINC [COXC74], [HETZ91], [LANG99] technique relies on two equal gain high power amplifiers (usually a power efficient class C amplifier is used), as illustrated in Figure 3-25. Similarly to EER, the modulated signal is fed to a signal separation unit, but this time the input signal $s(t) = V(t)\cos(\omega_c t + \emptyset(t))$ is separated into two constant amplitude phase-modulated signals: $s_1(t) = V\cos(\omega_c t + \varphi(t))$ and $s_2(t) = V\cos(\omega_c t + \theta(t))$, where $\varphi(t) = \emptyset(t) + \alpha(t)$ and $\theta(t) = \emptyset(t) - \alpha(t)$.Thus, as the EER technique, this configuration achieves driving the amplifiers with constant envelope signals. After addition the output signal is given as: $s_1(t) + s_2(t) = 2s(t)$, where $\cos(\alpha(t)) = \frac{V(t)}{V}$. So V can be chosen so that $|V| \leq max(|V(t)|) = V_{max}$. So setting $V = V_{max}$ we have $\alpha(t) = \cos^{-1}\left(\frac{V(t)}{V_{max}}\right)$.

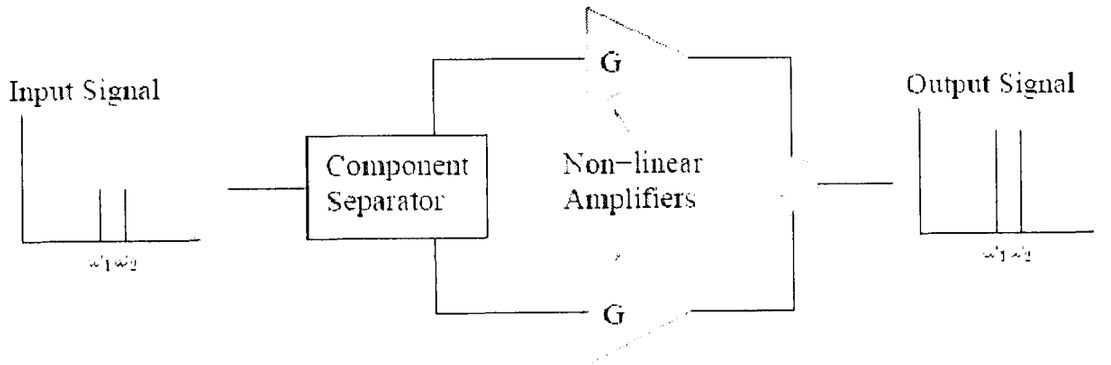

Figure 3-25: LINC principle

In practice it is difficult to implement the inverse cosine function with analogue components and a baseband DSP implementation is preferred. LINC is also sensitive to mismatches between the two paths, in terms of I-Q imbalance in up-conversion and the amplifier characteristics.

3.6.2.3 Combined Analogue-Locked Loop Universal Modulator (CALLUM)

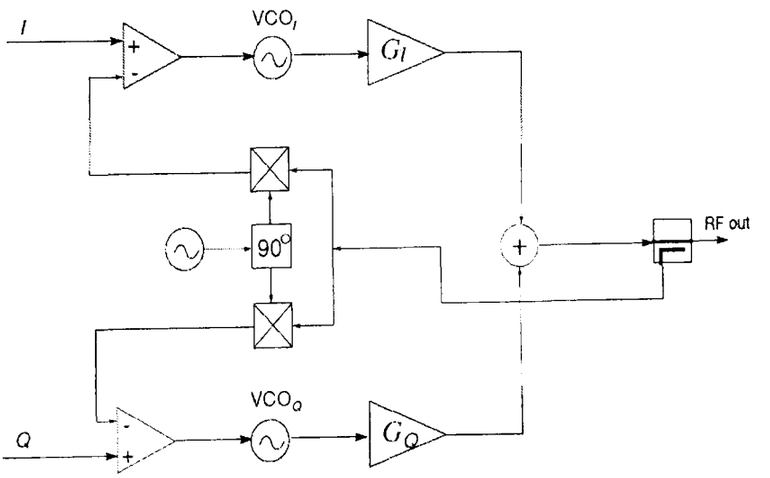

Figure 3-26: CALLUM basic architecture

CALLUM [BATE92], [JENN99] is an evolution of the LINC technique, and the basic architecture is shown in Figure 3-26. Again, similar to LINC, the objective of the circuit is to drive the high power (non-linear) amplifiers with constant envelope signals, and the (amplified) time varying waveform is generated by the combination of the amplifiers' outputs. The CALLUM architecture provides a relatively easy way for generating the constant envelope signals. As it is shown in Figure 3-26, differential amplifiers subtract the I and Q branches of the input signal from the corresponding down-converted outputs of the overall system. The error signals are then used to control voltage control oscillators (in each path), whose outputs then drive the high power amplifiers. It is noted that CALLUM is a type of feedback linearization technique, as these are described next.

3.6.3 Feedback Linearization

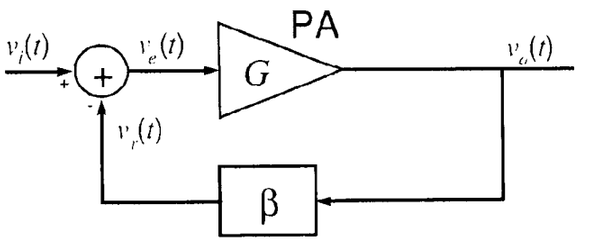

Figure 3-27: Generic structure of feedback linearizer

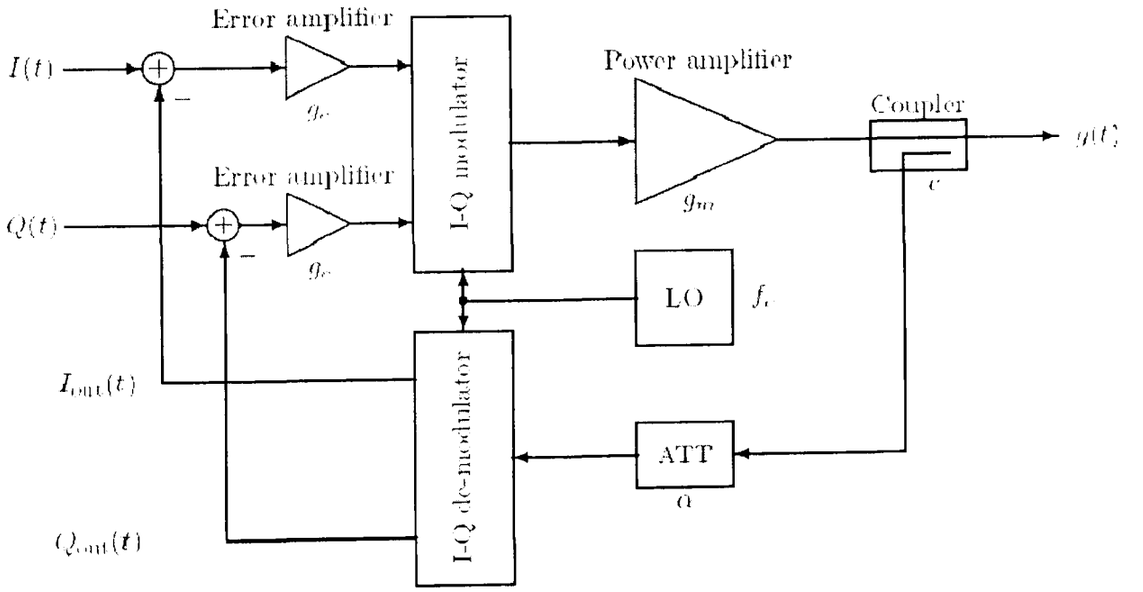

Figure 3-28: Architecture of Cartesian Feedback Linearizer

The principle of feedback linearization is illustrated Figure 3-27. The output of the non-linear amplifier is attenuated and subtracted from the input signal, so that the amplifier is driven by an error signal. It is easy to show that the closed loop gain is $G_c = G/(1 + \beta G)$, where G is the gain

of the non-linear amplifier. Therefore the feedback structure results in a reduction of the amplifier's gain, but it also attenuates the distortion products by a factor of $1/(1+\beta G)$ [KENN98]. A direct (RF) level implementation of the feedback linearizer is mainly applied to audio amplifiers [QIUJ05].

Feedback linearization of RF amplifiers is usually performed using a baseband variation, known as Cartesian feedback linearizer [PETR84]. The baseband implementation makes the feedback loop more robust to delay mismatches. Figure 3-28 shows the generic structure of the Cartesian feedback structure. It is observed that the error signal is generated at baseband, by subtracting the feedback attenuated and demodulated signal from the baseband input signal. Synchronization between the feed-forward and feedback branches is achieved through the local oscillator (LO) at the modulator/demodulator unit. Implementation issues (effects of phase misalignment) and descriptions of fully integrated Cartesian feedback linearizers are reported in [PIPI05], [DOWS03], [DOWS04].

3.6.4 Pre-distortion

As the name implies, pre-distortion consists of distorting the transmit signal, prior to amplification, according to a non-linear function that exhibits inverse transfer characteristics, to those of the amplifier. The combination of the two non-linear responses results into a linearized overall response. Depending on the position of the pre-distortion unit in the transmitter, two main categorizations can be made [ANDR96]:

- Analogue IF/RF pre-distortion
- Digital Baseband pre-distortion

Pre-distortion techniques are further categorized as adaptive or non-adaptive, depending on their ability to adapt their response to changes in the amplifier's characteristics, which occur due to temperature variations, aging and possibly also due to channel switching [ANDR96].

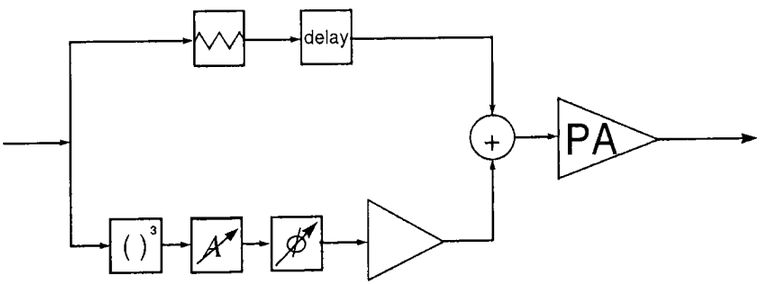

Figure 3-29: Cubic Analogue Pre-distorter

Analogue pre-distortion linearizers have the advantage of being small and inexpensive, but because of the accuracy to which the non-linear functions may be realized with analogue

components, they generally focus on the reduction of (only) third-order inter-modulation products. The non-linearity is typically modeled as a cubic function of the input signal, as illustrated in Figure 3-29 [MORR03]. In this configuration the input signal is split into a direct path that attenuates and delays the input signal, and a cubic non-linearity branch, which also includes voltage controlled amplitude and phase adjustments in order to achieve the desired non-linear response. The lower branch also includes a buffer amplifier in order to compensate the significant attenuation introduced by the cubic element. Experimentation results reported in [MORR03], showed that the cubic pre-distorter suppressed the 3rd order inter-modulation products by 18dB with a carrier frequency of 900MHz. However the technique, not only fails to suppress 5th order products, but on the contrary enhances them.

The deficiency of the 3rd order pre-distorter is addressed by the higher order non-linearity pre-distorter (with adjustable coefficients) that is reported in [YIYA00], [YANG02], whereas an efficient implementation of higher order non-linearities is proposed in [QIUJ05]. Analogue pre-distortion linearizers that rely on a "curve-fit" of the amplifier distortion characteristic have also been used to compensate higher order distortion, but this approach is inherently dependent on the particular amplifier for which the linearizer is designed [KENN98].

The design of fully analogue adaptive pre-distorters is a challenging task, and adaptation is commonly accommodated within a hybrid analogue-digital solution (analogue pre-distorter, with digitally optimized parameters). For example, [BERN97] reviews different (digital) optimization approaches (e.g. based on MMSE criterion), for determining the amplitude and phase parameters in 3rd and 5th order pre-distorters. In [GHAD94] the AM/AM and AM/PM characteristics of the pre-distorter are implemented using polynomial functions, whose coefficients are optimized digitally with a recursive least squares algorithm. Another common approach for adapting the pre-distorter parameters, is based on minimizing the measured out of band interference, as it was originally proposed in [STAP92]. Again digital level processing has to be performed in order to optimize the polynomial function coefficients for the analogue circuit. A fully analogue adaptation circuit, that tries to minimize the inter-modulation products, has been reported in [PARK00].

Analogue pre-distortion techniques can provide a cost-effective solution for linearizing the on-board TWTA, although the cost benefits of the analogue implementation are compromised if an adaptive implementation is required. In the recent years digital pre-distortion has been gaining in popularity (relative to analogue pre-distortion), mainly because of the rapid advancements in DSPs, FPGAs and ASICs, which allow cost effective implementations. Moreover digital pre-distortion techniques are intrinsically easier to be made adaptive [WOOY07]. In the next section digital pre-distortion is discussed in more detail.

3.6.5 Digital Pre-distortion

There are two main types of digital pre-distortion techniques [ANDR96]:

- Data Pre-distorters are implemented at baseband, before the shaping filter and they essentially compensate for the deformation of the constellation diagram, caused by the amplifier. They are simpler to implement (relative to signal pre-distorters), but they are not effective in eliminating adjacent channel interference. Moreover they are modulation format specific, and thus not suitable for random signals such as those encountered in CDMA and OFDM.
- Signal Pre-distorters, are also implemented at baseband, but they are placed after the pulse shaping filter and this makes them constellation format independent (and thus suitable for CDMA and OFDM signals, and relevant to the investigation in Chapters 6 & 7). Signal pre-distorters operate on (over-sampled – relative to symbol rate) signal samples, which are subjected to a non-linear distortion that is dependent on their amplitude level; according to the AM/AM and AM/PM characteristics of the amplifier.

Further to the classification of digital pre-distorter's, with respect to their position relative to the shaping filter, there is another level of categorization related to the generation of the distortion parameters. In particular digital pre-distorters are either based on a Look-Up Table (LUT) [NAGA89], addressed for example by the instantaneous signal power, or on some parametric non-linear function [GHAD94], which is typically a polynomial function of a 2nd or 3rd order. These two main types of digital pre-distorters are described in more detail below[3].

3.6.5.1 LUT-based Digital Pre-distortion

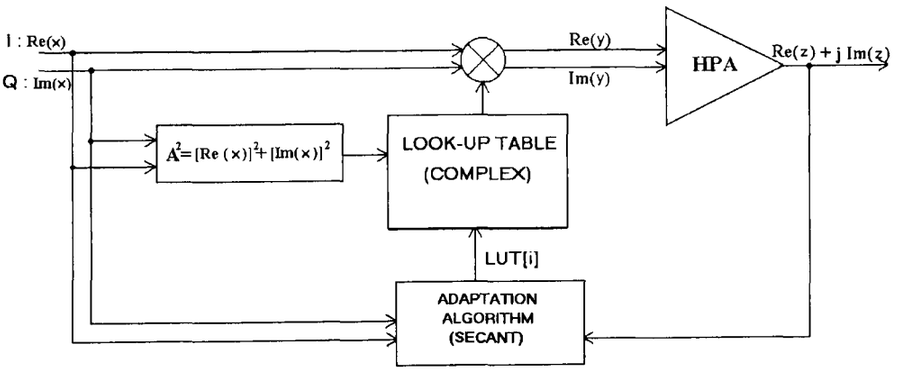

Figure 3-30: Generic Structure of the gain based LUT Pre-distorter

[3] A third type of digital pre-distorters based on neural networks has also been studied recently [CHEW03]

The first LUT-based digital pre-distorter was proposed in [NAGA89], where two LUTs, one for each of the I and Q components of the complex baseband signal, are used for storing scalar distortion parameters. The tables are addressed by quantized (according to some precision level) samples of the I and Q signal components. The generated distortion parameters are added to the original signal sample (which is properly delayed according to the delays involved in the table indexing process). In effect each possible complex input is mapped to a unique distorted complex output, and thus this type of LUT pre-distorter is commonly referred to as mapping pre-distorter. The main drawback of the mapping pre-distorter is the large size of the LUT, which is in the order of Megabits for a reasonable level of signal quantization. The large LUT size also results into slow adaptation to changes in the amplifier's characteristics. In [NAGA89] an adaptation delays of 10s at 16ksymbols/s (2 bits per symbol) was reported using a simplified iteration:

$$c_i(m+1) = c_i(m) + \mu\big(z(n) - z_{PA}(n)\big) \tag{3.32}$$

where μ (≤ 1) is positive step parameter, $c_i(m)$ is the value of the *i-th* LUT cell at iteration m, $z(n)$ is a sample at the pre-distorter's output and $z_{PA}(n)$ is the corresponding sample obtained from the (demodulated) amplifier's output.

A much more efficient LUT pre-distorter was proposed in [CAVE90], where the pre-distorter signal is generated by multiplying (rather than adding) the original signal sample with the complex LUT parameter. In this *gain based* pre-distorter, the LUT is addressed only by the quantized power level of the transmit sample; effectively taking into advantage the dependence of the amplitude and phase distortion only on the amplitude of the transmit signal. This approach reduces the table size dramatically, since only hundreds of cells are sufficient. In [CAVE90] a table of about 100 entries was used and this allowed an adaptation delay of 4ms at 16ksymbols/s. The generic structure of the gain based LUT pre-distorter is illustrated Figure 3-30.

In [CAVE90] a LUT adaptation algorithm based on the Secant (root finding) method was proposed. An alternative LUT adaptation algorithm, based on the method of successive substitution (also a root finding algorithm) was proposed in [CAVE97]. The optimal LUT point spacing, with respect to input power level, was studied in [CAVE99], where it was concluded that uniform spacing provides the optimal solution.

3.6.5.2 Polynomial-based Digital Pre-distortion

The polynomial pre-distorter is similar to the LUT gain pre-distorter, however instead of a table, two polynomial functions are used in order to generate the pre-distortion multiplicative parameter; one for the amplitude and the other the phase, as it is shown in Figure 3-31 [ANDR96]. The smaller number of parameters required to model the non-linearity allow faster adaptations

(relative to the LUT pre-distorter), which are typically performed by an LMS or an RLS iteration [GHAI94].

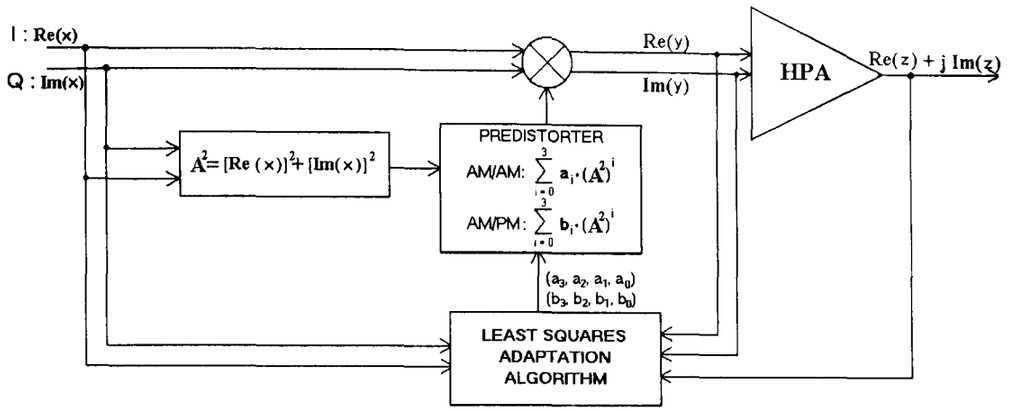

Figure 3-31: Generic Structure of the Polynomial Pre-distorter

Amongst the reviewed techniques, digital pre-distortion was identified as the most suitable class of linearization technique, for mitigating the effects of the TWTA in the satellite environment. This conclusion was based on the following competitive features of digital pre-distortion:

- The digital implementation allows easy and accurate adaptation to changes in the amplifier's characteristics, by updating the pre-distortion parameters (LUT entries or polynomial coefficients) [WOOY07].
- The pre-distortion unit does not need to be physically co-located with the amplifier, allowing remote linearization of the onboard TWTA (by pre-distorting the transmit signals at the gateway/terminal). This important feature is difficult to be achieved with analogue-RF linearizers.
- It has reduced implementation complexity and concurrently benefitting from the continuous improvements of Digital Signal Processing (DSP) circuitry. Thus a proven cost-effective solution [BOUM04].

3.7 Summary and Conclusions

The contents of this Chapter can be summarized as follows:

- A brief introduction to the physical layer of the satellite OFDM air interface was provided including a brief description of OFDM system model.
- One of the major drawbacks of OFDM is its higher PAPR resulting from a large number of independently modulated sub-carriers and therefore it is very sensitive to inherently non-linear on-board amplifier; resulting both in-band distortion and out-of-band distortion.

- In order to compensate the non-linear distortion, transmitter based compensation techniques were reviewed from the literature, namely: Power back-off, PAPR Reduction Method and Amplifier Linearization Methods.
- Since the power available on-board the satellite systems is limited, back-off method is not an attractive option as it comes at the expense of decreased power efficiency of the amplifier.
- Among the reviewed PAPR Reduction techniques, TR method is most competitive since it does not require transmission of additional information and, in addition, causes minimal impact on the available OFDM receivers by simply discarding the reserved sub-carriers.
- Among the reviewed PA linearization techniques, digital pre-distortion technique is most competitive because it not only allows easy and accurate adaptation with varying TWTA characteristics but also provides a cost effective solution by which it can be located at the gateway station.

The subsequent chapters 4 and 5 are separately dedicated to investigation of Tone Reservation (TR) technique and digital pre-distortion technique, respectively, when applied to mobile satellite systems employing OFDM air interface.

Chapter Four

4 Gradient Based Tone Reservation Technique for PAPR Reduction of OFDM Signals

4.1 Introduction

As discussed in chapter 3, a considerable research has already been carried out on various techniques for reducing the PAPR of OFDM signals. The ultimate goal of this research has been to produce specific algorithm implementations, which not only succeed in minimising the dynamic range of OFDM signals, but also largely satisfy some additional criteria, namely, introducing minimum bandwidth losses, lower rates of average power increase (increase in average power moves the signal operating point upwards on the amplifier characteristics, thus resulting in degradation of BER performance) and offering minimum implementation complexity (even if spectral constraints are to be associated). Taking as a background from among the existing methods, the Tone Reservation (TR) method initially proposed by Tellado [TELL99] and Gatherer and Polley [GATH97] is one of the most promising approaches, as indicated by the level of attention it has received in the literature.

Although derived independently, the methods in [TELL99] and [GATH97] are very similar and use a pre-computed projection of an impulse onto the reserved subcarriers to reduce the magnitude of large peaks. Moreover, they exhibit slower convergence when compared with the active-set algorithm proposed in [BRIA04], which is the most efficient existing algorithm for TR based PAPR reduction for OFDM signals. Since the active-set algorithm can only be applied to real problems, [BRIA04] uses the polygon approximation of circles in the complex plane, similar to [CHEN87]. Thus, the complexity of the algorithm depends on the chosen polygonal approximation. In addition, the computational complexity of the algorithm also depends on the maximum number of iterations used; the complexity increases with the number of iterations [BRIA04]. In order to avoid the computational complexity associated with the number of iterations, the algorithm is usually repeated for smaller number of iterations and thus, the performance is significantly reduced.

In this chapter, we propose a new gradient-based TR algorithm for creating the peak-cancelling signal in the time-domain by utilizing the reserved subcarriers. The algorithm follows a simple update rule and hence, exhibits low computational complexity and is thus, suitable for real time implementations. Furthermore, the proposed algorithm facilitates a simple incorporation of the spectral constraints by limiting the reserved subcarriers' power in the frequency domain with negligible computational cost. The computational complexity of the proposed algorithm is significantly smaller than the existing active-set based approach.

In the remainder of this chapter we first review the fundamental theory and concept behind the TR technique. In section 4.3, the analytical problem formulation of the TR technique is described, and this is followed by a review of previous research work in the TR technique. In section 4.5, the derivation of the proposed algorithm is presented along with the corresponding analytical equations. Subsequently, in Section 4.6 the convergence properties of the proposed algorithm are discussed in terms of the step size parameter. In Section 4.8, the complexity evaluation of the proposed algorithm is compared with the most efficient existing active-set algorithm in [BRIA04]. In Section 4.9, simulation results are discussed for three different subcarrier locations. The simulation results also show the effect of the spectral constraints. In addition, investigation is further extended in evaluating the performance of the TR algorithm in the presence of non-linear TWTA model. The performance is evaluated for different IBOs in terms of both the Bit Error Rate Performance and the reduction in spectral re-growth. Finally, the chapter concludes with summary and conclusions.

4.2 The Tone Reservation Scheme

In TR, the PAPR reduction of OFDM signals is essentially achieved through the incorporation of an additive 'peak-cancelling' signal. This peak-cancelling signal $c^m[n]$ is added to the original signal $x^m[n]$ such that the resulting signal $\bar{x}^m[n]$ minimizes the effect of troublesome peaks associated with the original signal $x^m[n]$. The above process can be formulated as [BRIA04]:

$$\bar{x}^m[n] = x^m[n] + c^m[n] \tag{4.1}$$

where m denotes the m^{th} OFDM block and n denotes the time index. Due to the linearity of the IFFT operation, we can also represent the additive operation in the discrete-frequency domain as:

$$\bar{X}^m[k] = X_k^m + C_k^m \tag{4.2}$$

where k indicates the sub-carrier location in the m^{th} OFDM block.

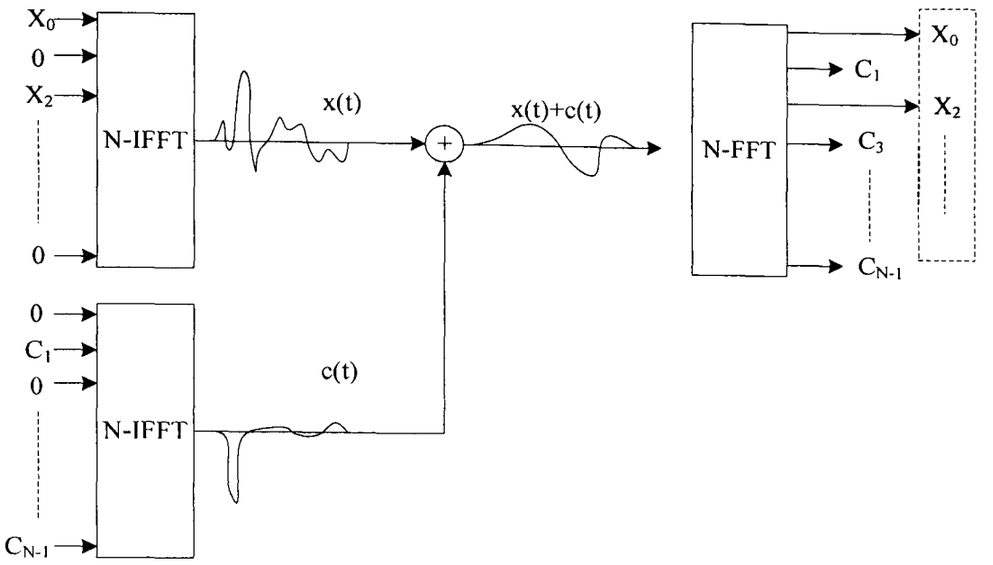

Figure 4-1: Demonstration of Tone Reservation Method

Equation (4.2) gives the following relation [BRIA04]:

$$\bar{x}^m[n] = \frac{1}{\sqrt{N}} \sum_{k=0}^{N-1} (X_k^m + C_k^m) e^{j2\pi kn/N} \tag{4.3}$$

where the frequency vector $\mathbf{C}^m = [C_0^m, \ \ldots \ , C_{N-1}^m]$ represents the PAPR reduction signal. The above additive PAPR reduction concept is demonstrated in Figure 4-1, where $x(t)$ and $c(t)$ represents the continuous-time signal version of $x^m[n]$ and $c^m[n]$, respectively.

The main objective is to design, based on some constraints, the signal $c^m[n]$ in order to reduce the peak power of a system. Despite being a distortion-less and an effective method for reducing the PAPR of the OFDM signal, TR techniques must also fulfil most of the following list of desirable properties [TELL99], [BRIA03]:

- The combined signal $x^m[n/L] + c^m[n/L]$ must show a significant PAPR reduction and this can be defined as:

$$PAPR(x^m[n/L] + c^m[n/L]) = \frac{max_n |x^m[n/L] + c^m[n/L]|^2}{E[|x^m[n/L]|^2]} \tag{4.4}$$

  It must be noted in the above definition of PAPR that the energy of the peak-cancelling signal $c^m[n/L]$ is not considered in the average power calculation. This is due to the fact that, in practice, it is the peak-power at the input of the HPA that causes the distortion, although the problem is extensively known as the PAPR problem. Moreover, the energy of the peak-cancelling signal $c^m[n/L]$ simply reduces the PAPR by inflating the average power in the denominator in equation (4.4). In order to avoid this problem and also provide a fair comparison the average power of the original data signal is considered.

- The receiver must be able to efficiently decode the data symbols $\mathbf{X}^m$ from the combined vector $\mathbf{X}^m + \mathbf{C}^m$ without any performance degradation. Moreover, the transmitter should not communicate with the receiver for the purpose of transferring any side information.
- Since the transmitter needs to generate the peak-cancelling signal for many OFDM signals the technique should be computationally efficient.
- The technique should not prevent the performance improvement obtained via any error control coding technique.
- These peak-cancelling signals should not reduce the data throughput significantly.
- It is necessary to easily incorporate the power constraint on the combined signal such as the new average power of the signal, $E[x[n] + c[n]]$ and the peak-power constraint on each individual sub-carrier. i.e. $|X_k^m + C_k^m|^2$.

4.3 Tone Reservation: Problem Formulation

As explained in Section 3.5.1.1, the oversampled versions of the continuous-time multicarrier signal are accurate predictors of the continuous-time PAPR. Therefore, all mathematical formulation, used in the following sections, will be based on the L-times oversampled version of the discrete-time signal $x^m[n]$. At this time, no assumption is made on the value of L unless explicitly stated.

As already mentioned, the main idea behind the tone-reservation based PAPR reduction technique is to design an additive signal $c^m[n/L]$ to form a lower peak-power signal $\bar{x}^m[n/L]$. Some sub-carriers in the frequency domain are reserved for the purpose of creating the additive signal $c^m[n/L]$. This process can be represented by the following matrix formulation:

$$\begin{bmatrix} \bar{x}_0^m \\ \bar{x}_{1/L}^m \\ \bar{x}_{2/L}^m \\ \vdots \\ \vdots \\ \bar{x}_{n/L}^m \\ \vdots \\ \vdots \\ \bar{x}_{(NL-1)/L}^m \end{bmatrix}_{NL\times 1} = \mathbf{F_1}^{-1} \begin{bmatrix} \bar{X}_0^m \\ \vdots \\ \bar{X}_{N/2-1}^m \\ 0 \\ \vdots \\ 0 \\ \bar{X}_{N/2}^m \\ \vdots \\ \bar{X}_{N-1}^m \end{bmatrix}_{NL\times 1} + \mathbf{F_1}^{-1} \begin{bmatrix} \bar{C}_0^m \\ \vdots \\ \bar{C}_{N/2-1}^m \\ 0 \\ \vdots \\ 0 \\ \bar{C}_{N/2}^m \\ \vdots \\ \bar{C}_{N-1}^m \end{bmatrix}_{NL\times 1} \tag{4.5}$$

Where $\mathbf{F_1}^{-1}$ represents the $NL \times NL$ inverse Fast Fourier Transform matrix with elements $f_{n,k} = \frac{1}{\sqrt{N}} e^{j2\pi nk/NL}$. The inclusion of $N(L-1)$ zeros both in the $\mathbf{X}^m$ and $\mathbf{C}^m$ vectors are used for interpolating the signal in the discrete-time domain [TELL99]. This matrix equation can be further simplified by excluding the zero padded portions together with the corresponding columns in $\mathbf{F_1}^{-1}$ to result in a simpler equation represented by:

$$\bar{\mathbf{x}}^m = \mathbf{F}^{-1}(\mathbf{X}^m + \mathbf{C}^m) \tag{4.6}$$

where $\mathbf{F}^{-1}$ is a sub-matrix of $\mathbf{F}_1^{-1}$ formed by selecting its first and last $N/2$ columns and the new matrix has dimensions $NL \times N$.

A set of pre-defined indices $\mathcal{U} = \{r_0, r_1, \ldots\ldots, r_{U-1}\}$ of U elements are reserved in the frequency domain for the purpose of reducing the PAPR of the OFDM signal. Since $\mathbf{X}^m$ and $\mathbf{C}^m$ do not use the same sub-carrier in the frequency domain, we can express them as follows:

$$X_k^m + C_k^m = \begin{cases} C_k^m, & k \in \mathcal{U} \\ X_k^m, & k \in \mathcal{U}^c \end{cases} \tag{4.7}$$

Since the symbol demodulation at the receiver is done in the frequency domain on a sub-carrier by sub-carrier basis, the sub-carrier reserved for the purpose of PAPR reduction can simply be discarded at the receiver, while the data bearing sub-carriers can be used to determine the transmitted bit stream.

Given the set $\mathcal{U}$, the tone reservation approach attempts the following optimization problem (minimax problem) [BRIA04]:

$$C^* = \underset{C \in \mathcal{C}}{\operatorname{argmin}} \|\mathbf{F}^{-1}(\mathbf{X}^m + \mathbf{C}^m)\|_\infty \tag{4.8}$$

Where $\mathcal{C}$ is the U-dimensional signal space of all possible peak-cancelling signals lying in the set of sub-carriers $\mathcal{U}$.

Alternatively, the optimization problem in equation (4.8) can also be formulated using equation (4.6) as;

$$C^* = \underset{C \in \mathcal{C}}{\operatorname{argmin}} \|\bar{\mathbf{x}}^m\|_\infty \tag{4.9}$$

4.4 Previous work

The idea of utilizing the reserved or unused sub-carriers to design the peak-cancelling signal was independently developed by Gatherer and Polley [GATH98] and Tellado and Cioffi [TELL99]. Both groups proposed a technique which iteratively projects the "peaky" portion of the signal onto the reserved sub-carriers. These techniques are very much related in the way they reduce the PAPR of the signal and they will be outlined in this section. In addition, in this section, the active set approach [BRIA04], which is the most efficient existing TR based algorithm for reducing the PAPR of OFDM in the literature, will also be outlined.

Gatherer and Polley [GATH98] jointly developed two algorithms for controlling the clipping of the multi-carrier modem; one based on the projection in the transmitter and the other based on the

parametric estimation in the receiver. Each of these algorithms can be independently implemented either in the transmitter or receiver and operated without the coordination of the far-end modem.

The first algorithm, Fourier Projection Algorithm (FPA), utilizes a time-domain shaping vector generated in the frequency domain for iteratively reducing the peak to average power by adding energy to the unused sub-carriers in the transmitter. The second algorithm, the Clipping Estimation and Correction (CEC) algorithm, operates in the receiver by estimating the position of the time-domain signal at which the clipping occurred. Based on the error amplitude and the phase in the frequency domain, the receiver constructs a correction vector to compensate the clipping [GATH98]. Due to the fact that the receiver based algorithm does not prevent the out-of-band distortion occurring at the transmitter, only the transmitter based algorithm is discussed here.

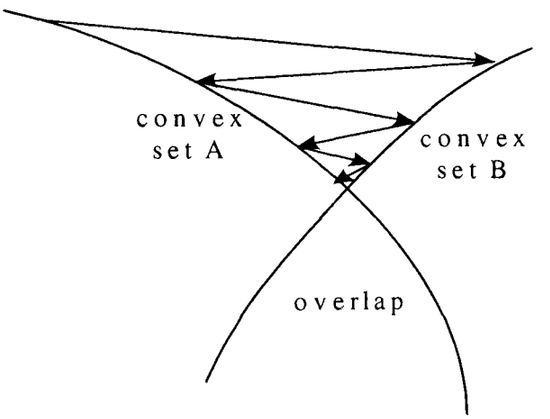

Figure 4-2: Implementation of the projection algorithm [GATH98]

FPA operates based on the Projection onto Convex Sets (POCS) technique where the peak level reduction is achieved by the iterative projections onto a set of convex sets, as shown in Figure 4-2. Assuming a subspace of complex matrix $\boldsymbol{S_X} \in \mathbb{C}^{N\times M}$, $N > M$ which maps M-length complex data vector $\boldsymbol{D} \in \mathbb{C}^M$ to $\boldsymbol{X}$ by the following relation [GATH98]:

$$\boldsymbol{X} = \boldsymbol{S_X D} \tag{4.10}$$

These convex sets are defined as [GATH98]:

1. The convex set $\boldsymbol{A}$ $(\boldsymbol{S_A})$ consisting of all vectors $\boldsymbol{y} \in \mathbb{C}^N$ such that $\|\boldsymbol{y}\|_\infty \leq A$ for some positive constant A.
2. The convex set $\boldsymbol{B}$ $\left(\boldsymbol{S_B} \in \mathbb{C}^{N\times\mathcal{U}}\right)$, where $\mathcal{U} = N - M$, orthogonal complement of $\boldsymbol{S_B} = \boldsymbol{S_X^{\perp}}$.

In the frequency domain, $\mathcal{U}$ subcarriers are reserved for designing the peak-cancelling signal and therefore, carrying no information. The data subcarriers are reflected in the vector $\boldsymbol{X}$. The projection of the resulting N-length time domain signal onto the first set can be used as the

operation in time domain that clips all samples with magnitude greater than the pre-specified level, A. The clipped signal is then projected back onto the second set; projection is done in the frequency domain, where only the information carrying sub-carriers are reset to their original values. The respective time-domain signal is then projected back onto the first convex set, and the entire process will be repeated until both projections yield no change. The POCS algorithm is as follows [GATH98].

1. Starting with $\boldsymbol{X}$, apply IFFT to get the time domain $\boldsymbol{x}$
2. Clip $\boldsymbol{x}$ (i.e. project onto $\boldsymbol{S_A}$) . If any element changes value go to step 3. Otherwise, return $\boldsymbol{x}$ and terminate.
3. FFT $\boldsymbol{x}$ and set the data subcarriers back to the original data values in $\boldsymbol{X}$. IFFT to get the new $\boldsymbol{x}$.
4. Return to step 2.

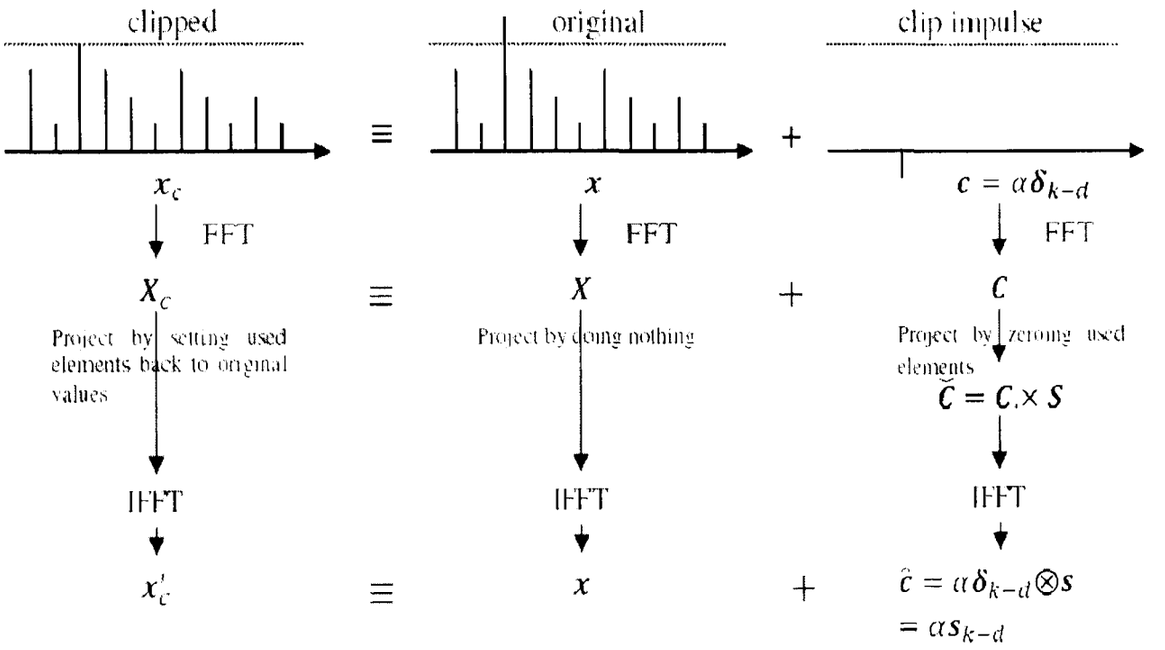

Figure 4-3: Decomposition of the POCS algorithm [GATH98]

The complexity order of this algorithm is the order of the FFT processing, $O(N \log N)$. By utilizing the linearity property associated with the FFT/IFFT processing, a reduced complexity algorithm was proposed in [GATH98]. Moreover, by considering the fact that the signal vector $\boldsymbol{x}$ has nearly independent Gaussian elements and therefore, is unlikely to have more than one or two clips in any vector. Thus, their effects can be handled independently and combined linearly. Using these features, the algorithm can be decomposed by set of pre-processed functions which can be completely iterated in the time-domain and thereby eliminates the FFT-IFFT loop in the original algorithm.

Figure 4-3 illustrates how the decomposition can be accomplished. Considering the first step, in which $\boldsymbol{x}$ is clipped to create $\boldsymbol{x}_c$ and $\boldsymbol{c} = \sum_{n=0}^{N-1} \alpha \delta_{n-d}$

$$\boldsymbol{x}_c = \boldsymbol{x} + \boldsymbol{c} \tag{4.11}$$

Taking the FFT on both sides yields $\boldsymbol{X}$ and $\boldsymbol{C}$.

$$\boldsymbol{X}_c = \boldsymbol{Q}_N(\boldsymbol{x} + \boldsymbol{c}) = \boldsymbol{X} + \boldsymbol{C} \tag{4.12}$$

Where $\boldsymbol{Q}_{N\times N}$ is $N \times N$ discrete Fourier transform matrix.

Projecting $\boldsymbol{X}_c$ onto the set of used subcarriers $\boldsymbol{S}_X$ gives us $\widetilde{\boldsymbol{X}}$, whereas projecting $\boldsymbol{x}$ onto the set of used subcarriers returns $\boldsymbol{x}$ unchanged. Projecting $\boldsymbol{C}$ onto $\boldsymbol{S}_B$, which effectively zeros out the subcarriers used for transmitting data, giving us :

$$\breve{\boldsymbol{C}} = \boldsymbol{C}.* \mathbf{1}_{\boldsymbol{S}_B} \tag{4.13}$$

Where $\mathbf{1}_{\boldsymbol{S}_B}$is the indicator function for $\boldsymbol{S}_B$. After the projections onto the convex sets, transforming the resulting signal back into time-domain:

$$\begin{aligned} \boldsymbol{x}'_c &= \boldsymbol{Q}_{N\times N}^{-1}\widetilde{\boldsymbol{X}} = \boldsymbol{Q}_{N\times N}^{-1}(\boldsymbol{X} + \breve{\boldsymbol{C}}) = \boldsymbol{Q}_{N\times N}^{-1}\boldsymbol{X} + \boldsymbol{Q}_{N\times N}^{-1}(\boldsymbol{C}.* \mathbf{1}_{\boldsymbol{S}_B}) \\ &= \boldsymbol{Q}_{N\times N}^{-1}\boldsymbol{X} + \boldsymbol{Q}_{N\times N}^{-1}\boldsymbol{C} \otimes \boldsymbol{Q}_{N\times N}^{-1}\mathbf{1}_{\boldsymbol{S}_B} \\ &= \boldsymbol{x} + \boldsymbol{c} \otimes \boldsymbol{s} \\ &= \boldsymbol{x} + \sum_{n=0}^{N} \alpha \boldsymbol{s}_{(n-d) mod\ N} \end{aligned} \tag{4.14}$$

Where $\otimes$ denotes the circular convolution [SAYE03]. Thus, the POCS approach may be completely iterated in the time-domain by simply applying scaled and shifted version of the shaping function $\boldsymbol{s}$ to $\boldsymbol{x}$.

1. IFFT the input vector to get $\boldsymbol{x}$.
2. Record the positions and amplitudes of any clip that would occur if $\boldsymbol{x}$ were clipped. If no clipping occurs return $\boldsymbol{x}$ and terminate.
3. For each clip add to $\boldsymbol{x}$ the shaping function scaled by the clipping amplitude and circularly shifted so it is centred about the clipping position.
4. Go back to step 2.

Although the second algorithm has significantly reduced the complexity of the approach, the convergence of the algorithm is still slow and therefore, may require infinite number of iterations or projections to achieve the optimal solution. Furthermore, it may even take many iterations to obtain a good, yet suboptimal, solution [BRIA04].

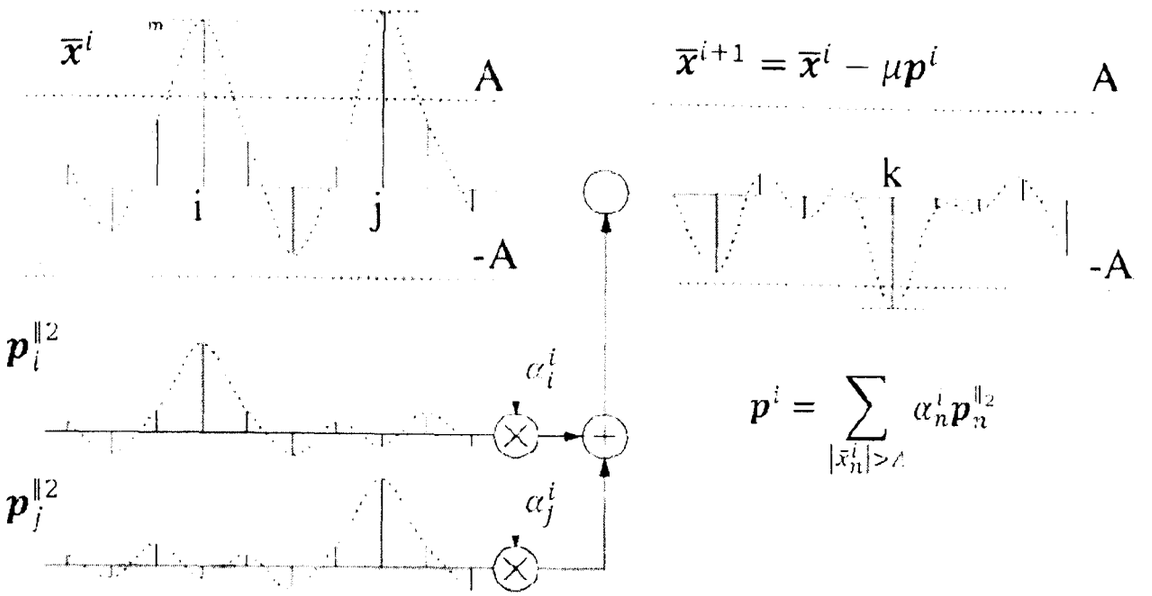

Figure 4-4: Illustration of the controlled clipper algorithm [TELL99]

Figure 4-4 illustrates the controlled clipper algorithm [TELL99], which iteratively calculates the peak-reduced time domain OFDM signal as follows:

$$\bar{x}^{i+1} = \bar{x}^i - \mu \sum_{|\bar{x}_n^i|>A} \alpha_n^i p_n^{\|_2} \tag{4.15}$$

where $\bar{x}^i$ is the peak-reduced signal at the i^{th} iteration, $\bar{x}^0 = x$, x is the OFDM signal, A is the target magnitude upper bound of the peak-reduced signal, α_n^i are the clipping noise samples at the i^{th} iteration, $p_n^{\|_2}$ is the prototype peak-cancelling (time domain) signal. In the ideal case, the prototype peak-cancelling signal must have minimum side lobes and therefore, the time domain prototype peak-cancelling signal must be equal to the impulse, i.e. $[1,0,0,\ldots\ldots,0] = e_0$, for optimal performance: every time when the TR algorithm cancels a peak in the given symbol, secondary peaks are not generated at other locations. However, this prototype signal requires all sub-carriers in the frequency domain and therefore, no sub-carriers will be available for useful data transmission. Thus, a methodology must be adopted to design the prototype peak-cancelling signal as close to e_0 as possible. In addition, this method must also satisfy the condition,

$$\text{number of Reserved Tones (R)} \ll \text{Number of subcarriers(N)}.$$

Accordingly, a Mean Square Error (MSE) based approach was considered in [TELL99] assuming a small portion of the sub-carriers reserved for designing the prototype signal. This MSE problem

formulation for designing the prototype peak-cancelling signal has a simple straight forward closed-form solution, given by[4]:

$$\boldsymbol{p}^{\|_2} = \frac{\sqrt{N}}{R}\mathbf{F}^H\mathbf{1}_R \tag{4.16}$$

where R denotes the number of reserved subcarriers in the frequency domain and $\mathbf{1}_R$ is a vector with ones assigned to those locations. Solving (4.16) directly, requires $2NLR$ real multiplications and $2NLR(R-1)$ real additions [TELL99]. The convergence rate of this algorithm slows down after several iterations, and therefore may require many iterations to obtain a reasonable PAPR reduction [BRIA04].

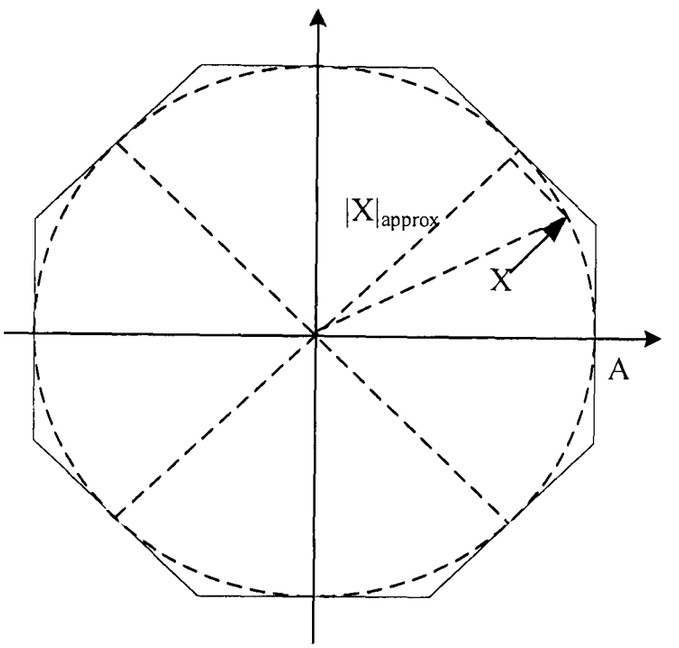

Figure 4-5: Polygonal approximation of the peak boundary

On the other hand, Korngold [BRIA04] proposed an algorithm, similar to the mathematical algorithm proposed in [CHAR78], which utilises the Linear Program (LP)-based active set approach for solving the complex plane optimization problem in (4.9) by separately looking at the real and imaginary coefficients of the samples. The problem is therefore equivalent to trying to fit the magnitude of all samples into a square in the complex plane; the square is used to approximate the peak boundary (a circle centered at the origin of the complex plane)[5]. Obviously, square approximation does not lead to optimal solution and therefore, it must be replaced by an octagonal boundary for closely approximating the circular boundary using a polygon. This is shown in

[4] This is the final equation which produces highest value at the first sample of the prototype signal and therefore, it is not biased by the sample location.

[5] A similar approach was used by complex FIR filter design technique presented in [CHEN87]

Figure 4-5 which approximates the peak boundary by an octagon of radius A. The magnitude of point X in the complex plane can be approximated by:

$$|X| \approx |X|_{approx} = max\left[\Re(X), \Im(X), \Re\left(Xe^{j\pi/4}\right), \Im\left(Xe^{j\pi/4}\right)\right] \qquad (4.17)$$

Where $\Re(\cdot)$ and $\Im(\cdot)$ represent the real and imaginary part of x, respectively. Therefore, all points that satisfy $|X|_{approx} \leq A$ will be within the octagon of radius A. Moreover, the reduction in the approximated peaks of the OFDM signal to A would result in an OFDM signal with actual peaks slightly larger than A. This new problem can be written as a linear program with four times more constraint equations than the originally proposed algorithm in [BRIA04]. Further phase rotations, e.g. 16-agon and 32-agon or larger, may produce well approximated results compared to the octagon approximation of the peak boundary. Since the complexity increases accordingly, a cost-performance trade-off dictates which boundary should be used in practice.

With this polygonal approximation, the complex OFDM vector $\boldsymbol{x}$ is written as a real vector $\hat{\boldsymbol{x}}$ consisting of the real and imaginary parts of $\boldsymbol{x}$ and its phase shifted versions. Similarly, the prototype peak-cancelling signal $\boldsymbol{p}_n^{\|_2}$ will also be written as a real vector $\hat{\boldsymbol{p}}$. The algorithm then maintains an active set containing the peaks of $\hat{\boldsymbol{x}}$, whose magnitudes are reduced to the same level as that in the previous iterations. Each sample x_{n_i} in the active set is associated with a peak-cancelling kernel $\hat{\boldsymbol{p}}_i$(a shifted version of $\hat{\boldsymbol{p}}$ whose peak is at n_i). These $\hat{\boldsymbol{p}}_i$ are weighted and summed together to form the peak-cancelling signal $\overline{\boldsymbol{p}}$. In each iteration, the weighting factors of $\hat{\boldsymbol{p}}_i$are calculated by solving a set of l linear equations, where l is the iteration number, to find the proper optimization direction. Then, the peak-cancelling signal $\overline{\boldsymbol{p}}$ will be scaled by μ[6] and subtracted from $\hat{\boldsymbol{x}}$. This will equally reduce the magnitude of all samples in the active-set. Likewise, the algorithm is repeated for more iterations.

There is an interesting problem which occurs in this approximated complex problem at the worst-case magnitude points outside the circle, which is called 'corner effect'; when the signal sample lies on corner of the reduced boundary. This has significant consequences on the convergence speed of the active-set approach. As the size of the polygon boundary increases, the number of corner points also increases and therefore, the distance between them decreases. Thus, a better circle approximation could cause slower convergence toward the optimal solution [BRIA04].

In real life applications the values of the reserved sub-carriers have to be limited as there are power spectral density constraints for different applications imposed by the standards for spectral compatibility reasons. Therefore, the average power levels of the reserved tones are constrained by the power spectral mask levels. This average power constraint can be converted to peak

[6] step size parameter, which represents the distance travelled in the decent direction.

magnitude constraints for algorithmic convenience, in which case we can write the peak minimization problem as the constrained optimization problem:

$$\begin{aligned} &\text{minimize } J(\boldsymbol{\rho}), \\ &\text{subject to } \boldsymbol{\rho} \leq \boldsymbol{\beta} \end{aligned} \tag{4.18}$$

Where $\boldsymbol{\beta}$ is the positive vector of peak magnitude constraints.

In Section 4.5, we present a gradient based framework used for directly minimizing the cost function in (4-9). Basic contributions and benefits of the proposed gradient-based approach can be listed as follows:

- Due to the fact that the information symbols are in the discrete-frequency domain, it may be very difficult to directly design $c^m[n]$ in the discrete-time domain. Therefore, the technique proposed in this chapter considers designing the C_k^m in the discrete-frequency domain and evaluating its performance on $\bar{x}^m[n]$
- This gradient based approach allows the direct treatment of the original problem in (4-9), instead of dealing with equivalent problems, by simply approximating the infinite-norm function using the p-norm function.
- The approach can easily be extended to incorporate the spectral constraints by simply limiting the reserved sub-carriers power in the frequency domain with negligible computation cost.
- The algorithm follows a simple update rule and hence, exhibits low computational complexity; thus, is suitable for the real time implementations. (A complexity comparison is given in Section 4.8).

4.5 Proposed Algorithm: A Gradient Based Approach

In this section, a step-by-step derivation of the proposed gradient based algorithm is elaborated. It should be noted that we use the oversampled versions of the above signals in order to closely approximate the continuous-time PAPR of the OFDM signal. As a common convention used in the literature, we denote the signals using the over-bar notation, if they are formed by the combination of both the information signals and peak-cancelling signal. For example, the oversampled signals are denoted by $\bar{x}[n/L]$, $\bar{y}[n/L]$ etc. Moreover, the algorithm is briefly described using a flow chart considering only the main steps to reduce the PAPR of a single OFDM signal.

4.5.1 Proposed Algorithm Derivation

As described in Section 3.5.1.1, the Nyquist-rate samples might not reveal the peaks of the continuous-time signal and therefore, it is desirable to show PAPR performance on over-sampled discrete-time signals. This oversampling is done by simply performing the IFFT to the frequency domain symbol vector, $\check{\mathbf{X}}$, formed by concatenating $N(L-1)$ zeros to the original frequency domain vector [SEUN05]:

$$\mathbf{X}' = [\check{X}_0, \check{X}_1, \ldots\ldots, \check{X}_{N/2-1}, 0, \ldots\ldots.0, \check{X}_{N/2}, \ldots\ldots, \check{X}_{N-1}]^T \tag{4.19}$$

According to equation (3.5), the OFDM signal is generated by:

$$\mathbf{x} = \mathbf{Q}\mathbf{X}' \tag{4.20}$$

Where $\mathbf{Q} = [Q_{lm}]_{NL\times NL}$ is the IFFT matrix with $Q_{lm} = \frac{1}{\sqrt{NL}} e^{j2\pi(l-1)(m-1)}$, $l = 1,2,\ldots,NL$ and $m = 1,2,\ldots\ldots,NL$.

In order to simplify equation (4.20), the zeros in the column vector $\mathbf{X}'$ and the corresponding columns in the matrix $\mathbf{Q}$ are eliminated in the following algorithmic formulations. Therefore, the reduced form of the equation (4.20) becomes:

$$\mathbf{x} = \mathbf{F}^{-1}\check{\mathbf{X}} \tag{4.21}$$

Where $\mathbf{F}^{-1}$is a matrix with size $NL \times N$ in which the columns are eliminated.

If we assume that V pilot symbols are assigned to V sub-carriers with indexes $\boldsymbol{l}_V = \{l_1, l_2, \ldots\ldots, l_V\}$ in the OFDM transmitter, equation (4.21) can be decomposed into (4.22), which is similar to equation (4.5) & (4.6):

$$\mathbf{x} = \mathbf{F}^{-1}\mathbf{X} + \mathbf{F}^{-1}\mathbf{C} \tag{4.22}$$

Where the column vector $\mathbf{C}$ consists of the sub-carriers to be used for PAPR reduction and the column vector $\mathbf{X}$ consists of the information to be transmitted from the transmitter to the receiver. The above equation can be further simplified into:

$$\mathbf{x} = \mathbf{y} + \mathbf{F}^{-1}\mathbf{C}, \qquad \text{where } \mathbf{y} = \mathbf{F}^{-1}\mathbf{X} \tag{4.23}$$

As common with all PAPR reduction schemes, our task now is to minimize the cost function given by (4.18):

$$J_\infty = \|\mathbf{x}\|_\infty = \|\mathbf{y} + \mathbf{F}^{-1}\mathbf{C}\|_\infty \tag{4.24}$$

The above defined function is an infinity-norm function and such functions are very often used in minimization problems because they are convex functions; therefore, are easily tractable in minimization problems [CHAR78]. We can show the convexity of this type of function by using

the triangle inequality and scaling properties of the norms [BOYE04]: for a given $\lambda \in [0,1]$. If we define the cost function as:

$$f(\mathbf{C}) = \|\mathbf{y} + \mathbf{F}^{-1}\mathbf{C}\|_{\infty} \tag{4.25}$$

Let $\mathbf{a}, \mathbf{b} \in \mathbb{C}^{N\times 1}$ be two vectors in the convex set. If their convex combination, $\lambda\mathbf{a} + (1-\lambda)\mathbf{b}$, also lies in the convex set then the cost function is a convex cost function. Substituting $\mathbf{C} = \lambda\mathbf{a} + (1-\lambda)\mathbf{b}$ in (4.25) gives:

$$\begin{aligned} f(\lambda\mathbf{a} + (1-\lambda)\mathbf{b}) &= \|\mathbf{y} + \mathbf{F}^{-1}(\lambda\mathbf{a} + (1-\lambda)\mathbf{b})\|_{\infty} \\ f(\lambda\mathbf{a} + (1-\lambda)\mathbf{b}) &= \|\lambda(\mathbf{y} + \mathbf{F}^{-1}\mathbf{a}) + (1-\lambda)(\mathbf{y} + \mathbf{F}^{-1}\mathbf{b})\|_{\infty} \\ f(\lambda\mathbf{a} + (1-\lambda)\mathbf{b}) &\leq \|\lambda(\mathbf{y} + \mathbf{F}^{-1}\mathbf{a})\|_{\infty} + \|(1-\lambda)(\mathbf{y} + \mathbf{F}^{-1}\mathbf{b})\|_{\infty} \\ f(\lambda\mathbf{a} + (1-\lambda)\mathbf{b}) &\leq \lambda f(\mathbf{a}) + (1-\lambda) f(\mathbf{b}) \end{aligned} \tag{4.26}$$

Therefore, the cost function of this form is a convex function and thus it can also be shown that the local minimum of a convex function is necessarily a global minimum.

Despite its convexity, the infinity-norm function in (4.25) is not differentiable due to its non-smooth nature. Thus, a simple gradient descent approach cannot be directly used for such cost functions. This necessitates converting the infinite-norm cost function to a differentiable one by approximating it using a p-norm cost function with a large p value, which is a differentiable cost function. Similar to [GONZ98], we take an approximated approach based on the p-norm approximation for infinite-norm:

$$J_p = \lim_{p\to\infty} \|\mathbf{x}\|_p \tag{4.27}$$

According to [BOYE04], the p-norm function can also be shown as a convex function for any value of p (can be proved using the similar approach used in equation (4.26)) and therefore, leads to a simplified optimization problem with smooth cost function. Accordingly the cost function defined in (4.25) can be minimized directly using an iterative approach similar to the steepest descent algorithm in [HAYK96].

The definition of p-norm is given by:

$$J_p = \|\mathbf{x}\|_p = \left[\sum_{r=1}^{NL} |x_r|^p\right]^{1/p} \tag{4.28}$$

Where $1 < p < \infty$ and $|x_r|^2 = x_r^* x_r$.

Equation (4.28) gives a family of cost function for different values of p: least square criterian, $p = 2$, to the minimax criterion , $p = \infty$, and the intermediate steps, $p = 2k$ with k a positive interger, can be called weighted least squares. However, our study focuses on the limiting case when p tends to infinity; minimax criterion.

Equation (4.28) can be further simplified into:

$$J_p = \left[\sum_{r=1}^{NL} (x_r^* x_r)^{p/2}\right]^{1/p} \tag{4.29}$$

The cost function can be differentiated with respect to the real and imaginary parts of the reserved tones in the frequency domain, $\mathbf{C}_\mathrm{R}$ and $\mathbf{C}_\mathrm{I}$, and the resulting expression can be combined into a single complex expression [HAYK96]:

$$\frac{\partial J_p}{\partial \mathbf{C}} = \frac{\partial J_p}{\partial \mathbf{C}_\mathrm{R}} + \mathrm{j}\frac{\partial J_p}{\partial \mathbf{C}_\mathrm{I}} \tag{4.30}$$

Expanding the column vector $\mathbf{x}$ in terms of the components of $\mathbf{y}$, $\mathbf{F}^{-1}$, and $\mathbf{C}$ will give the following:

$$\begin{aligned}(|x_r|^2)^{p/2} &= |x_r|^p \\ &= [(y_r + W_{r,1}C_1 + \ldots\ldots\ldots\ldots + W_{r,N}C_N)^*(y_r + W_{r,1}C_1 \\ &\quad + \ldots\ldots\ldots\ldots + W_{r,N}C_N)]^{p/2}\end{aligned} \tag{4.31}$$

Where row vector $\mathbf{W}_r$ denotes the r^{th} row of the matrix $\mathbf{F}^{-1}$.

The derivative of the cost function J_p with respect to the first element in the real vector of $\mathbf{C}$ is given by:

$$\frac{\partial J_p}{\partial C_{1,R}} = \frac{1}{p}\left(\sum_{r=1}^{NL}|x_r|^p\right)^{1/p-1}\frac{p}{2}\sum_{r=1}^{NL}(x_r^* x_r)^{p/2-1}\left[x_r^*\frac{\partial x_r}{\partial C_{1,R}} + x_r\frac{\partial x_r^*}{\partial C_{1,R}}\right] \tag{4.32}$$

The above equation (4.32) can be reduced to:

$$\frac{\partial J_p}{\partial C_{1,R}} = \frac{1}{2}(J_p)^{1-p}\sum_{r=1}^{NL}|x_r|^{p-2}(x_r^* W_{r,1} + x_r W_{r,1}^*) \tag{4.33}$$

Similarly, the derivative of the cost function $J_p$with respect to the first element in the imaginary vector of $\mathbf{C}$ is given by:

$$\frac{\partial J_p}{\partial C_{1,I}} = \frac{1}{p}\left(\sum_{r=1}^{NL}|x_r|^p\right)^{1/p-1}\frac{p}{2}\sum_{r=1}^{NL}(x_r^* x_r)^{p/2-1}\left[x_r^*\frac{\partial x_r}{\partial C_{1,I}} + x_r\frac{\partial x_r^*}{\partial C_{1,I}}\right] \tag{4.34}$$

The above equation (4.34) can be reduced to:

$$\frac{\partial J_p}{\partial C_{1,I}} = \frac{1}{2}(J_p)^{1-p}\sum_{r=1}^{NL}|x_r|^{p-2}\left(x_r^* W_{r,1} + x_r W_{r,1}^*\right) \tag{4.35}$$

Combining equation (4.33) and (4.35), the complex expression for the derivative of the cost function J_p with respect to the first element in the column vector **C** will be:

$$\begin{aligned}\frac{\partial J_p}{\partial C_1} &= \frac{\partial J_p}{\partial C_{1,R}} + j\frac{\partial J_p}{\partial C_{1,I}} \\ &= (J_p)^{1-p}\sum_{r=1}^{NL}|x_r|^{p-2}x_r W_{r,1}^*\end{aligned} \tag{4.36}$$

Equation (4.30) can be expanded as :

$$\frac{\partial J_p}{\partial \mathbf{C}} = \begin{bmatrix}\frac{\partial J_p}{\partial C_{1,R}}\\ \frac{\partial J_p}{\partial C_{2,R}}\\ \vdots\\ \vdots\\ \frac{\partial J_p}{\partial C_{N,R}}\end{bmatrix} + \mathrm{j}\begin{bmatrix}\frac{\partial J_p}{\partial C_{1,I}}\\ \frac{\partial J_p}{\partial C_{2,I}}\\ \vdots\\ \vdots\\ \frac{\partial J_p}{\partial C_{N,I}}\end{bmatrix} \tag{4.37}$$

Looking at equation (4.37), each element in the vector is similar to (4.36) and thus, the gradient vector of the cost function becomes:

$$\frac{\partial J_p}{\partial \mathbf{C}} = (J_p)^{1-p}\begin{bmatrix}\sum_{r=1}^{NL}|x_r|^{p-2}x_r W_{r,1}^*\\ \sum_{r=1}^{NL}|x_r|^{p-2}x_r W_{r,2}^*\\ \vdots\\ \sum_{r=1}^{NL}|x_r|^{p-2}x_r W_{r,N}^*\end{bmatrix} \tag{4.38}$$

Further reducing equation (4.38) gives:

$$\frac{\partial J_p}{\partial \mathbf{C}} = (J_p)^{1-p} \sum_{r=1}^{NL} |x_r|^{p-2} x_r \boldsymbol{W}_{r,:}^{*} \tag{4.39}$$

Replacing $\mathbf{W}$ by $\mathbf{F}^{-1}$in the above equation will give:

$$\frac{\partial J_p}{\partial \mathbf{C}} = (J_p)^{1-p} \sum_{r=1}^{NL} |x_r|^{p-2} x_r \left(\mathbf{F}_{r,:}^{-1}\right)^{*} \tag{4.40}$$

In order to find the gradient of the cost function defined in equation (4.18), we set $p \to \infty$ similar to the equation (4.28). Then, the cost function $J_p \to |x_b|$ and $r \to b$ and therefore, equation (4.40) becomes :

$$\frac{\partial J_{p\to\infty}}{\partial \mathbf{C}} \approx |x_b|^{-1} \left(\mathbf{F}_{b,:}^{-1}\right)^{*} x_b \tag{4.41}$$

where the subscript b represents the index of the maximum magnitude of the output sample. Moreover, the above equation is obtained by assuming that only one output sample has maximum magnitude compared with the others. In case of multiple equal maximum samples, a random selection of one sample has to be considered.

According to (4.41), the gradient vector is $N \times 1$, which means that all the sub-carriers in the frequency domain are used for designing the peak-cancelling signal. In practice, only a few sub-carriers are reserved for this purpose in order to sustain the overall data rate of the system. Accordingly the gradient vector now becomes a $V \times 1$ column vector and therefore, the search direction is reduced to V – dimension. Introducing this effect in equation (4.41) will result in:

$$\frac{\partial J_{p\to\infty}}{\partial \boldsymbol{\rho}} \approx |x_b|^{-1} \left(\mathbf{F}_{b,l_V}^{-1}\right)^{*} x_b \tag{4.42}$$

Where $\boldsymbol{l}_V$ denotes the corresponding columns of the matrix $\mathbf{F}^{-1}$ which multiplies the reserved sub-carriers in the frequency domain and the $V \times 1$ column vector $\boldsymbol{\rho}$ represents the pilot symbols used for designing the peak-cancelling signals. Furthermore, the values of $\boldsymbol{\rho}$ will be inserted with the data vector in the locations denoted by $\boldsymbol{l}_V$.

Using the above defined gradient, we formulate a simple gradient based algorithm which follows a simple update rule such that the cost function value is iteratively improved. The goal is to eventually reach the neighbourhood of a global minimum point of the convex cost function defined in equation (4.18). The gradient based equation for updating the reserved pilot symbols in the frequency domain is as follows:

$$\boldsymbol{\rho}^{\mathrm{i}} = \boldsymbol{\rho}^{\mathrm{i}-1} - \mu^{i} |x_b|^{-1} \left(\mathbf{F}_{b,l_V}^{-1}\right)^{*} x_b \tag{4.43}$$

Where μ^i is a step-size parameter and the effect of this on the algorithm are investigated in Section 4.6.

4.5.2 Simplified Case: p - norm cost function with two variables (one peak cancelling symbol)

Visualizing the cost function helps to understand the behaviour of the gradient-based algorithm. In this section we investigate a simplified case of the cost function (with two variables), in order to visualize its behaviour and also to understand the function characteristics when p takes different values.

Table 4-1: Parameters Used for the Investigation

Parameter	Value
Number of Sub-carriers	16
Oversampling Factor (L)	4
Number of Peak-Reduction Symbol	1
Location of the Peak-Reduction Symbol	1

Figure 4-6 shows the linear power of the OFDM signal samples used in the considered example (parameters are shown in Table 4-1). The real and imaginary parts of the peak-reduction symbol in the frequency domain is represented using X and Y, respectively.

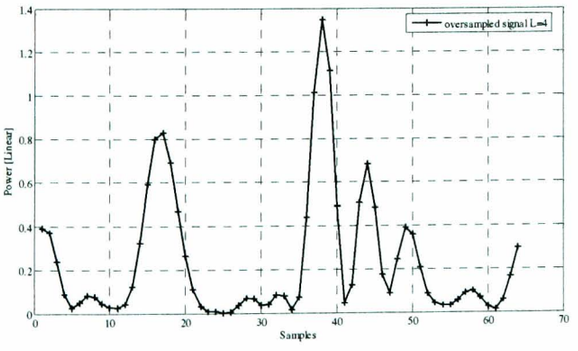

Figure 4-6: Power of the original OFDM sample

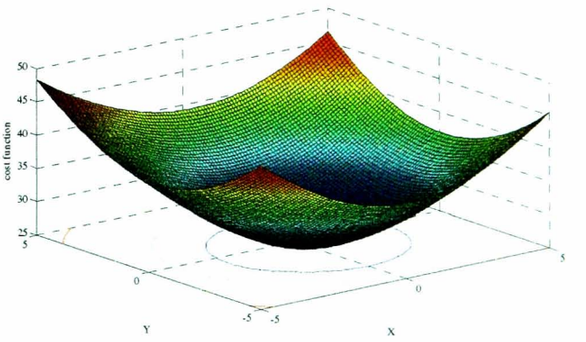

Figure 4-7: Cost function when p=1

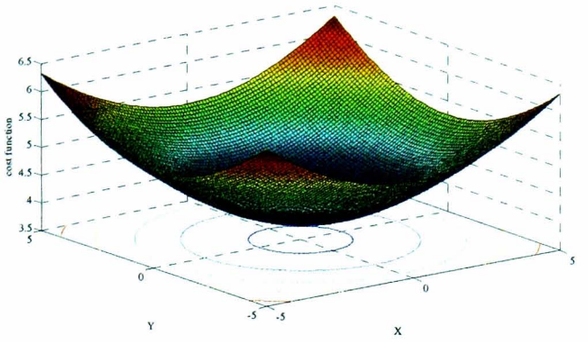

Figure 4-8: Cost function when p=2

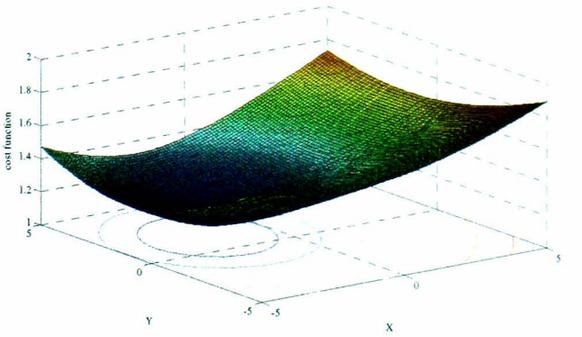

Figure 4-9: Cost function when p=10

Figure 4-7, 4-8, and 4-9 show the shape of the cost function for the cases p=1, p=2, and p=10, respectively. It can be observed that the cost function is smooth and convex, as illustrated by the shape of the contour lines.

From Figure 4-11 and 4-13 (p =100 and p=infinity, respectively) it is observed that the cost function becomes non-smooth when p takes higher values. In addition the peak power reduction capability shown in Figure 4-10 and 4-12 exhibit approximately similar performance when p=100 and p=infinity. In this way, similar behaviour was observed for different OFDM signals, with different information sequences. Accordingly, the approximation used for deriving the gradient of the infinite norm cost function, in the previous section, can be justified in the application of peak power reduction algorithms.

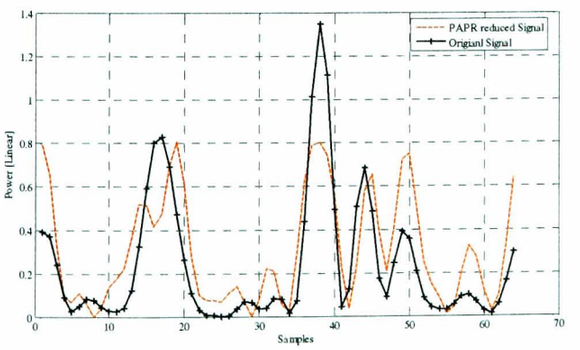

Figure 4-10: Peak Reduced Signal when p=100

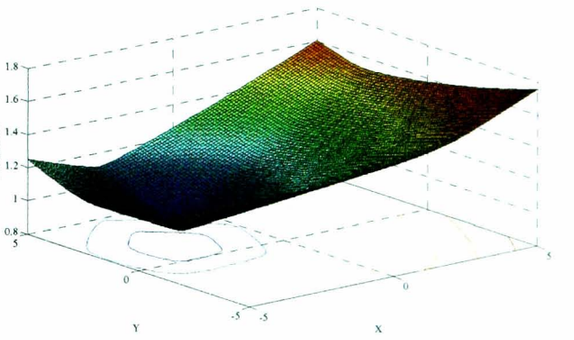

Figure 4-11: Cost Function when p=100

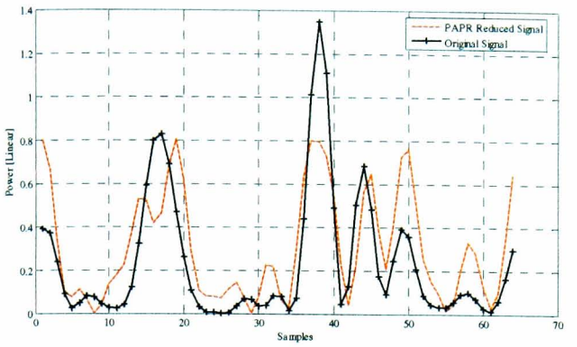

Figure 4-12: Peak reduced Signal when p=infinity

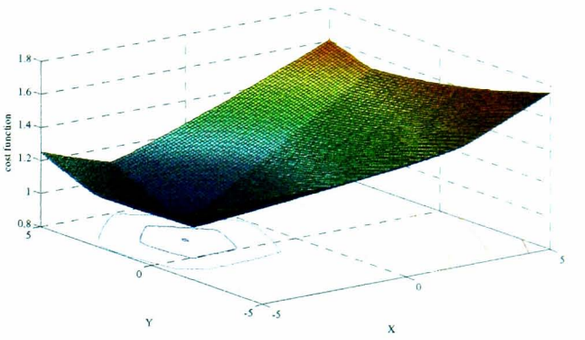

Figure 4-13: Cost Function when p=infinity

The numerical values of the real and the imaginary part of the peak-reduction symbol for different values of p are tabulated in Table 4.2. From these results, it is observed that the peak-reduction symbol for p=100 and p=infinity have approximately same power.

Table 4-2: Peak-Reduction for different values of p

p values	p-norm value	PAPR Reduction Symbol	
		Real Part	Imag. Part
p=1	25.5770	-0.1	-0.7
p=2	3.8730	0	0
p=10	1.1013	-2	1.4
p=100	0.9057	-2.6	1.6
p=infinity	0.8964	-2.6	1.7

4.5.3 Flow Chart Explanation of the proposed algorithm

In this section a simplified flow chart explanation of the proposed algorithm is presented, where the most important stages involved, in reducing the PAPR for a single OFDM symbol, are given.

As seen in the flow chart, Figure 4-14, the inverse fast Fourier transform is performed only once on the data signal. The corresponding peak-cancelling signal will be designed by following the simple update rule, given by equation (4.43), in the frequency domain. During the iteration process, the PAPR of the combined signal is evaluated and compared with the previously evaluated values. The best peak-cancelling signal will be chosen and added with the data signal in the time domain for transmission. Although the algorithm follows a direct minimization approach similar to the conventional steepest descent algorithms, the gradient obtained in each iteration is in fact not the exact gradient of the cost function. Instead it is an approximated gradient and

therefore, does not always monotonically reduce the cost function. Therefore, in order to speed-up convergence the value of the cost function at each iteration should be tracked and the best value retained until the end of pre-determined number of iterations. Extended simulations have shown that there is no significant performance advantage when the maximum number of iteration is increased.

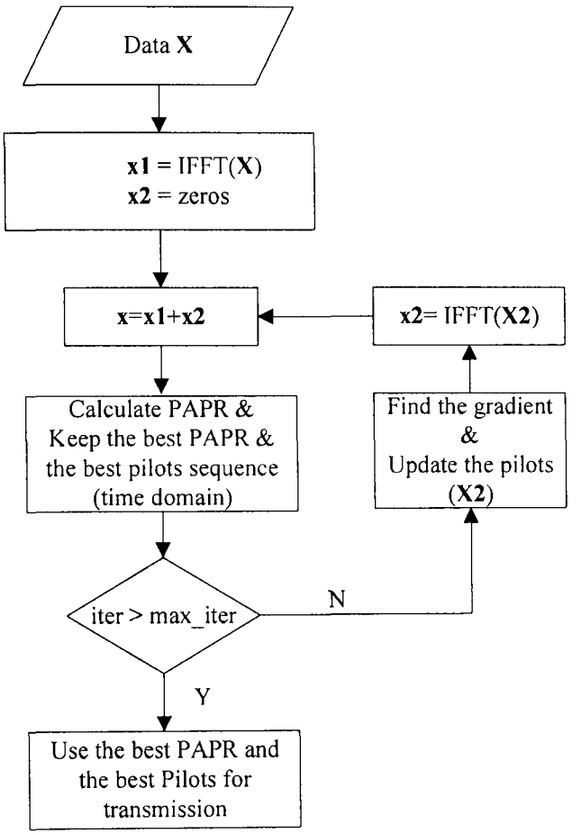

Figure 4-14: Simplified Flow Chart of the Proposed Algorithm for PAPR Reduction

4.6 Convergence behaviour

There are infinite numbers of tangential directions possible in a smooth bowl shaped function and therefore, the convergence curves usually produced in this kind of problem exhibits smooth curves. On the other hand, in the present problem, the convergence curves exhibit abrupt slope changes, as illustrated in Figure 4-15, which are explained by the non-smooth nature of the cost function. Moreover, the dependence of the abrupt slope changes on the step size parameters can also be observed; each of these different slopes corresponds to different maximum peak power being minimized. When the step size parameter is higher, the algorithm tends to minimize different maximum peak power of the signal within the considered number of iterations and therefore, it has more slope changes. However, the higher step size parameter also tends to cause oscillations in the minimum value of the cost function and therefore, creates the non-monotonic

nature explained in the previous sub-section (this introduces unnecessary complexity in tracking the minimum value of the cost function).

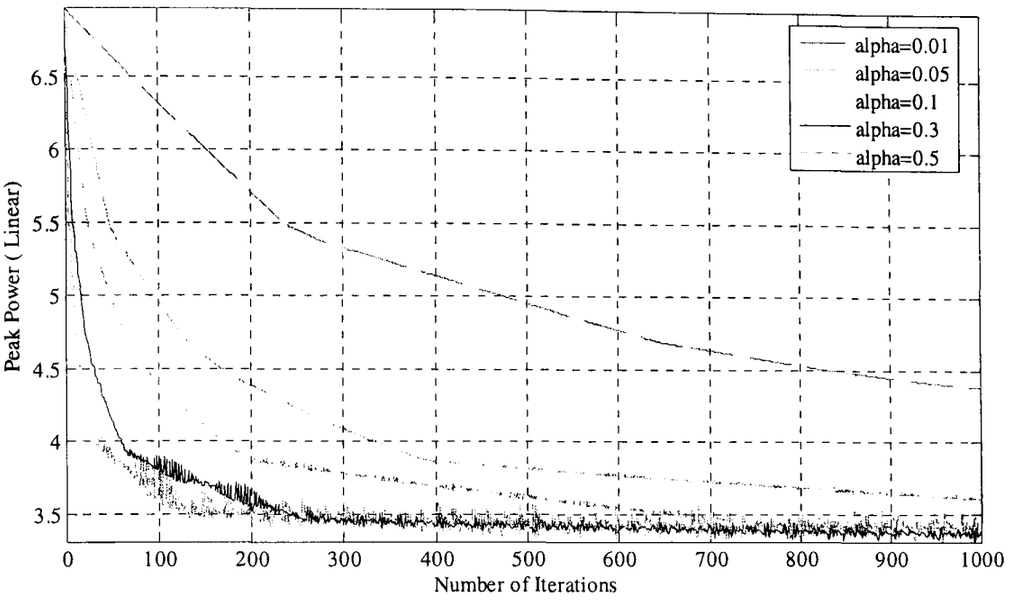

Figure 4-15: Convergence with different Step Size values (for No of subcarriers=256, Reserved subcarriers=8, oversampling factor=4)

4.7 Constrained Optimization

As was noted in the equation (4.18), the PAPR minimization encountered, in practice, is actually a constrained optimization problem, where the peak-cancelling signal cannot be designed from an arbitrarily chosen tone values. Instead, they should satisfy the Power Spectral Density (PSD) mask set by the communication standards. Therefore, the problem we need to solve is (4.18) rather than (4.9).

Since the proposed algorithm follows a simple update rule in the frequency domain, the algorithm can simply incorporate the necessary spectral constraint, by simply limiting the power amplitude or power of the pilot tones. As a result, after the update given by (4.43), we apply the following projection rule to each component of $\boldsymbol{\rho}$:

$$\mathbf{P}(\rho_k) = \begin{cases} \rho_k & |\rho_k| \le \beta_{k'} \\ \dfrac{\beta_k}{|\rho_k|}\rho_k & |\rho_k| > \beta_{k'} \end{cases} \tag{4.44}$$

Where β_k's are the magnitude constraint for the k^{th} component of $\boldsymbol{\rho}$. This projection operation is consistent with the Gradient Projection method [LEVI66] for minimizing functions over convex sets.

4.8 Complexity Analysis

In this section, we provide a complexity comparison study of the proposed algorithm against the existing active set method. The complexities of the algorithms are evaluated based on the total number of real multiplications, real additions and real divisions. Here, we count the complex multiplication as four real multiplications and two real additions [SAYE03].

4.8.1 Complexity Analysis of the Proposed Algorithms

Considering the complexity of our proposed algorithm, in each iteration, the execution time of the proposed gradient based algorithm is determined by the following steps of this algorithm:

1. Inserting pilots at the pre-determined sub-carrier locations and computing the corresponding time domain data and peak-cancelling signals: Since the data signal does not change during the iterations, we can neglect the complexity associated with the IFFT processing to generate the time-domain data signal. However, the complexity associated with the IFFT processing to generate the peak-cancelling signal must be taken into account, because this part must be repeated after every update of the pilot tones in step 3. On the other hand, the associated complexity can significantly be reduced by the property of the IFFT matrix: since the pilot is updated with the selected elements[7] in the IFFT matrix, we do not need to take the IFFT to compute the time domain contributions. Instead, the cyclic shifted version of the same kernel $\boldsymbol{p}$ as used in the active set approach [BRIA04] can be used.
2. Find the maximum absolute value of the time-domain sample which is essential for finding the gradient vector at each iteration. The determination of this peak point would require NL comparisons which can be performed using NL real additions and NL complex multiplications (for computing the magnitudes of the samples): equivalent to $4NL$ real multiplications and $3NL$ real additions.
3. Gradient Update: The length of the gradient vector is $M \times 1$. Thus, finding the gradient vector requires $6M$ real multiplications[8]. Similarly, gradient update also requires $2M$ real multiplications and $2M$ real additions.

Thus, total overall-complexity of the proposed algorithm is (for J iterations):

$$\mathcal{M}_{proposed} \approx \begin{cases} (4LNJ + 8MJ) & real\ multiplications \\ (3LNJ + 2MJ) & real\ additons \end{cases} \tag{4.45}$$

[7] Only the elements (in a row) that multiplies with the pilot locations.

[8] Step size multiplications with the $M \times 1$ sized vector is also taken into account.

Looking at equation (4.45), the complexity of the proposed algorithm is approximately of the order $O(J)$. Moreover, the complexity per single iteration is of the order $O(N)$.

4.8.2 Complexity Analysis of Active-Set Algorithm

Assume that the active-set algorithm uses the $(2G)$-agon approximation ($G = 4, 8, ...$). Then, the length of the OFDM signal vector and that of the peak-cancelling vector proceeded in each iteration is $2GLN$. According to [BRIA04], in each iteration, the execution time of the active-set algorithm is mainly determined by the following steps of this algorithm[9]:

1. Determining the active set descent direction

   This step involves solving a l linear equations and weight the l peak-cancelling kernels associated with the active set, where l is the iteration number. The complexity associated with the former can be ignored[10], if we assume a small number of iterations. However, the complexity associated with the latter is $2GLNl$ multiplications and $2GLN(l-1)$ additions [BRIA04].

2. Determining next active set constraint

   This step involves finding the optimal step size μ and then weight the peak-cancelling signal by μ. The complexity is mainly due to finding the optimal step size μ, whereas weighting the peak-cancelling signal by μ introduces only $2GLN$ real multiplications. Since each samples requires 4 additions and 2 divisions, the complexity introduced in finding the optimal step size μ is $8GLN$ real additions and $4GLN$ real divisions.

Thus, the overall complexity introduced by the active set method is (for J iterations):

$$\mathcal{M}_{Act} \approx \begin{cases} \left(2GLNJ + \sum_{l=2}^{J} 2GLNl\right) = 2GLN\left(\frac{J^2}{2} + \frac{3J}{2} - 1\right) & real\ multiplications \\ (4GLNJ) & real\ divisions \\ \left(\sum_{l=2}^{J} 2GLN(l-1) + 8GLNJ\right) = 2GLN\left(\frac{J^2}{2} - \frac{7J}{2}\right) & real\ additions \end{cases} \quad (4.46)$$

When comparing equations (4.45) and (4.46), the complexity of the active set method is of the order $O(J^2)$, which is larger than the complexity of the proposed algorithm. Moreover, in active

[9] The complexity associated with some steps in the algorithm is not considered here (for example finding the next peak, matrix inversion), however they all are included in the complexity computation of the proposed algorithm.

[10] In fact, this contributes a complexity equivalent to matrix inversion and the complexity therefore increases as the matrix size increases at each iteration.

set method, the complexity associated with a single iteration heavily depends on the iteration number and therefore leads to a complexity of the order higher than $\mathcal{O}(N)$.

4.9 Simulation Results

Table 4-3: Simulation Parameters

Parameters	Value
Num. of Sub-carriers	256
Number of Pilots (Frequency Domain)	11[11] (< 5% of the total sub-carriers)
Modulation	QPSK
DFT Spreading	245
Performance Metric	CCDF
Number of Iterations for each OFDM symbol	50
Oversampling Factor (L)	4
Pilot Locations	
Position 1	Equal-spaced starting from first location
Position 2	Suffix with the data block at both ends
Position 3	Randomly found best location[12]

The performance of the proposed algorithm was evaluated by means of computer simulations as shown in Figure 4-16. All the simulations were carried out for 10^5 OFDM blocks in order to obtain the probability up to 0.0001. The corresponding simulation parameters are given in Table 4-3. All the performances are evaluated based on the Complementary Cumulative Distribution Function (CCDF) curves of the PAPR of OFDM signal blocks. These curves represent the probability that the PAPR of an OFDM block is greater than some value, $PAPRo$, i.e.,

$$CCDF\big(PAPR(\mathbf{x})\big) = Prob(PAPR(\mathbf{x}) > PAPRo)$$

The simulated system consists of equal power QPSK modulation in the data carrying sub-carriers and the rest is reserved for designing the peak-cancelling signal. Moreover, a step size parameter of 0.3 was chosen in this investigation. Extended simulations have shown that this value makes the algorithm to minimize different maximum peaks values and there is no significant performance advantage between 0.5 and 0.3, as shown in Figure 4-15.

[11] Only 8 pilots used for the combined case (when combined with DFT spreading technique)

[12] In [BRIA04], the pilots are chosen in the following locations :{5, 25, 54, 102, 125, 131, 147, 200, 204, 209, 247}.

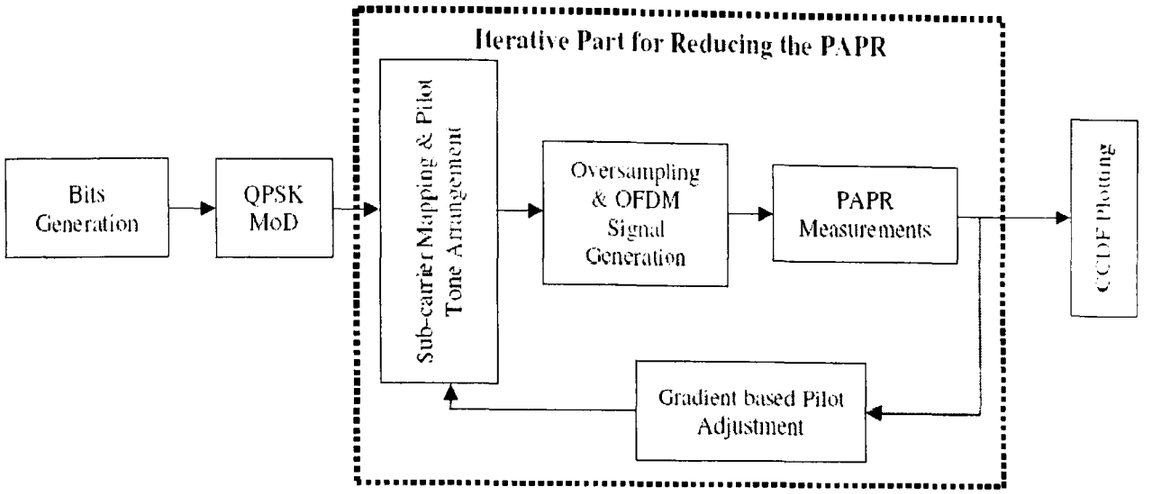

Figure 4-16: Simulation Model for Evaluating the PAPR Reduction Performance

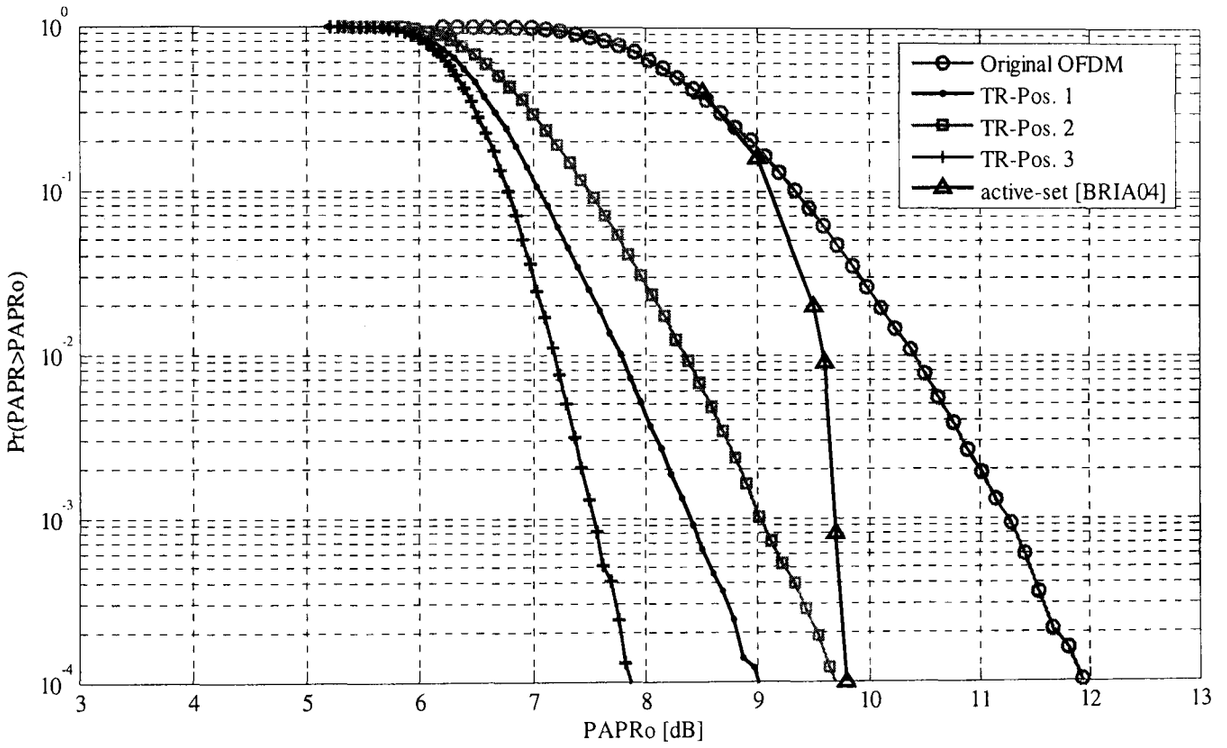

Figure 4-17: PAPR Reduction Performance of the Proposed Algorithm compared with active-set algorithm [BRIA04].

Figure 4-17 shows the performance obtained by the proposed gradient based TR algorithm for different pilot locations. It is observed that the PAPR reduction performance is pilot location dependent and it is better when the pilots are randomly[13] selected. In addition, Figure 4-17 also shows the PAPR reduction performance obtained by active set algorithm [BRIA04] for the pilot location case 3. It was shown that the algorithm converged after six iterations and therefore, no further PAPR reduction was achieved. It can be observed that the performance obtained by the

[13] Same pilot location used in [BRIA04] for active set algorithm investigation.

proposed algorithm is $2dB$ (at 10^{-4}) better than the active set approach. Moreover, as shown in Figure 4-18, the proposed algorithm provides improved PAPR reduction performance when the number of sub-carriers increased[14]. However, the performance is limited at higher number of subcarriers.

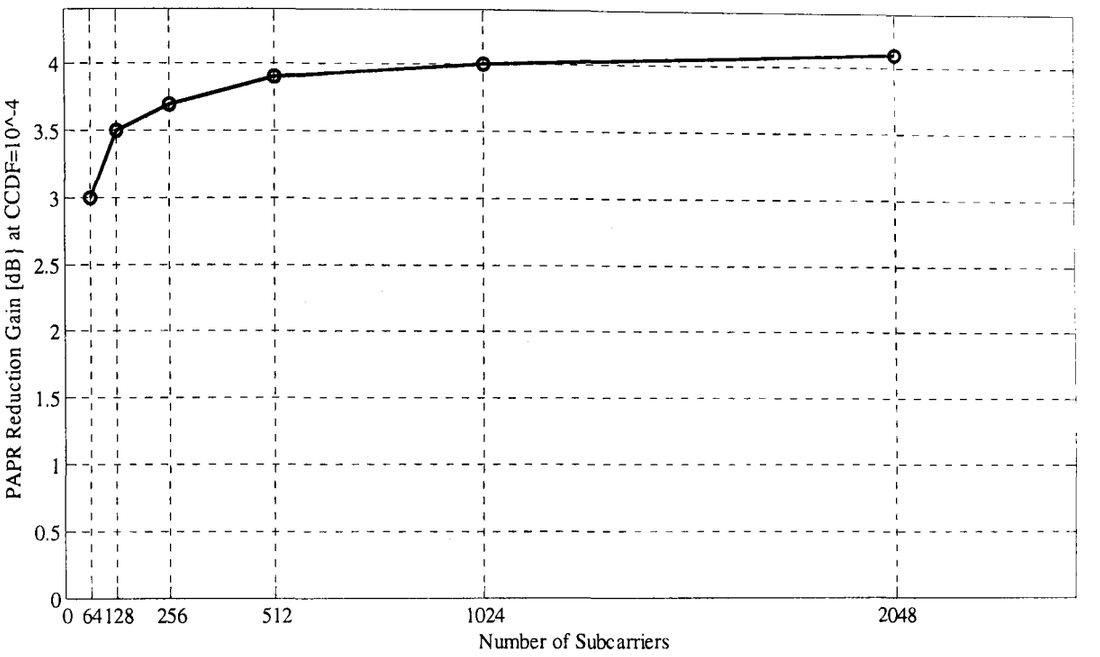

Figure 4-18: PAPR Reduction Performance with different Number of Sub-carriers

Figure 4-19 compares the above simulations results with the DFT spreading technique proposed in [HEUN07] for different pilot locations. It is observed that the proposed TR technique can achieve better results than the DFT spread OFDM systems. However, its performance appears to be dependent on the pilot arrangement with the OFDM block.

Figure 4-20 shows the PAPR reduction performances of the proposed algorithm for different pilot locations with the Power Spectral Density (PSD) mask constrained to the average power-level of the data tones. The performance of the algorithm is approximately similar to the DFT-spreading technique in all three cases. Among the three different pilot locations, the pilots located in the best locations (case 3) in the unconstrained scenario, is mostly affected by the incorporation of the PSD mask constrained. On the other hand, the pilot location case 2 is less affected. It can be commented that the more the pilots are scattered within the spectrum of the signal the more it is affected by the incorporation of the PSD spectral constraints.

[14] In all cases, 5% sub-carriers are uniformly allocated for creating the peak cancelling signal.

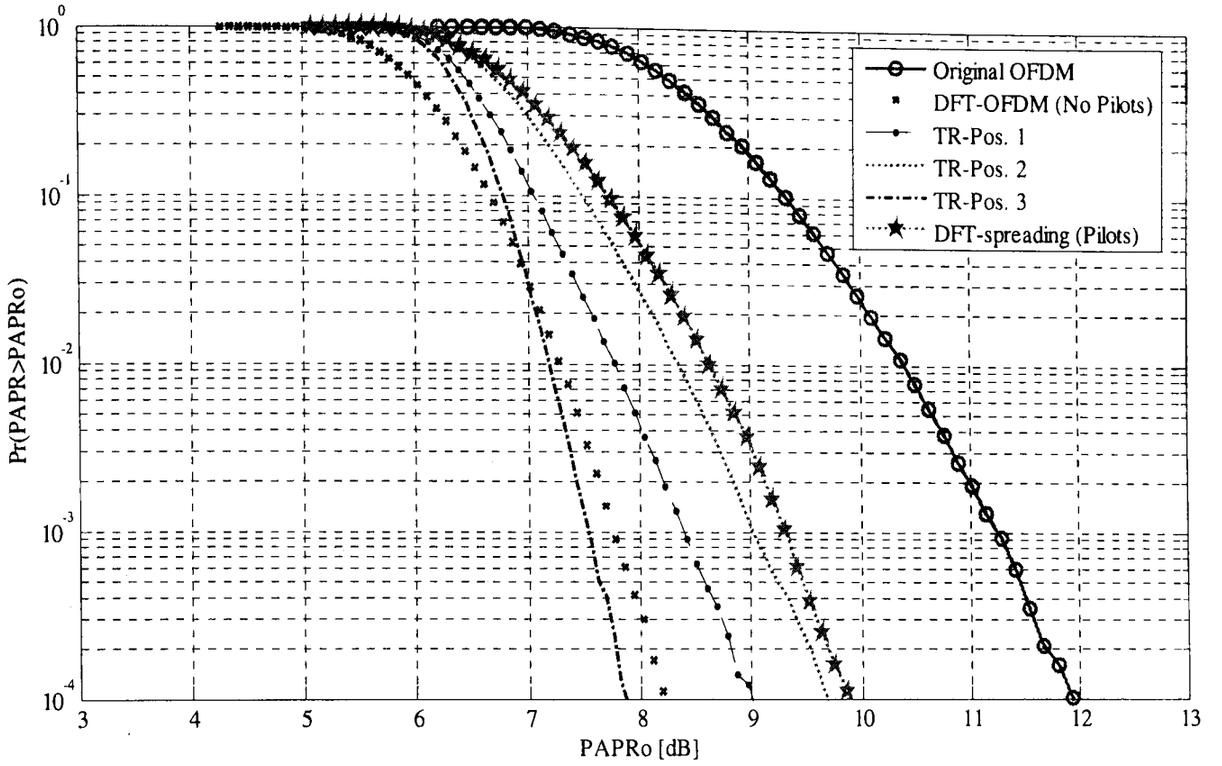

Figure 4-19: PAPR Reduction Performance of OFDM for different pilot locations- TR technique only.

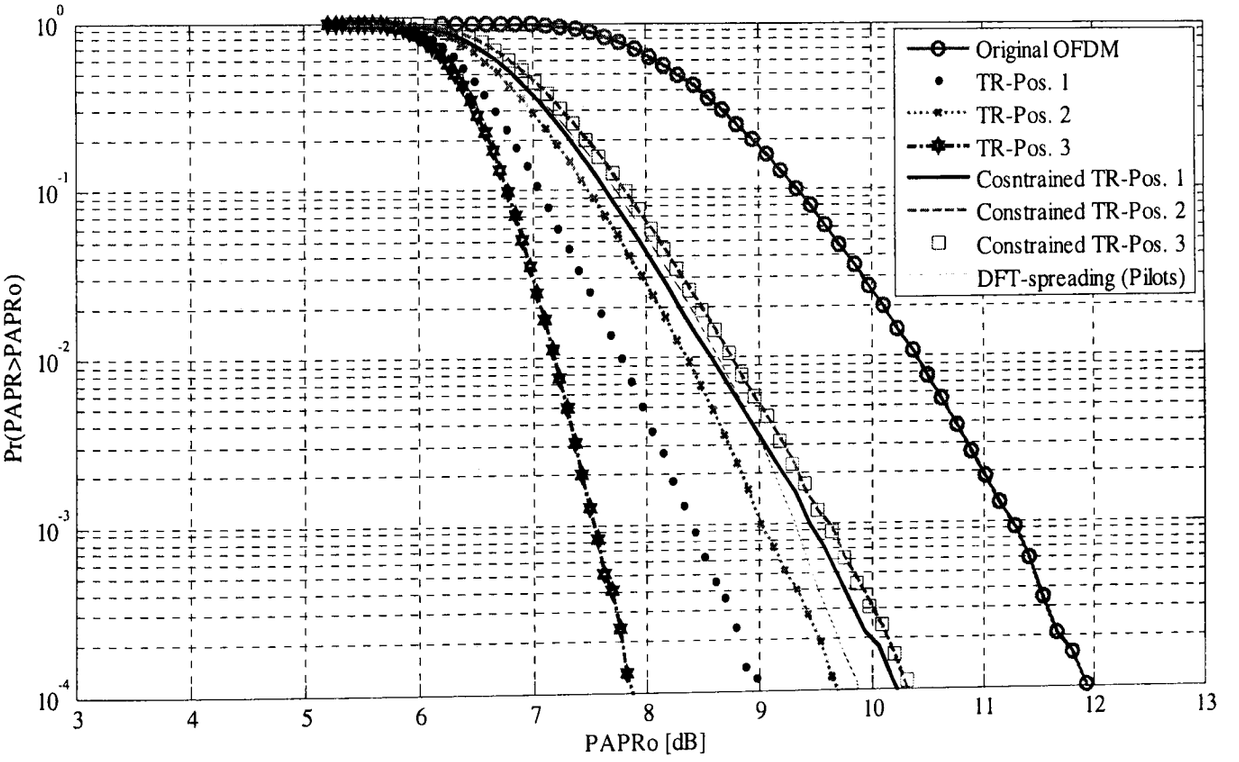

Figure 4-20: Flat PSD mask level over all sub-carriers is assumed

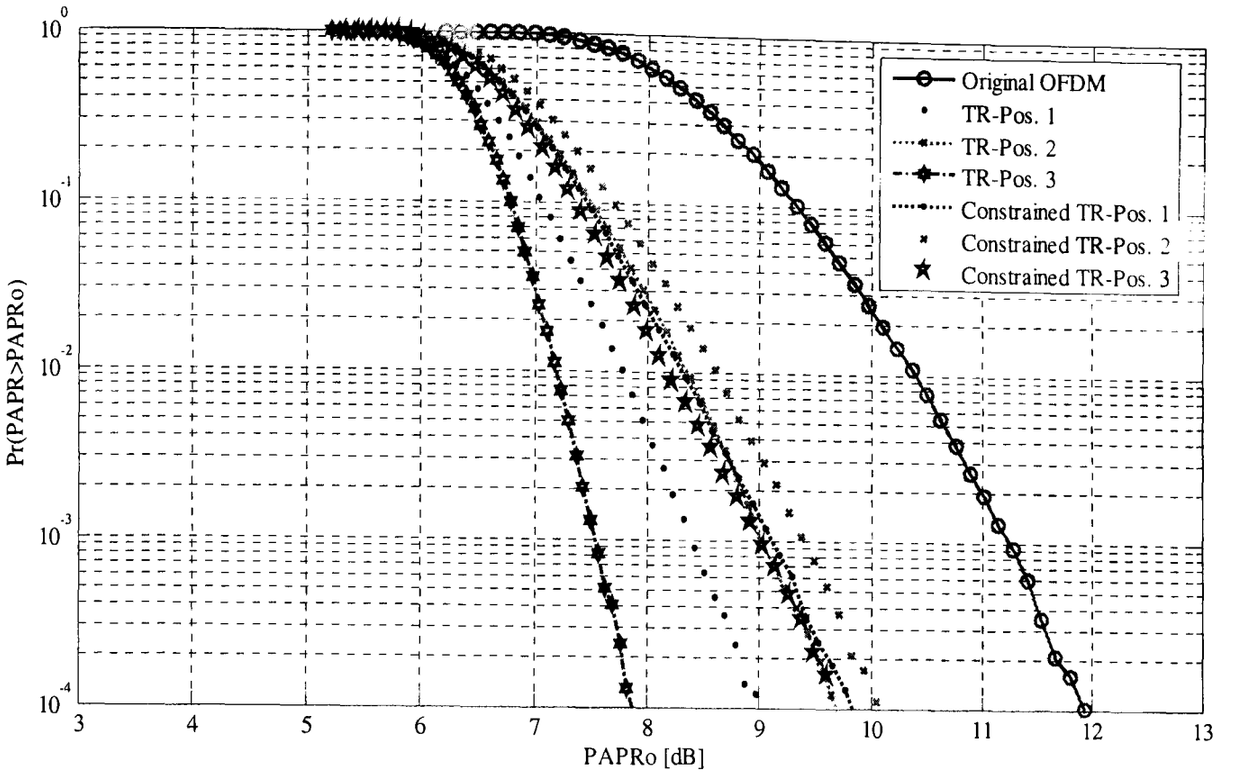

Figure 4-21: Loosely constrained TR only

In Figure 4-21, the PSD is increased by 50% in magnitude for each tone. Comparing this with Figure 4-20, we see that simulated PAPR reduction performance increases by about 0.6 dB, except suffixing the pilots at the end of the data block. The latter case provides only 0.2 dB improvement in the PAPR reduction performance.

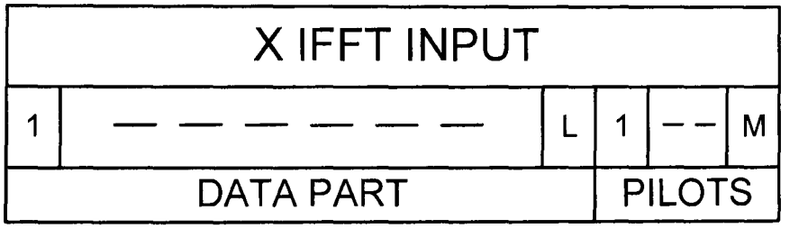

Figure 4-22: A typical example for Dummy Sequence Insertion (DSI) technique with *L*-data symbols and *M*-pilot symbols [HEUN04].

For systems, where bandwidth scarification cannot be afforded, the proposed technique can be introduced, without any further modifications, by simply incorporating the Dummy Sequence Insertion (DSI) approach proposed in [HEUN04]. In the DSI technique, all of the or fraction of the reserved subcarriers are chosen from the null sub-carriers in the OFDM systems and therefore, reduces the bandwidth inefficiencies. Figure 4-22 illustrates a typical example of the OFDM symbols and corresponding pilot arrangement used in such technique. Unlike the Partial Transmit Sequence (PTS) [MULL97] and Selected Mapping (SLM) [BAUM96] methods, in DSI the phases of the dummy sub-carriers are controlled to reduce the PAPR of the OFDM signal. Hence,

the transmitter does not need to communicate any side information to the receiver. Instead, it simply discards the reserved subcarriers in the frequency domain processing at the receiver.

In order to further reduce the PAPR of the OFDM signal, the proposed algorithm can simply be combined with other PAPR reduction techniques discussed in Chapter 3. Thus for instance the DFT pre-coding technique[15] proposed in [HEUN07] has been combined with the proposed algorithm, and Figure 4-23 illustrates the block diagram of the combined scheme. Moreover, 3GPP has recently launched a study item called 3GPP LTE (Long Term Evolution). In which, SC-FDMA is considered as the uplink candidate which uses DFT spreading technique to reduce the PAPR. Correspondingly, the combined scheme is also appropriate in such type of systems.

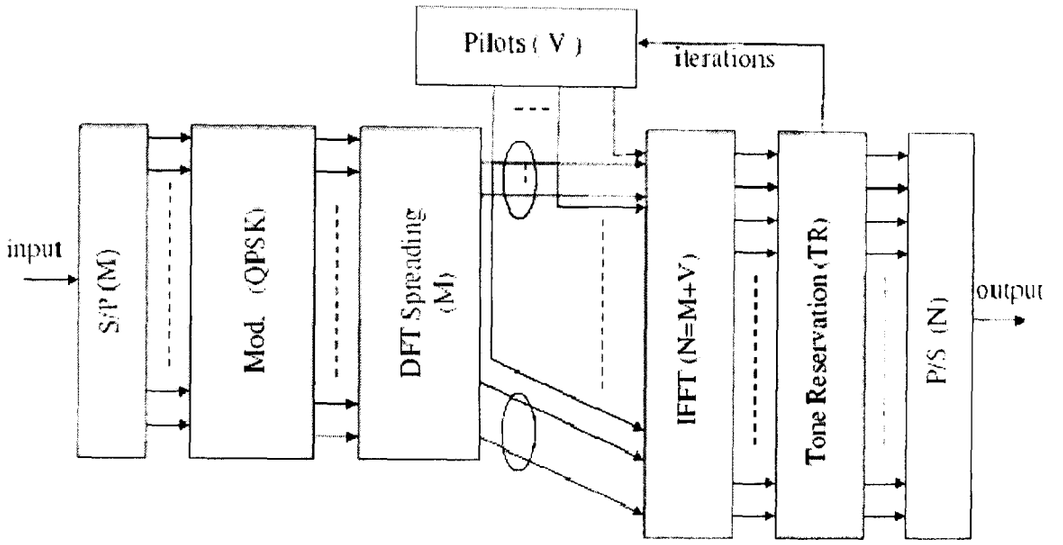

Figure 4-23: Block Diagram of a combined Scheme –TR and DFT spreading Technique [HEUN07].

Figure 4-24 shows the performance of the combined TR and DFT spreading schemes for different pilot locations. It is observed that the best performance is obtained for the case the pilots are suffixed with the data block (case 2).

Figure 4-25 shows similar simulations results as Figure 4-24, but using the restrictive spectral constraints, (equal to the average power-level of the data tones), and these constraints are incorporated in the frequency domain by using the projection rule in equation (4.44). It is observed that introducing spectral constraints into the combined schemes affects significantly the achievable PAPR reduction only for the case when the pilots located in the randomly selected best positions. In the other cases, the achievable PAPR reduction is only slightly affected by the incorporation of the spectral constraints.

[15] Three different type of pre-coding technique was investigated in [HEUN07]. However, we have considered only the first method.

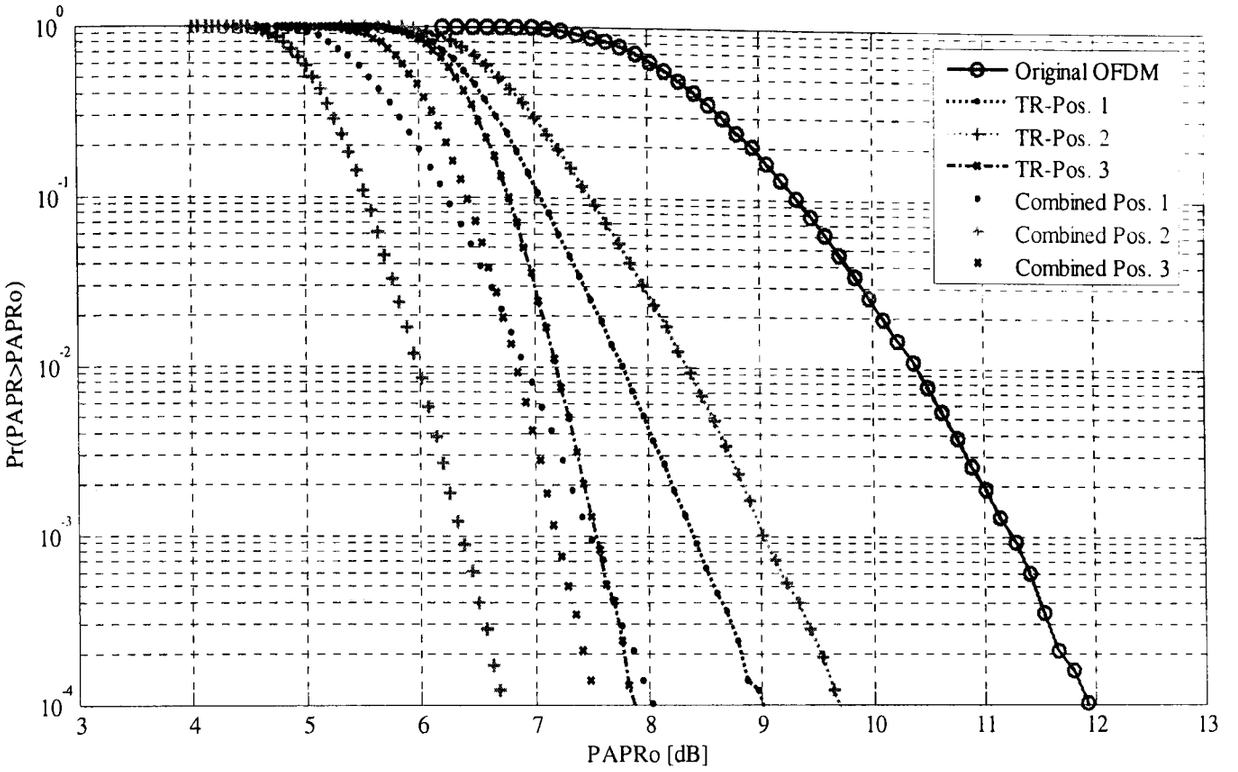

Figure 4-24: PAPR Reduction Performance of OFDM for different pilot locations - Combined technique.

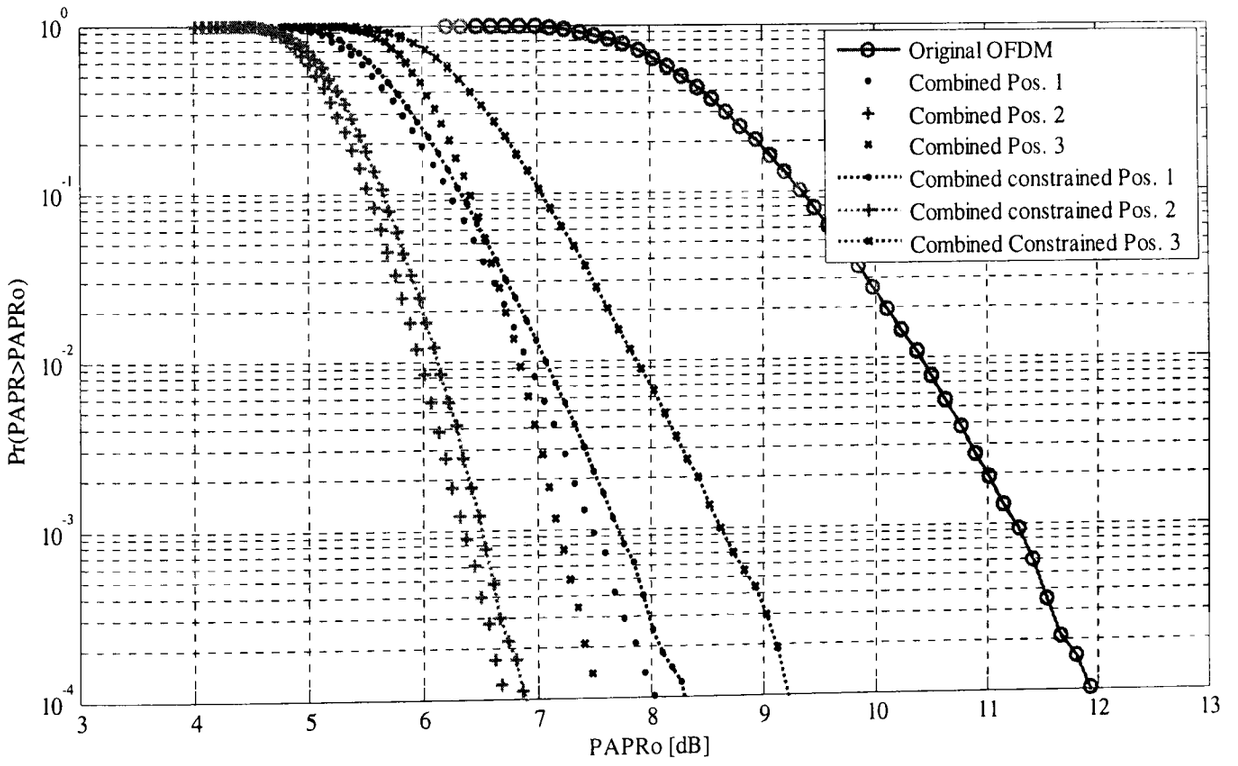

Figure 4-25: PAPR Reduction Performance of OFDM for different pilot locations- constraints applied.

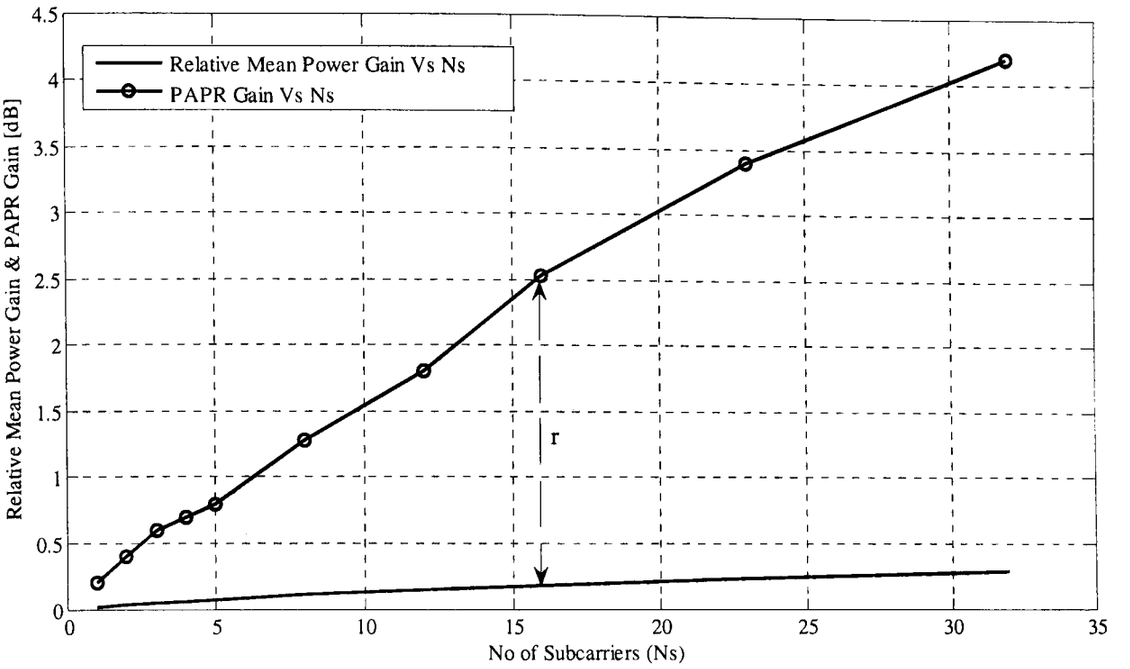

Figure 4-26: PAPR Reduction Gain ΔG and relative mean power increase ΔE for different number of pilots/subcarriers ($Ns = 1, 2, 3, 4, 5, 8, 12, 16, 23, 32$).

Since TR method is based on the addition of a peak-cancelling signal to reduce the PAPR of the OFDM signal, the transmitted power of the combined signal also increases. This obviously can damage the transmission quality (BER) if it is allowed to increase indefinitely; due to the upward movement of the operating point of the amplifier. The relative mean power increase, ΔE, due to PAPR reduction is defined as [TELL99].

$$\Delta E = 10 \log_{10} \frac{E(\|\boldsymbol{x} + \boldsymbol{c}\|^2)}{E(\|\boldsymbol{x}\|^2)} \tag{4.47}$$

This parameter must be as small as possible in order to be compatible with the existing power amplifier. Indeed, it is easy to understand that if the average power of the signal $\boldsymbol{x} + \boldsymbol{c}$ is indefinitely increased the resulting PAPR would reach $0dB$, but the signal cannot be transmitted.

On the other hand, the PAPR reduction gain[16], ΔG, must be kept as high as possible while keeping the ΔE small. Thus, it is necessary to have a balance between ΔG and ΔE.

Figure 4-26 shows the PAPR reduction gain ΔG obtained with various relative mean power increase ΔE for different number of pilot subcarriers, Ns. For example, when Ns is equal to 12 and 16, the power increase ΔE is equal to $0.15\ dB$ and $0.18\ dB$ respectively, while the difference r is equal to $1.65\ dB$ and $2.35\ dB$ respectively. Therefore, TR based PAPR reduction method based on the proposed algorithm offers an interesting trade-off between PAPR reduction gain and relative mean power increase, at the cost of slight spectral efficiency loss.

[16] PAPR reduction gain is measured at CCDF=10^{-3}.

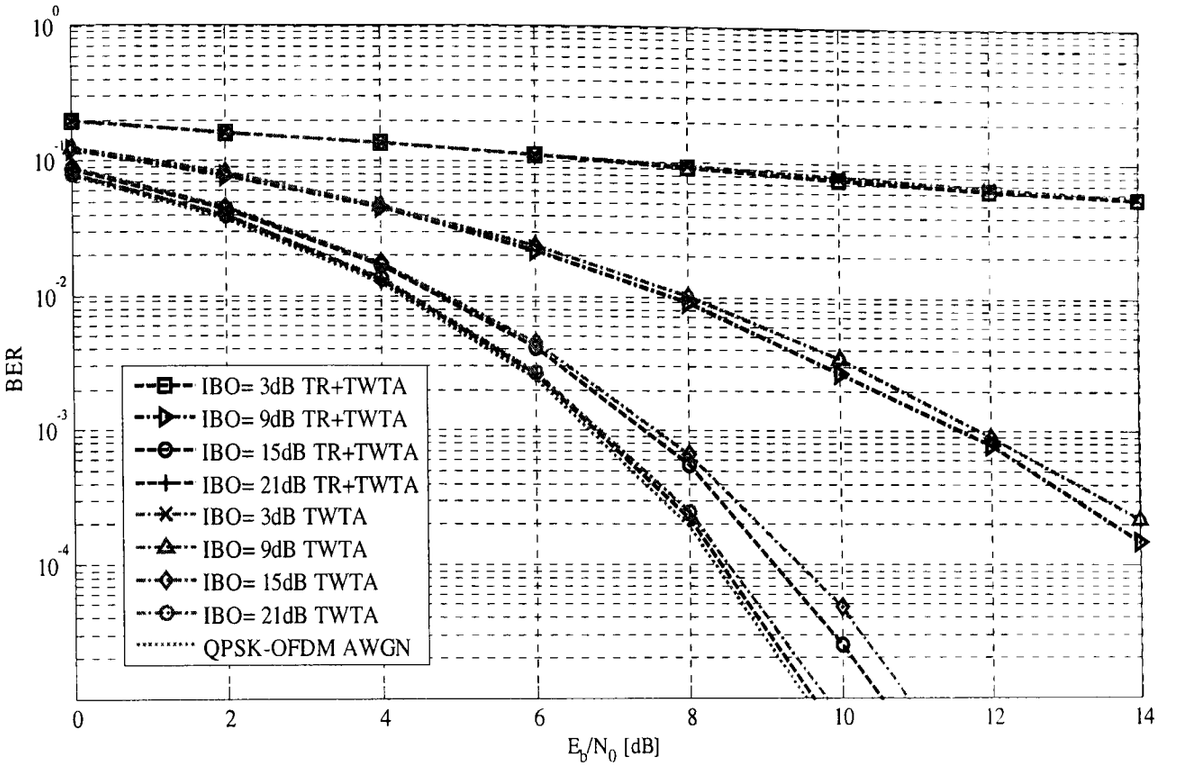

Figure 4-27: Uncoded BER Performance of PAPR Reduced OFDM Signal in the presence of TWTA non-linearity for different IBO

The performance of the proposed algorithm has so far evaluated in terms of the PAPR reduction capability. However, its performance must also be evaluated in terms of Bit Error Rate (BER) and spectral re-growth reduction in the presence of the TWTA model. Therefore, simulations were further extended to evaluate both uncoded BER performance and the spectral re-growth reduction for different IBOs in the presence of non-linear TWTA amplifier. These performances were first evaluated for the pilot position 3 and the results are shown in Figure 4-27 and 4-28. Figure 4-27 shows the BER performance of the PAPR reduced OFDM signal in the presence of non-linear TWTA, whereas Figure 4-28 shows the spectral re-growth at the output of the non-linear TWTA.

It is observed that there is slight improvement in the BER performance of the PAPR reduced (TR based) OFDM signal when the IBO is increased. However, the obtained BER performance advantage is not very significant. On the other hand, it is observed from Figure 4-28 that there is significant performance advantage in the reduction of spectral re-growth when the IBO is increased. Moreover, a further increment in IBO results a substantial spectral re-growth reduction. It can therefore be concluded that the TR based PAPR reduction technique becomes effective with larger IBO value. This fact provides the motivation to further extend the performance investigation of the proposed TR algorithm in the combined 'pre-distorter + TWTA' system. This will be considered in the next chapter.

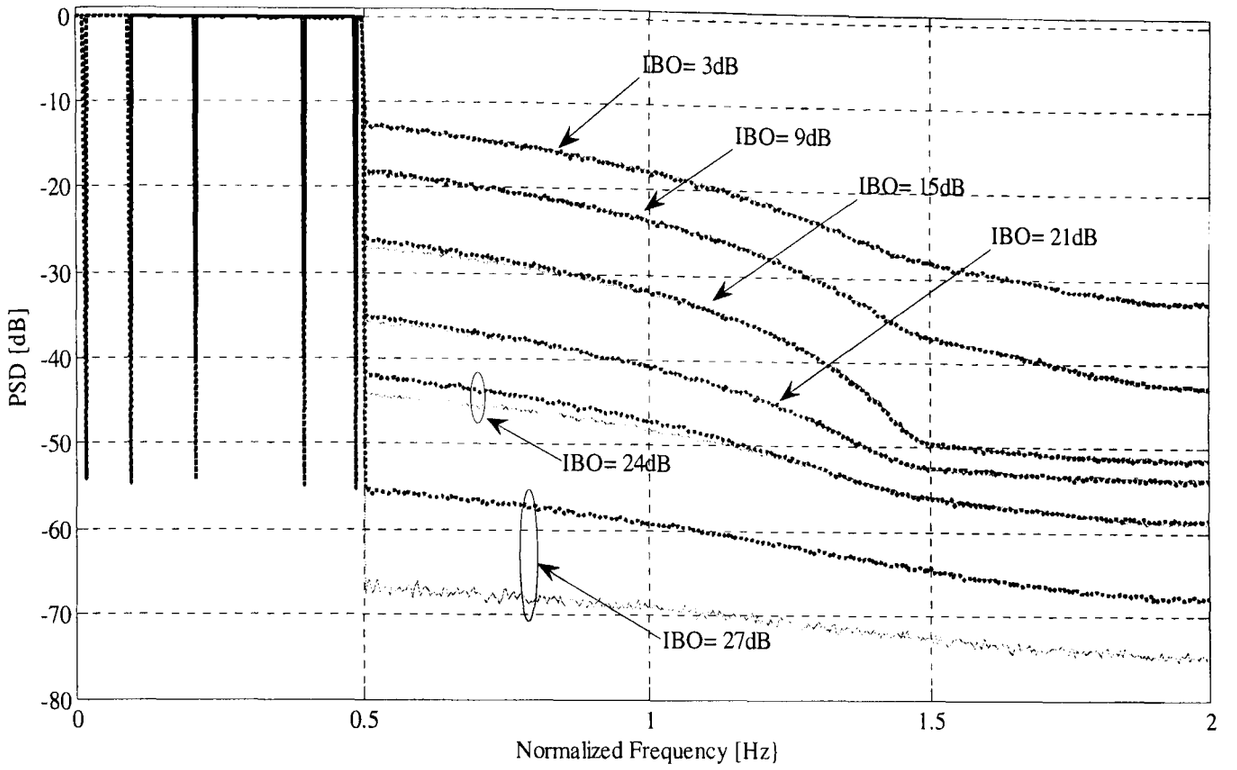

Figure 4-28: Output Power Spectra of the PAPR Reduced OFDM signal in the presence of TWTA non-linearity for different IBO

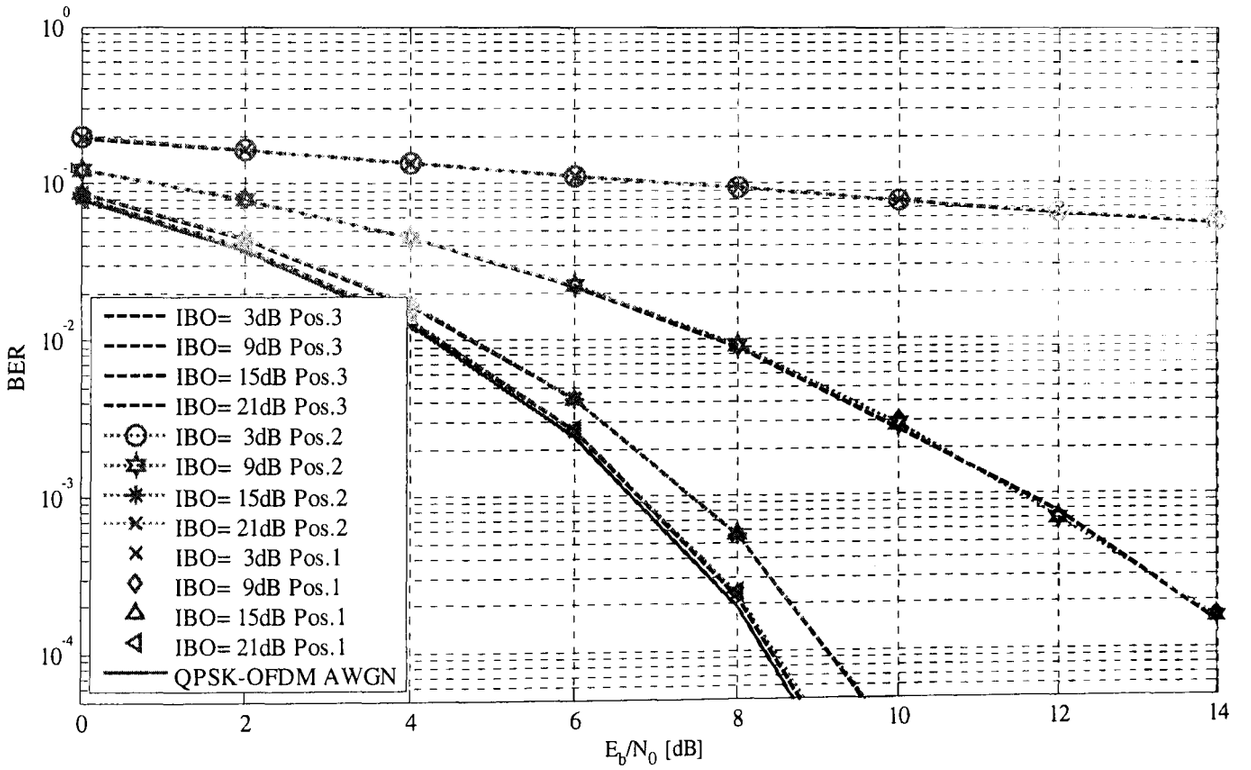

Figure 4-29: Comparison between BER Performances of PAPR Reduced OFDM Signal with three different pilot positions in the presence of TWTA non-linearity for different IBO

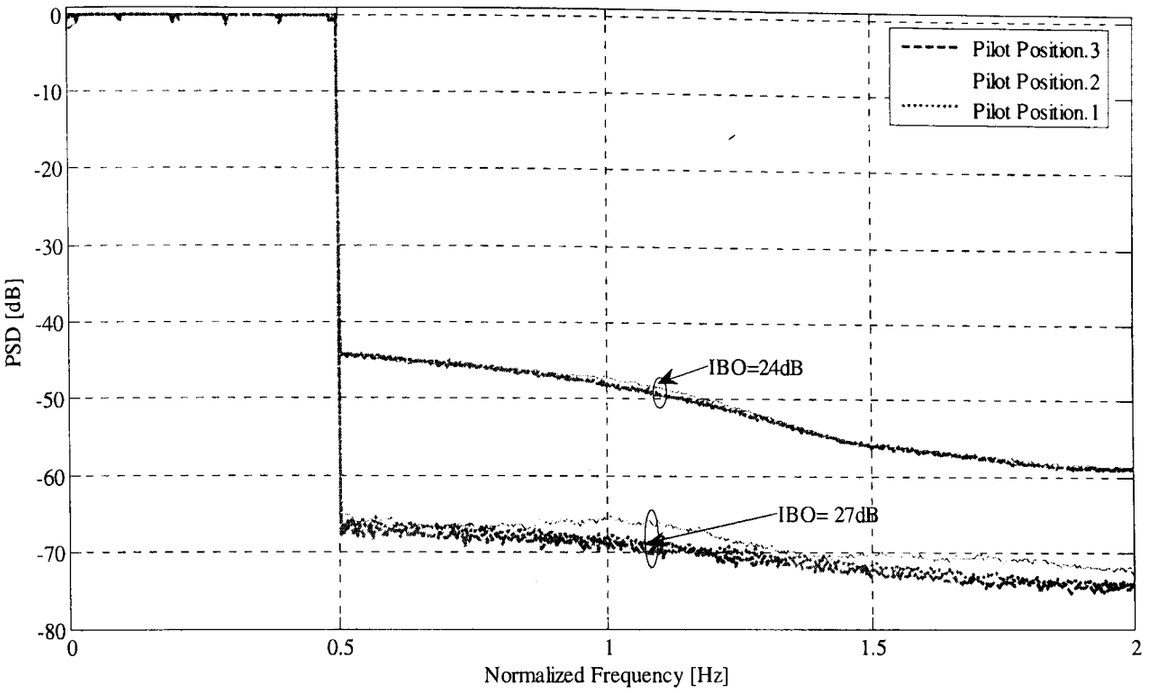

Figure 4-30: Comparison between Output Power Spectra of the PAPR Reduced OFDM signal with three different pilot positions in the presence of TWTA non-linearity for different IBO

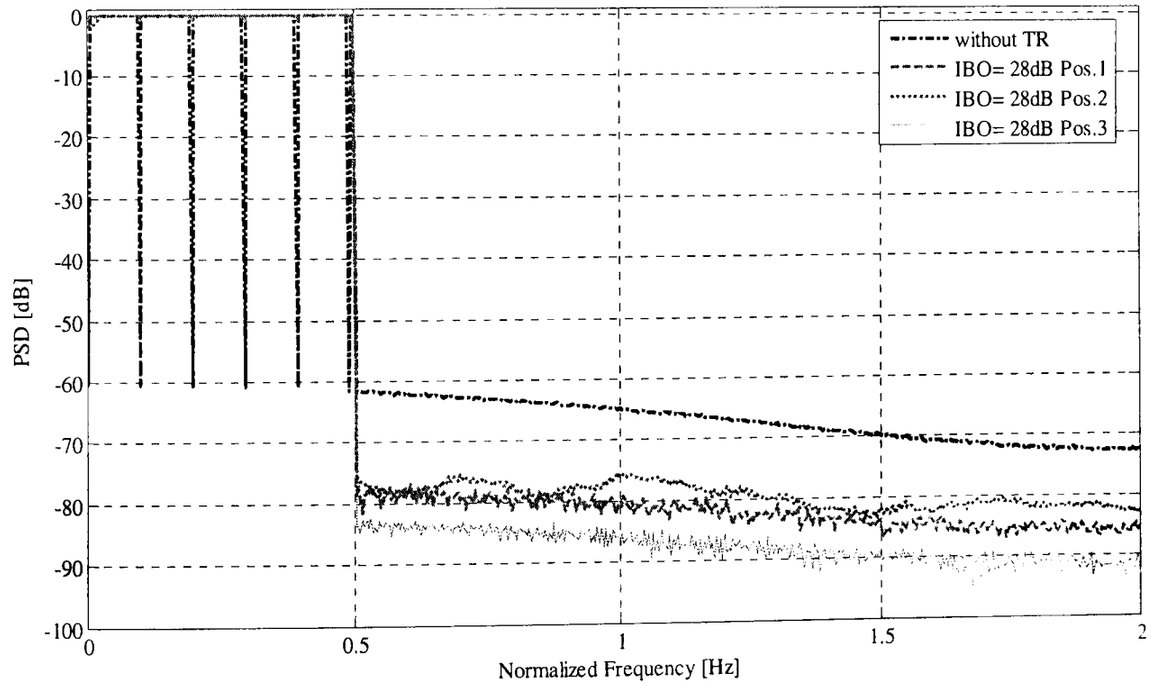

Figure 4-31: Comparison between Output Power Spectra of the PAPR Reduced OFDM signal with three different pilot positions in the presence of TWTA non-linearity when IBO= 28dB

Simulations were continued to provide the performance comparison between the different pilots positions used in the TR algorithm. Figure 4-29 shows the BER performance of the PAPR

reduced OFDM signal with three different pilot positions. It is observed that there is no significant difference in the BER performance.

Figure 4-30 and 4-31 show the reduction in spectral re-growth obtained at the output of the TWTA for different IBO values. It is observed that when the IBO is equal to 24 dB, there is no significant difference in the obtained spectral re-growth reduction in all three cases considered. However, when the IBO is increased to 27dB, the pilot position 3 provides significantly greater reduction in spectral re-growth than the other two cases. Among the rest, the pilot location 1 provides slightly larger reduction in the spectral re-growth when compared to the pilot location 2.

4.10 Summary and Conclusions

This chapter can be summarized as follows:

- As introductory topics, a detailed description of TR method together with the problem formulations and the related work were first provided.
- A low complexity gradient based algorithm was proposed for reducing the Peak-to-Average Power Ratio (PAPR) of OFDM signal using the Tone Reservation (TR) method, which outperforms the existing most efficient TR algorithm based on the active-set approach.
- The approach is very flexible in terms of the selection of search directions and can also be applicable for constructing efficient algorithm for problems involving similar non-smooth cost functions.
- The proposed technique performs better than the DFT spreading technique irrespective of the pilot locations. However, the performance significantly depends on the pilot locations.
- The more the pilots are scattered within the bandwidth, the more it is affected by the incorporation of spectral constraints. Moreover, the pilots can be loosely constrained to obtain a slightly improved PAPR reduction performance.
- The combined scheme (TR + DFT spreading) reduces further PAPR of OFDM signals and the best performance is observed when the pilots are suffixed to the data block at both ends.
- Introducing spectral constraints significantly affects the achievable PAPR reduction for the case when pilots are randomly located. While the performance in the other cases are slightly affected.
- It was also shown that the proposed algorithm offers an efficient trade-off between PAPR reduction gain and relative mean power increase, at the cost of slight spectral efficiency loss.
- TR based PAPR reduction technique becomes effective in the larger IBO level. Thus, it is essential to investigate the performance of the TR technique in the combined 'pre-distorter + TWTA' system.

- Pilot position 3 showed significant reduction in spectral re-growth over the other two pilot positions. However, the reduction is significant only in higher IBO level.

As already reviewed in the previous chapter, amplifier linearization is another approach for compensating the non-linear distortion introduced by the high power amplifiers and it will be investigated in the next chapter.

Chapter Five

5 Pre-distortion Techniques

5.1 Introduction

Following the literature survey on amplifier (memory-less) linearization techniques, provided in Chapter 3 (section 3.6), this chapter is concerned with evaluating the performances of pre-distortion techniques as a compensation approach for non-linear distortion introduced by the on-board satellite amplifier. Before embarking into the evaluation of the pre-distortion techniques, it is important to provide the mathematical modelling of the pre-distorter, along with that of the TWTA amplifier. Furthermore this chapter analyzes the performance of the TR technique[17] (also reviewed in section 4.2), within the combined 'Pre-distorter + TWTA' configuration.

The main objective of this study is to evaluate the pre-distorter's adaptation algorithm in the context of the remote adaptation scenario. Subsequently, the performance of two digital adaptive pre-distortion techniques, Lookup Table (LUT) based and Polynomial based pre-distorters, are evaluated and compared in terms of convergence speed and accuracy in the context of the remote adaptation scenario. More specifically, it is assumed that the observed training sequence at the output of the amplifier is contaminated by AWGN, and the effect of noisy training signals (on the adaptation and performance of the digital pre-distorters) is studied for different SNR levels via simulations. The comparisons were made using the conventional adaptation algorithms; Secant algorithm for the LUT pre-distorter and Minimum Mean Square Error (MMSE) parameter estimation for the polynomial pre-distorter. Due to the sensitivity of the Secant Algorithm towards the noisy feedback channel, a modified Secant based algorithm, based on the modified Newton-Raphson method in [HUAN04], was proposed for updating the LUT pre-distorter.

For the evaluation of the adaptation algorithms in the 'remote adaptation scenario', the following assumptions were considered throughout the study:

- A memory-less power amplifier model is assumed in all these investigations, which is a valid assumption for TWTA's in the considered bandwidth [MOHA04].

[17] The pilots were constrained to the average power level of the data tones.

- Ideal I-Q modulator and demodulator (i.e. no implementation-level inaccuracies have been modelled).
- Ideal delay matching circuits. So that, there is no implementation inaccuracies in calculating the error between the signal at the TWTA output and the corresponding input sample.
- Only the non-linear effects of the onboard TWTA are modelled and compensated. The gateway/handset amplifiers are assumed to be perfectly linear.
- Linearization techniques are assumed to be implemented at the gateway (i.e. no onboard processing functionalities are assumed).

In the remaining chapter, we first describe the mathematical modelling of the TWTA and Pre-distorter models used for investigation. Section 5.3 evaluates the performance, in terms of BER and spectral re-growth, of the proposed TR algorithm in the combined "pre-distorter + TWTA" system. Section 5.4 presents the performance comparison between the LUT based Polynomial based pre-distorters. The performance was evaluated in terms of the Relative Mean Square Error (RMSE)[18]. Moreover, comparison was also performed in terms of the computation complexity of the both algorithms in adaptation mode and in operation mode. In Section 5.5, a modified Secant algorithm is proposed for adapting the LUT pre-distorter, which showed performance improvement in the low SNR regions. Based on this, an adaptive strategy is proposed for updating the LUT pre-distorter in the remote adaptation scenario. Finally, the chapter is summarized with the important outcomes.

5.2 Mathematical Modelling of TWTA and Pre-distorter

In order to investigate the pre-distortion algorithms, it is essential to model the TWTA and Pre-distorter circuits. Thus, this section introduces the TWTA and Pre-distorter modelling incorporated in this thesis.

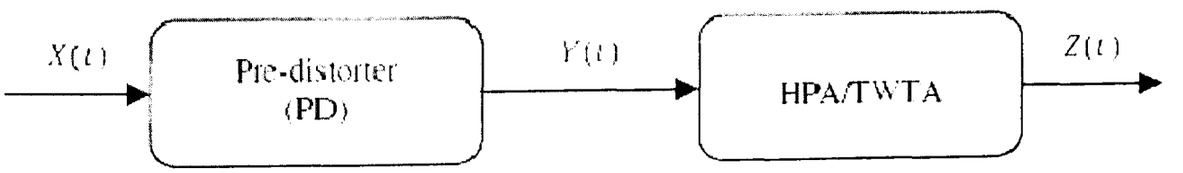

Figure 5-1: Simplified block diagram for the HPA with the Pre-distorter

Figure 5-1 shows a simplified block diagram for the HPA with the pre-distorter circuit typically used in communication systems. Let the input signal to the pre-distorter, output of the pre-

[18] Definition is given in section 5.4.

distorter or input to the HPA and output of the HPA be $X(t)$, $Y(t)$ and $Z(t)$, respectively. Their complex base-band representations are:

$$X(t) = \rho_{x(t)} e^{j\theta_{x(t)}} \tag{5.1}$$

$$Y(t) = \rho_{y(t)} e^{j\theta_{y(t)}} \tag{5.2}$$

$$Z(t) = \rho_{z(t)} e^{j\theta_{z(t)}} \tag{5.3}$$

Where $\rho_{x(t)}$, $\rho_{y(t)}$, $\rho_{z(t)}$ and $\theta_{z(t)}$, $\theta_{z(t)}$, $\theta_{z(t)}$ are the instantaneous amplitudes and phases of the complex signals $X(t)$, $Y(t)$, and Z(t), respectively.

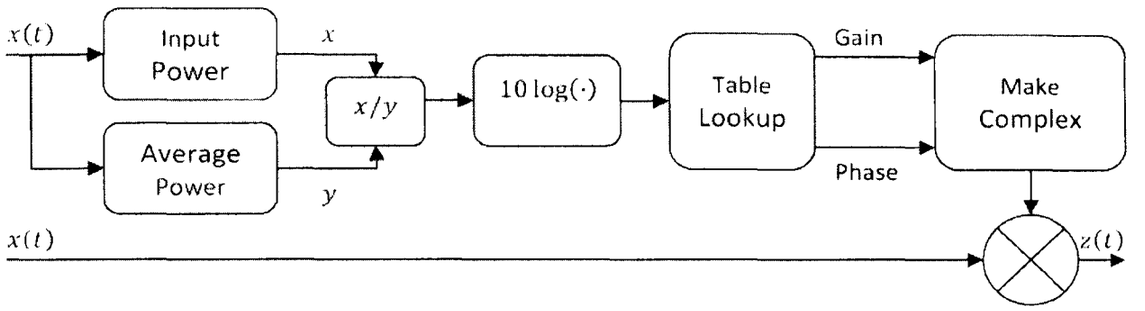

Figure 5-2: Simulation Model used for modelling the TWTA

The TWTA simulator block diagram is presented in Figure 5-2. In our simulations and analyses the LUT describing the TWTA's response is based on measurement data[19] provided in the EU-FP6 project MAESTRO [MAES06]. For simulation purposes the measurement data have been normalized with respect to the input and output saturation powers of the amplifier. The model illustrated in Figure 5-2 is based on [YUGA05], [NGUY03]. The instantaneous input power,$\rho^2_{x(t)}$, and the average power, $P_{x(t)}$ are input to the TWTA model as illustrated in Figure 5-2. The normalized input power will be:

$$P_{IN}(dB) = 10\log_{10}\left(\frac{\rho^2_{x(t)}}{P_{x(t)}}\right) \tag{5.4}$$

As illustrated in Figure 5-2, the Table Look up function will then output the Gain and the Phase for the corresponding input signal power defined in equation (5-4). The normalized complex gain, G, of the power amplifier is given by:

$$G = \sqrt{10^{\left(\frac{P_{HPA}-P_{IN}}{10}\right)}} e^{j\theta_{HPA}} \tag{5.5}$$

[19] Measurement data can be found in Appendix B.

where P_{HPA} and θ_{HPA} are the normalized output power in dB and the output phase in degrees is obtained from the HPA table lookup function. Considering the rest of the circuit in Figure 5-2, the output signal from the TWTA /HPA can be expressed as:

$$Z(t) = X(t)\sqrt{10^{\left(\frac{P_{HPA}-P_{IN}}{10}\right)}}e^{j\theta_{HPA}} \tag{5.6}$$

In order to model the combined effect of both the pre-distorter and the HPA, the block diagram in Figure 5-1 is further simplified as illustrated in Figure 5-3. Moreover, the direct line in Figure 5-2 which multiplies the complex gain of the amplifier will be replaced by the output signal from the pre-distorter. The pre-distorter model used for this purpose is described in the following.

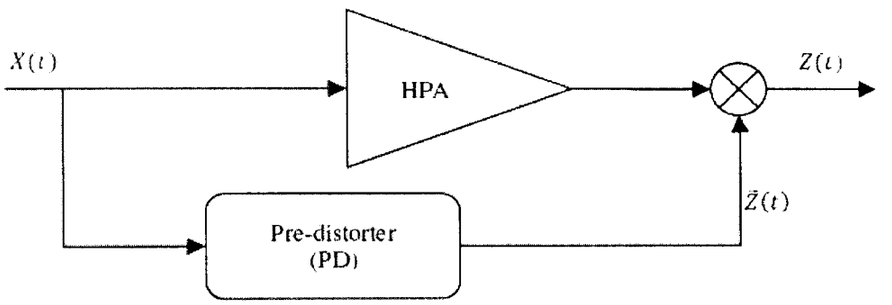

Figure 5-3: Simplified Block Diagram of Figure 5-1

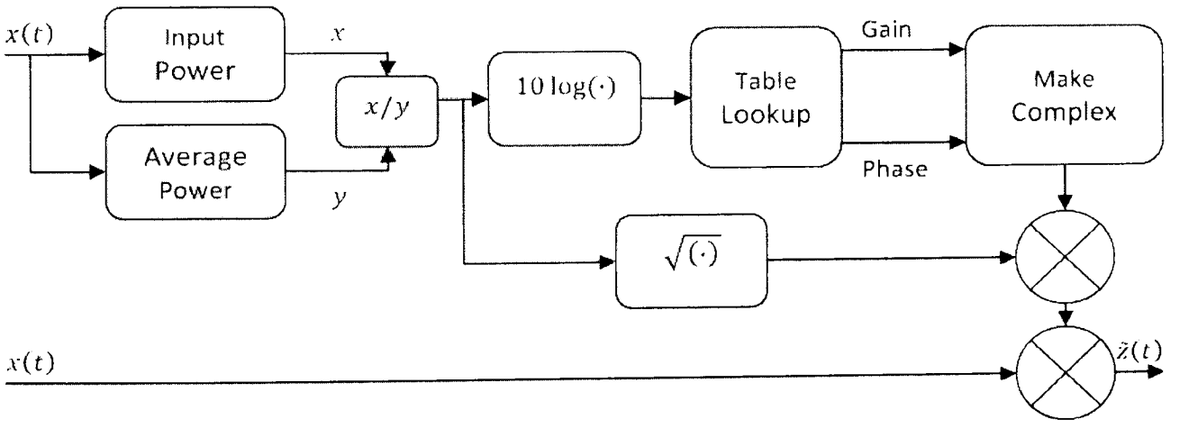

Figure 5-4: Simulation model used for modelling the Pre-distorter

Figure 5-4 illustrates a similar non-linear model to that illustrated in Figure 5-1, but this represents the pre-distorter modelling based on [NGUY03]. According to Figure 5-3, the pre-distorter is fed by the same signal as the input to the HPA block. The instantaneous input power and the average input power are represented by $\rho^2_{x(t)}$ and $P_{x(t)}$, respectively. Similar to equation (5-5), the complex gain, F, of the pre-distorter is given by:

$$F = \sqrt{10^{\left(\frac{P_{PD}-P_{IN}}{10}\right)}}e^{j\theta_{PD}} \tag{5.7}$$

where P_{PD} and θ_{PD} are the normalized output power in dB and output phase in degree obtained from the Pre-distorter's table lookup function. With reference to Figure 5-4, the output signal from the pre-distorter can be expressed as:

$$\tilde{Z}(t) = X(t)\sqrt{10^{\left(\frac{P_{IN}}{10}\right)}}\sqrt{10^{\left(\frac{P_{PD}-P_{IN}}{10}\right)}}e^{j\theta_{PD}} \tag{5.8}$$

The output signal of the combined system (Pre-distorter + HPA) can be determined by multiplying equations (5-8) and (5-5).

$$Z(t) = X(t)\sqrt{10^{\left(\frac{P_{IN}}{10}\right)}}\sqrt{10^{\left(\frac{P_{PD}-P_{IN}}{10}\right)}}e^{j\theta_{PD}}\sqrt{10^{\left(\frac{P_{HPA}-P_{IN}}{10}\right)}}e^{j\theta_{HPA}} \tag{5.9}$$

This can be further simplified into:

$$Z(t) = X(t)\sqrt{10^{\left(\frac{P_{PD}+P_{HPA}-P_{IN}}{10}\right)}}e^{j(\theta_{HPA}+\theta_{PD})} \tag{5.10}$$

Furthermore, according to equation (5-10), the amplifier will be perfectly linearized if the following conditions satisfied:

$$P_{PD}\,(dB) = \begin{cases} P_{IN}(dB) - P_{HPA}\,(dB), & P_{IN}\,(dB) \leq 0 \\ -P_{HPA}\,(dB), & P_{IN}\,(dB) > 0 \end{cases} \tag{5.11}$$

$$\theta_{PD}(degree) = -\theta_{HPA}\,(degree) \tag{5.12}$$

where equation (5-11) and (5-12) represent the AM-AM and AM-PM responses of the pre-distorter, respectively.

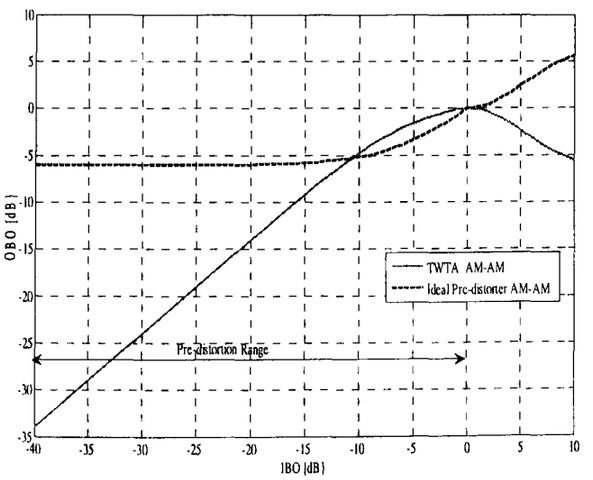

Figure 5-5: AM-AM Distortion of Ideal Pre-distorter

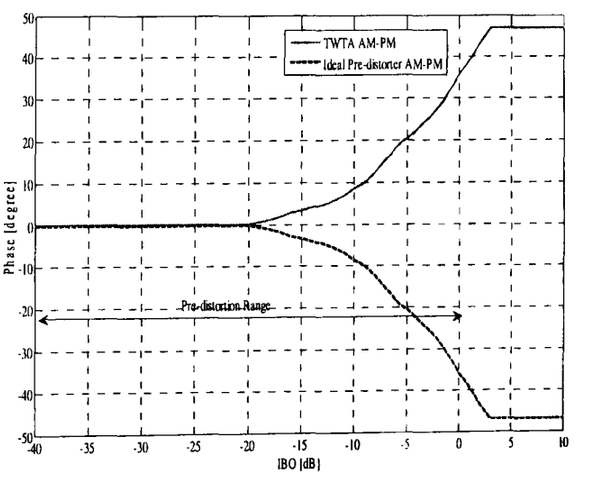

Figure 5-6: AM-PM Distortion of Ideal Pre-distorter

Figure 5-5 and 5-6 show the AM-AM and AM-PM characteristics of the ideal pre-distorters, respectively. It is observed that the pre-distorter's responses are inversion of the amplifier's responses and the resulting response will represent an ideal soft clipper. However, in practice, only a portion of the input signal range can be input to the pre-distorter and the input signal higher than the saturation power is clipped by the pre-distorter.

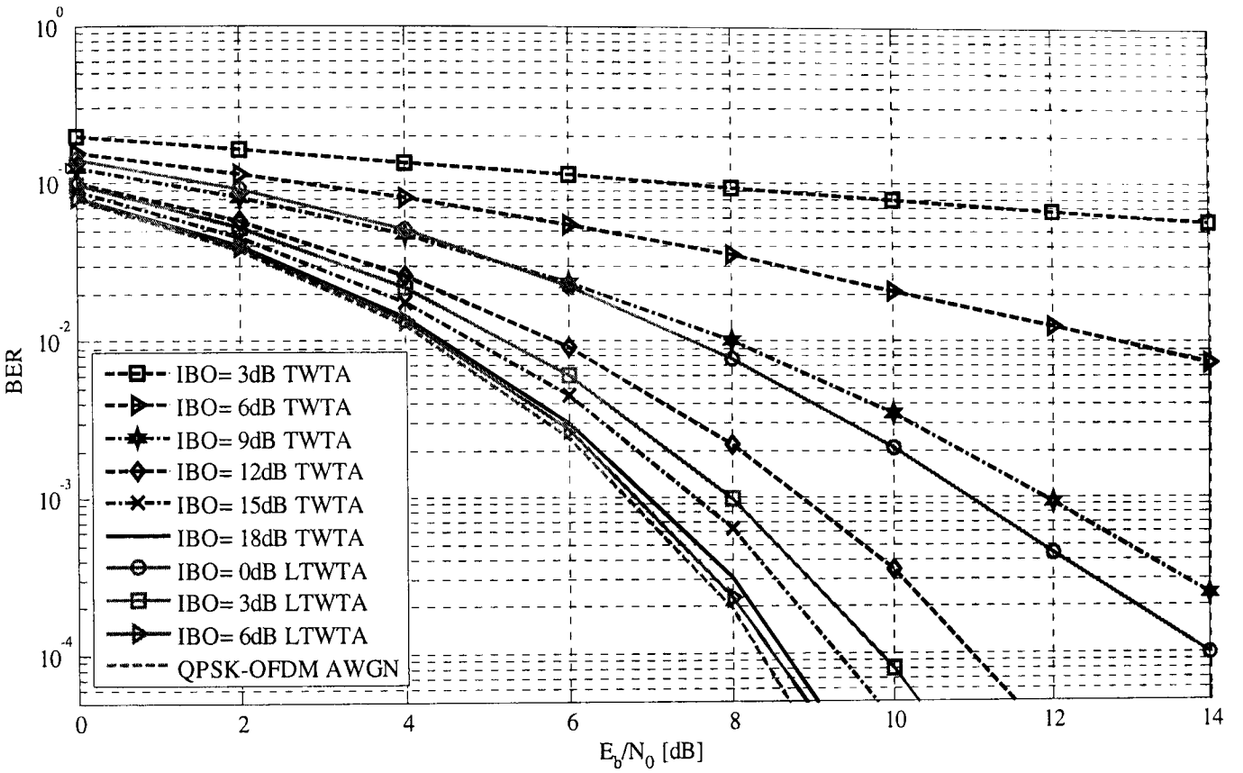

Figure 5-7: Uncoded BER Performance of OFDM signal in the combined 'ideal Pre-distorter + TWTA' for different IBO[20]

The performance of the ideal pre-distorter was investigated in terms of BER performances and the spectral re-growth at the output of the TWTA and the results are shown in Figure 5-7 and 5-8, respectively. The simulations are based on the simulation parameters listed in Table 4.3. It is observed from Figure 5-7 and 5-8 that the incorporation of the ideal pre-distorter significantly reduces the required IBO which is otherwise required to achieve the near theoretical ideal performance. Moreover, it can also be observed from Figure 5-7 that IBO level greater than 6dB is sufficient to compensate the in-band distortion introduced by the inherent non-linear TWTA. In addition, the spectral leakage performances obtained with the considered IBO level should also satisfy the spectral mask limitation introduced by the regulatory bodies.

[20] LTWTA means Linearized TWTA

The incorporation of the ideal pre-distorter reduces the required IBO level by around 12dB. Moreover, in the presence of the ideal pre-distorter, the performance advantage gained by a 3dB IBO increment is significantly greater than the performance advantage obtained when there is no pre-distorter.

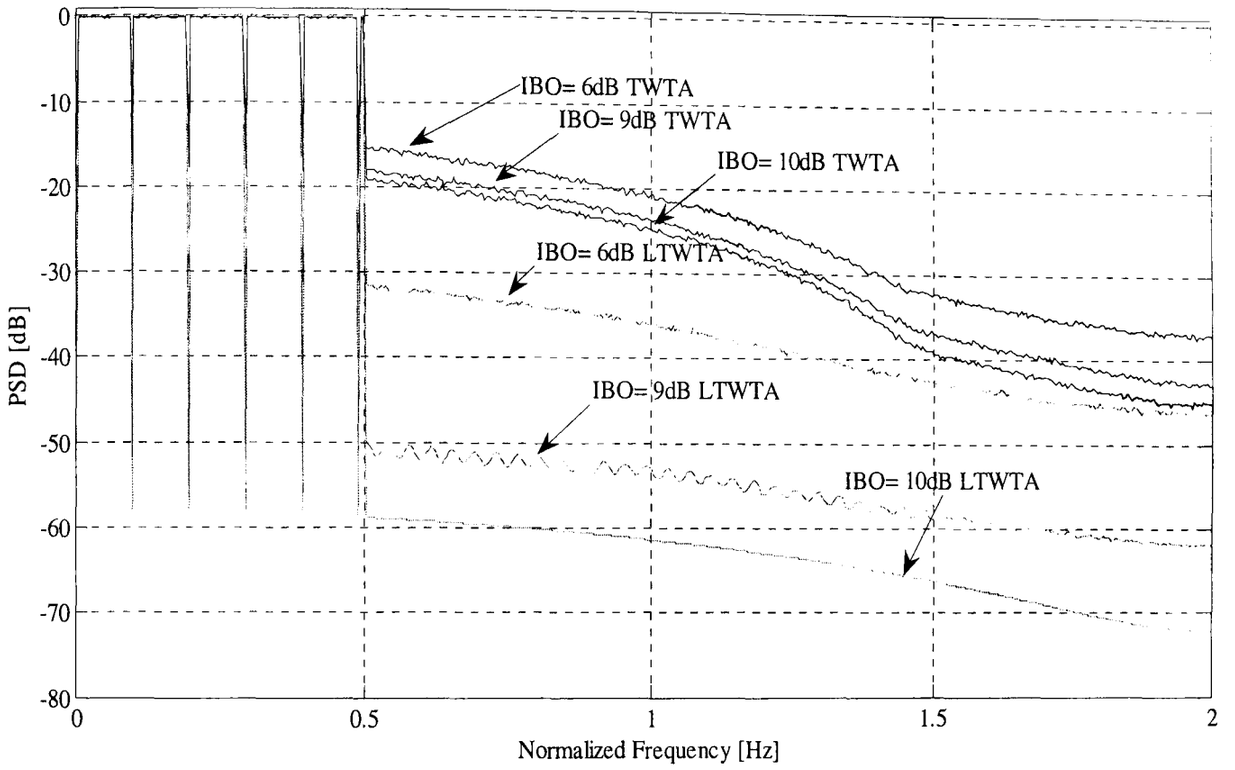

Figure 5-8: Power Spectra of the OFDM signal at the output of the combined 'Ideal Pre-distorter + TWTA' for different IBO

5.3 Performance Evaluation of PAPR Reduced OFDM signal in the combined 'ideal Pre-distorter + TWTA' Scenario

As concluded from chapter 4, the performance of the PAPR reduced OFDM signal is effective in the linear region of the TWTA. This was reflected in the fact that the obtained performance advantage was substantially increased with increasing IBO level. Due to this fact, it is essential to investigate the performance of the PAPR reduced OFDM signal for the case when the TWTA is preceded by the ideal pre-distorter.

In this section, we therefore evaluate the performance of the PAPR reduced OFDM signal, using TR method, in the combined 'ideal Pre-distorter + TWTA' scenario. The performances are evaluated in terms of BER performances and spectral re-growth at the output of the TWTA. The simulation results are based on the simulation parameters listed in Table 4.3 In addition, the

performances of the PAPR reduced OFDM signal was also compared for different pilot positions in the TR algorithm.

5.3.1 Performance Evaluation with Equally Spaced Pilots

In this section, we evaluate the performances of the PAPR reduced[21] OFDM signal in the combined 'ideal pre-distorter + TWTA' scenario with results reported in Figure 5-9 and 5-10. Figure 5-9 shows the BER performance for different IBO in the combined scenario, whereas Figure 5-10 shows the power spectra at the output of the TWTA for different IBO.

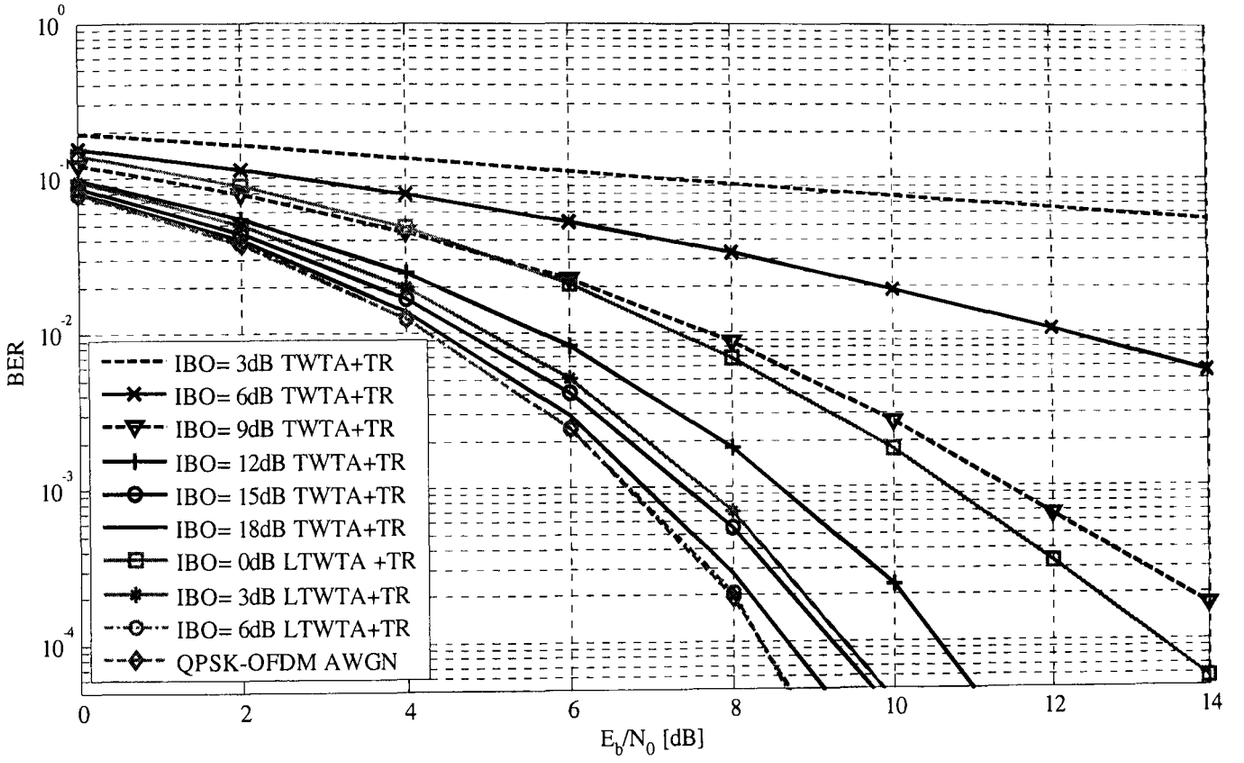

Figure 5-9: Uncoded BER Performance of PAPR Reduced OFDM signal in the combined 'ideal Pre-distorter + TWTA' for different IBOs

As shown in Figure 5-9, the performance obtained by the PAPR reduced OFDM signal in the linearized case is significantly greater than the case when there is no ideal pre-distorter present. Similarly, from Figure 5-10, a similar observation can be noticed in the output power spectrum at the output of TWTA. Moreover, in Figure 5-10, the performance is compared with that of the performance obtained without the PAPR reduction technique being applied. It is observed that there is a significant improvement in the performance advantage by the incorporation of PAPR reduction technique. It can therefore be concluded that the PAPR reduction technique and the Pre-distortion technique become very effective when they are combined.

[21] Pilot position 1 (Equally spaced locations) were used in reducing the PAPR of the OFDM signal.

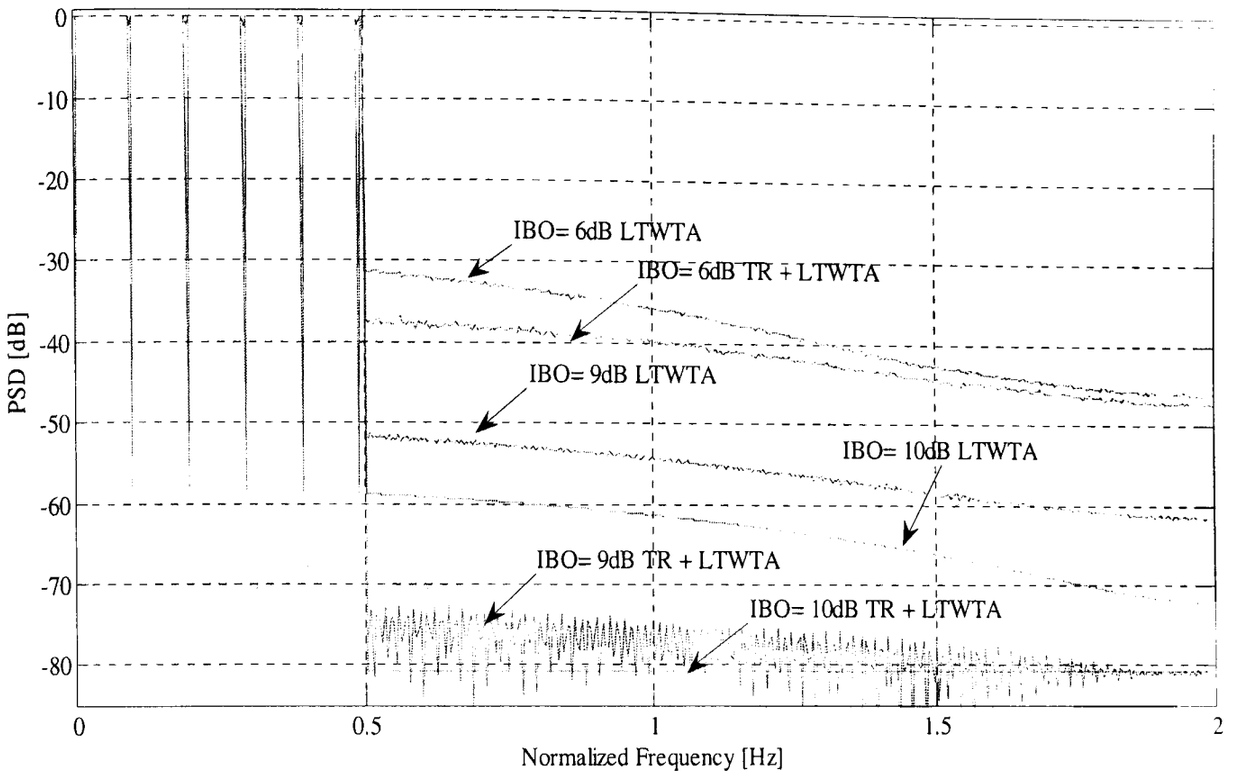

Figure 5-10: Power Spectra of the PAPR Reduced OFDM signal at the output of the combined 'Ideal Pre-distorter +TWTA' for different IBO

5.3.2 Performance Comparison with different pilot locations

In this section, we compare the performance of the PAPR reduction algorithm with different pilot locations, as already discussed in chapter 4. As in Section 5.3.1, the performance was compared in terms of the BER performance and the power spectra at the TWTA output. Figure 5-11 shows the BER performance of the PAPR reduced OFDM signal for different IBO, whereas Figure 5-12 shows the power spectra at the TWTA output for different IBO.

It is observed from Figure 5-11that there is no significant difference in the BER performance for the three different pilot locations investigated. On the other hand, as shown in Figure 5-12, there is a slight difference observed for the spectral re-growth. However, they are not significant due to the fact that the PAPR reduction obtained with the considered pilot locations was varied by about 0.2dB when the pilots are constrained. This variation in the PAPR reduction performance was shown in Figure 4-18.

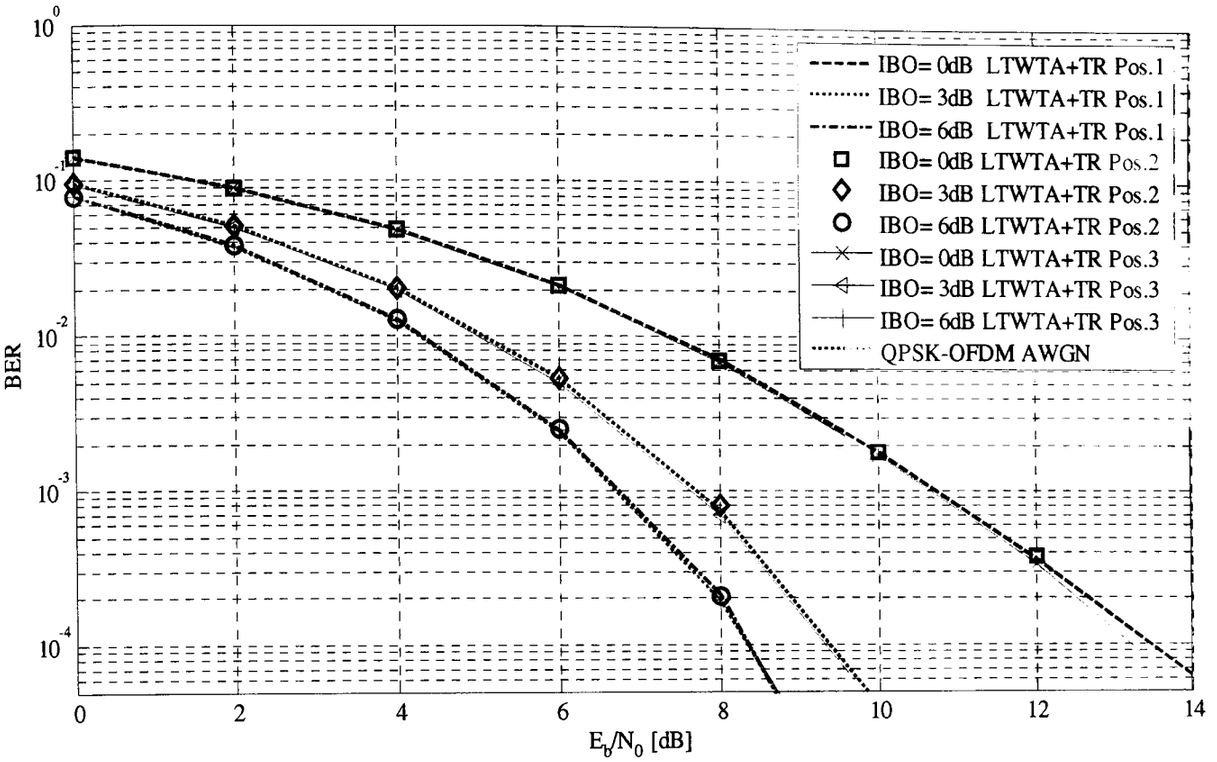

Figure 5-11: Uncoded BER Performance of PAPR reduced (with different pilot positions) OFDM signal in the combined 'ideal Pre-distorter + TWTA' for different IBOs

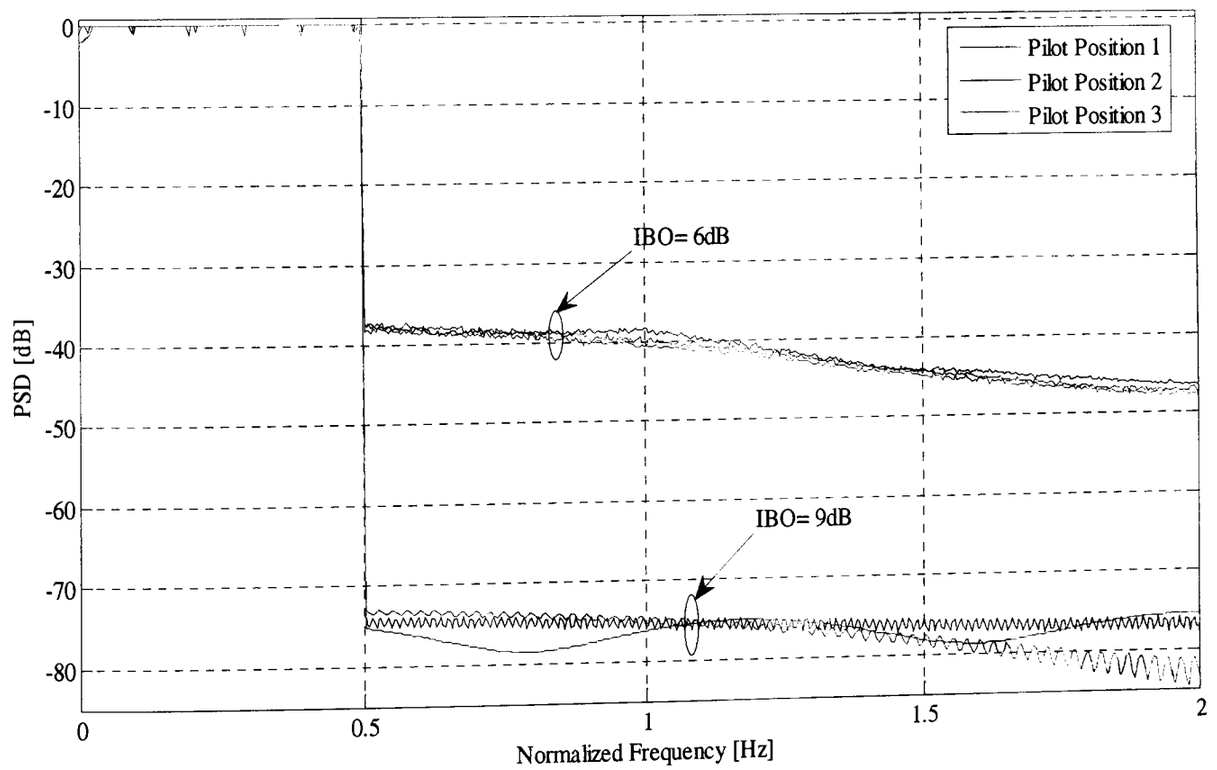

Figure 5-12: Power Spectra of the PAPR Reduced OFDM signal (with three different pilot positions) at the output of the combined 'ideal Pre-distorter + TWTA' for different IBO

5.3.3 Observations

The following main points can be observed from these simulation results:

- The TR technique becomes very effective when combined with a Pre-distortion technique[22]. The performance advantage is significantly greater than the performance advantage obtained with any single mitigation technique: TR technique or ideal Pre-distortion.
- The choice of pilot location did not significantly affect the performance in terms of both the BER performance and the spectral re-growth. This is because the PAPR reduction obtained with the considered pilot locations were only varied by about 0.2dB when the pilots are constrained.

5.4 Pre-distortion Technique: Comparison between Polynomial and LUT Pre-distorters in noisy feedback channel

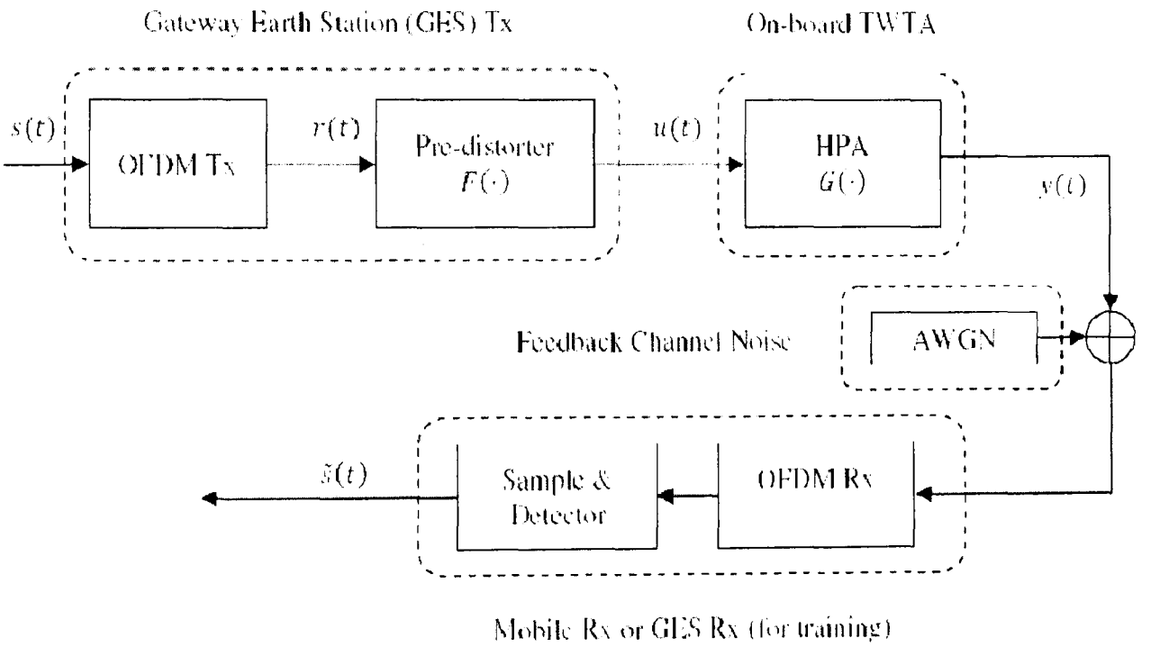

Figure 5-13: Typical OFDM communication system with Pre-distorter and HPA

In this section, we evaluate and compare the performance of LUT pre-distortion and Polynomial pre-distortion techniques in the context of a remote adaptation scenario, assuming that the observed training sequence at the output of the amplifier is contaminated with AWGN. This reflects the fact that the pre-distorter is assumed to be located in the modulator at the gateway

[22] An ideal pre-distortion model is used in this case.

earth station in the satellite system, illustrated in Figure 5-13[23]. The performance of the pre-distortion techniques is compared in terms of adaptation speed and accuracy of the adaptation algorithms employed. In the case of the LUT Pre-distorter, the performances were further evaluated for different LUT sizes, whereas, in case of polynomial pre-distorter, the performance was evaluated for both 3rd and 5th order polynomials. The performance was evaluated based on the Relative Mean Square Error (RMSE) [HUAN06] between the input and output of the concatenated pre-distorter and TWTA model, which can be expressed as:

$$RMSE = \boldsymbol{E}\{|r(t) - G(|F(|r(t)|)|)|^2\} \tag{5.13}$$

Where $\boldsymbol{E}\{\cdot\}$ denotes the expectation operator.

Following the training phase, the pre-distorter distorts the transmitting signal such that the combined system (Pre-distorter + TWTA) follows a linear overall response. The investigation was further extended to evaluate the computational complexity associated with the pre-distorters, both in the adaptation mode and in the operation mode. The complexity of the algorithms was evaluated based on the number of real multiplications and real additions per a single iteration of the algorithm. Here, we count the complex multiplication as four real multiplications and two real additions [SAYE03].

5.4.1 Performance Evaluation of the Secant-based LUT Pre-distorter

As reviewed in chapter 3 (section 3.6.5.1), there are various adaptation algorithms used for updating the LUT entries according to the PA variation. Among these, the pre-distortion adaptation algorithm based on the Secant method, proposed by J.K. Cavers in [CAVE90], is the most efficient in terms of computational complexity. Thus, we consider only the Secant method as a comparator.

The performance of the LUT based pre-distorters was evaluated for various Signal-to-Noise Ratio (SNR) values in the noisy feedback channel: 0 dB, 10 dB, 30 dB, inf dB.

5.4.1.1 Adaptation of the LUT pre-distorter based on Secant's Method

The assumed LUT-based pre-distorter model is shown in Figure 5-14. The linearization system initially incorporates a training phase in order to optimize the LUT entries. The pre-distortion process is accomplished by simply multiplying the transmitted signal samples with the complex LUT parameter. This complex parameter is derived from the LUT based on the addressing scheme used. In general, the LUT is addressed by the quantized power level of the transmit sample, using a linear scale; effectively taking advantage of the dependence of the amplitude and

[23] OFDM Tx & Rx blocks are not used for training purposes.

the phase distortion only on the amplitude of the transmit signal [CAVE90]. The impact of different LUT indexing techniques have been investigated in depth in [BOUM04], [CAVE99]. Thus, the thesis does not investigate this aspect.

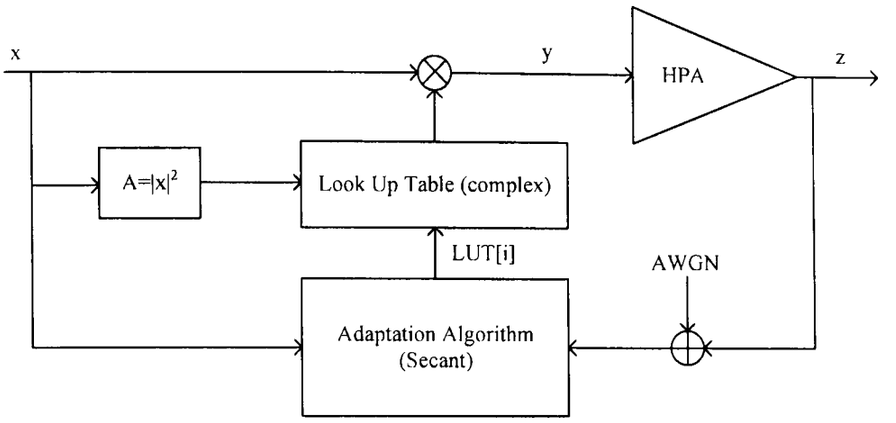

Figure 5-14: Generic Structure of the Gain based Pre-distorter with a noisy feedback channel

In more detail, assuming a training sequence $\boldsymbol{X}$ of N complex samples, is used for training the LUT pre-distorter of size L, and referring to Figure 5-14, the instantaneous squared amplitude A_i^2 $(0 \leq i \leq N)$ of the signal is extracted and quantized to the nearest of the L power levels (producing $(A^2)^{i,k}$), which correspond to the k^{th} table entry. Consequently the LUT outputs the complex pre-distortion parameter $F^{i,k}$, which multiplies the input sample x^i. The predistorted signal $y^{i,k} = F^{i,k}x^i$ is then input to the HPA, which outputs the distorted signal $z^{i,k}$. In the ideal case the pre-distorter perfectly compensates the amplifier's non-linearity so that $z^{i,k} = x^i$. In practice, however, there will be an error between the transmit signal and the output of the HPA, which is associated with the k^{th} LUT entry:

$$e^{i,k}(F^{i,k}) = z^{i,k}(F^{i,k}) - x^i \tag{5.14}$$

In [CAVE90] a numerical root finding technique (Secant's method) is used in order to iteratively determine the optimal value of F^k, which sets the error to zero. Thus during the training procedure the kth entry of the table is updated towards the optimal entry $(F^k)^*$. The Secant's method is a variation of the Newton-Raphson method, which iteratively evaluates a root of a continuously differentiable function by making use of the gradient of the function at each step [BURD89]. In particular:

$$F^{i+1,k} = F^{i,k} - \frac{e^{i,k}}{(e^{i,k})'} \tag{5.15}$$

Where $(e^{i,k})'$ is the first derivative of $e^{i,k}$ with respect to $F^{i,k}$. In the LUT training sequence, an analytic expression of $e^{i,k}$ is not available and therefore, only an approximation of the function's gradient can be evaluated based on instantaneous observations (finite difference approach):

$$\left(e^{i,k}\right)' \approx \frac{e^{i,k} - e^{i-1,k}}{F^{i,k} - F^{i-1,k}} \tag{5.16}$$

This approximation to the derivative constitutes the difference between the Newton-Raphson and Secant methods. Therefore, the update for the k[th] LUT entry is given by:

$$F^{i+1,k} = F^{i,k} - e^{i,k}\frac{F^{i,k} - F^{i-1,k}}{e^{i,k} - e^{i-1,k}} = \frac{e^{i,k}F^{i-1,k} - F^{i,k}e^{i-1,k}}{e^{i,k} - e^{i-1,k}} \tag{5.17}$$

5.4.1.2 Evaluation of convergence speed and accuracy

The convergence speed and accuracy of the LUT based pre-distorters were evaluated via simulations, by applying a training sequence, of N samples, in the concatenated models of the LUT based pre-distorter and the S-band TWTA[24]. The LUT entries were uniformly 'distributed' between the minimum and maximum[25] input signal power level: [0, 1] (in linear scale). Moreover the training sequence was chosen to ramp-up linearly in power: from 0 to 1 in steps of $1/L$ (linear scale). During the training phase of the LUT based pre-distorter, the output of the TWTA (which is fed-back for training the LUT) is contaminated by AWGN, in order to model the "remote training" of the pre-distorter (since it is assumed to be located at the gateway).

Following the training phase of the LUT, a long sequence[26] of random data signals was applied to the concatenated LUT and TWTA models, and the Relative Mean Square Error (RMSE) between the 'input' and (the noiseless in this case) 'output' signals was estimated according to (5-13). The results are tabulated in Table 5-1 to 5-4 for four LUT sizes: 32, 64, 128 and 1024.

Table 5-1: RMSE between input-output signals with a 32-element LUT pre-distorter, for different training sequence lengths and SNR levels in the feedback channel

	$L = 100$	$L = 500$	$L = 1000$	$L = 10000$
$SNR = inf.$	$2.44 \cdot 10^{-4}$	$2 \cdot 10^{-5}$	$2.4 \cdot 10^{-5}$	$2.4 \cdot 10^{-5}$
$SNR = 30dB$	0.0016	$6.16 \cdot 10^{-4}$	$2.5 \cdot 10^{-4}$	$2 \cdot 10^{-4}$
$SNR = 10dB$	0.211	0.02	0.0377	0.0277
$SNR = 0dB$	0.28	0.13	0.11	0.12

[24] The AM/AM and AM/PM characteristics of the simulated TWTA can be found in Appendix B

[25] Corresponding to the saturation point of the TWTA

[26] 1 millions samples long

Table 5-2: RMSE between input-output signals with a 64-element LUT pre-distorter, for different training sequence lengths and SNR levels in the feedback channel

	$L = 100$	$L = 500$	$L = 1000$	$L = 10000$	$L = 20000$
$SNR = inf.$	0.0936	$2.88 \cdot 10^{-5}$	$1.45 \cdot 10^{-5}$	$6.4 \cdot 10^{-6}$	$6.34 \cdot 10^{-6}$
$SNR = 30dB$	0.0918	0.0022	$3.88 \cdot 10^{-4}$	$2 \cdot 10^{-4}$	$1.86 \cdot 10^{-4}$
$SNR = 10dB$	0.2	0.0545	0.0528	0.0245	0.0265
$SNR = 0dB$	0.23	0.2	0.1476	0.145	0.143

Table 5-3: RMSE between input-output signals with a 128-element LUT pre-distorter, for different training sequence lengths and SNR levels in the feedback channel

	$L = 100$	$L = 500$	$L = 1000$	$L = 10000$	$L = 20000$
$SNR = inf.$	0.1812	$3.6 \cdot 10^{-5}$	$1.3 \cdot 10^{-5}$	$1.6 \cdot 10^{-6}$	$1.5 \cdot 10^{-6}$
$SNR = 30dB$	0.1813	0.002	0.0014	$2.19 \cdot 10^{-4}$	$2.13 \cdot 10^{-4}$
$SNR = 10dB$	0.22	0.11	0.0619	0.0247	0.0228
$SNR = 0dB$	0.22	0.23	0.22	0.15	0.16

Table 5-4: RMSE between input-output signals with a 1024-element LUT pre-distorter, for different training sequence lengths and SNR levels in the feedback channel

	$L = 1000$	$L = 10000$	$L = 20000$	$L = 40000$	$L = 60000$
$SNR = inf.$	0.2125	$6.4 \cdot 10^{-7}$	$2 \cdot 10^{-7}$	$2.28 \cdot 10^{-8}$	$2.52 \cdot 10^{-8}$
$SNR = 30dB$	0.214	$9.54 \cdot 10^{-4}$	$5 \cdot 10^{-4}$	$4.37 \cdot 10^{-4}$	$5 \cdot 10^{-4}$
$SNR = 10dB$	0.2524	0.0591	0.0451	0.0391	0.033
$SNR = 0dB$	0.22	0.20	0.17	0.14	0.14

Before commenting on these results, we will examine the complexity of the pre-distorter.

5.4.1.3 Complexity of LUT-based Pre-distorter

Adaptation Mode:

As described in Section 5.4.1.1, the adaptation process is based on the error between the two signals; the perfectly down-converted output signal and the corresponding delay matched signal at the input of the Pre-distorter. In addition, the algorithm needs to identify the LUT location to be

updated. Then, the Secant method will be applied to the identified LUT entry which requires two complex multiplications, two complex additions and a complex division.

However, the complexity associated with this is not considered in the adaptation mode. Instead, it will be considered in the operational mode. Moreover, the Secant method requires the knowledge of the LUT entries and of the errors at the preceding step. Thus, three times the LUT sized memory needs to be allocated.

Operational Mode:

The complexity in the operational mode can be divided into two consecutive phases: finding the right LUT entry (LUT address) and then multiplying the sample by the corresponding LUT entry. Finding the LUT address can be performed by using a square operation (real and imaginary part of the signal), as shown in Figure 5-14 and followed by a rounding operation:

$$address = round[(real^2 + imag^2)(LUT_{SIZE} - 1)] + 1 \qquad (5.18)$$

The above operation requires approximately three real multiplication and three real additions.

The obtained LUT entry will then be multiplied with the input signal sample to produce the pre-distorted signal output and therefore, resulting in a complex multiplication. The size of the LUT is directly proportional to the cost of the memory. However, it does not introduce any additional complexity.

The overall complexity of the LUT pre-distorter is presented in Table 5-5.

Table 5-5: Complexity Analysis per sample for LUT pre-distortion schemes (Secant)

Method	Mode	Real ×	Real +	Complex ÷
LUT Pre-distorter (Secant)	Adaptation	8	8	1
	Operation	4	2	0

5.4.1.4 Observations: LUT Pre-distorter using Secant Method

The following main points can be observed from the simulation results:

- Assuming a noiseless feedback channel (SNR= inf dB) in the adaptation phase, the accuracy improves with increasing LUT sizes. Moreover, the accuracy provided by the LUT pre-distorter improves by increasing the length of the training sequence: up to some point which depends on the size of the LUT.
- When AWGN (noisy channels) is applied to the feedback channel the accuracy provided by the pre-distorter becomes practically independent of the LUT size (within the range of the examined cases).

- The accuracy provided by the LUT pre-distorter deteriorates consistently and significantly with decreasing SNR.

5.4.2 Performance Evaluation of the Polynomial Pre-distorter

Similar to LUT based pre-distorters; polynomial based pre-distorters also utilize various adaptation algorithms for adapting the polynomial coefficients according to PA variations [BESB01]. However, we consider an adaptation algorithm in which the coefficients are derived based on Minimum Mean Square Error (MMSE) criterion. In this Section, we evaluate the performance of the polynomial pre-distorter, in which the coefficients are derived based on the MMSE criterion [LEEK01], [LAIH99]. The performance is mainly evaluated in terms of the convergence speed, accuracy and computational complexity.

The performance of the pre-distorter was evaluated for various Signal-to-Noise Ratio (SNR) values in the feedback noisy channel: 0 dB, 10 dB, inf dB . Moreover, both 3rd and 5th order polynomials are investigated.

5.4.2.1.1 Adaptation of the Polynomial Pre-distorter based on MMSE Estimation

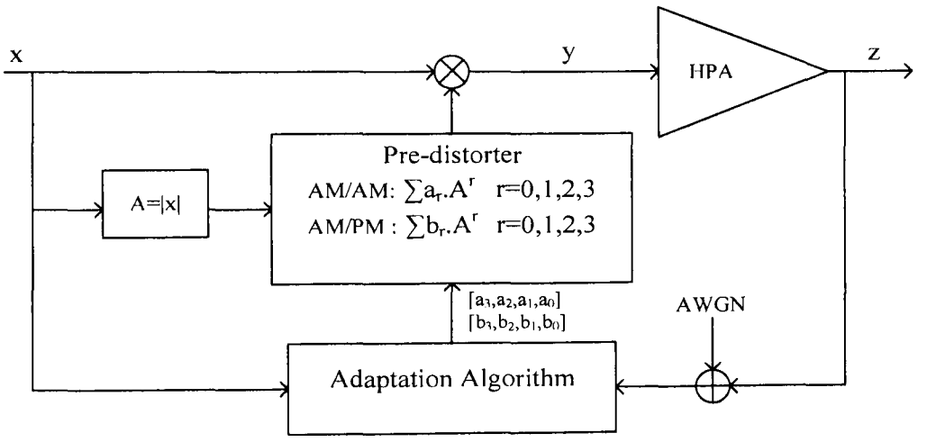

Figure 5-15: Generic Structure of the Polynomial Pre-distorter

The assumed polynomial pre-distorter model is shown in Figure 5-15. The linearization system initially goes through a training phase in order to optimize polynomial coefficients. The pre-distortion process is accomplished by simply multiplying the transmitted signal samples with the complex pre-distorter's output parameter. This complex parameter is derived from the polynomial evaluated by substituting the magnitude of the input sample. The polynomial model of the pre-distorter includes even-order terms in order to increase the modelling accuracy and therefore, lower order polynomials can be used [LEID04].

Assuming a training sequence $\boldsymbol{X}$ of N complex samples, is used for training the polynomial of order R, the amplitude and phase pre-distortions are represented by two real polynomials instead

of representing them as a complex polynomial. Referring to Figure 5-15, the instantaneous magnitude $A_{x,i}$ $(0 \leq i \leq N)$, of the signal is extracted and used to find the pre-distortion parameters $A_{q,i}$ and $\theta_{q,i}$. Subsequently, this is multiplied by the input signal sample x^i. The pre-distorted signal $y^{i,k} = A_{q,i}e^{j\theta_{q,i}}x^i$ is then input to the HPA, which outputs the distorted signal $z^{i,k}$. In the ideal case the pre-distorter perfectly compensates the amplifier's non-linearity so that $z^{i,k} = x^i$. In practice, however, there will be an error between the transmit signal and the output of the HPA, which is associated to the polynomial coefficients.

Two real polynomial functions of the instantaneous input magnitude are used in order to produce the amplitude and phase pre-distortion parameters. They can be represented:

$$A_{q,i} = \sum_{r=0}^{R} \alpha_r (A_{x,i})^r \tag{5.19}$$

$$\theta_{q,i} = \sum_{r=0}^{R} \beta_r (A_{x,i})^r \tag{5.20}$$

where R is the polynomial order, which in practice is usually chosen to be 3 or 5, and $\boldsymbol{\alpha} = [\alpha_0, \alpha_1, \ldots\ldots, \alpha_R]$, $\boldsymbol{\beta} = [\beta_0, \beta_1, \ldots\ldots, \beta_R]$ the polynomial coefficients [DING04]. In MMSE estimation, the objective is to determine the polynomial coefficients, which minimize the MSE:

$$\boldsymbol{\alpha}^* = arg \min_{\alpha} E[|e_A|^2] \tag{5.21}$$

$$\boldsymbol{\beta}^* = arg \min_{\beta} E[|e_\theta|^2] \tag{5.22}$$

The MSE can be estimated as:

$$E[|e_A|^2] = \frac{1}{N}\sum_{i=1}^{N}\left[\sum_{r=0}^{R} \alpha_r \{A_{x,i}\}^r - \frac{A_{y,i}}{A_{z,i}}\right]^2 \tag{5.23}$$

$$E[|e_\theta|^2] = \frac{1}{N}\sum_{i=1}^{N}\left[\sum_{r=0}^{R} \beta_r \{A_{x,i}\}^r - \frac{\theta_{y,i}}{\theta_{z,i}}\right]^2 \tag{5.24}$$

The optimal parameters can be determined by setting $\frac{\partial E[|e_A|^2]}{\partial \alpha_r} = 0$ and $\frac{\partial E[|e_\theta|^2]}{\partial \beta_r} = 0$ for all r. For $R = 2$ the minimization procedure leads to the following linear systems of equations:

$$\begin{bmatrix} E[(A_x)^4] & E[(A_x)^3] & E[(A_x)^2] \\ E[(A_x)^3] & E[(A_x)^2] & E[(A_x)] \\ E[(A_x)^2] & E[(A_x)] & 1 \end{bmatrix} \begin{bmatrix} \alpha_2 \\ \alpha_1 \\ \alpha_0 \end{bmatrix} = \begin{bmatrix} E[(A_x)^2 Y] \\ E[(A_x)Y] \\ Y \end{bmatrix} \tag{5.25}$$

$$\begin{bmatrix} E[(A_x)^4] & E[(A_x)^3] & E[(A_x)^2] \\ E[(A_x)^3] & E[(A_x)^2] & E[(A_x)] \\ E[(A_x)^2] & E[(A_x)] & 1 \end{bmatrix} \begin{bmatrix} \beta_2 \\ \beta_1 \\ \beta_0 \end{bmatrix} = \begin{bmatrix} E[(A_x)^2 H] \\ E[(A_x)H] \\ H \end{bmatrix} \tag{5.26}$$

Where $E[\cdot]$ represents expectations that are estimated by averaging over the N training sequence samples.

5.4.2.2 Evaluation of convergence speed and accuracy

With similar assumptions stated in Section 5.4.1.2, Table 5-6 and 5-7 provide corresponding results (to those in section 5.4.1.2) for the 3rd and 5th order polynomial pre-distorters, respectively. Before commenting on the tabulated results, it is noted that the simulations showed that the polynomial pre-distorters provide better accuracy when a pseudo-random training sequence is used, rather than a sequence with 'ramp-up' characteristics (as the one used for training the LUT pre-distorters).

Table 5-6: RMSE between input-output signals with a 3rd order polynomial pre-distorter, for different training sequence lengths and SNR levels in the feedback channel

	$L = 25$	$L = 50$	$L = 100$	$L = 500$	$L = 1000$
$SNR = inf.$	0.0016	$6.2 \cdot 10^{-4}$	$2.71 \cdot 10^{-4}$	$7.59 \cdot 10^{-5}$	$6.62 \cdot 10^{-5}$
$SNR = 10dB$	0.0014	$8.26 \cdot 10^{-4}$	$5.49 \cdot 10^{-4}$	$5.62 \cdot 10^{-4}$	$5.49 \cdot 10^{-4}$
$SNR = 0dB$	0.0048	0.0036	0.0034	0.0067	0.0050

Table 5-7: RMSE between input-output signals with a 5th order polynomial pre-distorter, for different training sequence lengths and SNR levels in the feedback channel

	$L = 25$	$L = 50$	$L = 100$	$L = 500$	$L = 1000$
$SNR = inf.$	0.0015	$7.0 \cdot 10^{-4}$	$1.73 \cdot 10^{-4}$	$7.35 \cdot 10^{-5}$	$3.84 \cdot 10^{-5}$
$SNR = 10dB$	0.0017	$7.6 \cdot 10^{-4}$	$4.67 \cdot 10^{-4}$	$3.65 \cdot 10^{-4}$	$3.3 \cdot 10^{-4}$
$SNR = 0dB$	0.0063	0.0072	0.0066	0.0083	0.0078

Table 5-6 and 5-7 show the RMSE performance of the 3rd and 5th order polynomials, respectively. It is observed that the performance of the 5th order polynomial is slightly better than the 3rd order polynomial pre-distorter. Moreover, Table 5-8 shows similar results obtained to those in Table 5-7, but by neglecting the even-order terms in the polynomial. It is observed that including even-order terms in the polynomial has significant effect on the accuracy of the polynomial based pre-distorters.

Table 5-8: RMSE between input-output signals with a 5th order polynomial pre-distorter (only odd terms), for different training sequence lengths and SNR levels in the feedback channel

	$L = 25$	$L = 50$	$L = 100$	$L = 500$	$L = 1000$
$SNR = inf.$	0.0025	0.0014	$7.51 \cdot 10^{-4}$	$3.23 \cdot 10^{-4}$	$3.92 \cdot 10^{-4}$
$SNR = 10dB$	0.0016	0.0014	$5.26 \cdot 10^{-4}$	$4.9 \cdot 10^{-4}$	$5.25 \cdot 10^{-4}$
$SNR = 0dB$	0.0035	0.0040	0.0041	0.0058	0.0049

5.4.2.3 Complexity of MMSE based Polynomial Pre-distorter

In order to evaluate the computational complexity of the MMSE based Polynomial pre-distorter, the 3rd order polynomial pre-distorter is considered herein.

Adaptation Mode:

It can be observed that the matrices in (5.25) and (5.26) are deterministic for a given training sequence and therefore they can be determined and inverted offline and only once. Therefore the only significant computations involved are the estimation of the expectation terms on the left hand sides of (5.25) and (5.26). Moreover, unlike for the Secant method, the estimate does not need to be updated at each step and therefore a single estimate can be produced after N samples. Such an approach would also be consistent with the relaxed requirement of relatively slow re-adaptation of the pre-distorter. Therefore the total computational requirements of the MMSE training approach are two polynomial evaluations and the estimation of the expectations terms.

However, this section only considers the complexity associated with the algorithm whilst the complexity associated with the calculation of pre-distortion parameters and finding the magnitude of the signal samples will be considered in the operational mode.

In the case of 3rd order polynomials, there are 14 expectation terms need to be estimated and therefore, it requires approximately 1-complex division, 14-real additions, 14-real divisions, 40-real multiplication and a 4×4 matrix inversion.

Operational Mode:

When used to pre-distort the input signal sample, the polynomial pre-distorter processes the sample into three consecutive phases. In the first phase, the magnitude of the complex signal sample is evaluated according to:

$$magnitude = \sqrt{real^2 + imag^2} \tag{5.27}$$

The above operation requires two real multiplications and real additions[27].

In the second phase, the pre-distortion parameters are found by simply evaluating the third order polynomial. The evaluation of a third order real function requires six real multiplications and two real additions.

Finally, the pre-distortion coefficient is multiplied by the input signal sample. This operation requires one complex multiplication which is equal to four real multiplication and two real additions.

The overall complexity of the 3rd order polynomial pre-distorter is presented in Table 5-9.

Table 5-9: Complexity Analysis per sample for polynomial pre-distortion schemes (MMSE)

Method	Mode	Real ×	Real +	Complex ÷
Poly. Pre-distorter (MMSE)	Adaptation[28]	40	14	1[29]
	Operation	18	7	0

5.4.2.4 Observations: MMSE based Polynomial Pre-distorter

The following main points can be observed from the simulation results:

- For the particular amplifier model, the 5th order polynomial provides slightly better accuracy than for the 3rd order.
- Including the even-order term provides significant performance improvement.
- The convergence speed of the polynomial pre-distorter is significantly faster relative to the LUT pre-distorter.
- The adaptation of the polynomial pre-distorter is significantly more resilient and stable to low SNR conditions relative to the LUT pre-distorter.

[27] The complexity of the square-root operation is not considered.

[28] Matrix inversion is not considered.

[29] 14 real divisions

- The complexity of the polynomial pre-distorter is significantly higher both in the adaptation and the operational modes of the pre-distorter.

As observed from the simulation results, the polynomial pre-distorter converges significantly faster than the LUT pre-distorter. However, the computational complexity, especially in evaluating the polynomials, in the polynomial pre-distorter dramatically increases if the pre-distorter is extended to use higher order polynomials; obviously, the complexity in the operational mode also increases [BESB01]. On the other hand, it is only the adaptation time that increases if larger sized Look Up Tables are employed and thereby, the complexity of the adaptation operation increases significantly [CAVE90]. In the next section, we extend our investigation on the LUT based pre-distorter based on a modified Secant algorithm which is based on the Newton-Raphson modification in [HUAN04].

Moreover, the performances of the two aforementioned pre-distortion techniques under different SNR assumptions are further evaluated through downlink (HSDPA, OFDM) and uplink (HSUPA, SC-FDMA) simulations and will be presented in chapters 6.

5.5 LUT Pre-distorter based on Modified Secant Algorithm

In this section, a modified Secant algorithm, derived from the modifications to [HUAN04], is investigated for the LUT based pre-distortion technique, assuming the feedback signal is only contaminated by additive white Gaussian noise in the training process. The transmission path of a typical OFDM based communication system, including TWTA, Pre-distorter, is depicted in Figure 5-13.

The performance of the algorithm is first evaluated under very noisy feedback channel conditions. Subsequently, they are also investigated for higher signal to noise ratio (SNRs) in the feedback channel. The performances are evaluated in terms of link-level performance and in the reduction of out-of-band radiation or adjacent channel interference (ACI). In addition, the investigations are further extended to evaluate the performance in terms of the following performance measures:

$$NMSE = \boldsymbol{E}\left\{\left|\frac{r(t) - G(|F(|r(t)|)|)}{r(t)}\right|^2\right\} \tag{5.28}$$

$$NMAE = \max\left|\frac{r(t) - G(|F(|r(t)|)|)}{r(t)}\right| \tag{5.29}$$

$$RMSE = \boldsymbol{E}\{|r(t) - G(|F(|r(t)|)|)|^2\} \tag{5.30}$$

$$RMAE = \max|r(t) - G(|F(|r(t)|)|)| \tag{5.31}$$

Where E denotes the expectation operator. NMSE and NMAE denote the normalized MSE and normalized maximum absolute error (MAE), whereas RMSE and RMAE denote the relative MSE and relative MAE, respectively. The NMSE and NMAE react to the error resulting from the pre-distorter in the small signal region, whereas RMSE and RMAE are more sensitive to the error near to the input signal saturation region. Thus, these performance indexes can provide a fair and comprehensive comparison for the adaptation algorithms employed. Moreover, it must be noted that although the input signal to the pre-distorter is random, the performance indexes above are not sensitive to the input signal itself if enough samples are taken[30] [HUAN06].

5.5.1 Modified Secant Method

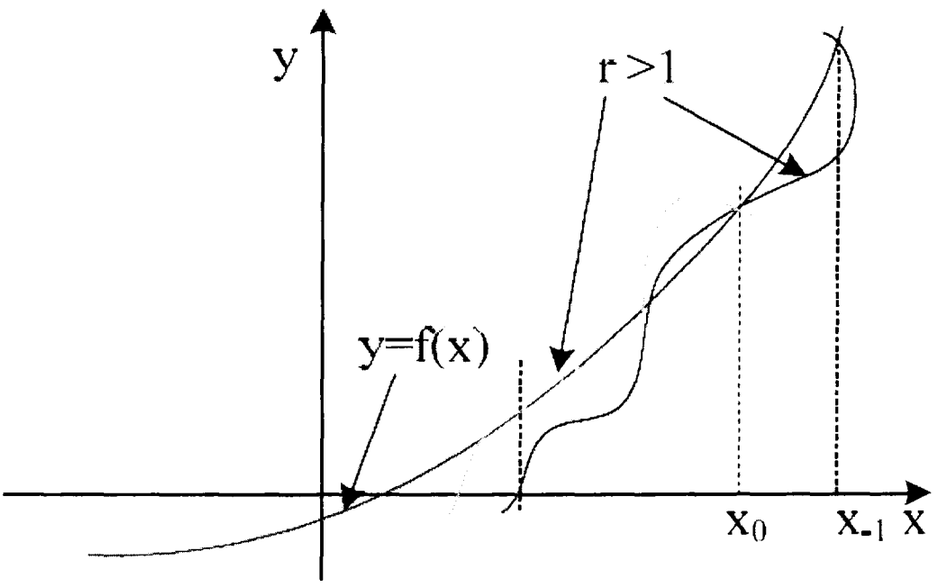

Figure 5-16: Modified Secant Method (Higher order Secant method)

In [HUAN04], the well-known linear Newton-Raphson method was modified to improve the performance and is referred to as the non-linear Newton-Raphson method. On the other hand, the main difference between the linear Newton-Raphson method and the Secant method is the approximation to the derivative of the function by finite difference value, shown in equation (5.16). Therefore, we adopt a similar modification with the conventional Secant method and thus, the modified Secant algorithm is given by:

[30] 1 million samples were used

$$F_i(k+1) = \left[F_i^r(k) - \left\{ rF_i^{r-1}(k)e(F_i(k)) \Big/ e'(F_i(k)) \right\} \right]^{1/r} \quad (5.32)$$

Where,

$$e'(F_i(k)) \approx \left[\{e(F_i(k)) - e(F_i(k-1))\} \Big/ \{F_i(k) - F_i(k-1)\} \right] \quad (5.33)$$

When $r = 1$, it reduces to the conventional Secant formulation. For higher values of r, the modified Secant method uses the curvature (a parabola for $r = 2$) rather than using the straight line for updating the LUT parameter at each iteration. This fact is illustrated in Figure 5-16.

Moreover, the algorithm was only experimented for real polynomial root finding problems and no work has been done for complex root finding problems and the optimal selection of the parameter, r. However, depending on the type of problem involved, the algorithm tends to become unstable for increasing values of parameter, r. Thus, it is appropriate to investigate this algorithm here.

5.5.2 Performance Evaluations

Table 5-10: Simulation Parameters

Simulation Parameter	Value
No. subcarriers in OFDM	512
Modulation Technique	QPSK
Oversampling rate	4 times
Input Back-off (IBO)	6 dB[31]
LUT size	128

In this section, the performances of the LUT pre-distorter based on the modified Secant algorithm is evaluated and compared under various feedback channel conditions.

Table 5-10 lists the simulation parameters used for investigation. It should be noted that although the LUT with larger sizes provide improved performance, the investigations are only performed using a 128 sized LUT pre-distorter [CAVE90]. In Section 5.4.1, the performance of Secant based LUT pre-distorter was evaluated under various feedback channel conditions and it was found that the performance was heavily degraded in noisy feedback channel conditions (lower SNRs). Due

[31] This was fixed in the investigation.

to this fact, in this section, the performance was first evaluated, in terms of out-of-band radiation power and link level performance, for noisy feedback channel conditions only (SNR = 0dB).

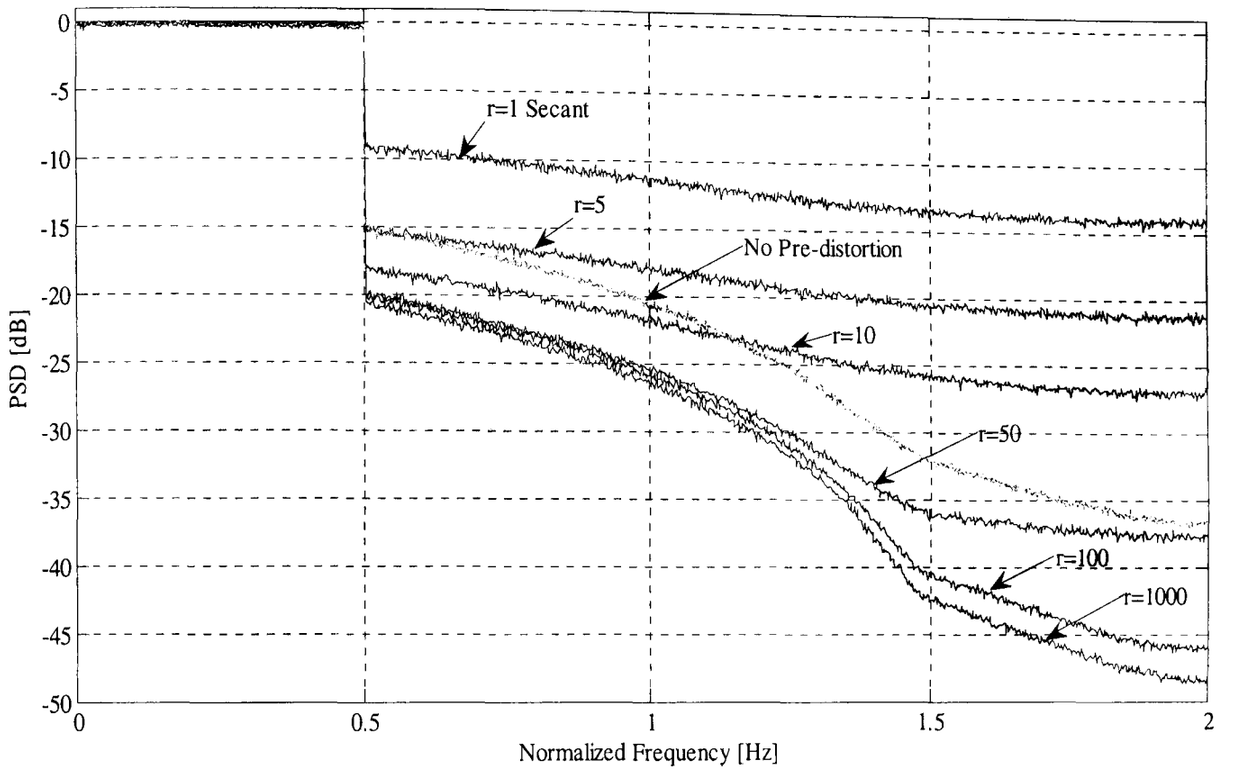

Figure 5-17: Spectrum of output signal from TWTA for different values of parameter, r. (SNR = 0dB and Length of training sequence, N = 500)

The spectrum of the output signal from the TWTA for different values of r is shown in Figure 5-17. It is observed that the modified Secant algorithm significantly reduces the adjacent channel interference (ACI) compared with the conventional Secant algorithm (case when $r = 1$). When $r = 1000$, approximately 35 dB improvement is observed at an offset, equal to twice the signal bandwidth, from the centre frequency. Moreover, from Figure 5-18, a similar improvement in the link-level performance is also observed. However, the improvement is significant only up to a certain value of parameter, r in both cases.

Similarly, the modified algorithm was further investigated for different lengths of training sequence and for this purpose, the case when $r = 100$ was chosen. Figure 5-19 shows the spectrum of the output signal from the TWTA for different lengths of training sequence. It is observed that the reduction of out-of-band radiation power is significantly reduced when the length of training sequence is larger than the LUT size, 128; for example $N = 500, 1000$, and 10000. However, in all these cases, there is no significant variation in the reduction of out-of-band radiation power.

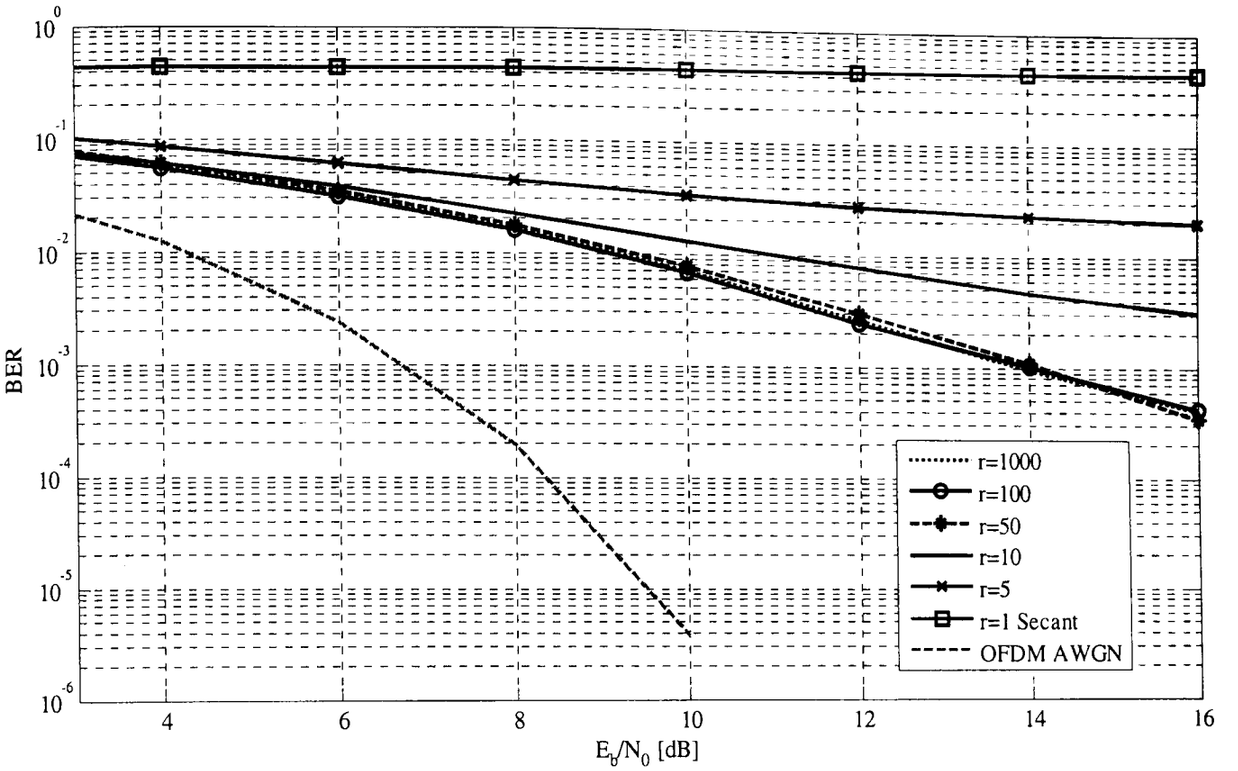

Figure 5-18: Link level performance of OFDM system for different values of parameter, r (SNR = 0dB and Length of training sequence, N = 500)

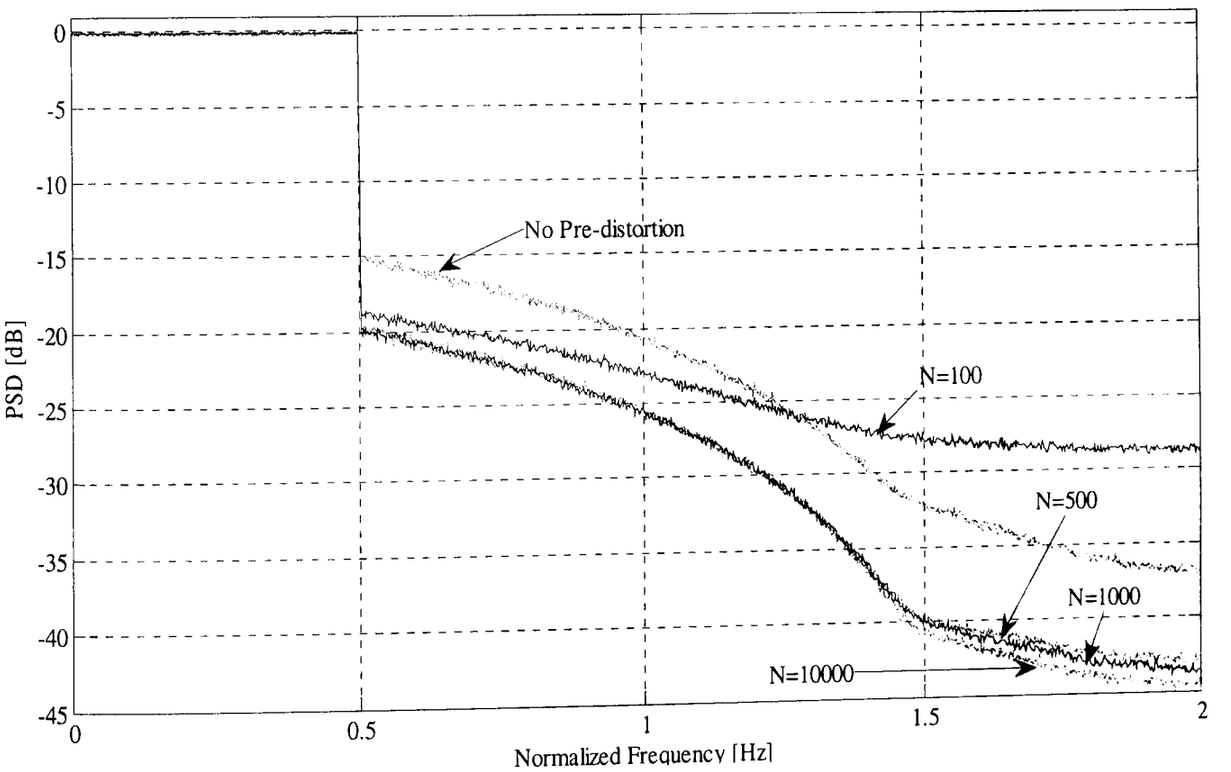

Figure 5-19: Spectrum of output signal from TWTA for different length of training sequence, N. ($SNR = 0dB$ and parameter, $r = 100$)

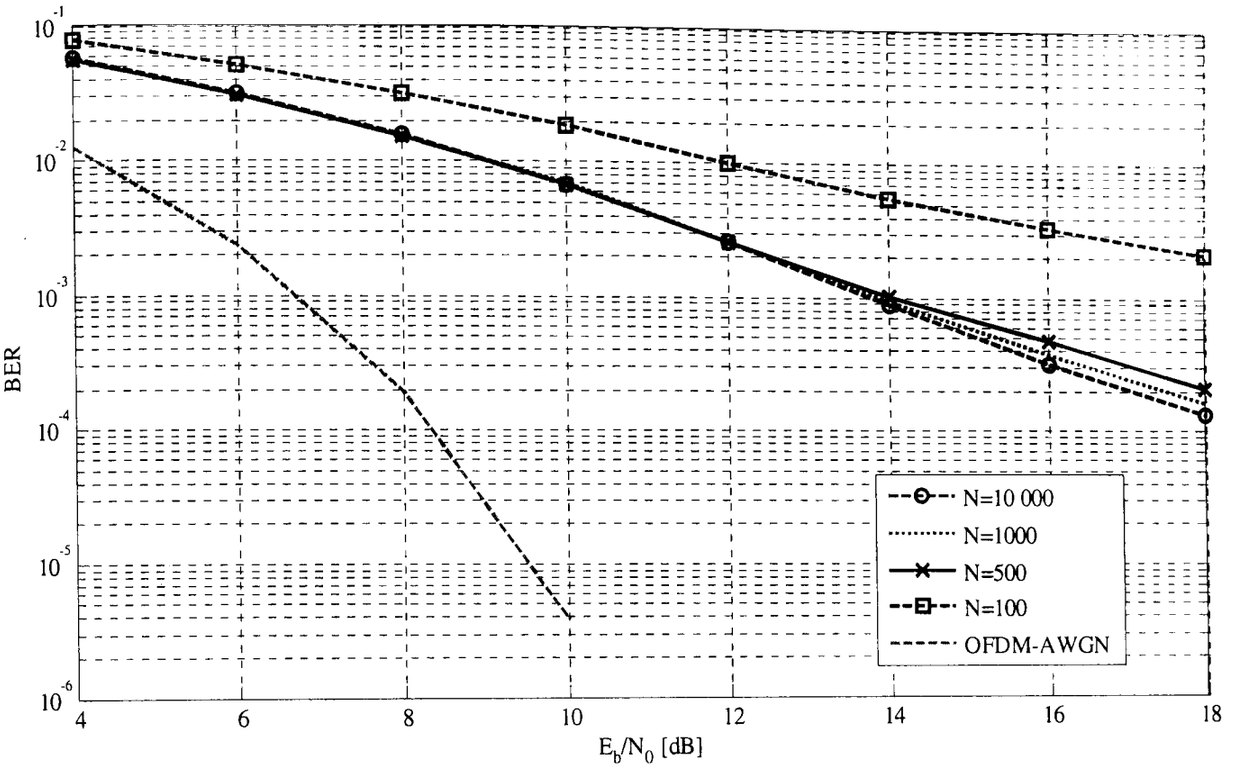

Figure 5-20: Link level performance of OFDM system for different length of training sequence, N. ($SNR = 0dB$ and parameter, $r = 100$)

On the other hand, Figure 5-20 shows the link level performance of the OFDM system for different lengths of training sequence. There is no significant difference in the Bit Error Rate (BER) performance when the length of the training sequences are 10000, 1000 and 500. However, the performance is significantly degraded when the length of the training sequence is 100, which is smaller than the size of the LUT, 128.

Investigations were further extended to evaluate the performance indexes given above. Figure 5-21 shows the evaluated performance indexes, NMSE, NMAE, RMSE and RMSE, for modified Secant algorithm with different values of parameter r under a very noisy feedback path from the satellite ($SNR = 0\ dB$). All these indexes shows performance improvement when the value of parameter r is increased. Moreover, the value of the parameter, r chosen from the above investigations is consistent.

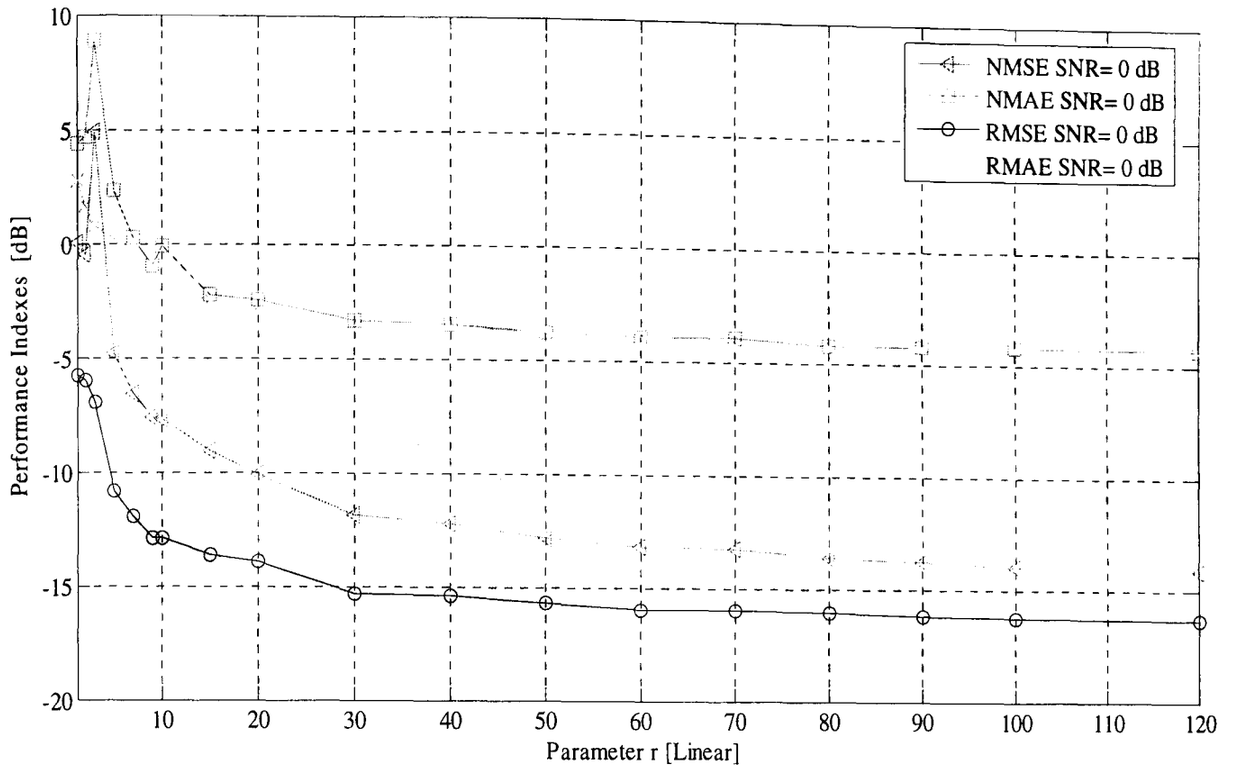

Figure 5-21: Performance comparison between different values for parameter, r for feedback channel $SNR = 0dB$

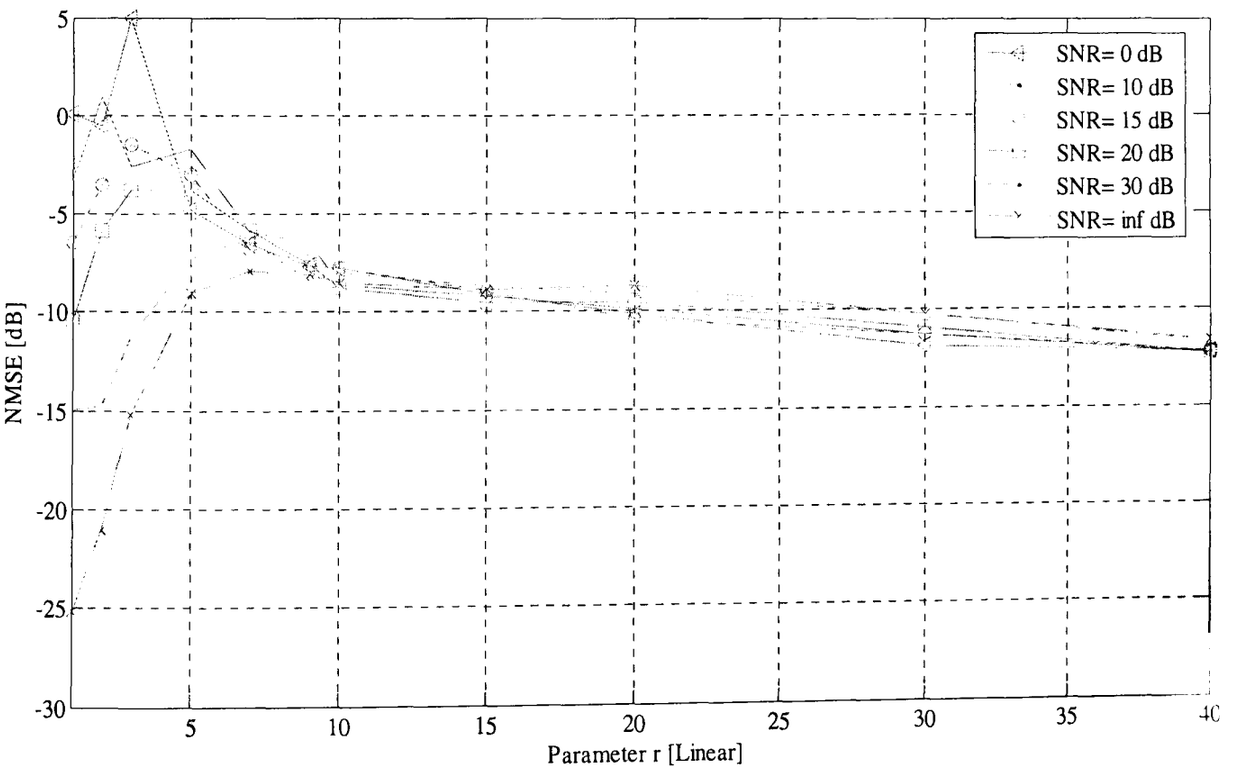

Figure 5-22: NMSE for different values of parameter r under different feedback channel conditions

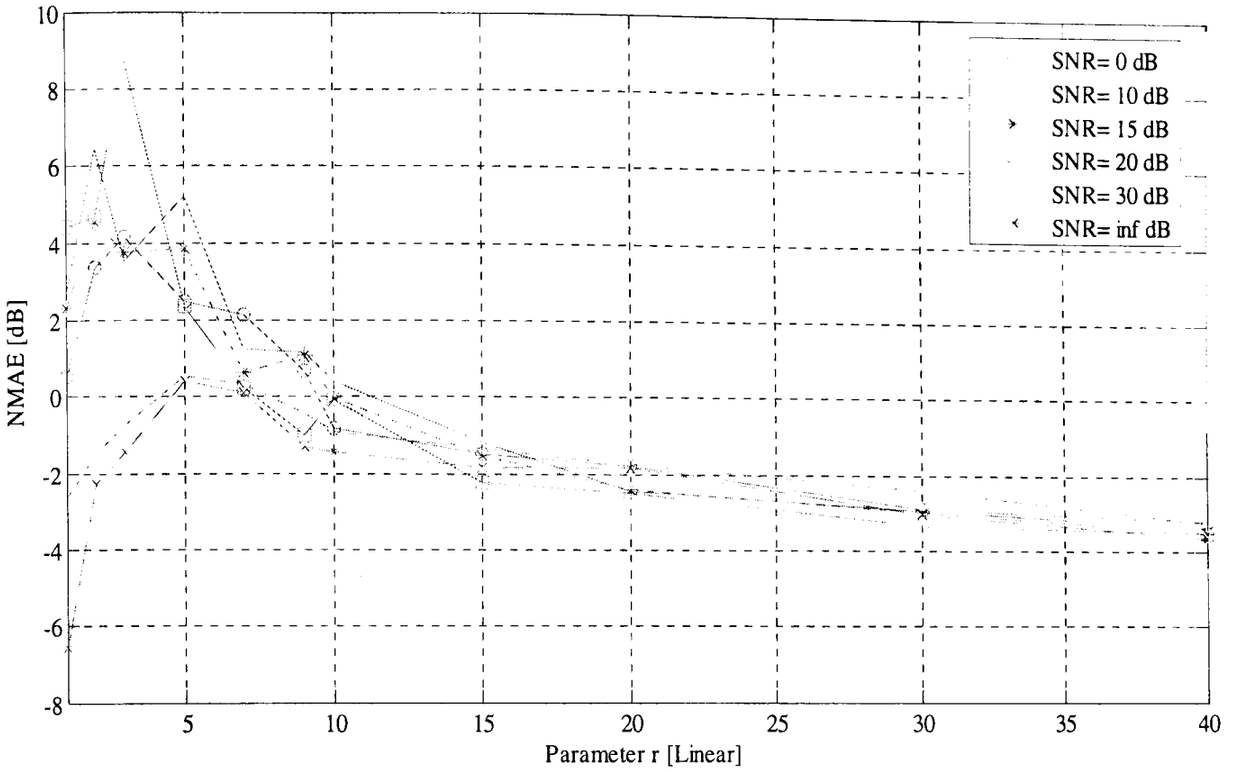

Figure 5-23: NMAE for different values of parameter r under different feedback channel conditions

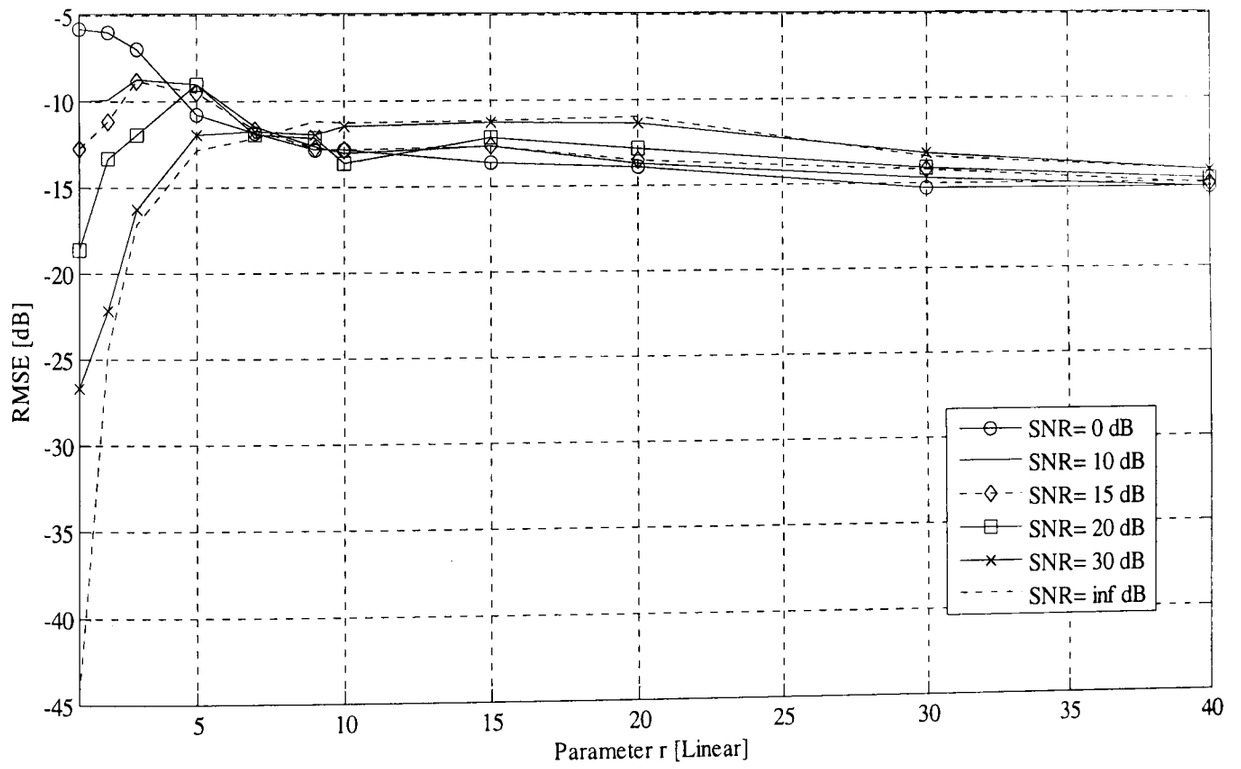

Figure 5-24: RMSE for different values of parameter, r under different feedback channel conditions

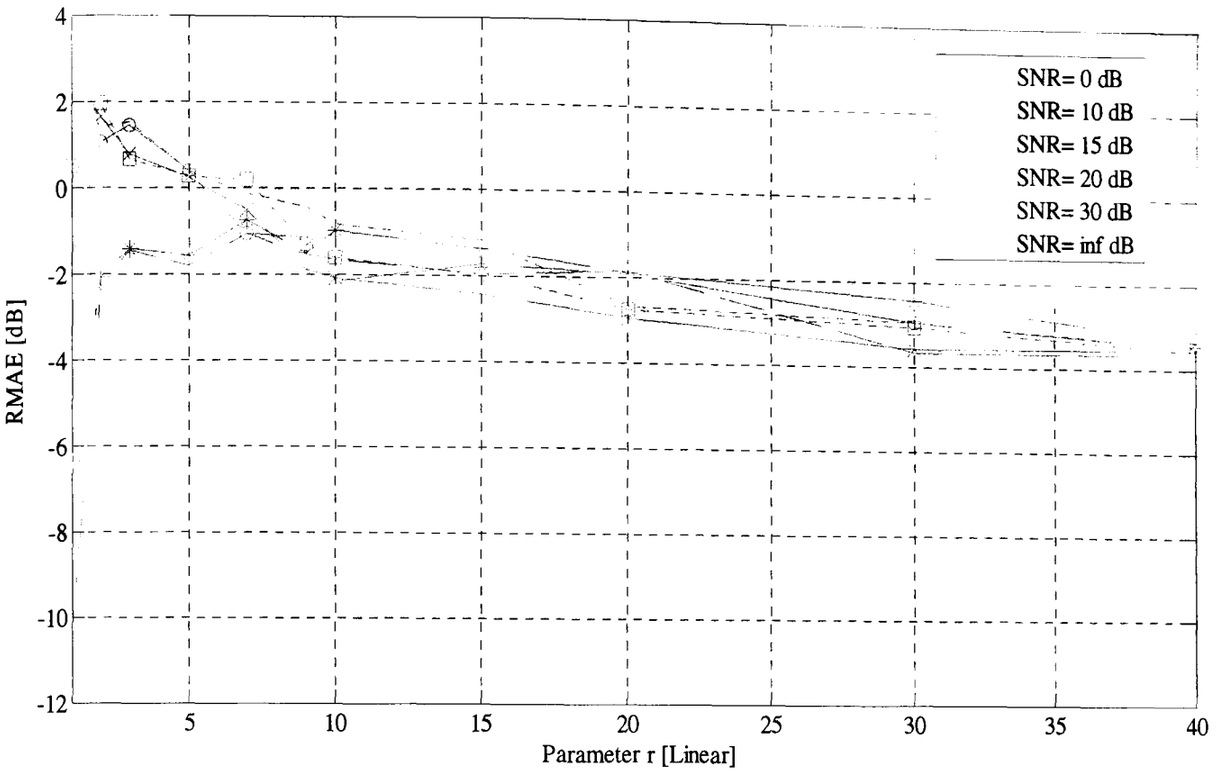

Figure 5-25: RMAE for different values of parameter, r under different feedback channel conditions

Similar performance indexes were evaluated for various feedback channel conditions in the feedback path from the satellite. Figure 5-22, 5-23, 5-24 and 5-25 shows the performance indexes NMSE, NMAE, RMSE, and RMAE, respectively, evaluated under different SNRs; $0, 10, 15, 20, 30$ and inf dBs. It is observed that when the feedback channel conditions are improved, the performance indexes show significant improvement at lower values of parameter, r. However, the improvement is significant only when the SNR in the feedback channel is greater than a certain value (i.e threshold SNR). Accordingly, an approximated threshold-SNR can be fixed at SNR =20 dB. Within this limit, the modified Secant algorithm outperforms the conventional Secant algorithm.

The simulations were further extended to evaluate the link level performance of both the modified Secant algorithm and the Secant algorithm in different feedback channel conditions by keeping the parameter, r constant at 100 and the length of the training sequence at 500. The evaluated performances are reported in Figure 5-26. It is observed that the conventional Secant based pre-distorter shows improvement when the SNR in the feedback channel is increased. However, it shows poor performance in very noisy channel conditions. On the other hand, the modified Secant based pre-distorter shows improved performance in noisy channel conditions. However, the performance improvement obtained by increasing the SNR in the feedback channel is limited. It is

also noted that the conventional Secant based pre-distorter outperforms the modified Secant based pre-distorter beyond a certain SNR in the feedback channel; approximately when SNR= 20 dB.

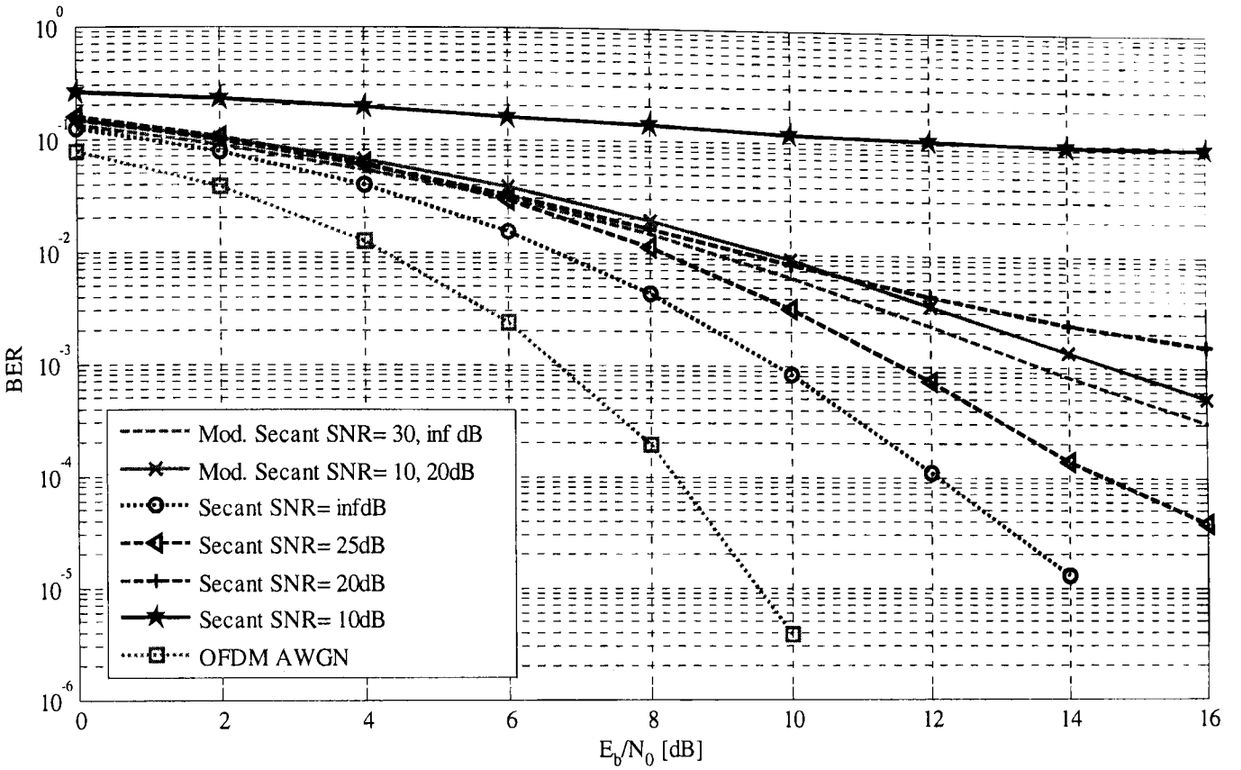

Figure 5-26: Link Level Performance of Modified Secant Algorithm for different SNRs ($r = 100$ and length of training sequence, $N = 500$)

5.5.3 Observations: Modified Secant Algorithm

The following main points can be observed from the simulation results:

- In the noisy feedback channel condition, the modified Secant algorithm provides improved performance in terms of both adjacent channel interference and link level performance. However, its performance is limited in noiseless feedback channel condition.
- The conventional Secant based algorithm provides better performance in the noiseless feedback channel conditions. On the other hand, it shows poor performance in noisy channel conditions.
- A threshold level in SNR = 20dB is observed, below this value modified Secant based pre-distorters provides performance improvement over the conventional Secant based pre-distorters.

5.6 Summary and Conclusions

This chapter can be summarized as follows:

- The TR technique becomes very effective when combined with Pre-distortion technique. The performance advantage is significantly greater than the performance advantage obtained with any single mitigation technique: TR technique or ideal Pre-distortion.

- The polynomial pre-distorter shows more robustness than the LUT pre-distorter in the noisy feedback channel conditions. However, its complexity is greater than the LUT pre-distorter.

- 5^{th} order polynomial shows improved performance advantage when compared with the 3^{rd} order polynomials. Moreover, polynomial pre-distorters with even-order terms show significant performance advantage compared with the pre-distorter without even-order terms.

- The modified Secant algorithm showed significant performance advantage in noisy feedback channel conditions. However, it showed a limited improvement in noiseless feedback channel conditions. Thus, the parameter r must be adapted according to the SNR in the feedback channel conditions, keeping $SNR = 20\text{dB}$ as an approximate threshold level.

Chapter Six

6 Performance Comparison of OFDM based and HSPA based Air Interfaces in the Wideband Mobile Satellite Channel

6.1 Introduction

As briefly discussed in chapter 2, evaluating the performance of OFDM based air interfaces over the forward and return link of the hybrid satellite-terrestrial system is of high relevance to future Mobile Satellite Systems. Such systems will offer not only complementary coverage to terrestrial LTE-UMTS cellular networks, but also the possibility of satellite operators deploying their autonomous mobile networks by taking advantage of the terrestrial component in such hybrid architectures. Moreover, the newly formed ETSI Mobile Satellite Systems (MSS) group[32] has recently started investigating the LTE air interfaces in the hybrid network.

The main objective of this chapter is thus to evaluate the performance of the OFDM based air interfaces, based on the 3GPP standard, over the hybrid satellite-terrestrial channel, represented by the power delay profiles given in Appendix A. The evaluated performance is compared with the performance of the High Speed Packet Access (HSPA) air interfaces, which represent the highest data rate version of the WCDMA based UMTS standards. As illustrated in Figure 6-1, the performance is evaluated in two different systems, namely Long Term Evolution (LTE) Satellite Systems and S-DMB type systems. In LTE satellite systems, HSDPA and OFDM are compared in the forward link whereas HSUPA and SC-FDMA are compared in the return link. The forward link comparison is also equally appropriate to S-DMB type system.

The performance comparisons have been based on a tested and validated (C++) link-level simulator of T-UMTS Release 6 (HSUPA) and Release 5 (HSDPA)[33], which are already

[32] The MSS group was formed in early 2008 by merging the ETSI S-UMTS and ETSI GMR standardization groups.

[33] The link-level simulator includes the UMTS Release99 specifications.

available. These simulators have been extended to include different mobile satellite channel models, as produced via measurements within the European FP6 MAESTRO project [MAES06], and also the non-linear response of the on-board satellite TWTA. Main consideration is given to evaluating the physical layer performance (Block Error Rate (BLER) Vs E_b/N_0) based on the 3GPP 25.814, 25.896 standards. Accordingly, no special focus has been made to modify the existing parameters in the standard and any other issues related to both OFDM and SC-FDMA systems, for example: channel equalization, pulse shaping, etc.

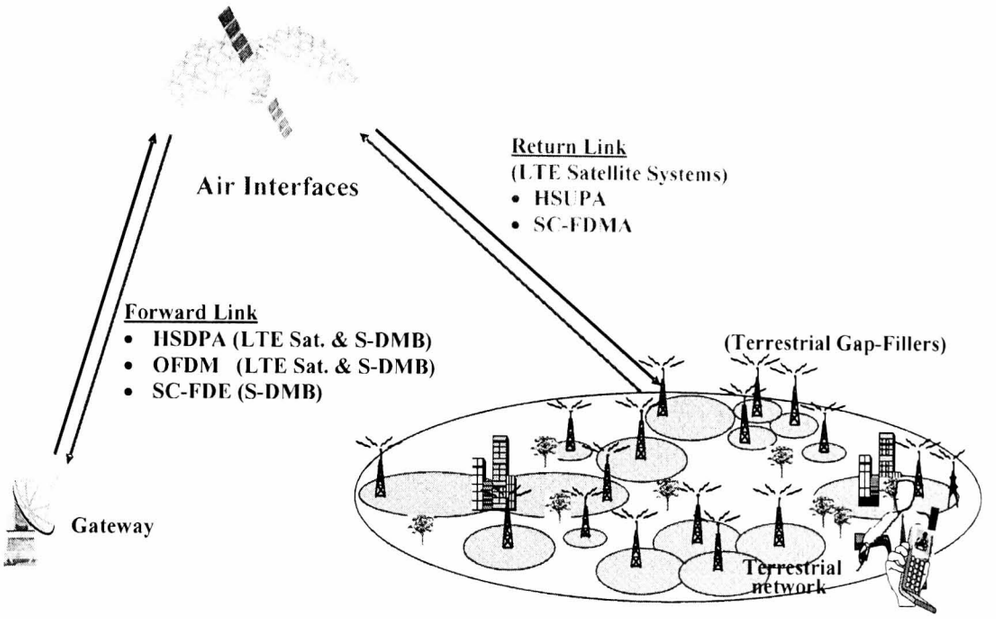

Figure 6-1: Considered System Scenario together with the air interfaces in the Forward and Return links

This chapter also proposes the use of Single Carrier Frequency Domain Equalization (SC-FDE) as an alternative air interface to OFDM, within satellite digital multimedia broadcasting systems (S-DMB). In particular, SC-FDE, due to its single carrier nature, implicitly removes the problem of high PAPR OFDM signal properties. In addition, SC-FDE has similar overall complexity compared to OFDM and also provides similar overall performance in a linear channel environment [FALC02]. A comparison of OFDM and SC-FDE systems was performed assuming a perfectly linearized satellite channel and ideal channel estimation.

The chapter first introduces both SC-FDE and SC-FDMA air interfaces along with their system models. Section 6.3 provides performance evaluation and comparison in the forward link of the non-linear wideband mobile satellite channel. Both LTE satellite system and S-DMB type system are considered. In the LTE satellite system, OFDM and HSDPA are considered whereas in the S-DMB type system SC-FDE and OFDM are considered. However, the results obtained in LTE satellite system are also applicable to S-DMB type system. On the other hand, SC-FDMA and HSUPA is considered in the return link of the non-linear wideband mobile satellite system and as

most appropriate to LTE satellite systems which incorporates a return link. Emphasis in the return link study is also given to realistic channel estimation, taking into account the effect of amplifier's non-linearity. Furthermore, the investigation of a CAZAC (Constant Amplitude Zero Auto Correlation) reference signals in the non-linear channel estimation for SC-FDMA is also included. For this purpose, the Zadoff- Chu sequence was considered due to its wide applications in communication systems and its recent recommendation for Random Access Channel (RACH) preamble [YANG06]. Other elements addressed in this chapter are the impact of linearization techniques, 3rd order polynomial pre-distortion technique described in chapter 5, and their effect on the channel estimation using CAZAC sequence. Finally, the chapter is summarized with the important outcomes. In addition, appropriate air interfaces for LTE satellite and S-DMB type systems are recommended based on the link-level investigation.

6.2 Overview of Air Interfaces

In this section, SC-FDE and SC-FDMA are introduced along with their system models. The SC-FDMA and Orthogonal Frequency Division Multiple Access (OFDMA) are multi-user versions of SC-FDE and OFDM, respectively. A DFT spread orthogonal frequency multiplexing is utilized in SC-FDMA whereas the multiple accesses in OFDMA are based on the assignment of the subset of subcarriers to individual users. Thus, the SC-FDE is introduced in comparison to OFDM whereas SC-FDMA is introduced in comparison to OFDMA.

6.2.1 SC-FDE

6.2.1.1 Overview of SC-FDE

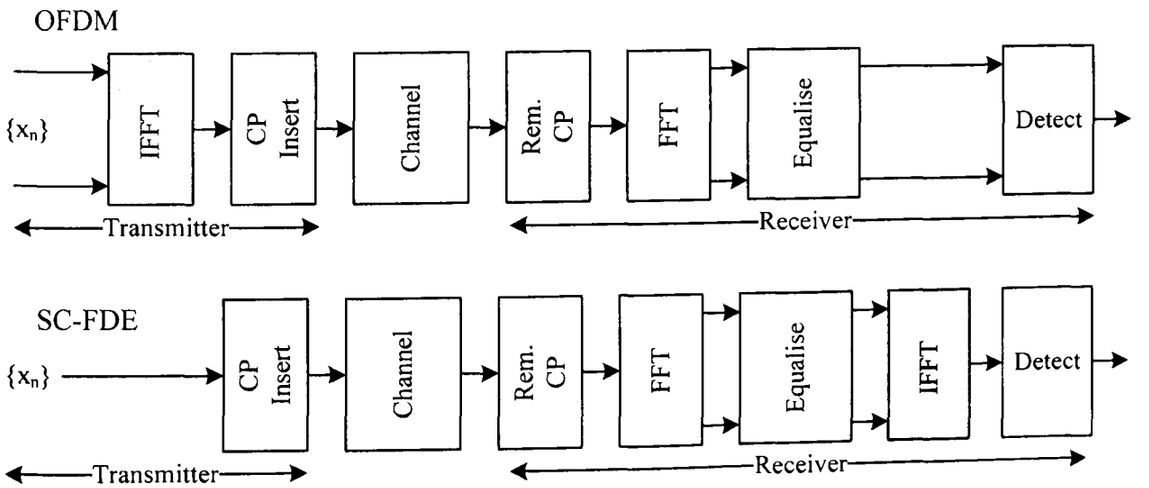

Figure 6-2: Transmitter and Receiver Structures of OFDM and SC-FDE Systems

Though OFDM provides efficient low complexity equalization in broadband communication systems, it suffers from the drawback of high PAPR, which does not exist with conventional single carrier system. In [FALC02], single carrier with Frequency Domain Equalisation (FDE) was proposed as another way to fight the frequency fading channel. It delivers performance similar to the OFDM system with essentially the same overall complexity, even for long excess delay spread [SARI95]. Figure 6-2 shows the block diagram of SC-FDE and compares it with that of OFDM.

In the transmitter of SC-FDE, the CP is added, which is a copy of the last part of the block, to the input data at the beginning of each block in order to prevent the inter-block interference (IBI) and also to transform the linear convolution of the channel to circular convolution. It must be noted that the circular convolution is equivalent to point-wise multiplication in frequency domain and thereby, simplifies the equalization or channel inversion process in the receiver. Thus, similar to OFDM, SC-FDE also provides low-complexity equalization, independent of the channel memory order and the signalling constellation. However, in SC-FDE both the FFT and IFFT processing takes place on the receiving end, and hence the transmission is single-carrier. It is also noted that the use of CP can be substituted by a silent period [ZHOU01] or a training sequence [DENE01]. The lack of IFFT processing at the transmitter makes SC-FDE inherently more resilient to the amplifier's non-linear distortion. Simulation results which confirm this can be found in [HORL04].

The SC-FDE receiver transforms the received signal into the frequency domain by applying FFT and does the equalisation process in the frequency domain. Most of the well-know time domain equalization techniques, such as minimum mean-square error (MMSE) equalisation, decision feed-back equalisation (DFE), can be applied to the FDE and the details of the frequency domain implementation of these techniques are found in [DHAH01], [BENV02], [PANC05]. After the equalisation, the signal is brought back to the time-domain by applying IFFT and the detection is then performed.

Many recent papers can be found, which provide comparisons between the two approaches (see [HORL04] and references therein). Comparing the OFDM and SC-FDE systems, they both use the same communication component blocks and the only difference between the two is the location of the IFFT block. Thus, a similar link level performance and spectral efficiency can be expected.

However, there are distinct differences that make them perform differently. In the receiver, the data detection is performed on a sub-carrier basis for OFDM, whereas it is performed after applying the IFFT to the equalised data in SC-FDE (time domain). Due to this reason, the OFDM

system is very sensitive to spectral nulls. Furthermore, OFDM symbols are expanded with parallel transmission of the data block during the elongated time period.

In summary, SC-FDE has the following advantages over OFDM:

- Low PAPR due to single carrier modulation at the transmitter
- Robustness to spectral null
- Lower sensitive to carrier frequency offset

On the other hand, it is also interesting to note that a SC-FDE receiver has the capability to receive OFDM signals and conversely the OFDM transmitter to transmit SC-FDE signals. In other words, a dual mode system can be featured by simply incorporating a convertible modem switching the IFFT block between the transmitter and receiver at each end of the link.

In the remainder of this section a model of a SC-FDE system will be provided and then simulation results will be presented, which compare the performance of OFDM and SC-FDE in an S-DMB type of system.

6.2.1.2 SC-FDE System Model

Let $\mathbf{u}_i$ be the i^{th} block of transmitted data, which consists of K QAM symbols. The subsequent insertion of the CP, can be represented as a linear matrix of size $(C+K)\times K$ which has the form $\mathbf{T}_{CP} = [\mathbf{0}_{C\times(K-C)}, \mathbf{I}_{C\times C}; \mathbf{I}_{K\times K}]$[34], where C is the length (in samples) of the CP. Thus the resulting signal can be expressed as: $\bar{\mathbf{u}}_i = \mathbf{T}_{CP}\mathbf{u}_i$ and consists of $P = (C+K)$ samples. Provided that timing is recovered accurately at the receiver, the received signal which contains complete observation of $\mathbf{u}_i$ is given as:

$$\bar{\mathbf{x}}_i = \mathbf{H}_0\bar{\mathbf{u}}_i + \mathbf{H}_1\bar{\mathbf{u}}_{i-1} + \bar{\mathbf{n}} \tag{6.1}$$

where $\bar{\mathbf{n}}$ is a vector which contains samples of the Gaussian noise in the receiver's circuitry.

In (6.1) it is assumed that the channel is modelled as an FIR filter of $L+1$ taps: $\mathbf{h} = [h(0), h(1), \ldots\ldots, h(L)]$, and $\mathbf{H}_0$ represents the $P\times P$ Toeplitz channel filtering matrix, which is given as:

[34] MATLAB notation is used.

$$\mathbf{H}_0 = \begin{bmatrix} h(0) & 0 & 0 & 0 & 0 \\ . & h(0) & 0 & 0 & 0 \\ h(L) & . & h(0) & 0 & 0 \\ 0 & h(L) & . & . & 0 \\ 0 & 0 & h(L) & .. & h(0) \end{bmatrix} \tag{6.2}$$

$\mathbf{H}_1$ models the edge effect caused by the excess delay spread of the propagation channel and results in ISI with the previously transmitted symbol $\overline{\mathbf{u}}_{i-1}$.

$$\mathbf{H}_1 = \begin{bmatrix} 0 & .. & h(L) & .. & h(1) \\ .. & .. & 0 & h(L) & .. \\ 0 & 0 & 0 & 0 & h(L) \\ .. & .. & .. & .. & .. \\ 0 & 0 & 0 & .. & 0 \end{bmatrix} \tag{6.3}$$

It is observed that provided $C \geq L$ the entries of $\overline{\mathbf{x}}_i$ affected by ISI, are only those which contain the CP. Incorrect timing recovery will result in collecting observations, which contain more than L symbols from $\overline{\mathbf{u}}_{i-1}$ and thus failing to avoid ISI through the removal of the CP. On the other hand, if the observation window is delayed (instead of being ahead in time) then even a slight timing error will result in ISI with $\overline{\mathbf{u}}_{i+1}$.

The removal of the CP at the receiver can be modelled by a linear matrix: $\mathbf{T}_R = [\mathbf{0}_{K\times C}, \mathbf{I}_{K\times K}]$, which effectively also removes the second term in the summation in (6.1). Thus the resulting signal is given as:

$$\mathbf{x}_i = \mathbf{T}_R \mathbf{H}_0 \mathbf{T}_{CP} \mathbf{u}_i + \mathbf{n} = \hat{\mathbf{H}} \mathbf{u}_i + \mathbf{n} \tag{6.4}$$

The effect of the inclusion and removal of the CP is that the effective channel matrix $\hat{\mathbf{H}}$ has a circulant structure:

$$\hat{\mathbf{H}} = \begin{bmatrix} h(0) & 0 & .. & 0 & h(L) & .. & h(1) \\ .. & h(0) & .. & .. & 0 & h(L) & .. \\ h(L) & .. & .. & 0 & .. & 0 & h(L) \\ 0 & h(L) & .. & h(0) & 0 & .. & 0 \\ .. & 0 & .. & .. & h(0) & 0 & .. \\ 0 & .. & .. & h(L) & .. & h(0) & 0 \\ 0 & 0 & .. & 0 & h(L) & .. & h(0) \end{bmatrix} \tag{6.5}$$

A circulant matrix is defined by the first row only, and each row is obtained by cyclically shifting the previous row to the right. The most important property of circulant matrices is that they all share the same set of singular vectors. Those singular vectors form the FFT matrix. In other words, any circulant matrix is diagonalised by the FFT matrix:

$$\mathbf{\Lambda} = \mathbf{F}\widehat{\mathbf{H}}\mathbf{F}^{-1} \tag{6.6}$$

where $\mathbf{\Lambda} = diag(\omega^0, \omega^1, .., \omega^{K-1})$ and ω^i is the channel response at the i^{th} frequency bin and:

$$\mathbf{F} = \frac{1}{\sqrt{K}} \begin{bmatrix} 1 & 1 & 1 & .. & 1 \\ 1 & e^{-\frac{j2\pi}{K}} & e^{-\frac{j4\pi}{K}} & & e^{-\frac{j(K-1)2\pi}{K}} \\ 1 & e^{-\frac{j4\pi}{K}} & e^{-\frac{j8\pi}{K}} & & e^{-\frac{j(K-1)4\pi}{K}} \\ .. & .. & .. & .. & .. \\ 1 & e^{-\frac{j(K-1)2\pi}{K}} & e^{-\frac{j(K-1)4\pi}{K}} & .. & e^{-\frac{j(K-1)(K-1)2\pi}{K}} \end{bmatrix} \tag{6.7}$$

Thus following the FFT processing at the receiver the system input-output relationship becomes:

$$\mathbf{y}_i = \mathbf{F}\mathbf{x}_i = \mathbf{\Lambda}\mathbf{F}\mathbf{u}_i + \mathbf{F}\mathbf{n} \tag{6.8}$$

Equation (6.8) suggests that the simplest zero-forcing (ZF) equalization can be performed such that the whole system is modelled as:

$$\hat{\mathbf{u}}_i = \mathbf{F}^{-1}\mathbf{\Lambda}^{-1}\mathbf{\Lambda}\mathbf{F}\mathbf{u}_i + \mathbf{F}^{-1}\mathbf{\Lambda}^{-1}\mathbf{F}\mathbf{n} \tag{6.9}$$

The ZF equalising matrix $\mathbf{\Lambda}^{-1}$ exists as long as the channel frequency response does not have zeros on the FFT grid. Even if some of the ω^i are close to zero, the estimate becomes unreliable due to excessive noise amplification. This problem is ameliorated by the MMSE equalization approach [DHAH01]:

$$w_i = \frac{\omega_i^*}{|\omega_i|^2 + \frac{1}{SNR}} \tag{6.10}$$

Decision feedback equalization can also be employed (see [BENV02] and references therein), which provides better performance than the linear equalizers but with increased computational cost.

Following the single-tap equalization process and the IFFT processing, the soft signal estimates can be used in order to make the symbol decisions, or alternatively input to the channel decoder.

6.2.2 SC-FDMA

6.2.2.1 Overview of SC-FDMA

SC-FDMA utilizes single carrier modulation and frequency domain equalization (FDE), but has a similar performance and essentially the same overall complexity as those of the OFDM system. It can be viewed as an extension to single carrier frequency domain equalisation (SC-FDE) in order to accommodate multiple user access [HYUN06a]. Due to its inherent single carrier structure, it facilitates lower PAPR as compared to an OFDMA scheme and this is one of the main technical reason that has been put forward by 3GPP members as an alternative to OFDMA in the return link of the next generation mobile communication systems [HYUN06b].

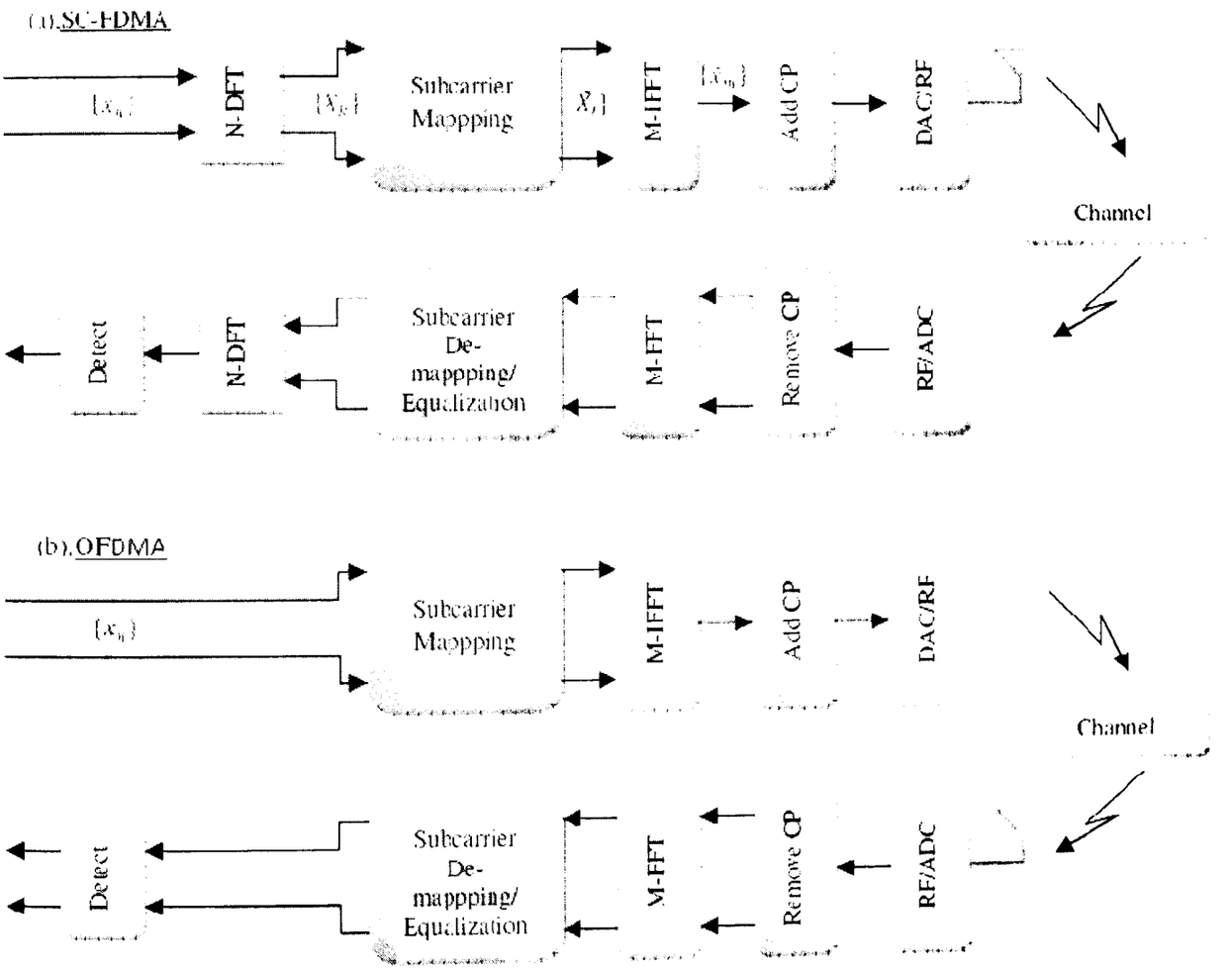

Figure 6-3: Transmitter and Receiver structure of (a).SC-FDMA and (b).OFDMA systems

Figure 6-3 shows a block diagram of the SC-FDMA system, and compares it with the conventional OFDMA system. SC-FDMA can be regarded as a DFT-spread OFDMA, where time

domain data symbols are transformed to the frequency domain by DFT before classical OFDMA modulation. Orthogonality between users is maintained by the fact that each user occupies different sub-carriers in the frequency domain, similar to OFDMA [HYUN06a].

As seen from Figure 6-3, the transmitter of the SC-FDMA system converts a binary input signal to a sequence of modulated sub-carriers. Specifically, a baseband modulator transforms the binary input to a multilevel sequence of complex numbers x_n in one of several possible modulation formats including QPSK, 16-QAM, 64-QAM. The modulation symbols $\{x_n\}$ are then grouped into blocks, each containing N symbols. The first step in modulating the SC-FDMA sub-carriers is to perform an N-point DFT to produce a frequency domain representation X_k of the input symbols. It then maps each of the N-DFT outputs to one of the $M(> N)$ orthogonal sub-carriers that can be transmitted. If $N = M/Q$ and all terminals transmit N symbols per block, the system can handle Q simultaneous transmissions without co-channel interference. Q is known as the bandwidth expansion factor of the symbol sequence. The result of the sub-carrier mapping is the set $\bar{X}_l$ $(l = 0,1,2,\ldots,M-1)$ of complex sub-carrier amplitudes, where N of the amplitudes are non-zero. As in OFDMA, an M-point IFFT transforms the sub-carrier amplitudes to a complex time-domain signal $\tilde{x}_m$. Each $\tilde{x}_m$ are then transmitted sequentially.

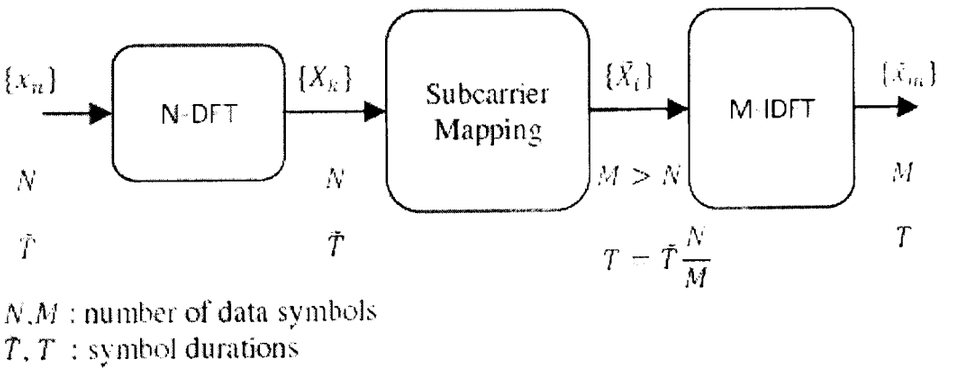

Figure 6-4: Generation of SC-FDMA transmit symbols. There are M total number of sub-carriers, among which $N(< M)$ sub-carriers are occupied by the input data

In addition to the above signal processing, the transmitter also performs two additional processing functions prior to transmission: insertion of cyclic prefix (CP) and linear filtering referred to as pulse shaping. The CP insertion operation is similar to OFDMA as described in chapter 3. Similarly, it prevents Inter-Block Interference (IBI) caused by the multipath propagation while the pulse shaping filter operation reduces the out-of-band signal energy before transmission.

Figure 6-4 details the generation of SC-FDMA transmit symbols. There are M sub-carriers, among which $N(< M)$ sub-carriers are occupied by the input data. In the time domain, the input symbol has symbol duration of T seconds and the symbol duration is compressed to $\tilde{T} = (N/M)T$ seconds after SC-FDMA modulation.

At the receiver, the received signal is transformed into the frequency domain via FFT processing and then the frequency domain equalization is applied to the de-mapped sub-carriers. After the equalization process, the signal is transformed into the time domain via IDFT processing, where detection and decoding takes place.

Depending on how DFT-spread symbols are mapped onto the sub-carriers in the IFFT block, SC-FDMA can be classified into two types: Localized SC-FDMA (LFDMA) and Distributed SC-FDMA (DFDMA). As shown in Figure 6-5, in LFDMA the DFT spread symbols are mapped onto consecutive points in the IDFT block, whereas, in DFDMA, the DFT spread symbols are mapped onto the entire bandwidth with zeros assigned to the unused sub-carriers. The case of $M = Q \cdot N$ for the distributed mode with equi-distance between occupied sub-carriers is called Interleaved FDMA (IFDMA) [HYUN06a].

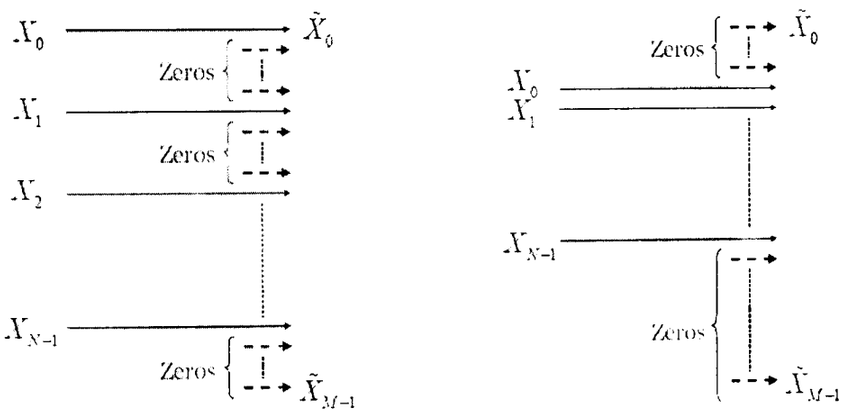

Figure 6-5: Sub-carrier Mapping modes: Localized and Distributed [HYUN06b].

The LFDMA can potentially achieve multi-user diversity in frequency selective fading if it assigns each user to sub-carriers in a portion of the signal band where that user has favourable transmission characteristics (high channel gain). Multi-user diversity depends heavily on independent fading among different transmitters. It also requires channel-dependent scheduling (CDS) of sub-carriers. CDS requires the system to monitor the channel quality as a function of frequency for each user terminal, and adapts sub-carrier assignment to changes in the channel frequency response of all the terminals. On the other hand, DFDMA/IFDMA, does not need to

rely on CDS in order to exploit the frequency diversity since each user is effectively spread over the entire signal band, and in this sense is more effective than LFDMA. However, since sub-carriers of different users are allocated adjacent to each other; it is more sensitive to frequency errors (eg. Frequency offset, Doppler spread), and also channel estimation becomes more challenging since coherency across the frequency domain is not available as in LFDMA.

Moreover, LFDMA with CDS has the potential for considerably higher capacity in terms of number of users than IFDMA [HYUN06a]. We therefore restrict the investigation herein to LFDMA based systems.

6.2.2.2 SC-FDMA System Model

Let $\mathbf{u}_i$ be the i^{th} block of transmitted data, which consists of N QPSK symbols. The first processing stage is the DFT spreading, which can be modelled by the linear DFT matrix $\mathbf{Q}$ of dimensions $N \times N$. The subsequent zero insertions and sub-carrier mappings can also be modelled as linear transformations on the DFT spread signal, which we denote as $\mathbf{M}$ sized $M \times N$. The remainder of the baseband processing stages at the transmitter are the IFFT and CP insertion, which are modelled by the linear matrices $\mathbf{F}^{-1}$ sized $M \times M$ and $\mathbf{T}_{CP}$ sized $(M + L + 1) \times M$, respectively. Thus following all these processing stages the transmit SC-FDMA signal is given as: $\mathbf{x}_i = \mathbf{T}_{CP}\mathbf{F}^{-1}\mathbf{M}\mathbf{Q}\mathbf{u}_i$.

Provided that timing is recovered accurately at the receiver, the received signal which contains complete observation of $\mathbf{u}_i$ is given as:

$$\mathbf{y}_i = \mathbf{H}_0\mathbf{x}_i + \mathbf{H}_1\mathbf{x}_{i-1} + \mathbf{n} \tag{6.11}$$

where $\mathbf{n}$ is a vector which contains samples of the Gaussian noise in the receiver's circuitry (zero mean and variances of σ^2). In (6.11) it is assumed that the channel is modelled as an FIR filter of $L + 1$ taps: $\mathbf{h} = [h(0),..h(L)]$, and $\mathbf{H}_0$ represents the $P \times P$ Toeplitz channel filtering matrix, which is given as:

$$\mathbf{H}_0 = \begin{bmatrix} h(0) & 0 & 0 & 0 & 0 \\ . & h(0) & 0 & 0 & 0 \\ h(L) & . & h(0) & 0 & 0 \\ 0 & h(L) & . & . & 0 \\ 0 & 0 & h(L) & .. & h(0) \end{bmatrix} \tag{6.12}$$

$\mathbf{H}_1$ models the edge effect caused by the excess delay spread of the propagation channel and results into ISI with the previously transmitted symbol $\mathbf{x}_{i-1}$.

$$\mathbf{H}_1 = \begin{bmatrix} 0 & .. & h(L) & .. & h(1) \\ .. & .. & 0 & h(L) & .. \\ 0 & 0 & 0 & 0 & h(L) \\ .. & .. & .. & .. & .. \\ 0 & 0 & 0 & .. & 0 \end{bmatrix} \tag{6.13}$$

The removal of the CP at the receiver can be modelled by a linear matrix: $\mathbf{T}_R = [\mathbf{0}_{K\times C}, \mathbf{I}_{K\times K}]$, which effectively also removes the second term in the summation in (6.11). Thus the resulting signal is given as:

$$\bar{\mathbf{y}}_i = \mathbf{T}_R \mathbf{H}_0 \mathbf{T}_{CP} \mathbf{F}^{-1} \mathbf{M} \mathbf{Q} \mathbf{u}_i + \mathbf{T}_R \mathbf{n} = \hat{\mathbf{H}} \mathbf{F}^{-1} \mathbf{M} \mathbf{Q} \mathbf{u}_i + \bar{\mathbf{n}} \tag{6.14}$$

The effect of the inclusion and removal of the CP is that the effective channel matrix $\hat{\mathbf{H}}$ has a circulant structure:

$$\hat{\mathbf{H}} = \begin{bmatrix} h(0) & 0 & .. & 0 & h(L) & .. & h(1) \\ .. & h(0) & .. & .. & 0 & h(L) & .. \\ h(L) & .. & .. & 0 & .. & 0 & h(L) \\ 0 & h(L) & .. & h(0) & 0 & .. & 0 \\ .. & 0 & .. & .. & h(0) & 0 & .. \\ 0 & .. & .. & h(L) & .. & h(0) & 0 \\ 0 & 0 & .. & 0 & h(L) & .. & h(0) \end{bmatrix} \tag{6.15}$$

A circulant matrix is defined by the first row only, and each row is obtained by cyclically shifting the previous row to the right. The most important property of circulant matrices is that all share the same set of singular vectors. Those singular vectors form the FFT matrix. In other words, any circulant matrix is diagonalised by the FFT matrix:

$$\mathbf{\Lambda} = \mathbf{F} \hat{\mathbf{H}} \mathbf{F}^{-1} \tag{6.16}$$

where $\mathbf{\Lambda} = diag(\lambda^0, \lambda^1, .., \lambda^{K-1})$ and λ^0 is the channel response at the i^{th} frequency bin and:

$$\mathbf{F} = \frac{1}{\sqrt{K}} \begin{bmatrix} 1 & 1 & 1 & .. & 1 \\ 1 & e^{-\frac{j2\pi}{K}} & e^{-\frac{j4\pi}{K}} & & e^{-\frac{j(K-1)2\pi}{K}} \\ 1 & e^{-\frac{j4\pi}{K}} & e^{-\frac{j8\pi}{K}} & & e^{-\frac{j(K-1)4\pi}{K}} \\ .. & .. & .. & .. & .. \\ 1 & e^{-\frac{j(K-1)2\pi}{K}} & e^{-\frac{j(K-1)4\pi}{K}} & .. & e^{-\frac{j(K-1)(K-1)2\pi}{K}} \end{bmatrix} \tag{6.17}$$

Thus following the FFT processing at the receiver the system input-output relationship becomes:

$$\bar{\bar{\mathbf{y}}}_i = \mathbf{F}\bar{\mathbf{y}}_i = \Lambda\mathbf{M}\mathbf{Q}\mathbf{u}_i + \mathbf{F}\bar{\mathbf{n}} \tag{6.18}$$

Following the FFT processing and channel estimation (using localized pilot tones transmitted in the short blocks), MMSE equalization is performed in the frequency domain[35] (prior to IDFT de-spreading). Denoting as $\hat{\lambda}_i$ the estimated channel response of the i^{th} sub-channel, the MMSE estimate of the signal sample on the i^{th} sub-carrier, is obtained as:

$$\hat{x}_i = \frac{\hat{\lambda}_i^*}{\hat{\lambda}_i\ \hat{\lambda}_i^* + \frac{1}{SNR}}\bar{\bar{y}}_i \tag{6.19}$$

where $\bar{\bar{y}}_i$ is the sample of the i^{th} sub-channel, following FFT. The MMSE equalization, although being effective in suppressing noise amplification compared to zero-forcing equalization, it introduces a small complication in calculating the channel reliability scaling on the soft demodulated signal, for Turbo decoding. This issue is discussed in more detail in Appendix G.

6.3 Air Interface Comparisons in the Forward Link

6.3.1 Performance Comparison between OFDM and HSDPA in the Forward Link of the Wideband Mobile Satellite Channel[36]

This section provides link-level simulation results on the performance of WCDMA (HSDPA) and OFDM, in the downlink of wideband mobile satellite system. The simulator was modified to include the hybrid terrestrial-satellite channel model shown in Figure 6-6. While the result provided within [ATTA05] were mainly in the form of throughput against E_c/I_{or} curves (for different scenarios), the simulation results presented in this section are in the form of BLER against E_b/N_0[37]. This change in the performance measure has been introduced because BLER against E_b/N_0 curves is a more typical measure of the link performance, particularly in OFDM based systems. Moreover the performance evaluations of HSDPA and OFDM, presented in this report, focus on the single transmission case (i.e. the HARQ protocol is de-activated), and as such the BLER performance provides a good measure of performance (compared to the multi-transmission case, where throughput is more suitable).

[35] Zero-Forcing equalization provided worse performance.

[36] Also applicable to S-DMB type systems.

[37] In the HSDPA simulator, E_b/N_0 cannot be defined directly as an input parameter. The methodology followed for defining E_b/N_0 values in the HSDPA simulator is described in Appendix E.

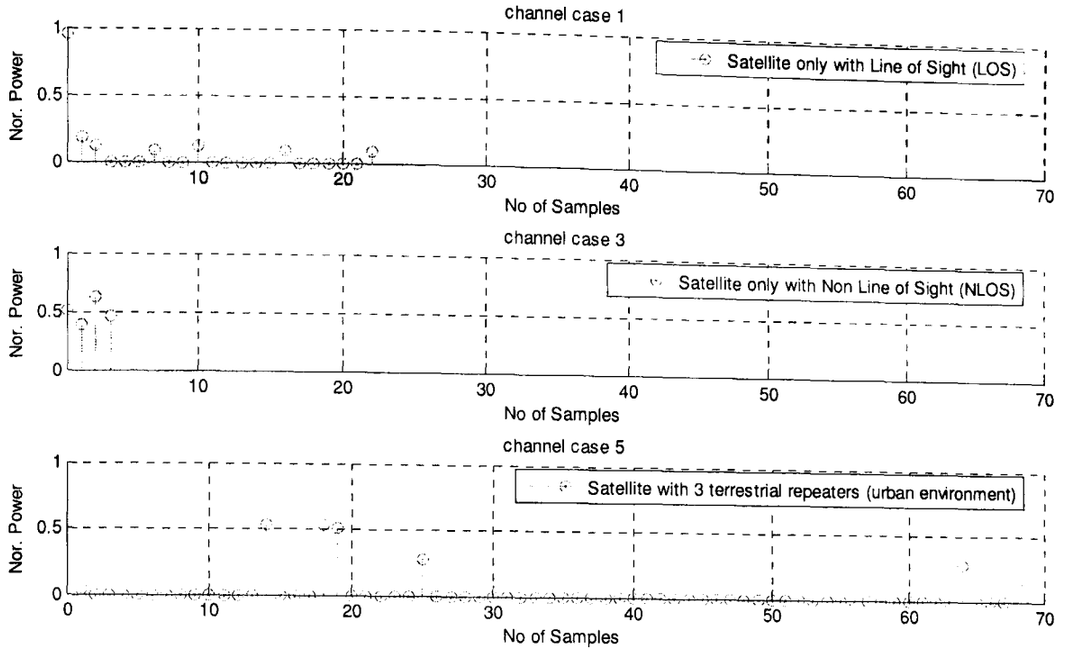

Figure 6-6: Multipath Power Delay Profile, representive for Integrated Terrestrial-Satellite System, Sampling Frequency=7.68 MSamples/sec[38]

Table 6-1: OFDM simulation Parameters (set 1 from 3GPP 25.892)

Parameters	Set 1
TTI duration (msec)	2
FFT size (points)	512
OFDM sampling rate (Msamples/sec)	7.68
Ratio of OFDM sampling rate to UMTS chip rate	2
Guard time interval (cyclic prefix) (samples/μsec)	56 / 7.29
Subcarrier separation (kHz)	15
# of OFDM symbols per TTI	27
OFDM symbol duration (μsec)	73.96
# of useful subcarriers per OFDM symbol	299
OFDM bandwidth (MHz)	4.485

For the simulation of OFDM, some parts of the HSDPA simulator (data multiplexing functions, receiver demodulator, pilot channel multiplexing and channel estimation functions) were modified based on [3GPP892] and described in Appendix D. The OFDM transmission parameters (FFT size, sampling rate, CP length, etc.) have been selected according to the reference parameter set 1 provided in [3GPP892], listed in Table 6-1. The vehicular speed was assumed to be 100km/h and this value applies for all results presented in this section.

[38] The delay spread of the channel will be reduced for lower sampling frequency.

Table 6-2: Information bit payload and code block sizes for each transport format assuming 10 WCDMA or OFDM data units allocated to a single user per 2 ms TTI [3GPP892]

Modulation	Code Rate	Information Bit Payload	24-bit CRC Addition	Code Block Segmentation	R=1/3 Turbo Encoding	Rate Matching
QPSK	1/3	3200	3224	1×3224	9684	9600
QPSK	1/2	4800	4824	1×4824	14484	9600
QPSK	2/3	6400	6424	2×3212	19296	9600
QPSK	3/4	7200	7224	2×3612	21696	9600
QPSK	4/5	7680	7704	2×3852	23136	9600
16QAM	1/3	6400	6424	2×3212	19296	19200
16QAM	1/2	9600	9624	2×4812	28896	19200
16QAM	2/3	12801	12825	3×4275	38611	19200
16QAM	3/4	14400	14424	3×4808	43308	19200
16QAM	4/5	15360	15384	4×3846	46200	19200

For comparing the two multiplexing techniques, coding and modulation parameters were chosen according to one of the test cases provided in Appendix A.1.3 in [3GPP892]. The specific details of the test scenario are highlighted on Table 6-2, where it is assumed that 10 parallel codes and 10 data units are allocated to a single user (per 2ms TTI) in WCDMA(HSDPA) and OFDM, respectively. In OFDM each 2ms TTI consists of 3 time slots, where each carries 9 OFDM symbols. The multiplexing of the QPSK data symbols across the available time-frequency resources (in OFDM) was described in Appendix D. It also describes the essential modifications primarily based on 3GPP 25.892, to the T-UMTS simulator in order to replace the WCDMA multiplexing (and related processing functionalities at the transmitter and receiver models) with OFDM multiplexing.

Before embarking on the presentation of the mobile satellite performance results, the performance of the OFDM simulator is validated against results produced independently by LG and the validated results are presented in Appendix F [3GPPLG].

6.3.1.1 Simulation Results – OFDM Vs. HSDPA

Figure 6-7 gives the performances of the two multiplexing techniques for different satellite channel profiles, by assuming no amplifier and perfect channel estimation. It is observed that OFDM performs better over the 'satellite only' channels, whereas WCDMA performs substantially better over the 'SAT+IMR' channel. This is due to the advanced rake receiver used in the HSDPA system which has a larger window length to be able to detect the delayed signals by assigning fingers (six fingers used) to them. These features of the rake receiver reduce the self-interference induced by the multipath channel and effectively exploit the multipath diversity. Furthermore, the extended cyclic prefix length showed approximately 2 dB gain (at BLER=10^{-3}) in the OFDM performance, which is still significantly below the HSDPA performance.

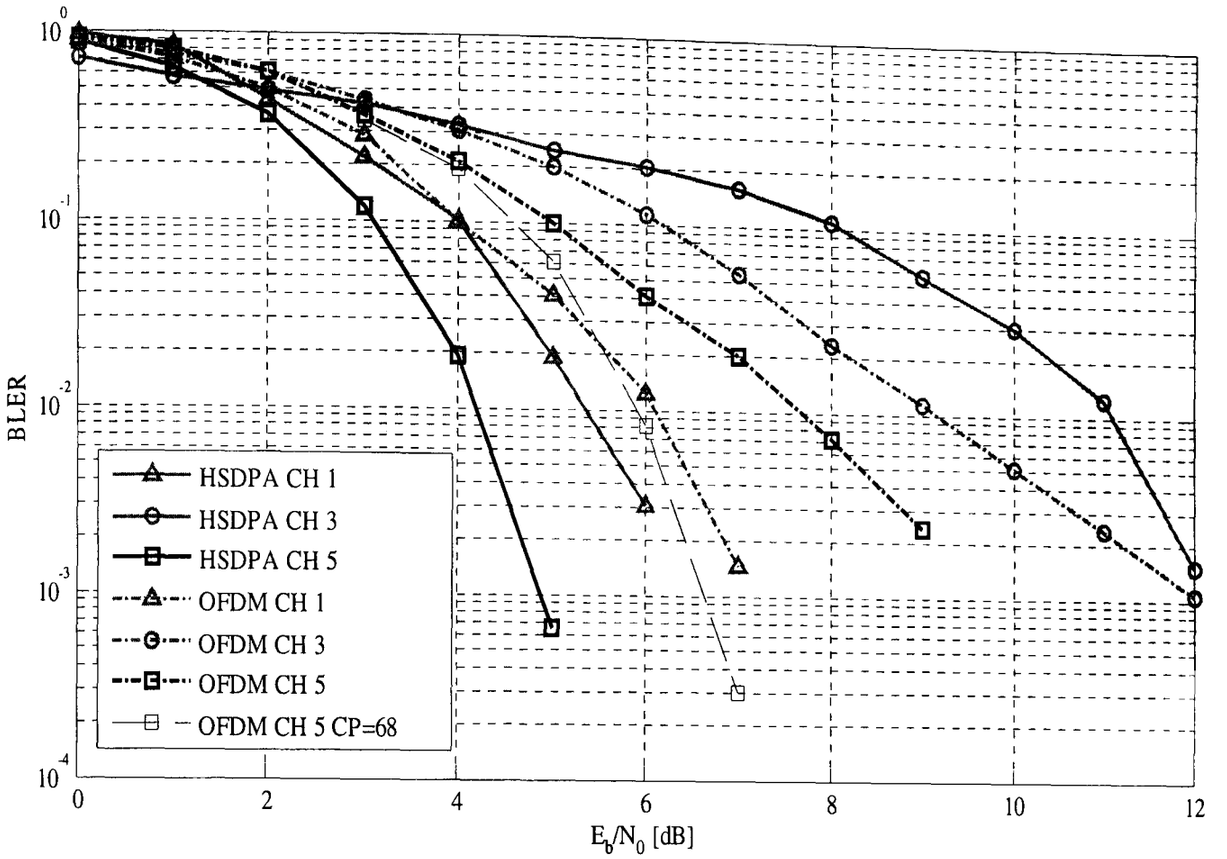

Figure 6-7: Performance of HSDPA and OFDM for different mobile channel profiles, assuming no amplifier distortion and perfect channel estimation

Table 6-3: Coherence Bandwidth/Time of the considered multipath channels

Channel Type	Mobile Velocity [Km/h]	Coherence BW [kHz]	Coherence Time[39] [ms]
Case '1'	100	366	1.7
Case '3'	100	2560	1.7
Case '5'	100	114	1.7

Figure 6-8 shows similar results to those in Figure 6-7, except for the assumption of realistic channel estimation. In the HSDPA simulation the common pilot channel is used for channel estimation, to which 10% of the total transmit power is allocated.

[39] Doppler frequency, $f_{d,max} = \frac{vf_c}{c} = \frac{100*3}{1.08} = 277.8$ Hz. Thus, coherence time $= \frac{0.4628}{277.8} = 1.7$ms

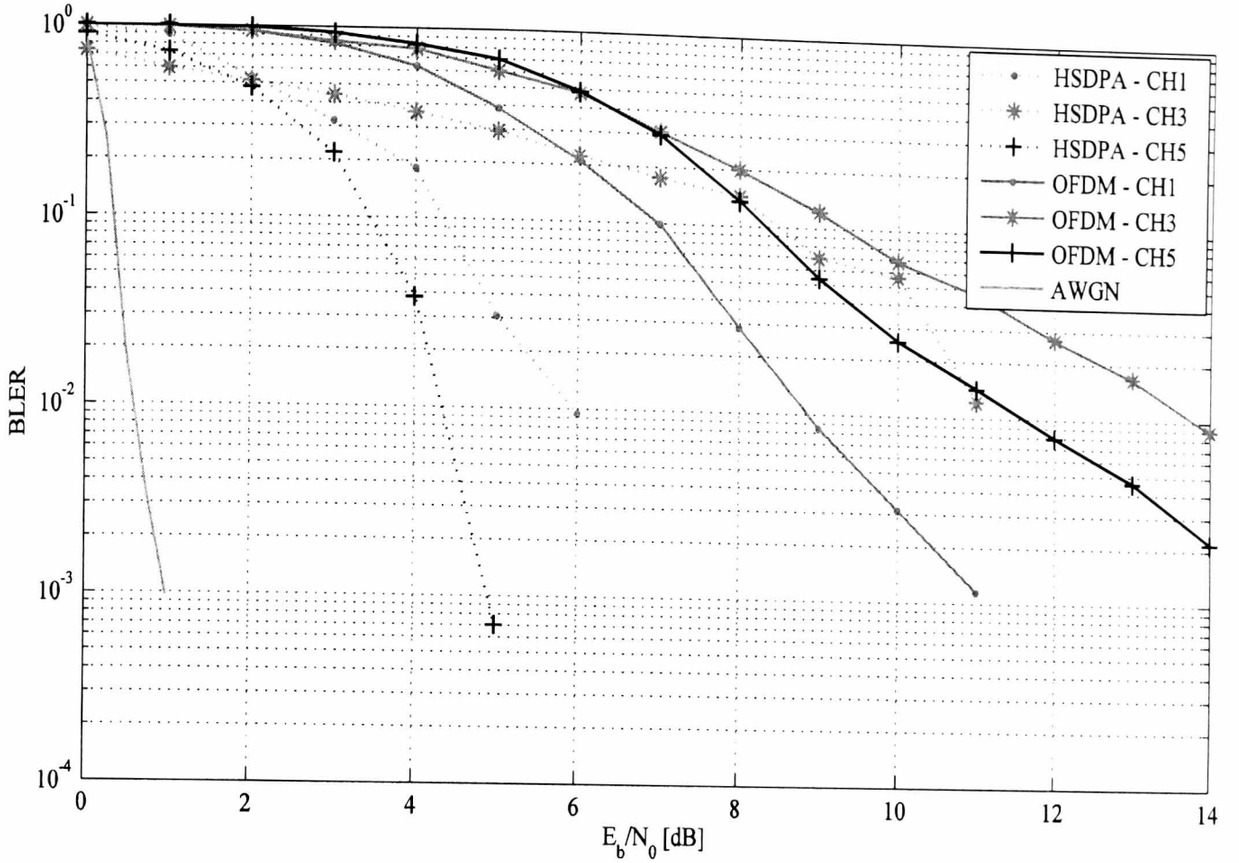

Figure 6-8: Performance of HSDPA and OFDM for different mobile channel profiles, assuming no amplifier distortion and pilot-based channel estimation

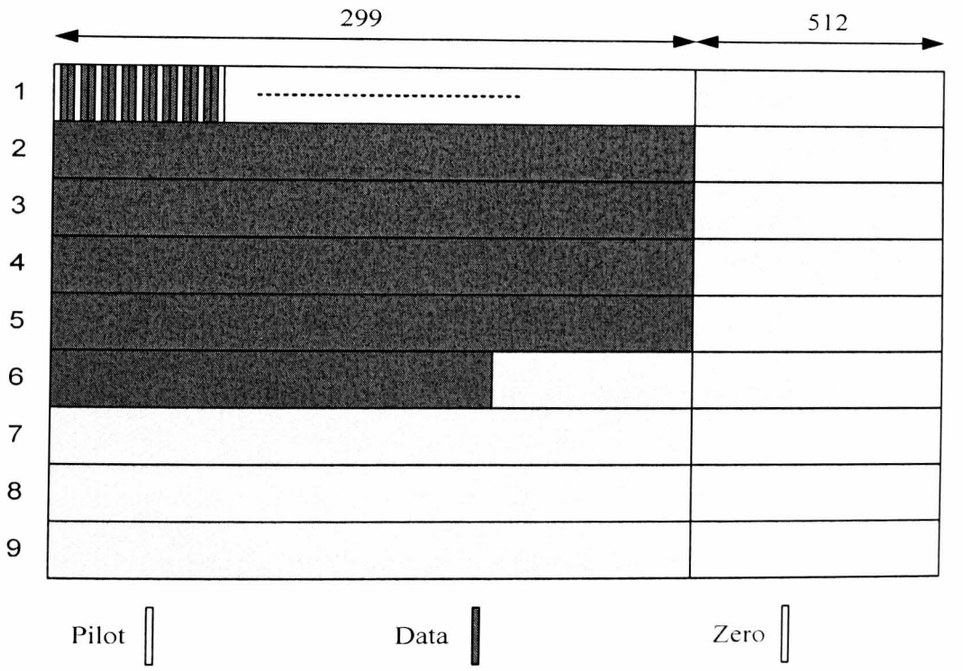

Figure 6-9: Slot Structure in OFDM with pilot tones

In OFDM, 100 pilot tones are placed in the first (frequency-domain) OFDM symbol in each slot[40]. The slot structure with pilot tones is shown in Figure 6-9. After the sub-channels which carry the pilots are estimated then interpolation is performed across the frequency domain for estimating the responses of the intermediate sub-channels. Since 1600 QPSK symbols are mapped in each slot, only the first 6 (out of the 9 available) OFDM symbols are used. The sub-channels are assumed to be fixed within the remaining five OFDM symbols in the slots which carry data. Thus the channel estimates, obtained for the first symbol are re-used directly for equalizing the remaining symbols in the block. This estimation approach across the time dimension is consistent with the coherence time of the radio channel for the particular carrier frequency and vehicular speed. In particular the coherence time of the channel is approximately 1.7ms, whereas the time separation between the first and sixth symbol in the slot is about 0.4ms. The overhead introduced by the pilot tones in OFDM is less than 6%, and 10% of the total power is allocated to the pilot channel.

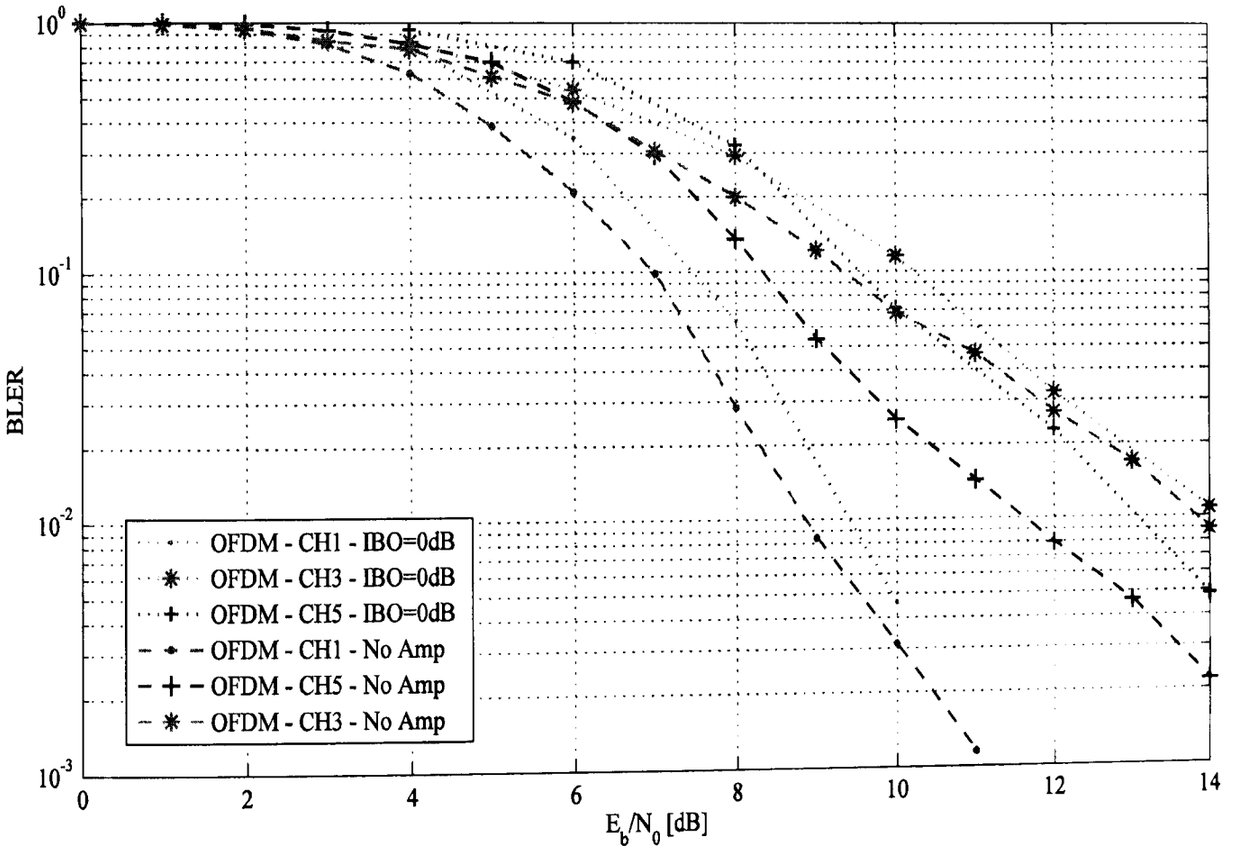

Figure 6-10: Performance of OFDM for different mobile channel profiles, assuming amplifier distortion and pilot based channel estimation

[40] Pilot locations in frequency domain = {1,4,7,10, ...,295,298}.

The results show that HSDPA suffers only small performance degradation, relative to the perfect channel estimation case. On the other hand the performance of OFDM is severely degraded with the pilot-based channel estimation (up to 5dB). It is thought that this large performance degradation is due to the inherent lack of averaging in the frequency domain channel estimation. More precisely, each estimate relies on a single (noisy) observation and thus the estimation errors are characterized by large variances.

Another important point is that, the design of the pilot sequence plays an important role in the performance of OFDM, when the non-linearity is applied. If the pilot tones are given fixed values, this results in a large magnitude periodic pattern, following the IFFT processing. As the amplifier compresses these signals a large proportion of energy in the pilot channel is lost and this leads to very poor estimation performance. Thus it is important that the pilot pattern is characterized by low PAPR following in the time domain. In the simulation a random pilot sequence was used, and thus improved results can be obtained (in the presence of the non-linearity), through a more elaborate design of the pilots.

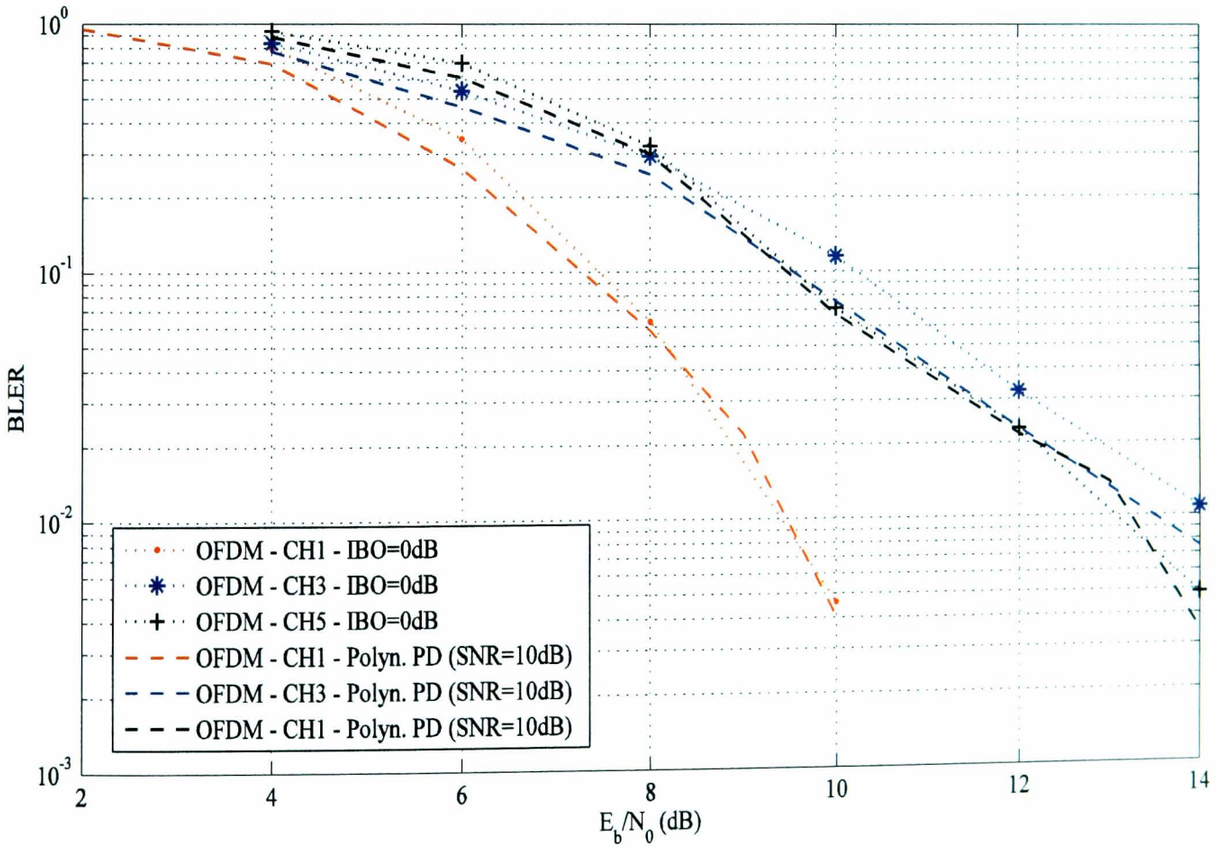

Figure 6-11: Performance of OFDM for different mobile channel profiles, assuming amplifier distortion, pilot based channel estimation and 3rd order polynomial pre-distortion

Figure 6-10 shows the performance of OFDM with the amplifier non-linearity and with realistic channel estimation. The relatively small performance degradation introduced by the non-linearity is explained by the large number of null sub-carriers in each OFDM symbol. In effect the IFFT processing spreads the total power, which is concentrated in the 299 active sub-carriers, across 512 time samples. This results in reduced average time domain power, and in effect the amplifier is driven 'naturally' at about 2.3dB below the saturation point. Figure 6-11 examines the effect of the 3rd order polynomial pre-distorter under the same assumptions. It is observed that in this case the pre-distorter does not yield any performance benefits, except for channel case 3, in which approximately 0.5dB are gained.

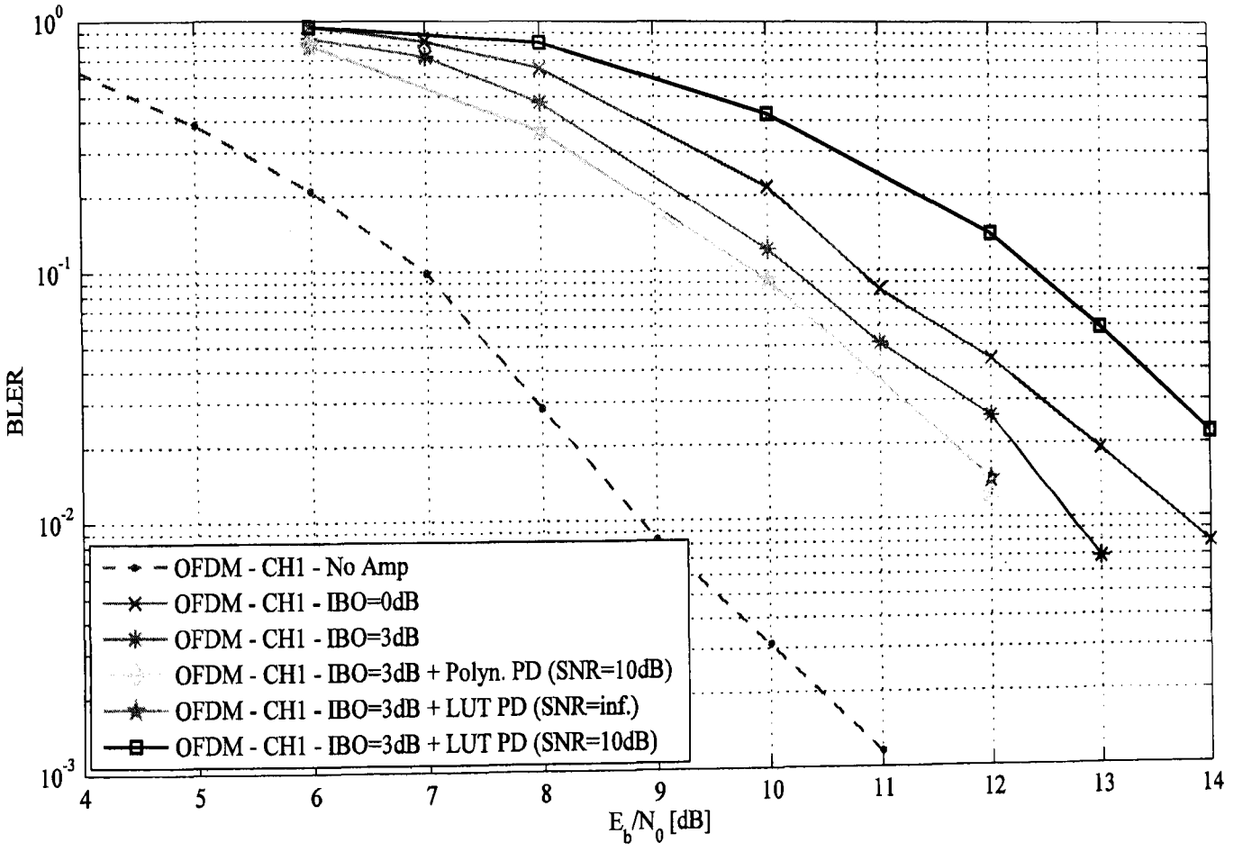

Figure 6-12: Performance of OFDM for channel profile 1, by normalizing the saturation point of the amplifier at the average power of the time domain signal

Figure 6-12 examines the performance of OFDM in channel profile 1, by normalizing the saturation point of the TWTA at the average power of the time domain samples (after IFFT). Thus in this case the 2.3 dB back off introduced by the zero sub-carriers is (artificially) removed so that the average power of the time-domain signals is at the saturation point of the amplifier. It is observed that under these assumptions the amplifier substantially degrades the link performance: up to 5dB with IBO= 0dB. By applying an input back-off of 3dB, the performance is improved by 0.5dB-1dB.

The effect of pre-distortion on the link performance is also shown in Figure 6-12. In particular both the 64-element LUT and 3rd order polynomial pre-distorters were simulated. It can be seen that the combination of the 3rd order polynomial pre-distortion and 3dB IBO, yields a further performance improvement by about 0.5-0.6dB (even by assuming that training is performed in relatively poor SNR conditions (10dB)). On the other hand the LUT pre-distorter provides a similar gain only when it is assumed that training was performed in noiseless conditions. When the SNR in the feedback channel is assumed to be 10dB, in the training stage of the LUT, then the LUT pre-distorter considerably degrades the overall link performance. These results are consistent with the simulation results presented in section 2, which showed that the adaptation of the LUT becomes unreliable when noise is applied in the received training sequence.

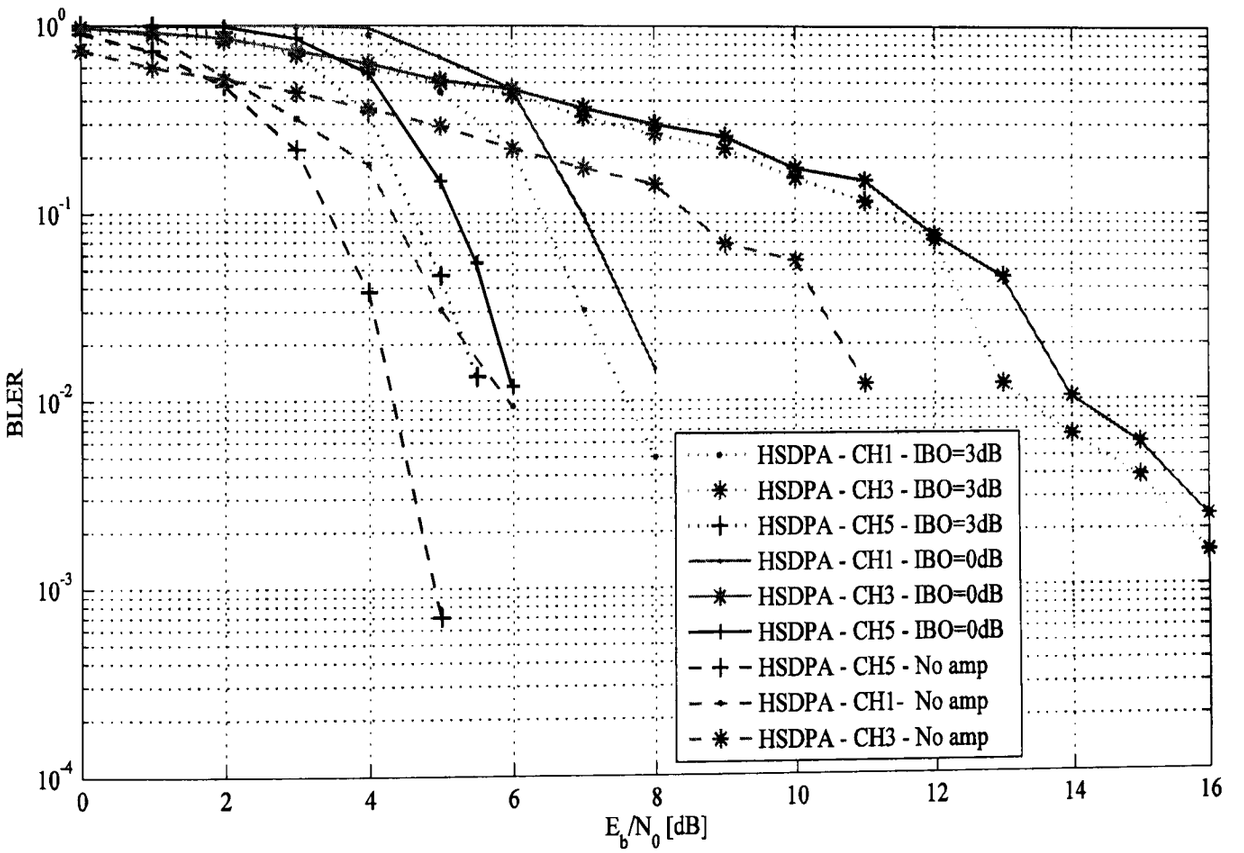

Figure 6-13: Performance of HSDPA, assuming amplifier distortion and pilot-based channel estimation for IBO of 0dB and 3dB

Figure 6-13 illustrates the performance of HSDPA in the presence of the amplifier non-linearity and realistic channel estimation, for IBO of 0dB and 3dB. It is observed that in HSDPA the amplifier introduces a more moderate performance degradation compared to OFDM, when both techniques are assumed to drive the amplifier at the saturation point. In particular in HSDPA the

degradation is in the order of 2dB with IBO= 0dB and applying 3dB IBO gives an improvement of 0.3-0.4dB. On the other hand OFDM shows more resilience to the non-linearity when the effect of zero sub-carriers is not normalized (Figure 6-10).

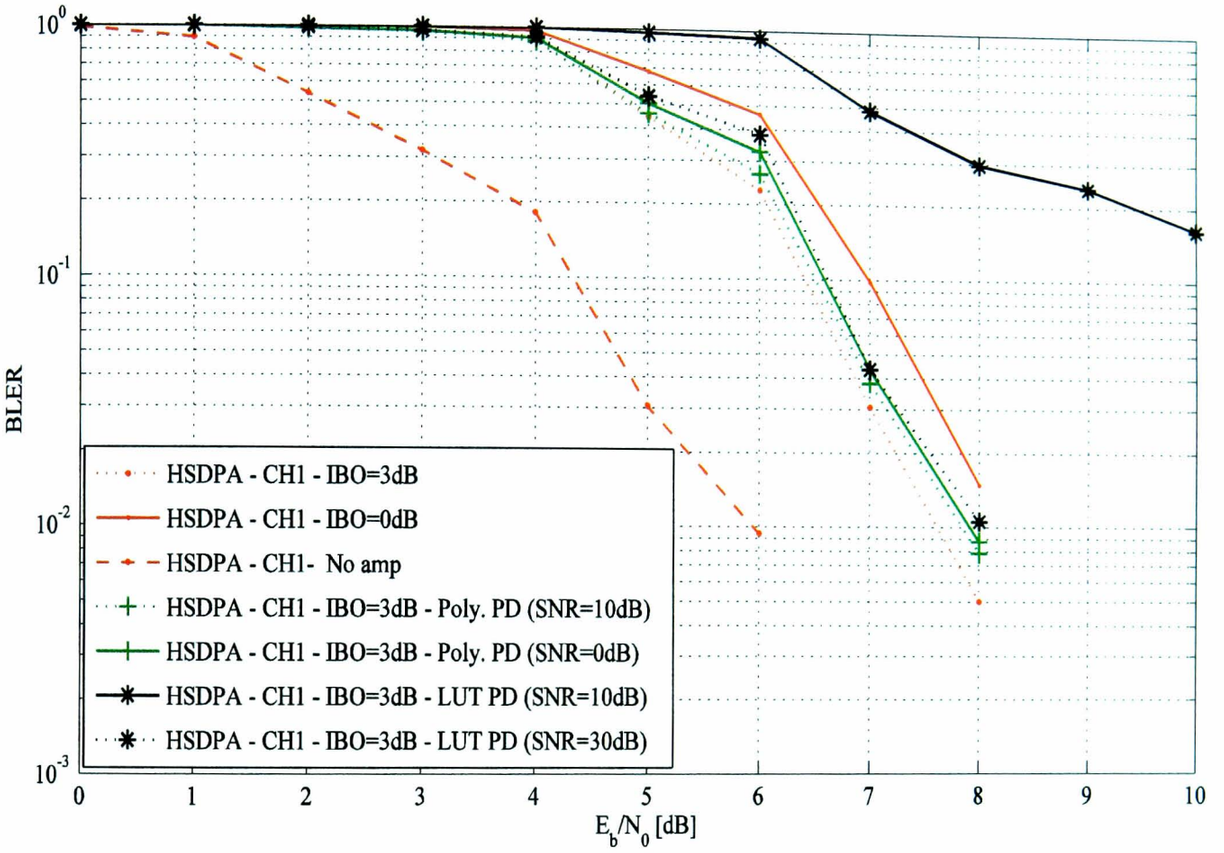

Figure 6-14: Performance of HSDPA for Channel Profile 1, assuming amplifier distortion, pilot-based channel estimation and Digital Pre-distortion

Figure 6-14 shows the impact of digital pre-distortion on the performance of HSDPA for channel profile 1 (satellite only). It is first observed that with the particular back-off level the linearizer does not offer any performance improvements, relative to without pre-distortion and IBO= 3dB. This can be explained by the fact that the amplifier's output back-off is about 1.5-2dB when the input back-off is 3dB, and thus there is some power benefit when the amplifier is not linearised. These results suggest that the back-off level needs to be carefully calibrated in order to maximize the performance benefits of the pre-distorter.

The second point to be noted from Figure 6-14 is that (as in OFDM) the polynomial pre-distorter performs robustly even with very low SNR in the feedback channel (during the training phase of the pre-distorter). On the other hand the LUT pre-distorter performs poorly even with a moderate

SNR level (10dB) and it requires higher SNR levels in order to approach the performance of the polynomial pre-distorter

6.3.2 As an Alternative to OFDM for S-DMB: Single-Carrier Frequency Domain Equalization (SC-FDE)

6.3.2.1 Performance Comparison of SC-FDE and OFDM for the S-DMB System

The performance of the SC-FDE and OFDM based S-DMB systems have been evaluated through simulations. Table 6-4 summarizes the selected system parameters. It can be observed that the power amplifier has been assumed to be perfectly linearized over its operating region. Hence the only distortion which takes place is on instantaneous signal samples, which 'enter' the saturation region (IBO>0dB) and are normalized to a power of 0dB. This setup can be considered as equivalent to ideal pre-distortion. It is noted that in the SC-FDE system the power of the transmit sequence is constant, hence only one point on the power amplifier is operated. In the SC-FDE system linear MMSE equalization is applied. It is also pointed out that in order to make the comparison between the two techniques as fair as possible, in the OFDM system all 512 sub-carriers have been assumed to carry useful data.

Table 6-4: Simulation Parameters

Parameter	Assumption/Value
Information Block Size	4800 bits
Coding	1/3 Turbo [5,7]
Modulation	QPSK
FFT/IFFT size	512
Number of FFT Blocks per Frame	15
CP Length	56 samples
Symbol Rate	7.68Ms/s
Vehicle Speed	100Km/h
Channel Power Delay Profile	Case 6 [Appendix A]
Turbo Decoding	Log-MAP (8 iterations)
Power Amplifier	Perfect Linearization over Operating Region
Channel Estimation	Perfect
Timing/Frequency Synch.	Perfect

Referring to Figure 6-15, it is observed that without the power amplifier's non-linearity, OFDM performs about 0.5-1dB better than SC-FDE. With the amplifier present however and 0dB back-off, SC-FDE provides a 2dB benefit. The performance of the two systems becomes approximately the same when 3dB back-off is applied in the OFDM system. Therefore, at least for this ideal linearization case, SC-FDE allows the amplifier to be driven at saturation, whereas OFDM requires some back-off in order to perform at the same level.

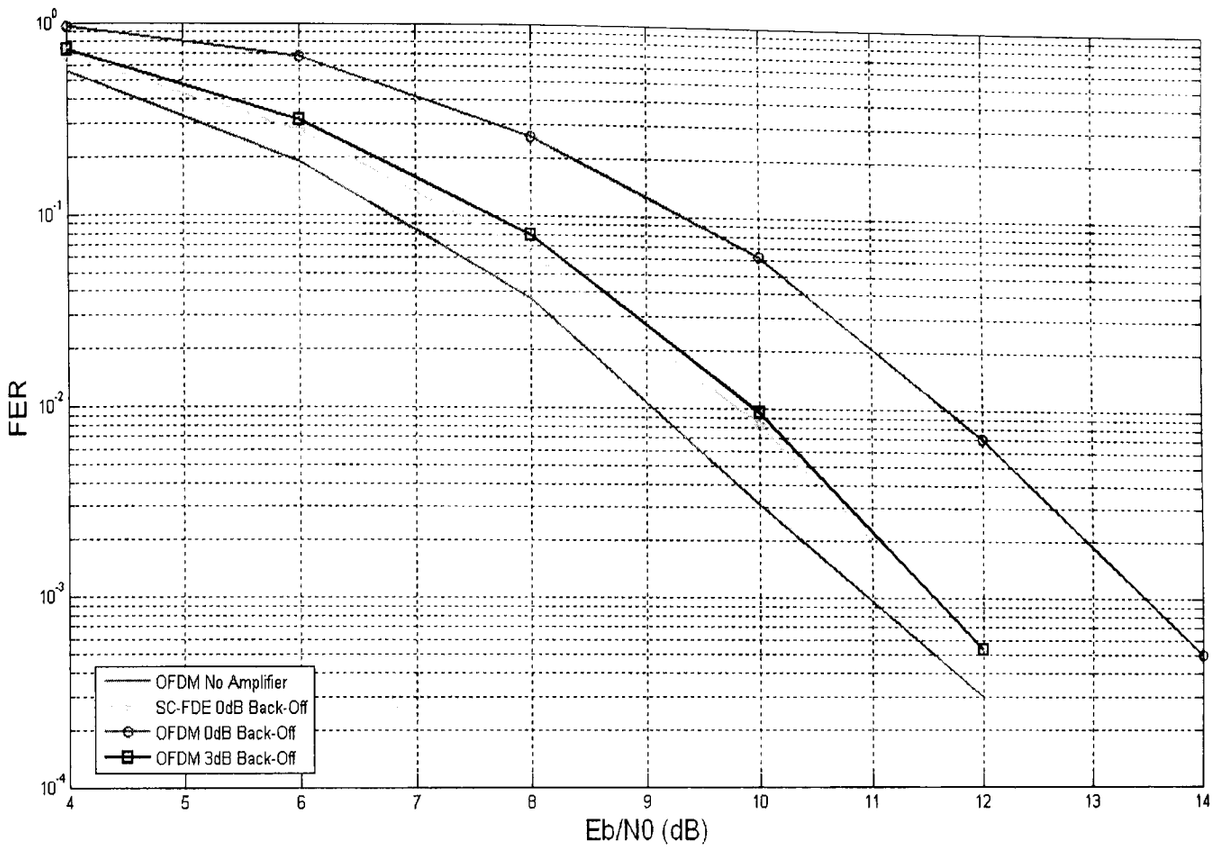

Figure 6-15: Performance comparison between OFDM and SC-FDE based S-DMB System-Channel case 6.

6.4 Air Interface Comparisons in the Return Link[41]

6.4.1 Performance Comparison between SC-FDMA and HSUPA in the Return Link of the Wideband Mobile Satellite Channel

This section presents simulation results for evaluating and comparing the performance of HSUPA and SC-FDMA in the return-link of the wideband satellite channel. The simulations have been based on a detailed (C++) link-level (T-UMTS) HSUPA simulator, which was modified for the purposes of this study; for modelling the hybrid satellite-terrestrial environment (satellite channel profiles and TWTA). Additionally, the power control function was disabled in the HSUPA simulator in order to produce BLER against E_b/N_0 curves. The HSUPA simulator diagram is presented in Appendix C with its important features summarized. In addition, a new link-level SC-FDMA simulator based on 3GPP 25.814 was developed using MATLAB software.

[41] Applicable only to Long Term Evolution Satellite systems.

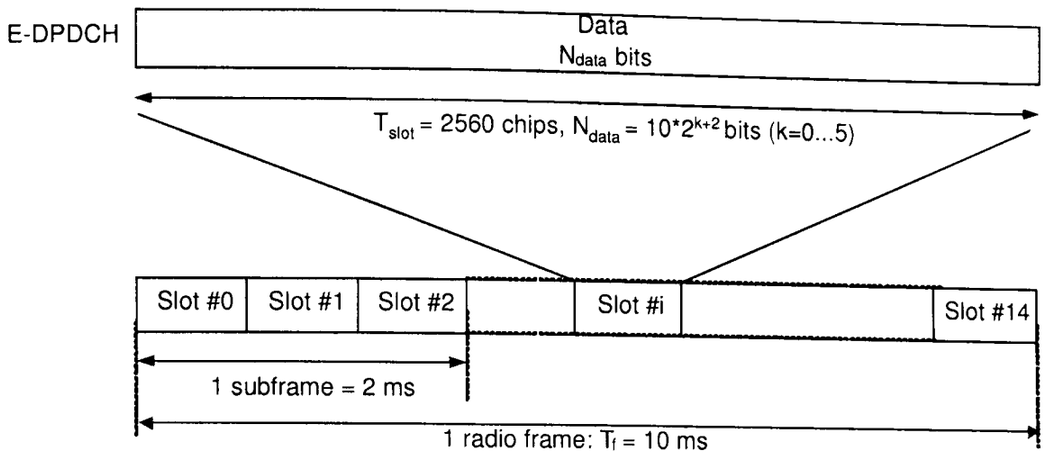

Figure 6-16: E-DPDCH Frame Structure [3GPP896]

Table 6-5: Transmission Parameters Used in the WCDMA (HSUPA) Simulations [3GPP896]

Transport Block Size	Number of Code Blocks	Modulation	OVSF Code	Code Rate	β_c	β_{eu}	Rate after 2 Tx (kbps)
320[1]	1	QPSK	C(4,1)	0.33	15	11	16
640[1]	1	QPSK	C(4,1)	0.33	15	15	32
1280[1]	1	QPSK	C(4,1)	0.33	15	21	64
1920[1]	1	QPSK	C(4,1)	0.33	15	27	96
2560[1]	1	QPSK	C(4,1)	0.33	15	30	128
5120	2	QPSK	C(4,1)	0.33	15	42	256
7680	2	QPSK	C(4,1)	0.40	15	53	384
10240	3	QPSK	C(4,1)	0.53	15	60	512
12800	3	QPSK	C(2,1)	0.33	15	67	640
15360	4	QPSK	C(2,1)	0.40	15	75	768
17920	4	QPSK	C(2,1)	0.47	15	84	896
20480	5	QPSK	C(2,1)	0.53	15	95	1024

[1] Repetition has been used to achieve the given data rates

Concerning the simulation of HSUPA, a 10 ms TTI was used in the HSUPA simulator, although a 2ms TTI is also supported in the standard [3GPP808]. The structure of the Enhanced Dedicated Physical Data Channel (E-DPDCH), which is defined for carrying data in HSUPA, is shown in Figure 6-16. The Enhanced Dedicated Physical Control Channel (E-DPCC), which for the purposes of the simulator is used for channel estimation, is transmitted in parallel to the E-DPDCH, and also has the same framing structure. In particular, following spreading, the E-DPCC chips are mapped onto the orthogonal component of the QPSK signal, while E-DPDCH chips are mapped onto the in-phase component. In the simulations the total transmitter power is assumed to be equally divided between the two channels.

The simulated transmission parameters, which are highlighted in Table 6-5, were selected according to one of the evaluation cases described in section A.2.2.2 in [3GPP896]. As in the

forward link simulations, a single transmission was assumed in the simulations, and thus the HARQ protocol was deactivated.

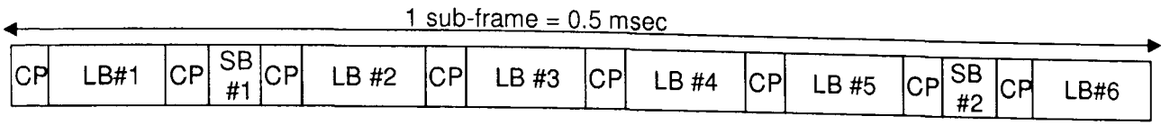

Figure 6-17: Sub-Frame Format in SC-FDMA with two Short Blocks per Sub-Frame [3GPP814]

For the simulation of SC-FDMA, the sub-frame format and transmission parameters defined in [3GPP814] were adopted. The sub-frame format is illustrated in Figure 6-17; each sub-frame consists of 6 long blocks that are obtained after the IFFT processing and the CP insertion. Two short blocks, used for carrying reference signals, are multiplexed in-between the long blocks, as shown in Figure 6-17. According to [3GPP814], the minimum TTI duration is equal to a single sub-frame, 0.5ms.

Table 6-6: Transmission Parameters used for the simulation of SC-FDMA

Parameter	Value
Assumed Spectrum Allocation	5MHz
Symbol Rate	7.68MS/s
Sub-Frame Duration	0.5ms
Long Block Size (microsecond/ Number of occupied	66.67/300/512
Short Block Size (microsecond/ Number of occupied	33.33/150/256
CP duration	(4.04/31) x 7 (i.e. for the 7 out of 8 blocks in the sub-frame)
Sub-Carriers per Resource Unit	25 (6 Resource Units per Long Block)
Resource Unit Mapping Type	Localized
Points in the DFT Spreading	25
Reference Signal Structure for Uplink Channel	Localized sub-carriers (carried by the short-blocks)

Table 6-6 gives the reference parameters that are used for the simulation of SC-FDMA. Coding and modulation parameters were selected as for HSUPA (QPSK, code rate 1/3[42] and transport block size of 2560 bits). It is noted that depending on the Resource Units (RUs) allocated to a single user, several SC-FDMA sub-frames might be required to transmit a single transport block. This is in contrast to HSUPA where it is assumed that the whole block is transmitted within a single TTI.

[42] In fact the code rate in the simulated scenario is 0.266, where the additional redundancy is obtained through repetition, as specified in section A.2.2.2 in [3GPP896].

6.4.1.1 Return-Link Simulation Results in the Wideband Mobile Satellite Channel - SC-FDMA Vs. HSUPA

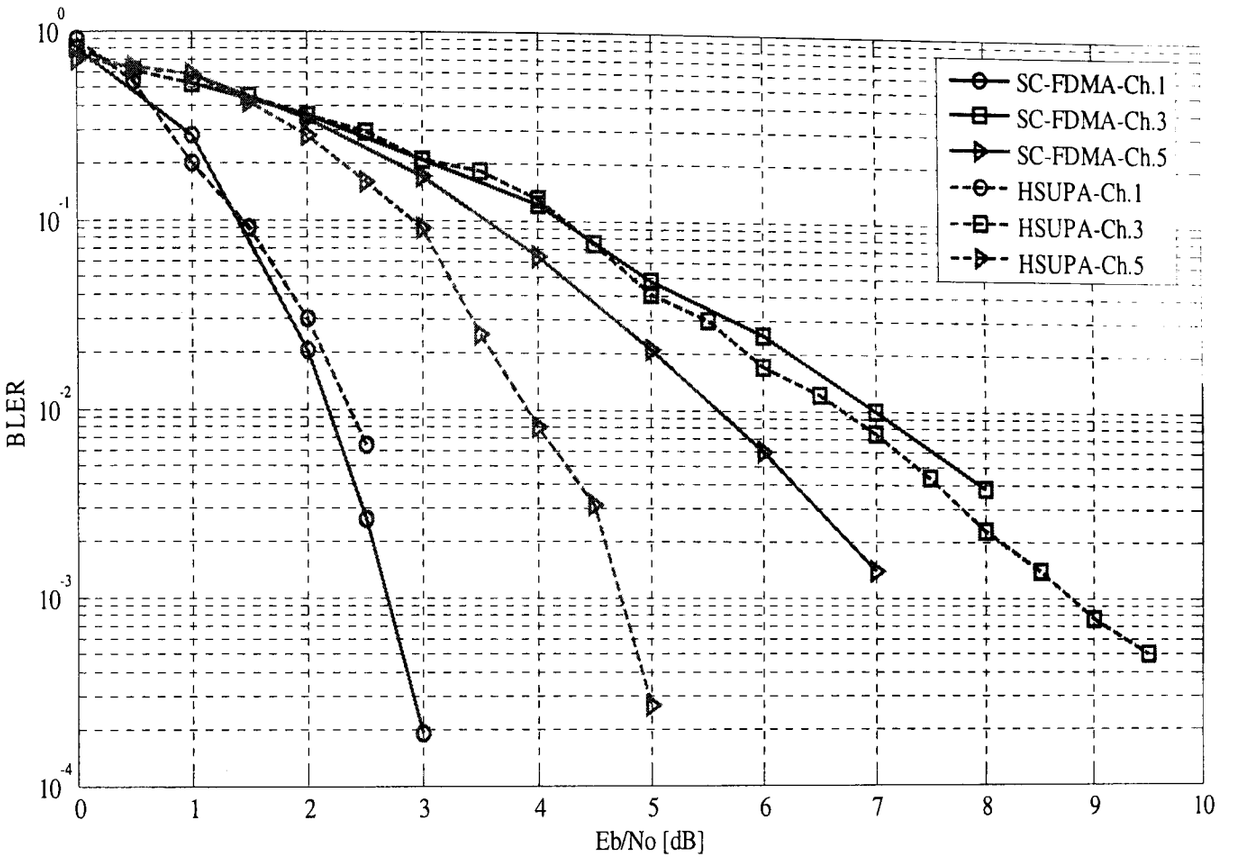

Figure 6-18: Performance of HSUPA and SC-FDMA for different mobile channel profiles, assuming no amplifier distortion and perfect channel estimation

Figure 6-18 shows the performance of WCDMA (HSUPA) and SC-FDMA in different satellite channel profiles, assuming no amplifier distortion and perfect channel estimation. Moreover, in this simulation scenario it is assumed that the complete transmit power is allocated to data (i.e. no power is allocated to the pilot channels), and also a vehicular speed of 100km/h[43] was specified.

For the simulation of SC-FDMA it was assumed that a single user is allocated a single resource unit (of 25 sub-carriers) per OFDM symbol. Thus 26 sub-frames are required in order to transmit a complete transport block. This benefits the turbo decoder since different parts of the block experience uncorrelated mutipath fading. As shown in Figure 6-18 three satellite channel profiles were simulated. 'Channel 1' and 'Channel 3' model satellite-only channels, whereas 'Channel 5' models the combination of satellite and three terrestrial repeaters (urban environment); their power delay profile is shown in Figure 6-6. It is observed that both techniques provide

[43] This value applies to all results presented in this section.

approximately the same performance over the 'satellite-only' channel profiles. HSUPA performs better over the combined 'satellite+repeater' profile. This result is not very surprising, since the rake receiver (which was allowed to have 6 fingers) is able to detect long delayed channel taps and allocated a finger to them. On the other hand the SC-FDMA receiver is limited by the CP length, which for Channel 5 is significantly shorter than the maximum excess delay spread of the channel.

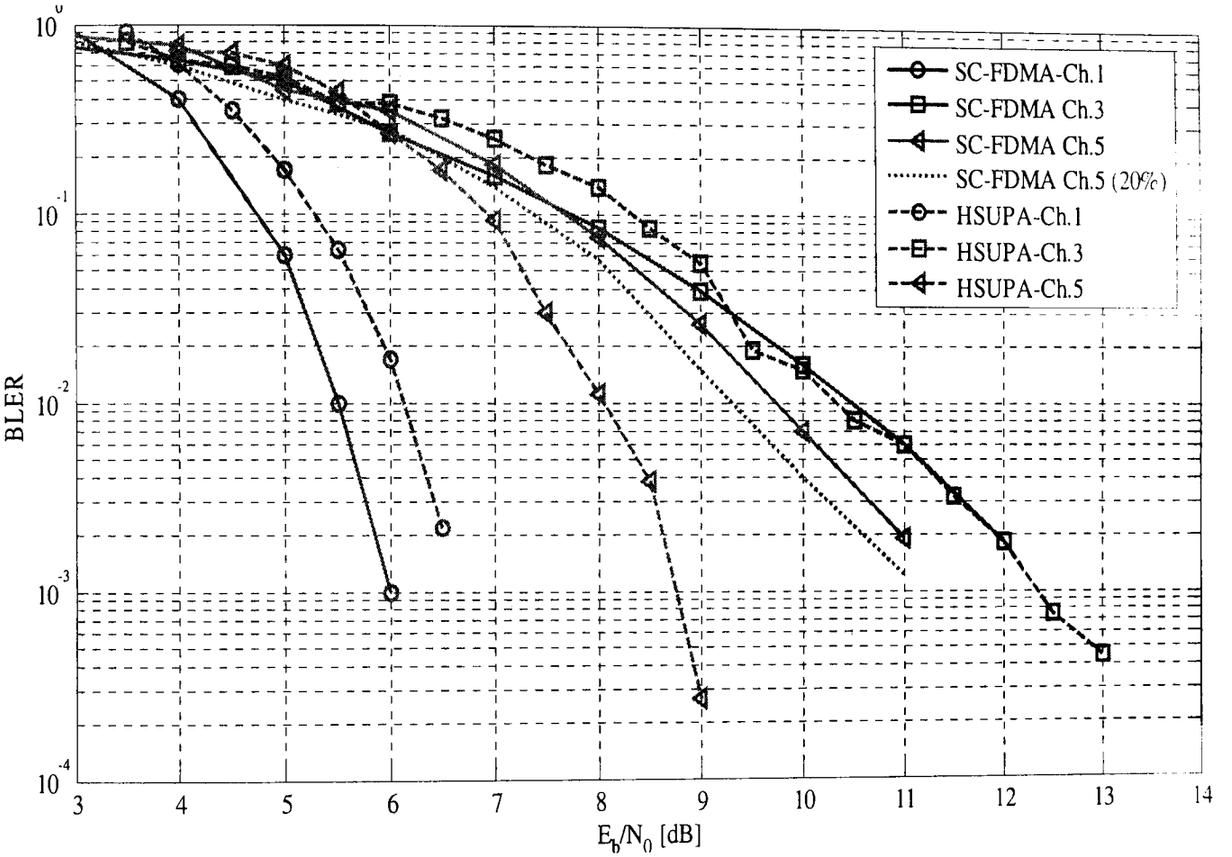

Figure 6-19: Performance of HSUPA and SC-FDMA for different mobile channel profiles, assuming no amplifier distortion and pilot-based channel estimation

Figure 6-19 gives analogous results, but in this case realistic (pilot-based) channel estimation is assumed. As explained previously, in HSUPA 50% of the available power is allocated to the E-DPCC (as recommended in the HSUPA standard [3GPP896]) and thus there is automatically a 3dB deficit in the link performance. On the other hand in SC-FDMA 26 pilot tones (and 150 data symbols) were transmitted per sub-frame (~1/7), and the power allocation (between data and pilots) was also kept at this proportion. Although in HSUPA the channel estimates are more reliable than in SC-FDMA (due to the higher power allocated to the pilot channel and the noise averaging effect, which is not present in the SC-FDMA channel estimation algorithm), the overall

performance of the two techniques is analogous to the perfect channel estimation scenario. Figure 6-19 also provides a curve of SC-FDMA over Channel 5, which corresponds to increasing the power allocated to the pilots from 14% to 20%. It is observed that this provides a small performance improvement. In general, it is commented that the interpolation type channel estimation approach does not provide good accuracy, because each sub-channel estimate relies on a single sample. Alternative channel estimation approaches could yield improved performance in SC-FDMA.

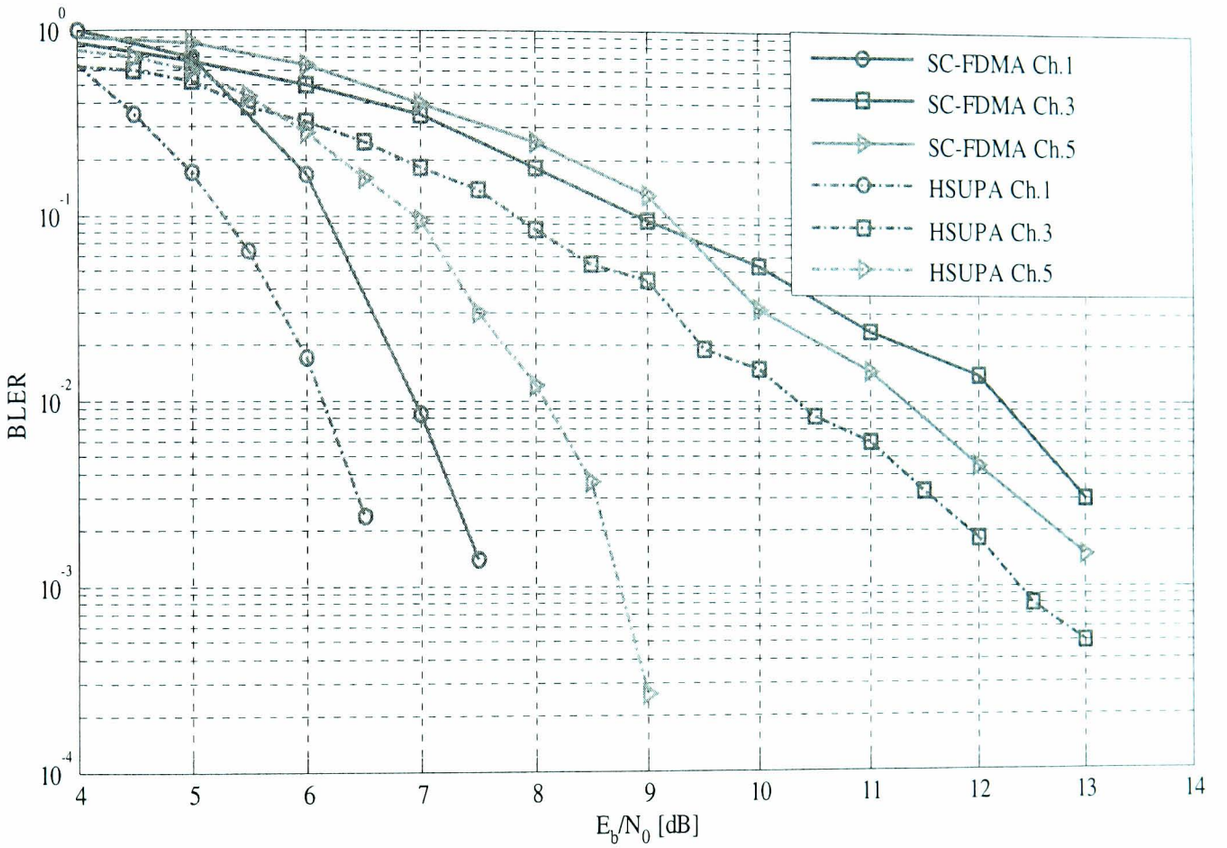

Figure 6-20: Performance of WCDMA and SC-FDMA for different mobile channel profiles, with amplifier distortion (0dB IBO) and pilot-based channel estimation

Figure 6-20 compares the performances of the two techniques in the presence of the TWTA non-linearity and IBO of 0dB. Realistic (pilot based) channel estimation was applied for these simulations. It is first pointed out that in the HSUPA simulator only a single user is transmitting at each time, and also in the simulated scenario only a single code is used. This means that there is no superposition of the signals in the code/user domains and thus the transmit signal samples have deterministic amplitudes; fixed at 0dB. Thus, the amplifier is driven consistently at IBO=0dB, and thus only a fixed phase shift of 47 degrees is introduced by the TWTA. Thus, as far as the in-band distortion is concerned, it can be corrected almost perfectly through channel estimation. This is

demonstrated by the simulation results, as the HSUPA results are almost identical to those presented in Figure 6-19 (no amplifier case).

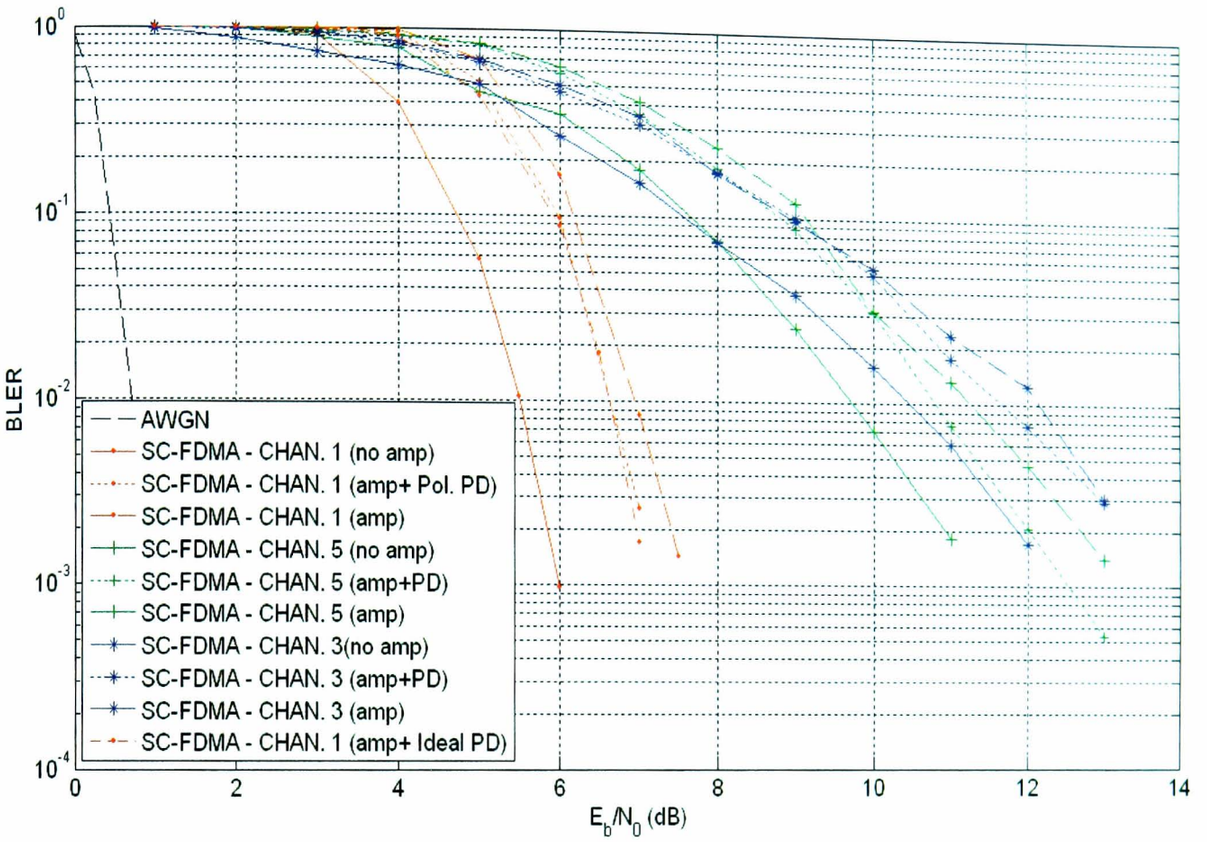

Figure 6-21: Performance of HSUPA and SC-FDMA for different mobile channel profiles, with amplifier distortion (0dB IBO, Polynomial Pre-distortion and pilot-based channel estimation

On the other hand, in the SC-FDMA technique there is a significant variation in the amplitudes of the signal samples (due to the IFFT processing) and this results in some performance degradation compared to the results of Figure 6-19 (in the order of 1.5-2dB). Figure 6-21 illustrates the performance of SC-FDMA when a third order polynomial (assuming 10dB SNR in the feedback channel) is used for compensating the amplifier non-linearity, for the three channel satellite channel profiles. The IBO was again set at 0dB[44] . It is observed that the pre-distorter yields only a small performance advantage (0.3-0.7dB). This result suggests that the performance degradation is primarily due to the saturation region of the amplifier which cannot be compensated by the pre-distorter. It can also be concluded, based on this result that pre-distortion does not bring any significant advantage to the link performance, since the non-linearity is effectively mitigated to a large extend through channel estimation and strong channel coding. Figure 6-21 also shows the performance of SC-FDMA when an ideal pre-distorter is used (perfectly linear operating region).

[44] An IBO of 3dB (without pre-distortion) was also simulated but it did not provide noticeable performance improvements relative to the IBO=0dB case.

It is observed that the performance of the polynomial pre-distorter is very close to the performance of the ideal pre-distorter and thus no additional performance improvements can be expected by practical pre-distortion techniques.

An important point to be noted, from Figure 6-20 and 6-21, is that the performance of SC-FDMA, in the presence of the non-linearity, depends heavily on the structure of the pilot sequences used for channel estimation. In particular if the selected sequence is characterized by high PAPR in the time domain (after IFFT), then a large proportion of its energy is saturated by the TWTA, and this results in poor channel estimation and substantially degraded link performance. Therefore careful design of the pilots will lead to limited performance losses due to the amplifier's non-linearity. For the results presented in Figure 6-20, several pilot sequences were generated randomly in the frequency domain, and the one which provided the best link performances was retained for further simulations in Figure 6-21. Obviously this approach does not provide optimal selection of the pilot sequence, and thus the results presented in Figure 6-20 and 6-21 can be improved through better selection of the pilot sequence.

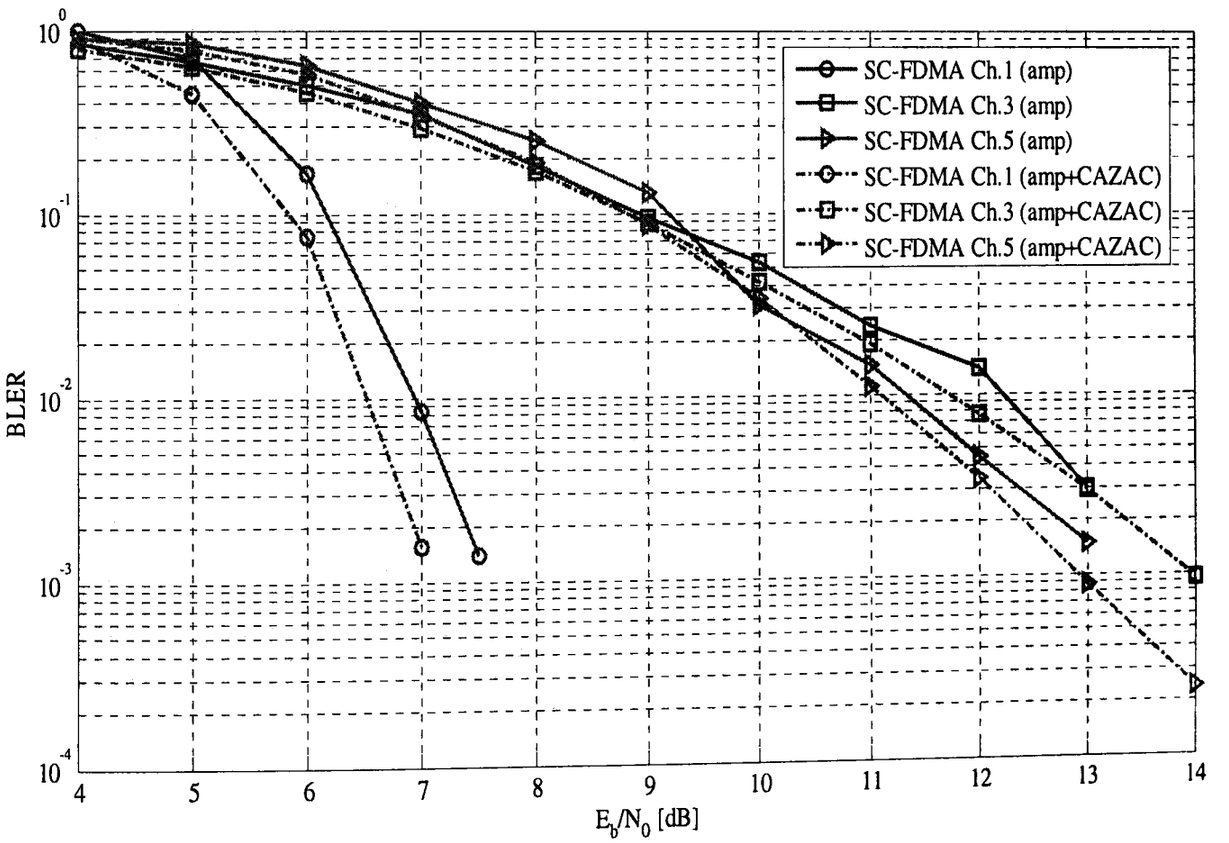

Figure 6-22: Performance of SC-FDMA for different mobile channel profiles with realistic channel estimation using CAZAC sequence

According to [3GPP814], a Constant Amplitude Zero Auto Correlation (CAZAC) sequence is proposed as a potential candidate for pilot pattern of SC-FDMA because its amplitude is constant

both in time and frequency domain, perfect zero circular autocorrelation property and lower cross correlation between two different sequences (allow to provide orthogonality among different RS sequences). They are also named as polyphase sequences with good periodic or optimum correlation properties [KUMA85]; generalized chirp-link polyphase sequence [POPO92].

However, 3GPP 25.814 does not recommend any specific type of CAZAC [3GPP814]. We therefore consider the Zadoff-Chu sequence for investigating the channel estimation in the presence of amplifier non-linearity because it is widely used in radar systems. Moreover, its application as a Random Access Channel (RACH) preamble was strongly recommended due to its attractive autocorrelation and cross-correlation properties [YANG06].

A Zadoff-Chu sequence of length N can be expressed in time domain as:

$$c_k(n) = exp\left[-\frac{j2\pi k}{N}\left(\frac{n^2}{2}+qn\right)\right] \text{ for even length of } N \tag{6.20}$$

$$c_k(n) = exp\left[-\frac{j2\pi k}{N}\left(n\frac{n+1}{2}+qn\right)\right] \text{ for odd length of } N \tag{6.21}$$

where $n = 0,1,2,\ldots\ldots,N-1$, q is any integer and k is the index of the Zadoff-Chu sequence within the set of Zadoff-Chu sequences of length N. Moreover, k implies the maximum number of Zadoff-Chu sequences which can be used in the uplink system, which is any integer relatively prime with N.

Figure 6-22 shows similar results for SC-FDMA as in Figure 6-20 , but with Zadoff-Chu sequence used as a reference signal (RS) sequence for channel estimation purposes. According to [3GPP814], this reference sequence is carried by the two short blocks (SBs) in the sub-frame structure shown in Figure 6-17. These SBs were later removed from the latest 3GPP standards and the RS is carried by the 4th symbol[45] in the time slot. It is observed from Figure 6-22 that the performance is slightly[46] improved when compared with the performance of SC-FDMA in Figure 6-20.

The investigation was further extended to evaluate the similar scenario considered in Figure 6-21 and the results are shown in Figure 6-23. A performance improvement in the range 0.3 – 0.8 dB is observed at higher E_b/N_0 values. However, the improvement is not very significant when compared with the improvement obtained via the random pilot sequence method as in Figure 6-21.

[45] There are seven symbols (when normal cyclic prefix is used) in the sub-frames and the fourth symbol is in the middle of the sub-frame.

[46] The best sequence was retained via a trial and error method.

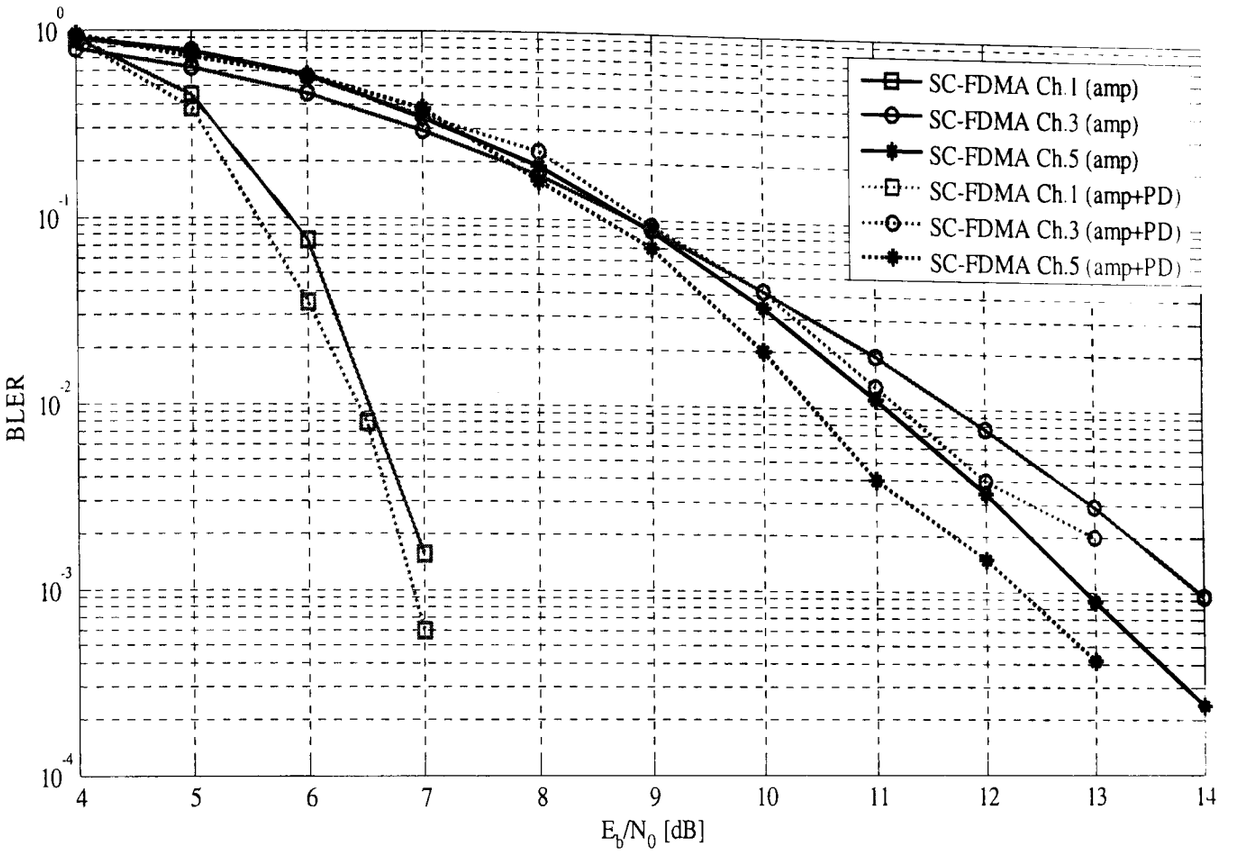

Figure 6-23: Performance of SC-FDMA for different mobile channel profiles with realistic channel estimation using CAZAC sequence (3rd order polynomial pre-distorter)

Another important point worth discussing is the effect of the null sub-carriers on the average power level of the signal in the time-domain (after IFFT), and consequently on the practical operating point of the amplifier. Clarifying this, if a specific power level is allocated to the data symbols in the frequency domain (prior to IFFT), to achieve a particular E_b/N_0 level, then the presence of the null samples in the IFFT will result in the time domain samples having a significantly reduced average power level. For example if the average power level of the transmit signals prior to the IFFT is P and only L out of N sub-carriers are non-zero, then the average power level in the time domain sequence will be $P * (L/N)$. Given that the maximum number of non-zero sub-carriers is 300 out of 512, then under these assumptions, in the worst case the amplifier will be driven 'naturally' (i.e. without applying any IBO) about 2.3dB away from the input saturation point.

Figure 6-24 shows the performance of the SC-FDMA with all 300 sub-carriers being used in the uplink transmission, and without normalizing the saturation point of the amplifier to the average time domain signal power level. Firstly it is observed that the link performance with ideal channel estimation is worse compared to the one shown in Figure 6-18. This is due to fewer sub-frames

being required to transmit one code block (about 2 as compared to 26, when one resource unit is assumed to be occupied). This results in reduced exploitation of time diversity in the multipath channel, as observed by the channel decoder. The most significant point to be noted from Figure 6-24 is that the effect of the amplifier's non-linearity on the link performances is almost negligible, and this is due to this natural input back-off resulting from having 212 null sub-carriers.

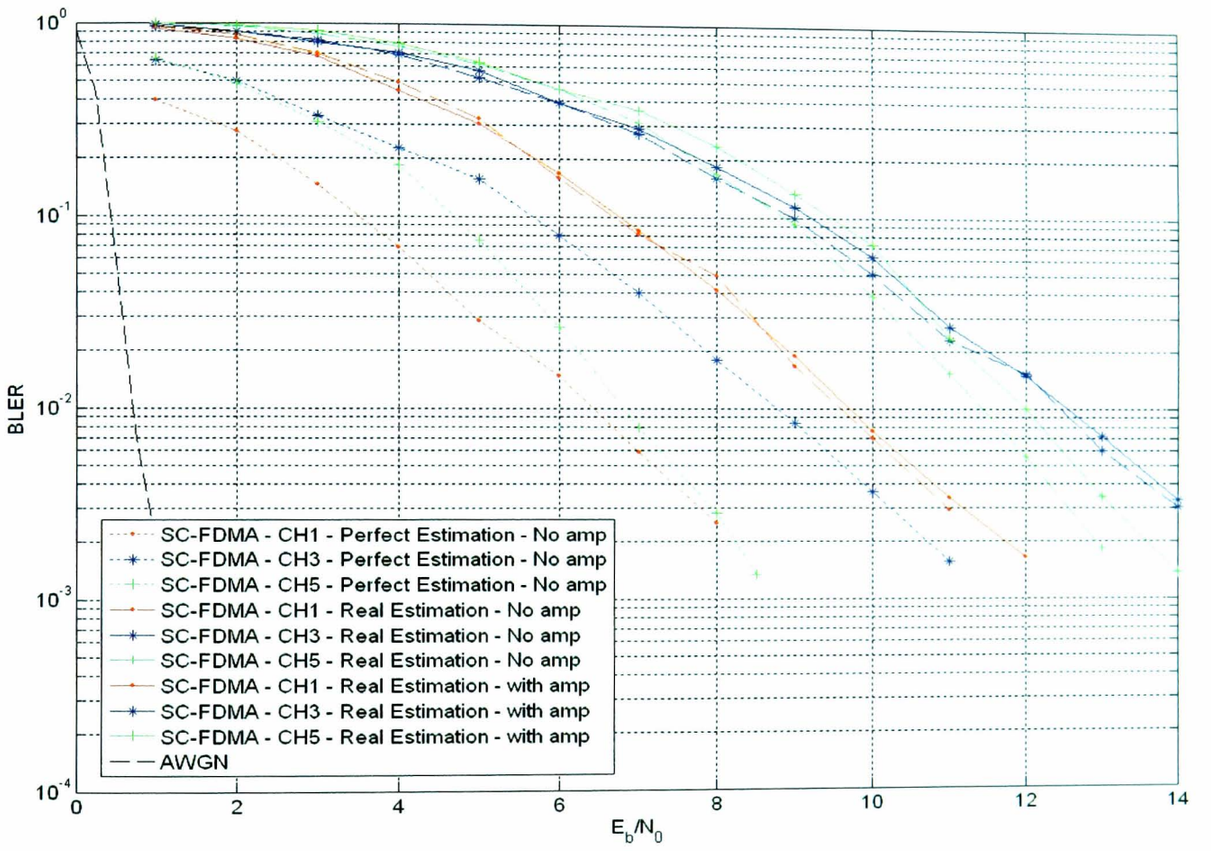

Figure 6-24: Performance of SC-FDMA in the presence of the TWTA model without normalizing the saturation point of the amplifier to the average time domain signal power level. Single user assumed to occupy all 300 sub-carriers

In the extreme case where only a single user is active and uses just one resource unit, then the IBO resulting from null sub-carriers is about -13.1dB. In this case the amplifier introduces negligible phase distortion, while the OBO in this region of the TWTA is almost uniformly 6dB higher than the IBO. The results obtained in this scenario are shown in Figure 6-25, where it is observed that the amplifier simply adds 6dB of power to the transmit signal.

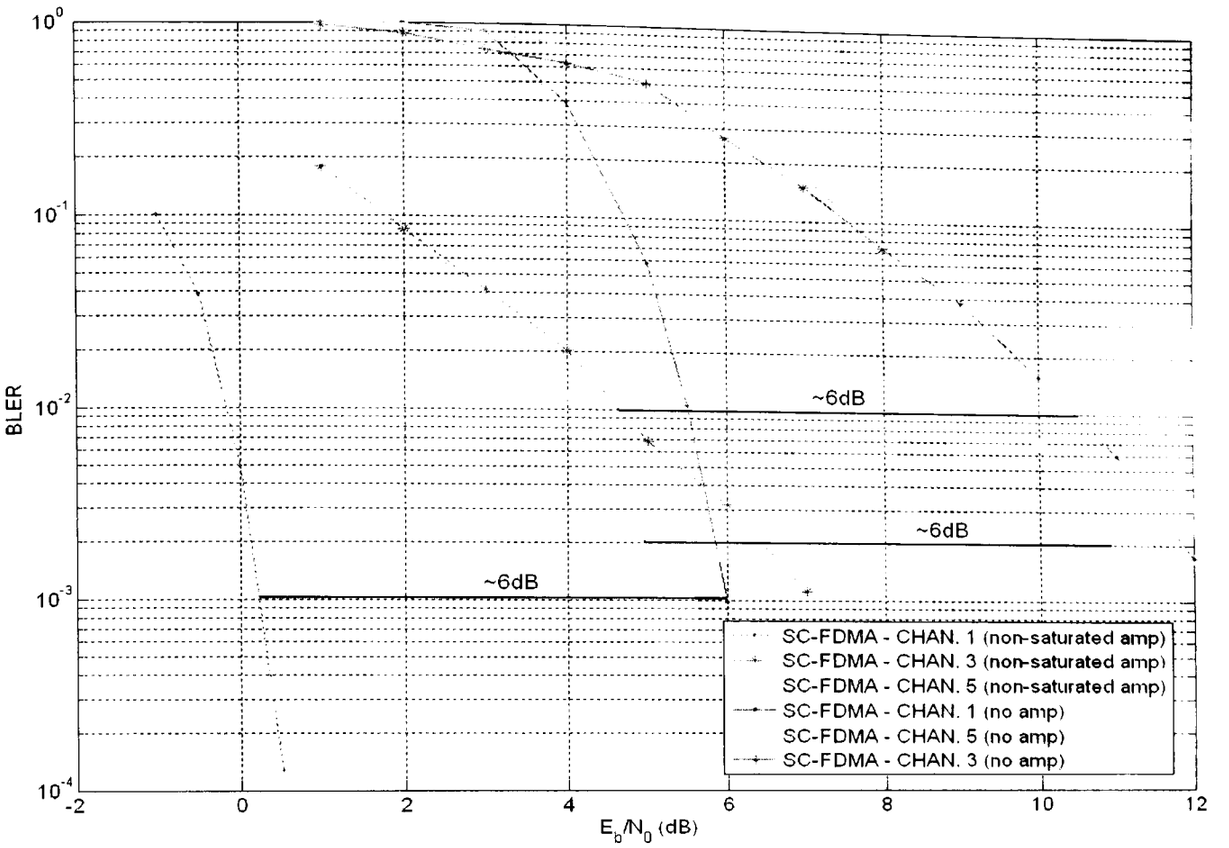

Figure 6-25: Performance of SC-FDMA in the presence of the TWTA model without normalizing the saturation point of the amplifier to the average time domain signal power level. Single user assumed to occupy 25 sub-carriers

6.5 Summary & Conclusions

The following main points can be concluded based on the simulation results:

In the Forward Link:

- A (C++) link-level OFDM simulator was modelled by modifying an established HSDPA simulator. The new simulator supports a satellite channel model and amplifier non-linearity.
- In the 'satellite-only' channel profiles, and with the assumption of perfect channel estimation, OFDM performs marginally better than HSDPA. On the other hand HSDPA (with 6 fingers in the rake receiver) provides substantially better performance in the 'SAT+IMR' channel profile.
- The performance of HSDPA is not significantly degraded when realistic channel estimation is used. On the other hand, with the channel estimation approach used, OFDM suffers very large performance degradation. In practice this level of degradation can be

considered as unacceptable and a more reliable channel estimation approach needs to be examined.

- The non-linearity marginally degrades the performance of OFDM and this is due to the large number of zero points in the IFFT which reduced the average power level of the time domain sequence. Under this assumption, pre-distortion does not offer any significant performance benefits.
- The non-linearity significantly degrades the performance of OFDM when the saturation point of the amplifier is normalized to the average power of the time domain signals. In this case amplifier back off and pre-distortion helps to partially recover the link performance.
- The polynomial pre-distorter performs robustly even when the adaptation is performed over a noisy channel (at SNR= 10dB). On the other hand the LUT pre-distorter performs well only when adaptation is performed in noise-less conditions. Furthermore, LUT pre-distorter becomes unreliable in the noisy condition and therefore, provides worse performance than without performing pre-distortion at all.
- The amplifier non-linearity degrades the performance of HSDPA by around 2-2.5dB. Input back-off helps to partially recover this performance loss. With an IBO of 3dB, pre-distortion does not offer any performance benefits. These results suggest that the input back-off needs to be calibrated carefully in order to maximize the performance benefits offered by the pre-distorter. Finally, as with OFDM, the polynomial pre-distorter performs robustly even when training is performed under poor SNR conditions, in contrast to the LUT pre-distorter which requires a high SNR to perform robustly.

In the Return Link:

- In the 'satellite only' channel profiles, and under the assumption of perfectly linear amplifier response, HSUPA and SC-FDMA provide approximately the same performance
- In the 'SAT+IMR' channel profile, HSUPA yields substantially better performance than SC-FDMA (this result shows that provided the rake receiver has enough fingers to cover the dominant channel taps, HSUPA can perform well in environments with very large excess delay spreads)
- In the scenarios examined the degradation introduced by the amplifier, on the performance of HSUPA, was negligible because the transmit signal samples had fixed amplitudes.
- For SC-FDMA, the amplifier leads to a performance degradation in the order of 1.5-2 dB, when it is assumed that the saturation point of the amplifier is normalized at the average

power level of the transmit signals. These results show that channel estimation and strong channel coding substantially limit the effects of the non-linearity.

- The structure of the pilot tones in SC-FDMA has a large impact on the link-performance, in the presence of the non-linearity. Pilot sequences based on the CAZAC sequence slightly improve the performance when compared with the case that the sequence was selected from a trial-and-error approach.
- Ideal pre-distortion yields relatively small performance improvements (0.3-0.7dB). Moreover the 3rd order polynomial pre-distorter achieves these improvements, even when noisy conditions are assumed in the training phase.
- Under the simulation assumption adopted, the pre-distorter does not introduce a very significant benefit in the performance of SC-FDMA. This suggests that the main degrading factor is the saturation region of the amplifier that cannot be linearised.
- The null sub-carriers result in a reduction of the average transmit power level in the time domain signals. This introduces a 'natural' back-off which substantially limits the degrading effects of the non-linearity. If this assumption applies in a practical system then the effects of the non-linearity on the performance of SC-FDMA can be concluded to be very limited.

Recommendations based on the BLER Vs. E_b/N_0 performance comparison:

Table 6-7: Recommendation of Air Interface for S-DMB type System

Direction	Air Interface
Forward Link	**SC-FDE** • Delivers better performance than OFDM in the non-linear mobile satellite environment due to low PAPR characteristics. • It has the same overall complexity as OFDM technique and therefore, can co-exist with the OFDM receivers with the help of a convertible modem.

The investigation in this chapter is only based on the link-level performance (BLER Vs. E_b/N_0) of the air interfaces in the single user scenario. The HSPA based air interfaces perform better than OFDM based air interfaces both in the forward and return links of the satellite system. Based on this fact, one might consider to recommend the HSPA based air interfaces for the LTE satellite system.

However, the study is by no means complete and conclusive on the comparison between the air interfaces. A further study must be carried out to provide the comparison in terms of outage

probability, number of users, air interface delay, spectral efficiency, receiver complexity for increased bandwidths and the achievable capacity improvement from the upper layers point of view. Thus it cannot be concluded from this study that HSPA would be preferred option.

Considering an S-DMB type system, SC-FDE demonstrates significant improvement compared with OFDM system due to its low PAPR characteristic. Moreover, it has the same overall complexity as OFDM and the capability to co-exist with the OFDM based receivers via a convertible modem. Thus, it can be recommended for the forward link of the S-DMB system as shown in Table 6-7.

Chapter Seven

7 Conclusions and Future Work

7.1 Conclusions

In this thesis, we have investigated physical layer performance of the OFDM-based air interfaces, in particular OFDM and SC-FDMA, for future mobile satellite systems aiming to provide the complementary services to the continuously evolving terrestrial UMTS systems. In order to implement OFDM in the satellite systems, the issue related to the non-linear distortion introduced by the on-board power amplifier to the OFDM signals was also addressed. Investigation was performed whilst keeping maximum commonalities with the already available 3GPP based terrestrial standards. This minimal impact evolutionary criteria approach is further supported by the Mobile Satellite System (MSS) frequency allocation in IMT-2000 specification, which is adjacent to the present T-UMTS.

Firstly, TR based PAPR reduction techniques were considered as one of the possible transmitter based mitigation techniques for compensating the non-linear distortion. Although several methodologies have been proposed to implement TR, they are not completely optimal in terms of complexity and performance. A novel gradient based algorithm was proposed which provides higher PAPR reduction performance with reduced computational complexity than TR techniques based on the active set algorithm, the most efficient algorithm presently existing. The algorithm performs better than the DFT- spreading technique irrespective of the pilots/tone locations. However, the performance depends critically on the pilot locations. When spectral constraints are applied, the PAPR reduction performance in all cases is affected. The more scattered the pilots within the bandwidth, the more it is affected by the incorporation of spectral constraints. Moreover, the pilots can be loosely constrained to obtain a slightly improved PAPR reduction performance. It was also shown that the proposed algorithm offers an efficient trade-off between PAPR reduction gain and relative mean power increase, at the cost of slight spectral efficiency loss. From the extended investigation in the non-linear TWTA environment, it was shown that the proposed algorithm becomes effective at larger IBO levels. The impact here is in the improved TR algorithm and in inputs to future standard pilot allocations.

Chapter 5 introduced the mathematical modelling of the pre-distorter, along with that of the TWTA. The performance of the proposed algorithm for TR based PAPR reduction technique, with pilots are constrained to the average power level of the data tones, was investigated within the combined ' Pre-distorter + TWTA'. The performance obtained showed that the TR technique becomes effective when combined with amplifier linearization techniques. Moreover, the performance advantage is significantly greater than the improvement obtained with any single mitigation technique: TR technique or pre-distortion. Thus, the impact is that the pre-distortion technique and the TR technique must be combined in order to efficiently mitigate the non-linear distortion introduction by the TWTA. Further investigation showed that the choice of pilot location does not show significant performance variation in terms of BER and spectral re-growth performance.

Two different digital pre-distortion techniques based on the LUT and polynomial modelling approach were evaluated and compared in terms of computational complexity, convergence speed and accuracy in the context of the satellite-gateway remote adaptation scenario. More specifically, it was assumed that the observed training sequence at the output of the amplifier was degraded by AWGN, and the effect of noisy training signals (on the adaptation and performance of the digital pre-distorters) was studied for different SNR. Comparisons were made using the conventional adaptation algorithms; Secant algorithm for the LUT pre-distorter and Minimum Mean Square Error (MMSE) parameter estimation for the polynomial pre-distorter. When AWGN was applied on the feedback channel the accuracy provided by the pre-distorter becomes practically independent of the LUT size (within the range of the examined cases). The accuracy provided by the LUT pre-distorter deteriorated consistently and significantly with decreasing SNR. On the other hand, the adaptation of polynomial pre-distorter is more resilient to low SNR conditions relative to the LUT pre-distorter.

It is also observed from the simulation results that the polynomial pre-distorter converges significantly faster than the LUT pre-distorter. However, the computational complexity, especially in evaluating the polynomials, in the polynomial pre-distorter dramatically increases if the pre-distorter is extended to use higher order polynomials; obviously, the complexity in the operational mode also increases. On the other hand, it is only the adaptation time that increases if large sized Lookup Tables are employed and thereby, the complexity of the adaptation operation significantly increases.

Due to the sensitivity of the Secant algorithm towards the noisy feedback channel, a modified Secant based algorithm based on the modified Newton-Raphson method was proposed for updating the LUT pre-distorter. In the noisy feedback channel conditions, the modified algorithm showed performance improvement in terms of both adjacent channel interference and link level performance. However, its performance is limited in the noiseless feedback condition. On the

other hand, the conventional Secant based algorithm showed better performance in the noiseless feedback channel conditions and poor performance in noisy channel conditions. Thus, the chapter recommends an adaptive strategy based on an approximate threshold SNR level of 20dB; the modified Secant algorithm can be used when the SNR in the feedback channel is less than 20dB and the conventional Secant algorithm can be used otherwise.

Chapter 6 provides a comparison study between the OFDM based and HSPA based air interfaces in the forward and return link of LTE satellite systems. In the forward link, the comparison was made between OFDM and HSDPA whereas SC-FDMA and HSUPA were considered in the return link. Three different satellite channel profiles were simulated.

In the 'satellite-only' channel profiles, and with the assumption of perfect channel estimation, OFDM performs moderately better than HSDPA. On the other hand HSDPA (with 6 fingers in the rake receiver) provides substantially better performance in the 'SAT+IMR' channel profile. The non-linearity significantly degrades the performance of OFDM when the saturation point of the amplifier is normalized to the average power of the time domain signals. However, a moderate degradation was observed when the saturation point of the amplifier is not normalized to the average power of the time domain signals. This is due to the larger number of zero points in the IFFT reducing the average power of the time domain signal.

This chapter also proposed the use of Single Carrier Frequency Domain Equalization (SC-FDE) as an alternative air interface to OFDM, within satellite digital multimedia broadcasting (S-DMB) systems. A comparison of OFDM and SC-FDE systems was performed assuming a perfectly linearized satellite channel assuming ideal channel estimation. With 0dB back-off, SC-FDE provides 2dB performance gain over OFDM system. The performance of the two systems becomes approximately the same when 3dB back-off is applied to OFDM system. Therefore, at least for this ideal linearization case, SC-FDE allows the amplifier to be driven at saturation, whereas OFDM requires some back-off in order to perform at the same level.

In the return link of the LTE satellite system, HSUPA and SC-FDMA provide approximately the same performance when the 'satellite only' channel profile is considered with ideal channel estimation. However, HSUPA yields substantially better performance than SC-FDMA in the 'SAT+IMR' channel profile. This is because the rake receiver has enough fingers to cover the dominant channel taps and therefore, effectively exploit the multipath diversity. Moreover, SC-FDMA showed improved performance when the channel is estimated using the CAZAC sequence.

Although HSPA based air interfaces demonstrate advantages over OFDM based air interfaces in terms of BLER performance in the LTE satellite systems, considering OFDM based air interfaces is appropriate due to the following reasons:

- Terrestrial systems are moving towards OFDM based air interfaces, for example 3GPP LTE.
- OFDM based air interfaces are more spectrally efficient than HSPA based air interfaces.
- The complexity of the HSPA receiver increases tremendously for larger bandwidths, which are proposed in the LTE standards.
- OFDM based air interfaces provides another dimension (Frequency) for resource allocation and scheduling. This can improve the throughput from the upper layer point of view.
- Efficient integration of MIMO antennas to OFDM based system.

7.2 Implications of the Research

The results of the study carried out in this thesis have some interesting implications, particularly for the OFDM based mobile satellite systems, and their future evolution. These are outlined as follows:

1. A gradient based algorithm for reducing the PAPR of OFDM signals using a TR technique was proposed in chapter 4. The algorithm showed lower computational complexity and improved performance compared with the most efficient existing active set based algorithms. Due to the fact that the TR based algorithm does not depend on the transmitter based information at the receiver for correctly decoding the received signal, the proposed algorithm is appropriate to the future mobile satellite systems in order to improve the transmitter power efficiency.

2. The investigation in chapter 5 showed that the proposed algorithm becomes more effective when it is combined with power amplifier linearization. In other words, the combination of power amplifier linearization technique and the TR based algorithm can always outperform their individual performances. Therefore, the TR based algorithm must be combined with the amplifier linearization technique in order to significantly improve the power efficiency of the system.

3. The comparison in chapter 5 showed that the polynomial pre-distorter is more robust in the noisy environment than the LUT based pre-distorters. It also showed faster convergence than the LUT pre-distorter. However, the complexity associated with the polynomial pre-distorter is greater than that of the LUT based pre-distorter. Thus, using the polynomial pre-distorter in the noisy environment provides performance advantage but at some extra cost.

4. An adaptive strategy based on an approximate threshold SNR of 20dB was proposed for remotely adapting the LUT based pre-distorter via the feedback channel degraded by AWGN. The proposal is based on the modified Secant algorithm defined by the parameter r. Depending on the SNR value in the feedback channel, r can range between 100 to 1. Thus, the conventional Secant based algorithm ($r = 1$) can be used when the SNR is greater than 20dB and the modified Secant algorithm can be used otherwise.

5. The performance of OFDM based air interfaces based on 3GPP standards[47] were investigated in the non-linear wideband satellite channel. The comparison study with the HSPA based air interfaces showed that the HSPA based air interfaces can outperform OFDM based air interfaces if the Rake receiver is able to cover the larger excess delay spread of the mobile satellite channel. However, the complexity of the receiver is higher than the OFDM based receivers for increased bandwidths.

6. The channel Estimation for the SC-FDMA system in the presence of amplifier non-linearity was investigated using Zadoff-Chu based CAZAC sequence and showed improved performance when compared with the trial-and-error approach.

7. SC-FDE was proposed for S-DMB type systems and can easily be incorporated into the future OFDM based receivers via a convertible modem. SC-FDE provides performance similar to OFDM based systems with 3dB back-off applied in the presence of ideally linearized power amplifier.

7.3 Future Work

The work carried out in this thesis for investigating OFDM based air interfaces for future mobile satellite systems is by no means a complete and conclusive work on the subject. The study has lead to many open problems and avenues for further research that could extend the present work and may bring to light new insights and understanding. Some of the directions in which the present work could be extended are pointed out in the following:

1. The proposed gradient based TR algorithm uses a constant step size parameter for updating the gradient direction at each iteration. Thus, the convergence of the algorithm must be

[47] The OFDM and SC-FDMA air interfaces are based on the 3GPP 25.892 and 25.814 standards, respectively.

investigated in detail in order to efficiently update the gradient and thereby, reducing further PAPR of the OFDM signal. Furthermore, the TR approach can be extended to mitigate the distortion caused by insufficient cyclic prefix, as demonstrated in [MALK07]. This is most appropriate to future mobile satellite systems which shows larger excess delay spread compared to terrestrial based systems.

2. In this thesis, the memory effect in the power amplifier characteristics was not considered because of the 5MHz bandwidth consideration. The scalable bandwidth configuration is one of the main features of 3GPP LTE based systems. Similarly, IMT-Advanced systems considered greater bandwidths up to 100MHz. Thus, the power amplifier memory effect must be taken into consideration when investigating the pre-distortion algorithm for future mobile satellite systems. Again, its performance in the remote adaptation scenario, assuming feedback channel with AWGN noise, needs further investigation.

3. The comparison between OFDM based and HSPA based air interfaces were based on Block Error Rate performances and therefore, are not comprehensive. In order to provide a comprehensive study, both systems must be compared in terms of capacity/throughput, outage probability, number of users, air interface delay, spectral efficiency, and receiver complexity for different bandwidths. This needs further study.

4. The SC-FDE and OFDM systems were compared only in the perfect channel estimation scenario. It would be interesting to compare their performance in the non-linear channel with realistic channel estimation scenarios. This needs further investigation of the channel estimation algorithms for SC-FDE and OFDM. Moreover, the channel estimation of the SC-FDMA system in the presence of non-linearity needs further investigation due to its recent modification in the 3GPP 36.211 standard, where only one short block is considered rather than two blocks as in the previous 3GPP 25.814 standard.

APPENDIX A: Measured Power Delay Profiles from the MAESTRO Project

Table A-1: S-DMB propagation channel, Case-1

Case-1: Satellite LOS with many rays		
Delay [ns]	Power [dBm]	Rice Factor [dB]
0	-91.9	10
195.3	-106.3	-inf
260.4	-110.1	-inf
846.3	-112.5	-inf
1171.9	-110.2	-inf
1953.1	-112.5	-inf
2734.3	-112.5	-inf

Table A-2: S-DMB propagation channel, Case-3

Case-3: Satellite NLOS with many rays		
Delay [ns]	Power [dBm]	Rice Factor [dB]
0	-108.5	-inf
195.3	-110.9	-inf
260.4	-106.6	-inf
390.6	-109.3	-inf

Table A-3: S-DMB propagation channel, Case-5

Case-5: Satellite+3 IMRs (without processing delay) – open area		
Delay [ns]	Power [dBm]	Rice Factor [dB]
0	-91.8	7
1692.7	-67.8	-inf
1757.8	-80.7	-inf
2278.6	-67.5	-inf
2343.7	-72.8	-inf
2408.8	-69.6	-inf
3190.0	-73.1	-inf
8203.0	-74.8	-inf
8268.1	-78.4	-inf
8788.9	-81.6	-inf

Table A-4: S-DMB propagation channel, Case-6

Case-6: Satellite+3 IMRs (without processing delay) – large delay		
Delay [ns]	Power [dBm]	Rice Factor [dB]
0	-91.7	7
8203.0	-74.4	-inf
9179.5	-86.3	-inf
10872.2	-85.4	-inf
11002.4	-86.8	-inf
12630.0	-86.4	-inf
18098.6	-89.2	-inf
18424.1	-73.6	-inf
18498.2	-88.6	-inf
22981.3	-89.3	-inf

APPENDIX B: Measurement Data for Travelling Wave Tube Amplifier from MAESTRO Project.

IBO [dB]	OBO [dB]	Phase [degree]
-20.00	-14.00	0
-19.00	-13.10	0.492354354
-18.00	-12.10	1.112191762
-17.00	-11.10	1.892520826
-16.00	-10.10	2.874896914
-15.00	-9.20	3.392625066
-14.00	-8.20	3.9425375
-13.00	-7.40	4.634836238
-12.00	-6.50	5.465516055
-11.00	-5.60	6.675322835
-10.00	-4.80	8.350519192
-9.00	-4.00	10
-8.00	-3.30	12.48797921
-7.00	-2.70	15.20555538
-6.50	-2.40	16.5882523
-6.00	-2.10	18.13966376
-5.50	-1.90	19.42976289
-5.00	-1.60	20.38319041
-4.50	-1.40	21.45295369
-4.00	-1.20	22.65324783
-3.50	-1.00	24
-3.00	-0.80	25.09320103
-2.50	-0.60	26.31979275
-2.00	-0.40	27.7735732
-1.50	-0.30	29.48974274
-1.00	-0.10	31.41531664
-0.50	0.00	33.57584609
0.00	0.00	36
0.5	0	37.49981555
1	-0.1	39.18263627
1.5	-0.2	41.07079217
2	-0.4	43.18933794
2.5	-0.7	45.10999935
3	-1	47
3.5	-1.3	47
4	-1.6	47
4.5	-2	47
5	-2.4	47
5.5	-2.8	47
6	-3.1	47
7	-3.9	47
8	-4.6	47
9	-5.1	47
10	-5.6	47

APPENDIX C: HSUPA Simulator Architecture

HSUPA has been defined (in Release 6 of UMTS) in order to complement in the uplink the higher speeds and reduced delays, provided by HSDPA in the downlink. As in HSDPA these enhancements are facilitated by the introduction of (carefully selected-low complexity) advanced features that are highly compatible with previous Releases (99, 4 and 5). In particular the following key features have been introduced:

Enhanced Dedicated Channel (E-DCH)

E-DCH has been defined as a new (enhanced) uplink channel in the physical layer, while retaining the Release 99 DCH. E-DCH is supported by three new downlink signalling channels:

- *Enhanced HARQ Indicator Channel (E-HICH)*, which is used to acknowledge E-DCH transmissions from the mobile terminal.
- *Enhanced Absolute Grant Channel (E-AGCH)*, which delivers absolute scheduling information to the mobile terminals: allocated data rate and maximum allowed power.
- *Enhanced Relative Grant Channel (E-RGCH)*, which delivers relative scheduling information to the mobile terminals: increase/decrease allocated resources relative to previous value.

HARQ

HARQ is defined in a similar manner as in HSDPA:

- Stop and wait protocol, based on synchronous downlink ACK/NACKs, and on synchronous retransmissions in the uplink.
- The number of parallel processes depends on the TTI: 8 processes for the 2ms TTI and 4 processes for the 10ms TTI.
- Pre-emption is not supported by E-DCH (ongoing re-transmissions are not pre-empted by higher priority data for a particular process).
- Incremental redundancy shall be supported by the specifications with Chase combining as a sub-case:
    - The UTRAN configures the UE to either use the same incremental redundancy version (RV) for all transmissions, or to set the RV according to set of rules based on E-TFC, Retransmission Sequence Number (RSN) and the transmission timing.

Optional use of 2ms TTI

In HSUPA the use of short (2ms) TTI is provided (optionally) for better utilization of the short term channel capacity. In the satellite environment resource allocation changes are limited by the propagation delay, and thus the standard 10ms TTI is sufficient.

Fast Scheduling

A more efficient scheduling mechanism allows better use of the available spectrum and power budget. In particular this is controlled by the Node B, which uses QoS-related information from the SRNC as well as requests from the UE to determine the amount of resource to be made available to each UE. The resource level is allocated using E-AGCH and E-RGCH channels.

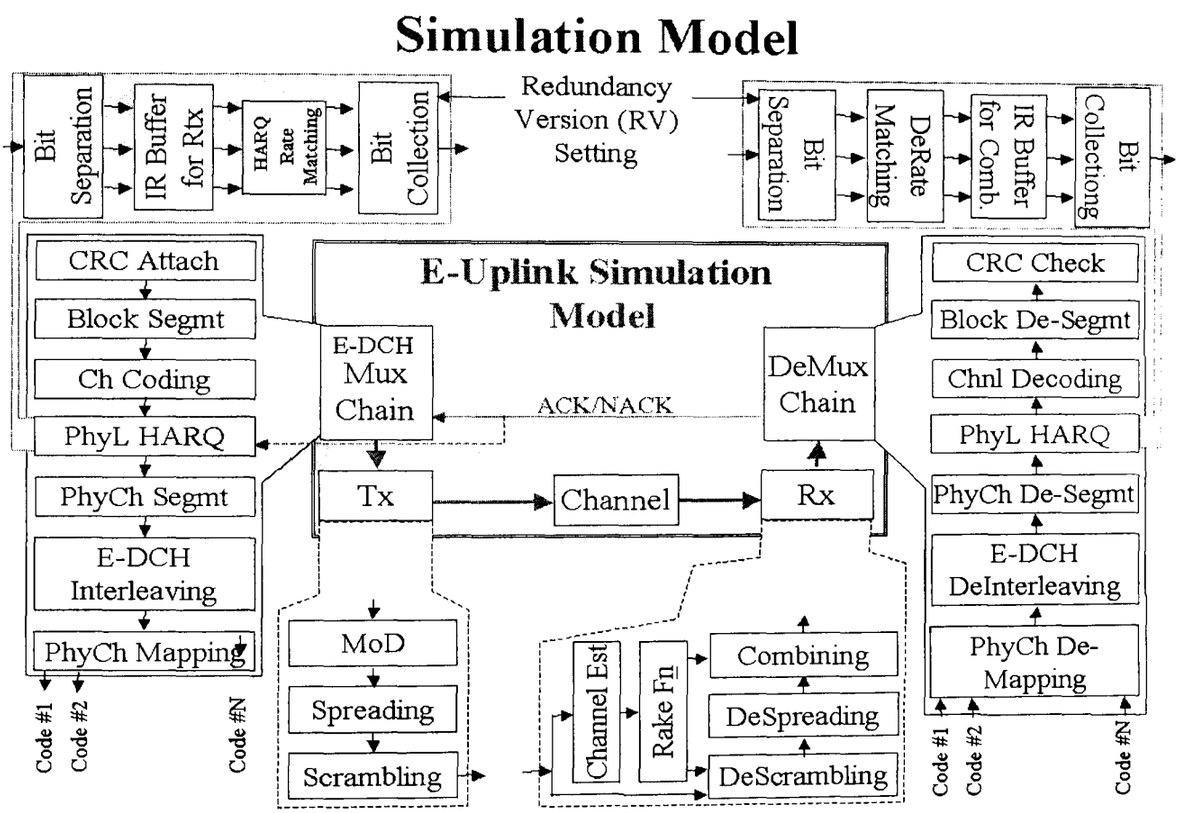

Figure C-1: HSUPA Simulation Model

Figure C-1 illustrates the HSUPA simulator model used for evaluating the return link performance in this investigation. The main characteristics of the simulator are summarized as:

- Simulates Enhanced Uplink as per [3GPP808]
- Inner and Outer Loop Power Control
- Receive Antenna Diversity

- Channel Estimation (Ideal or through DPCCH).
- Antenna Correlation
- Up to 6 Stop and Wait (SAW) HARQ processes with Chase Combining and Incremental Redundancy (deactivated for the purpose of this study)
- Up to 8 retransmissions for an HARQ process (deactivated for the purpose of this study)
- TTI of 10 ms
- Handover: Soft / Softer (currently disabled in the present version as it needs testing for E-Uplink)
- Variable Inter-TTI Interval specification
- Variable Power Ratio of DPCCH/E-DPDCH
- Variable number of Rake Fingers with the option of combining 'm' best out of 'n' paths where n > m
- Turbo Decoder with Max-Log Map algorithm
- Scheduling functions are not implemented.

APPENDIX D: HSDPA Simulator Architecture and Its Extension to OFDM

In order to study the performance of OFDM, as an alternative multiplexing technique[48] to CDMA in the downlink of wideband mobile satellite system, physical layer processes in the HSDPA simulator have been modified, as these are shown within the boxes in Figure D-1. These modifications have been primarily based on [3GPP892], and are discussed in more detail below. It must be noted that the performed modifications are transparent to processes not included in the boxes, and thus the advanced features of the HSDPA protocol can be simulated in conjunction with OFDM.

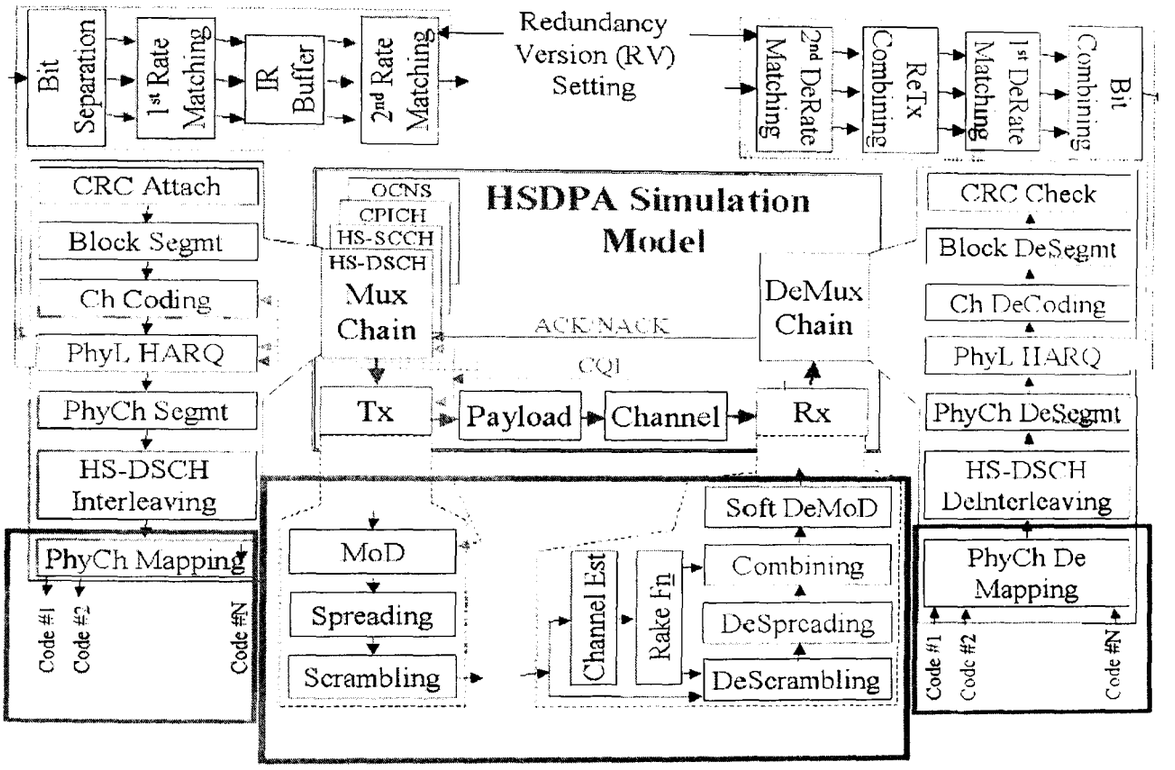

Figure D-1: Modified Physical layer procedure for introducing OFDM in HSDPA [ATTA05]

The essential modifications start just after the MoD block and end just before the Soft DeMoD block, as shown within the central box. In particular, the modulated symbols are obtained from the HSDPA simulator and are subjected to: OFDM modulation processing, channel processing, and OFDM demodulation processing. Finally the OFDM demodulated data is sent to the soft demodulation block. Another important modification introduced in the HSDPA simulator, is the multiplexing/de-multiplexing procedures, as these are fundamentally different to those specified currently in HSDPA. These are described in more detail in the following.

[48] And also multipath interference suppressing technique

According to [3GPP892], data multiplexing is performed in both time and frequency dimensions. In the frequency dimension, data symbols are mapped on different sub-carriers whereas the presence of multiple OFDM modulated blocks within a time slot, N_{OFDM}, is exploited in the time dimension. Subsequently, an OFDM Data-Unit is composed by a sub-set of the available OFDM sub-carriers, N_{SC}. The useful frequency band is divided into N_B Data-Units. Thus, the N_B incoming QPSK/QAM symbol sequences are inserted row-wise by filling adjacent Data-Units of the OFDM time-frequency matrix, as depicted in Figure D-2. This time-frequency matrix has a size of $N_{SC} \times N_{OFDM}$.

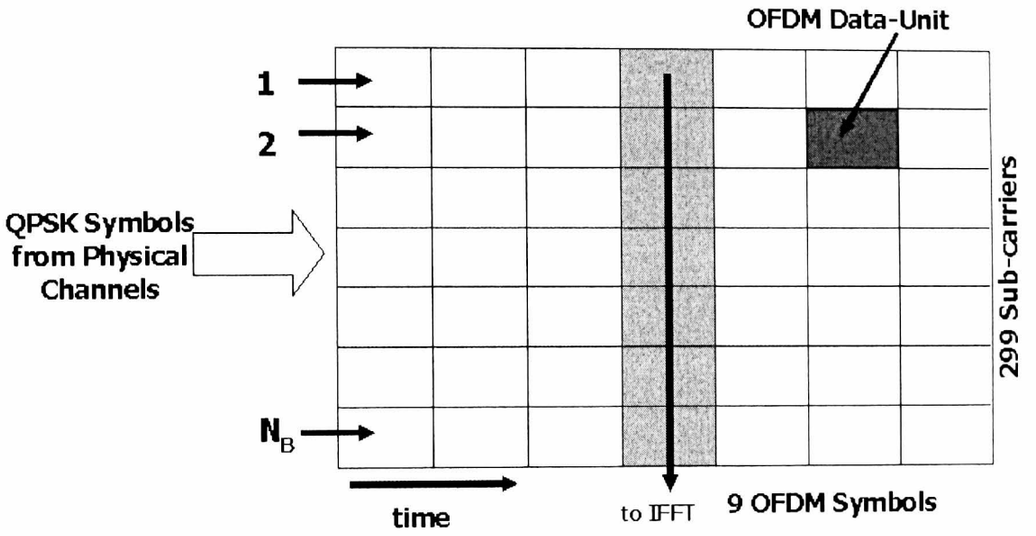

Figure D-2: OFDM time-frequency channel mapping

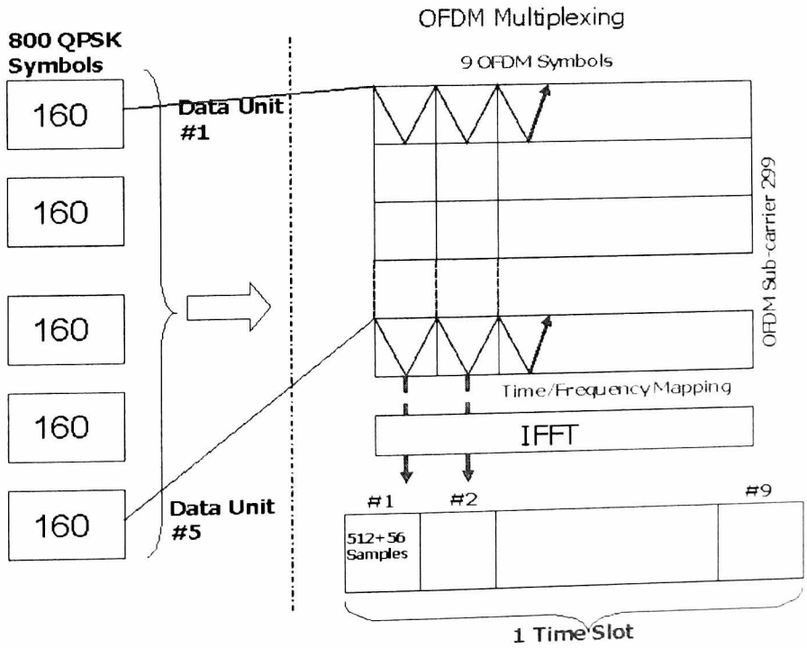

Figure D-3: example of time-frequency multiplexing for parameter set-1 and 5 Data Units

Finally, each column, composed by N_{SC} sub-carriers, is processed by the OFDM modulator that consists of a zero-padding block and a N-point IFFT (Inverse Fast Fourier Transform) processor. An example of OFDM multiplex is depicted in Figure D-3, assuming the parameter Set-1 from [3GPP892] and $N_B = 5$. In order to facilitate the IFFT/FFT, a member function was included inside the appropriate class, which returns the IFFT or FFT output for the input by doing appropriate parameter settings. This single module was separately validated with the IFFT/FFT function available in matlab.

Next, the OFDM blocks are serialized by using a parallel-to-serial converter and then it is sent for channel processing by setting the channel profile parameter and scaled additive white Gaussian noise samples. At this point, the interference noise model, previously simulated for the WCDMA (HSDPA), is switched off.

At the receiver, the OFDM processed data are received after the channel processing with the selected channel profile. This received data is then sent through the OFDM demodulator, which works exactly in the same way as the OFDM modulator, but in the reverse order. Thereafter, the OFDM demodulated symbols are sent to the HSDPA simulator for further processing which are already available with the simulator like demodulation, BER calculation, etc.

APPENDIX E: Procedure for determining the orthogonality factor in the HSDPA simulator for setting the $\mathbf{E_b/N_o}$ value in the simulations

The technique described in this Appendix, for determining the code orthogonality factor for some particular multipath channel profile and defining the E_b/N_0, is available in [JAAN02].

In the HSDPA simulator E_b/N_0 values cannot be directly defined for obtaining BLER against E_b/N_0 results. Instead the link quality input parameters are E_c/I_{or} , Geometry factor $G = I_{or}/I_{oc}$. However, the parameter E_b/N_0 is related to E_c/I_{or} and I_{or}/I_{oc} and is given by the following relationship:

$$\frac{E_b}{N_0} = \frac{(W/R)(E_c/I_{or})}{(1-\alpha)+(1/G)} \tag{E.1}$$

where,

W	:-	Chip Rate
R	:-	Bit Rate
E_c/I_{or}	:-	Transmitted Energy per chip on a chosen channel relative to the total transmitted power spectral density at the base station.
α	:-	Code orthogonality factor
G	:-	Geometry factor which is I_{or}/I_{oc}.

According to the above equation, it is essential to have three unknown parameters, E_c/I_{or}, $I_{or}/I_{oc}$and α, to define a particular E_b/N_0 value. Except the orthogonality factor, the other two parameters, E_c/I_{or} and I_{or}/I_{oc}, can be defined as input parameters to the HSDPA simulator. In general, the orthogonality factor takes various values depending on the wireless channels. For instance, it is assumed to be 1 for static channels. However, its value in the multipath channel has to be estimated in order to estimate the E_b/N_0 by varying the parameters E_c/I_{or} and I_{or}/I_{oc}.

In order to determine the orthogonality factor of a particular multipath channel, we first have to fix I_{or}/I_{oc} and then find out the corresponding E_c/I_{or} value which gives a certain BLER. The process was repeated for different values of parameter I_{or}/I_{oc} . The observations were then plotted as shown in Figure E-1 and E-2, which were obtained for multipath channel profiles case 3 and 5, respectively. Due to the fact that the BLER is kept constant at a particular level, the parameter E_b/N_0 is also expected to be constant. Substituting the observations in the above equation will result in a set of equations with two unknowns α and E_c/I_{or}. They can be easily found by using the method of least squares curve fitting techniques.

Channel Case 3: $\alpha = 0.9834$

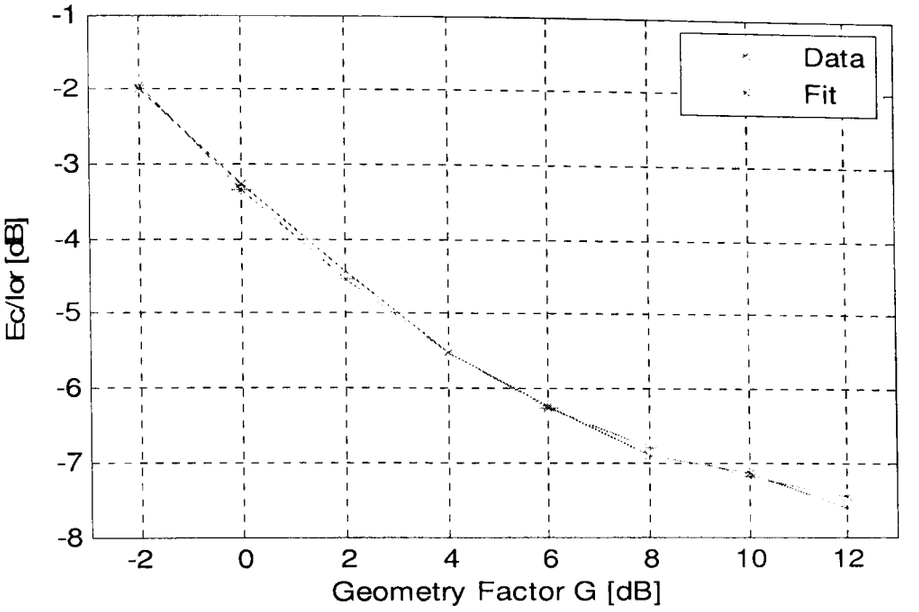

Figure E-1: Curve Fitting for determining the code orthogonality factor for channel profile 3

Channel Case 5: $\alpha = 0.4680$

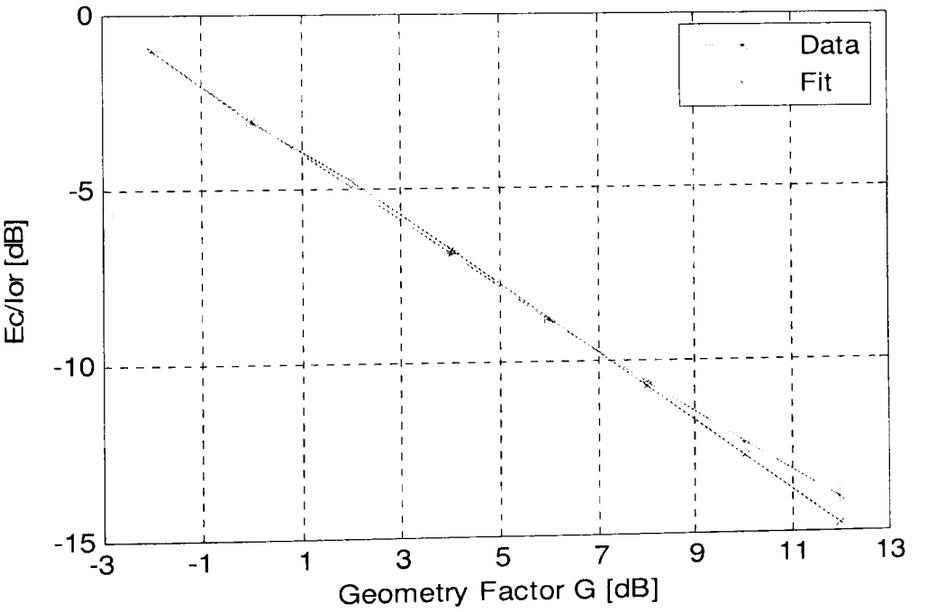

Figure E-2: Curve Fitting for determining the code orthogonality factor for channel profile 5

APPENDIX F: OFDM Simulator: Validation

The performance of the OFDM simulator has been validated by replicating the results provided in [3GPPLG], for the OFDM reference parameter set 1, QPSK modulation and code rate of 1/3. The validation results are provided for the following fading channel profiles:

- Flat Fading Raleigh at 3 km/h and 120 km/h
- ITU Pedestrian A channel at 3 km/h
- ITU Vehicular A channel at 120 km/h
- ITU Vehicular B channel at 120 km/h

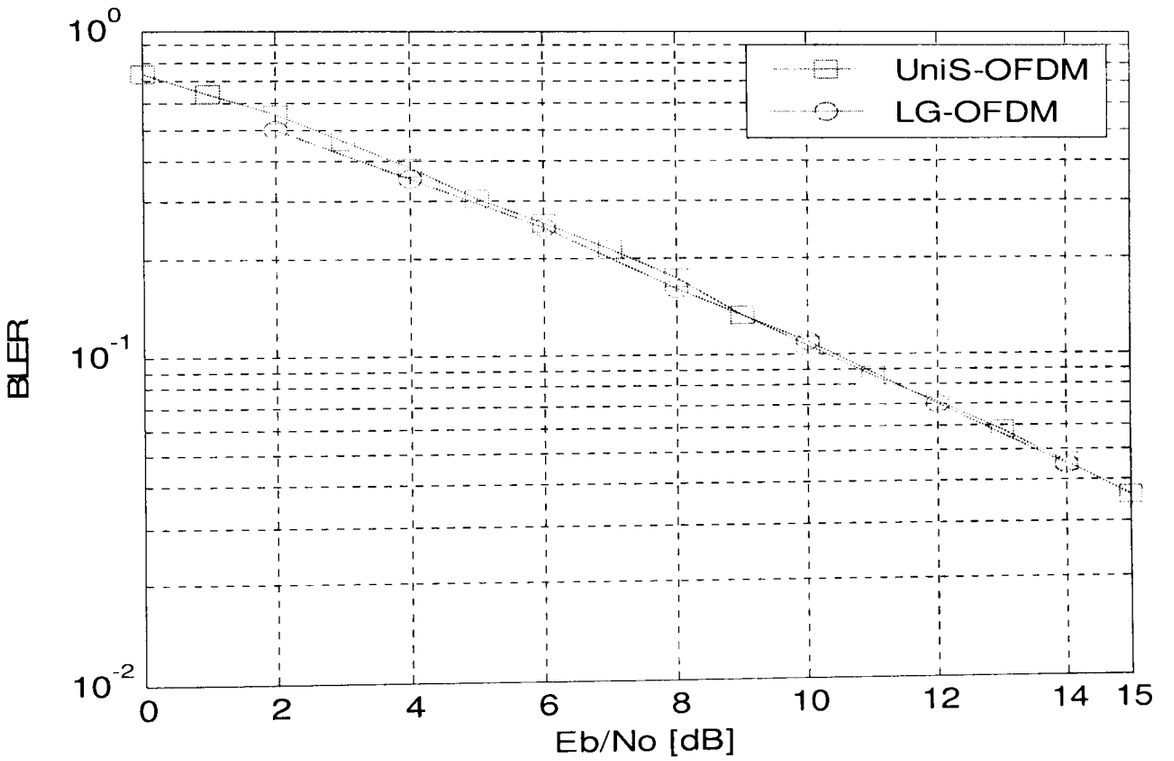

Figure F-1: BLER Performance of OFDM in a Flat Fading Rayleigh Channel at 3km/h

In this simulation, it is assumed that 10% of each symbol is used for overhead and all the available resources are allocated to single user. Moreover ideal channel estimation is assumed. The UniS results appear to match closely the LG results, and this gives a good indication that the OFDM simulator is correctly calibrated.

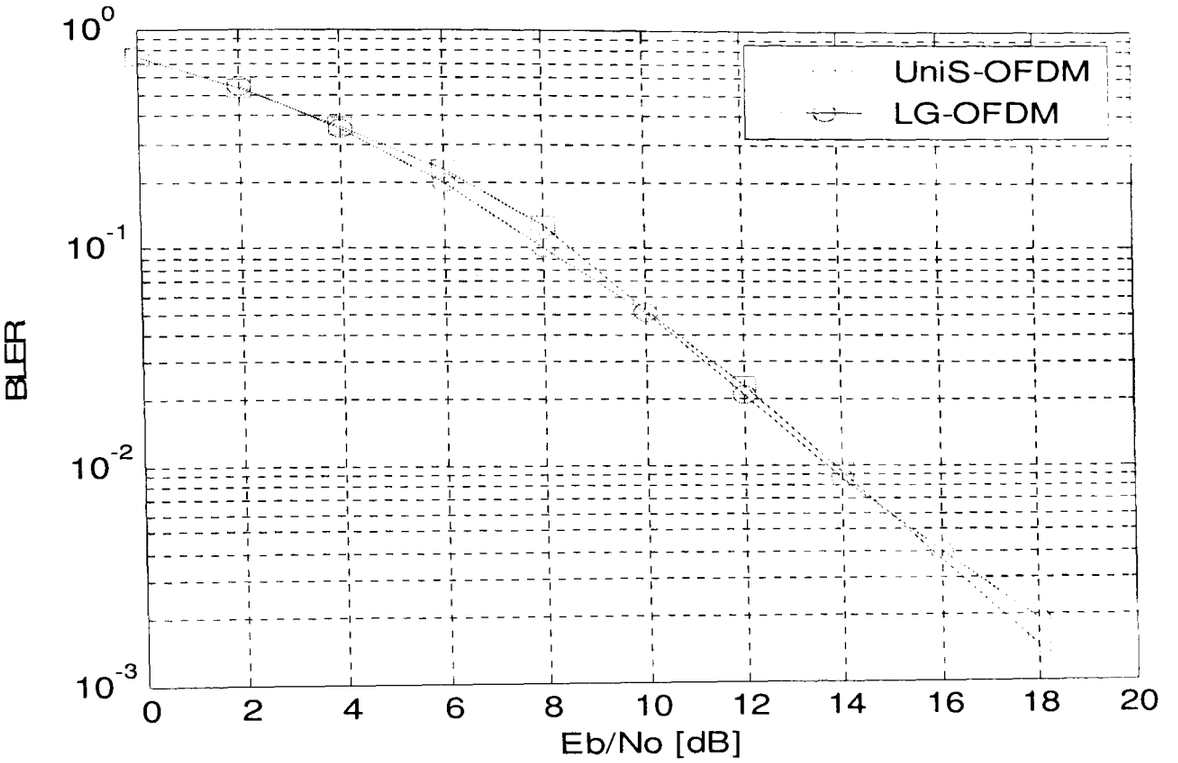

Figure F-2: BLER Performance of OFDM in a Flat Fading Rayleigh Channel at 120km/h

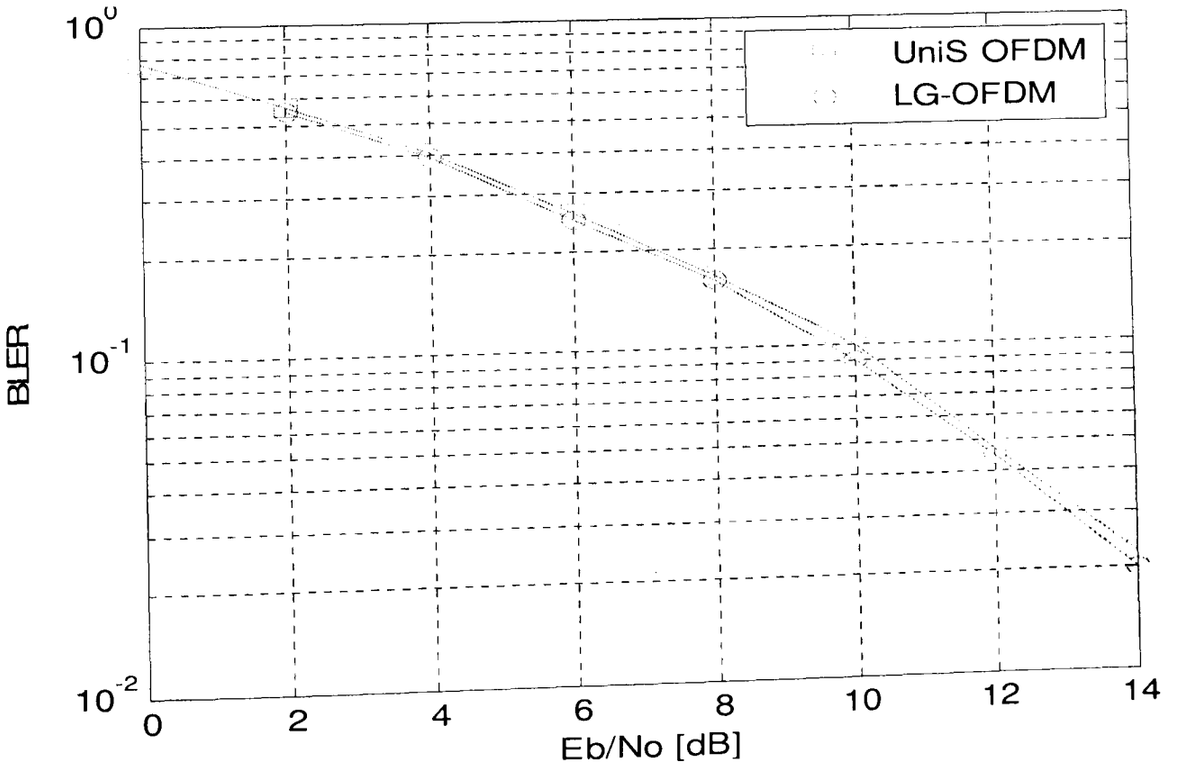

Figure F-3: BLER Performance of OFDM in the Pedestrian A channel at 3km/h

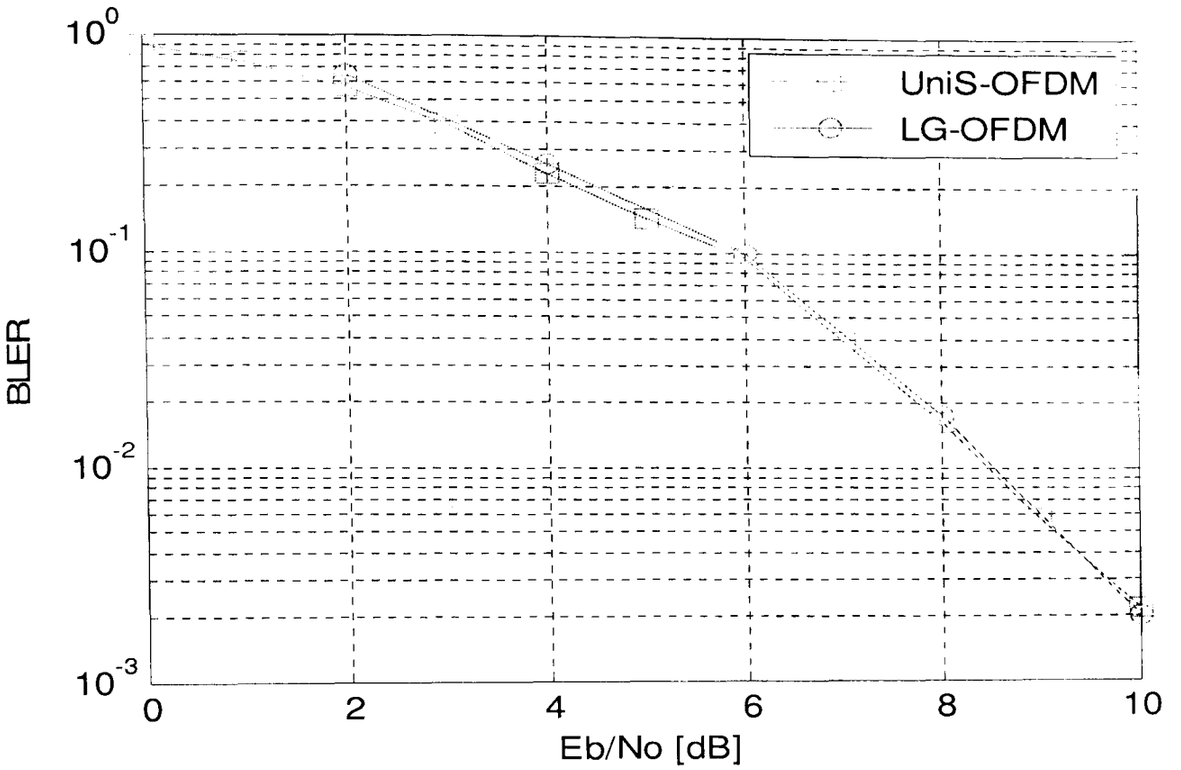

Figure F-4: BLER Performance of OFDM in the Vehicular A channel at 120km/h

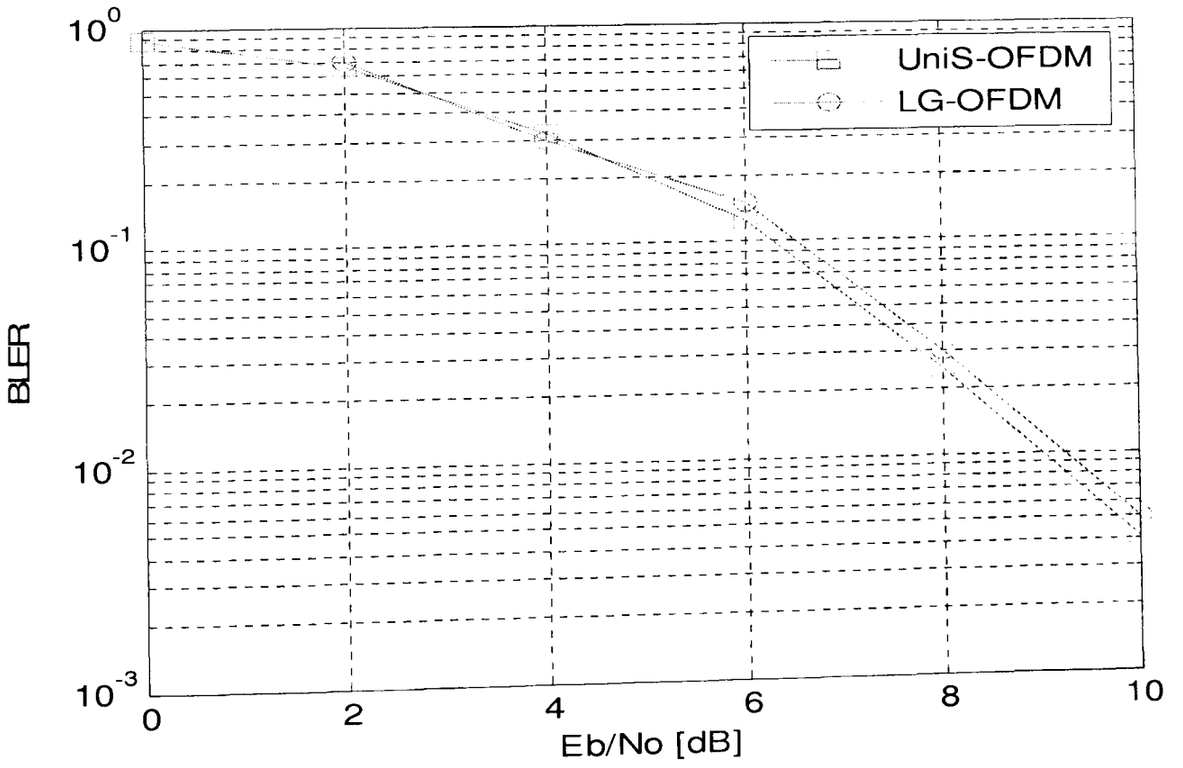

Figure F-5: BLER Performance of OFDM in the Vehicular B channel at 120km/h

APPENDIX G: Log-Likelihood Ratios Calculation in SC-FDMA with MMSE Equalization

In order to calculate the channel reliability values for turbo decoding purpose, we start the explanation from equation (6.18), following the FFT processing at the receiver:

$$\bar{\bar{\mathbf{y}}}_i = \mathbf{F}\bar{\mathbf{y}}_i = \mathbf{\Lambda M Q u}_i + \mathbf{F}\bar{\mathbf{n}} \tag{G.1}$$

where the FFT processing does not have any effect on the statistics of the noise. In SC-FDMA MMSE equalization is performed:

$$\mathbf{z} = \mathbf{T}\bar{\bar{\mathbf{y}}}_i = (\mathbf{\Lambda}^*\mathbf{\Lambda} + \frac{1}{SNR}\mathbf{I})^{-1}\mathbf{\Lambda}^*\mathbf{\Lambda M Q u}_i + \underbrace{(\mathbf{\Lambda}^*\mathbf{\Lambda} + \frac{1}{SNR}\mathbf{I})^{-1}\mathbf{\Lambda}^*\mathbf{F}\bar{\mathbf{n}}}_{\mathbf{w}} \tag{G.2}$$

where $\mathbf{T}$ represents the diagonal MMSE equalization matrix. The remaining part of the processing is to demap the data symbols ($\mathbf{M}^{-1}$), which does not affect the statistics of the signal or noise, and finally to carry out the IDFT dispreading. With respect to the statistics of the noise, the latter has the effect that variance of the noise samples becomes:

$$\sigma_w^2 = Mean(|diag(T)|^2) \cdot \sigma^2 \tag{G.3}$$

Moreover the MMSE equalization does not cancel perfectly the inter-subcarrier interference and this effectively results in increased noise power and a bias that need to be taken into account in the calculation of the log-likelihood ration for the log-MAP decoder.

In order to determine this inter-subcarrier interference power and bias, let us consider only the signal part in (G.2) and denote:

$$\mathbf{z}' = (\mathbf{\Lambda}^*\mathbf{\Lambda} + \frac{1}{SNR}\mathbf{I})^{-1}\mathbf{\Lambda}^*\mathbf{\Lambda M Q u}_i = (\mathbf{\Lambda}^*\mathbf{\Lambda} + \frac{1}{SNR}\mathbf{I})^{-1}\mathbf{\Lambda}^*\mathbf{\Lambda}\bar{\mathbf{u}}_i \tag{G.4}$$

Adding and substracting $\frac{1}{SNR}(\mathbf{\Lambda}^*\mathbf{\Lambda} + \frac{1}{SNR}\mathbf{I})^{-1}\bar{\mathbf{u}}_i$ on (G.4) we get:

$$\mathbf{z}' = (\mathbf{\Lambda}^*\mathbf{\Lambda} + \frac{1}{SNR}\mathbf{I})^{-1}\mathbf{\Lambda}^*\mathbf{\Lambda}\bar{\mathbf{u}}_i + \frac{1}{SNR}(\mathbf{\Lambda}^*\mathbf{\Lambda} + \frac{1}{SNR}\mathbf{I})^{-1}\bar{\mathbf{u}}_i - \frac{1}{SNR}(\mathbf{\Lambda}^*\mathbf{\Lambda} + \frac{1}{SNR}\mathbf{I})^{-1}\bar{\mathbf{u}}_i \tag{G.5a}$$

$$\mathbf{z}' = \bar{\mathbf{u}}_i - \frac{1}{SNR}(\mathbf{\Lambda}^*\mathbf{\Lambda} + \frac{1}{SNR}\mathbf{I})^{-1}\bar{\mathbf{u}}_i \tag{G.5b}$$

where the second term in (G.5b) models the inter-subcarrier interference.

Following the IDFT processing, the bias introduced on some *m-th* (QAM) signal sample is:

$$B_m = -(\frac{1}{SNR}[\mathbf{Q}^{-1} \cdot diag\{(\mathbf{\Lambda}^* \mathbf{\Lambda} + \frac{1}{SNR}\mathbf{I})^{-1}\}]_1)\bar{u}_i^m \tag{G.6}$$

where $[.]_1$ denotes the first element in the vector, $diag\{\}$ denotes a vector obtained from the diagonal of the input matrix, and $\bar{u}_i^m$ is the *m-th* transmit data point.

Moreover, following the IDFT processing, the inter-subcarrier interference power on some *m-th* signal sample is:

$$I_m = mean(|W_m|^2) \tag{G.7}$$

where $W_m = \frac{1}{M-1}\sum_{m=2}^{M}(\frac{1}{SNR}[\mathbf{Q}^{-1} \cdot diag((\mathbf{\Lambda}^* \mathbf{\Lambda} + \frac{1}{SNR}\mathbf{I})^{-1})]_m)$, and assuming signals have constant amplitudes.

Thus, assuming QPSK modulation the log-likehood ratios to be input to the Log-MAP decoder are determined as:

$$L_m = \frac{4\hat{u}_m(A - B_m)}{(\sigma_w^2 + I_m)/2} \tag{G.8}$$

where A is the signal amplitudes on the I or Q branches

List of Publications

Conference Publications:

1. Janaaththanan S., Kasparis C., Evans B.G., "**Performance Comparison between Adaptive LUT and Polynomial based Pre-distorters in the Forward Link of Mobile Satellite Systems**", submitted to *27th AIAA International Communications Satellite Systems Conference (ICSSC).*

2. Janaaththanan S., Kasparis C., Evans B.G., "**Improved Adaptation Algorithm for LUT-based Pre-distorter with Noisy Training Phase in OFDM based Satellite System**", *26th AIAA International Communications Satellite Systems Conference (ICSSC)*, San Diego, California, U.S.A, 11-14 June 2008.

3. Janaaththanan S., Kasparis C., Evans B.G.,"**A Gradient Based Algorithm for PAPR Reduction of OFDM using Tone Reservation Technique**", *IEEE Vehicular Technology Conference, 2008. VTC Spring'08*, Singapore, pp.2977-2980, 11-14 May 2008.

4. Janaaththanan S., Kasparis C., Evans B.G., "**Comparison of SC-FDMA and HSUPA in the Return Link of Evolved S-UMTS**", *International Workshop on Satellite and Space Communications (IWSSC)*, pp.56-60, Austria, 13-14 Sept. 2007.

5. Janaaththanan S., Kasparis C., Evans B.G., "**Feasibility Study of Adaptive LUT-based Pre-distorter for OFDM in Non-linear Satellite Downlink Channel**", *International Workshop on Satellite and Space Communications (IWSSC)*, pp.126-129, Madrid, Sept. 2006.

6. Janaaththanan S., Kasparis C., Evans B.G., "**A Comparison between OFDM and SC-FDE over Wideband Satellite Downlinks**", *24th AIAA International Communications Satellite Systems Conference (ICSSC)*, San Diego, California, U.S.A, 11-14 June 2006.

References

[3GPP08] 3GPP, "About 3GPP". [Online] http://www.3gpp.org/Highlights/LTE/LTE.htm, [cited on 14th Jul. 2008].

[3GPP808] 3GPP TSG RAN, "Feasibility Study for Enhanced Uplink for UTRA FDD", Release 6, TS-25.808, V6.0.1, (2006-10).

[3GPP814] 3GPP TSG RAN, "Physical Layer Aspects for Evolved Universal Terrestrial Radio Access (UTRA)", Release 7, TS-25.814, V7.1.0, (2006-08).

[3GPP848] 3GPP TSG RAN, "Physical Layer Aspects of UTRA High Speed Downlink Packet Access", Release 4, TS-25.848, V4.0.0, (2004-06).

[3GPP892] 3GPP TSG RAN, "Feasibility Study for OFDM for UTRAN enhancement", Release 6, TS-25.892, V6.0.0, (2004-06).

[3GPP896] 3GPP TSG RAN, "Feasibility Study for Enhanced Uplink for UTRA FDD", Release 6, TS-25.896, V6.0.0, (2004-07).

[3GPPLG] LG Electronics, "Performance comparison of the OFDM configuration sets", 3GPP TSG RAN, WG #32-030497, May 2003.

[ALAV05] Alavi, A., Tellambura, C., and Fair, I., "PAPR reduction of OFDM signals using partial transmit sequence: an optimal approach using sphere decoding", *IEEE Comm. Letters,* vol.9, no.11, pp. 982-984, Nov. 2005.

[ANDR05] Andrikopoulos, I., et al, "Demonstration with field trials of a satellite-terrestrial synergistic approach for digital multimedia broadcasting to mobile users", *IEEE Trans. on Wireless Communications*, vol.12, no.5, pp. 82-90, Oct. 2005.

[ANDR96] D'Andrea, A.N., Lottici, V., and Reggiannini, R., "RF power amplifier linearization through amplitude and phase predistortion", *IEEE Trans. on Communications,* vol.44, no.11, pp. 1477-1484, Nov. 1996.

[ARMS02] Armstrong, J., "Peak-to-average power reduction for OFDM by repeated clipping and frequency domain filtering", *IET Electronics Letters* , vol.38, no.5, pp. 246-247, Feb. 2002.

[ATTA05] Atta ul Quddus, "Link-Level Performance Characterisation and Optimisation of UTRA FDD Downlink", PhD thesis, University of Surrey, UK, Dec. 2005.

[BATE92] Bateman, A., "The combined analogue locked loop universal modulator (CALLUM)", *IEEE Vehicular Technology Conference, VTC'92,* pp. 41-47, May 1992.

[BAUM96] Bauml, R.W., Fischer, R.F.H., and Huber, J.B., "Reducing the peak-to-average power ratio of multicarrier modulation by selected mapping", *IET Electronics Letters,* vol. 32, pp. 2056-2057, Oct. 1996.

[BENV02] Benvenuto, N., and Tomasin, S., "On the comparison between OFDM and single carrier modulation with a DFE using a frequency-domain feedforward filter", *IEEE Trans. on Communications,* vol.50, no.6, pp. 947-955, Jun. 2002.

[BERN97] Bernardini, A., and De Fina, "Analysis of Different Optimization Criteria for IF Predistortion in Digital Radio Links With Nonlinear Amplifiers", *IEEE Trans. on Communications*, vol. 45, no. 4, pp. 421-428, Apr. 1997.

[BESB01] Besbes, H., Le-Ngoc, T., and Lin, H., "A fast adaptive polynomial predistorter for power amplifiers", *IEEE Global Telecommunication Conference, GLOBECOMM' 01*, vol. 1, pp. 659–663. Jul. 2001,

[BOUM04] Boumaiza, S., Jing Li, Jaidane-Saidane, M., and Ghannouchi, F.M., "Adaptive digital/RF predistortion using a nonuniform LUT indexing function with built-in dependence on the amplifier nonlinearity", *IEEE Trans. on Microwave Theory and Techniques*, vol.52, no.12, pp. 2670-2677, Dec. 2004

[BOYE04] Boyed, S., and Vandenberghe, L., "Convex Optimization", Cambridge University Press, 2nd Edition, 2004.

[BRIA04] Brian S Krongold and Douglas L. Jounes, "An Active-Set Approach for OFDM PAR Reduction via Tone Reservation", *IEEE Trans. on Signal processing*. vol. 52, no 2, pp. 495-509, Feb. 2004.

[BURD89] Burden, R.L., and Fires, J.D., "Numerical Analysis", PWS Publishing Co. Boston, MA, USA, Fourth edition, 1989.

[CAVE90] Cavers, J.K., "Amplifier Linearization using a digital pre-distorter with fast adaptation and low memory requirements", *IEEE Trans. on Vehicular Technology*, vol. 39, pp. 31-40, Nov. 1990.

[CAVE97] Cavers, J.K., "The Effect of Quadrature Modulator and Demodulator Errors on Adaptive Digital Predistorters for Amplifier Linearization", *IEEE Trans. on Vehicular Technology*, vol. 46, no. 2, pp. 456-466, May 1997.

[CAVE99] Cavers, J.K., "Optimum Table Spacing in Predistorting Amplifier Linearizers" , *IEEE Trans. on Vehicular Technology*, vol. 48, No. 5, pp. 1699-1705, Sep. 1999.

[CHAN95] Changsoo Eun, and Powers, E.J., "A predistorter design for a memory-less nonlinearity preceded by a dynamic linear system", *IEEE Global Telecommunications Conference, 1995. GLOBECOM '95*, vol.1, no.4, pp.152-156, 14-16 Nov. 1995.

[CHAR78] Charalambous. C., and Conn, A.R., "An efficient method to solve the minimax problem directly", *SIAM Journal on Numerical Analysis*, vol. 15, no. 1, pp. 162-187, Feb. 1978.

[CHEN03] Chen, H., and Haimovich, A., "Iterative estimation and cancellation of clipping noise for OFDM signals", *IEEE Comm. Letters.*, vol. 7, no.7, pp. 305 – 307, Jul. 2003.

[CHEN87] Chen, X., and Parks, T., "Design of FIR filters in the complex domain", *IEEE Trans. on Acoustics, Speech, Signal Processing*, vol. 34, pp. 144–153, Feb. 1987.

[CHEN99] Cheng-Po Liang, Je-Hong Jong, Stark, W.E., and East, J.R., "Nonlinear amplifier effects in communications systems", *IEEE Trans. on Microwave Theory and Techniques*, vol.47, no.8, pp.1461-1466, Aug. 1999.

[CHEW03] Chew Lee, K., Gardner, P., "A Novel Digital Predistorter Technique Using an Adaptive Neuro-Fuzzy Inference System", *IEEE Comm. Letters*, vol. 7, no. 2, pp. 55-57, Feb. 2003.

[CION05] Cioni, S., Corazza, G.E., Neri, M., and Vanelli-Coralli, A., "OFDM vs. HSDPA comparison for satellite digital multimedia broadcasting systems", *IEEE Global Telecommunications Conference, GLOBECOM '05*, vol.5, no. 3, pp. 5-9 , 28 Nov.-2 Dec. 2005.

[CION06] Cioni, S., Corazza, G.E., Neri, M., and Vanelli-Coralli, "On the Use of OFDM radio interface for satellite digital multimedia broadcasting systems", *International Journal of Sat. Comm. and Network.*, vol.24, pp. 153-167, Jan. 2006.

[COSK03] Coskun, A.H., and Demir, S., "A mathematical characterization and analysis of a feedforward circuit for CDMA applications", *IEEE Trans. on Microwave Theory and Techniques*, vol.51, no.3, pp. 767-777, Mar. 2003.

[COST99] Costa, E., Midrio, M., and Pupolin, S., "Impact of amplifier nonlinearities on OFDM transmission system performance", *IEEE Comm. Letters*, vol.3, no.2, pp.37-39, Feb. 1999.

[COXC74] Cox, D. C., "Linear amplification with nonlinear components". *IEEE Trans. on Communications*, vol. 22, no. 12, pp. 1942–1945, Dec. 1974.

[CRIPP06] Cripps, S. C., "RF Power Amplifiers for Wireless Communications", Boston, MA: Artech House, 2nd Edition, 2006.

[DAVA02] Davarian, F., "Sirius Satellite Radio: Radio entertainment in the sky", *IEEE Aerospace Conference Proceedings,* vol.3, no.5, pp. 1031-1035, Jul. 2002.

[DAWS03] Dawson, J. L., Lee, T. H., "Automatic Phase Alignment for a Fully Integrated Cartesian Feedback Power Amplifier System", *IEEE Journal of Solid-State Circuits*, vol. 38, no. 12, pp. 2269-2279, Dec. 2003.

[DAWS04] Dawson, J. L., Lee, T. H., "Cartesian Feedback for RF Power Amplifier Linearization", *Proc. of American Control Conference*, pp.361-366, Jun. 2004

[DENE01] Deneire, L., Gyselinckx, B., and Engels, M., "Training sequence versus cyclic prefix-a new look on single carrier communication", *IEEE Comm. Letters,* vol.5, no.7, pp.292-294, Jul. 2001.

[DHAH01] Al-Dhahir, N., "Single-carrier frequency-domain equalization for space-time block-coded transmissions over frequency-selective fading channels", *IEEE Comm. Letters,* vol.5, no.7, pp.304-306, Jul. 2001.

[DING04] Lei Ding, Zhou, G.T., Morgan, D.R., Zhengxiang Ma, Kenney, J.S., Jaehyeong Kim, and Giardina, C.R., "A robust digital baseband predistorter constructed using memory polynomials", *IEEE Trans. on Communications,* vol.52, no.1, pp. 159-165, Jan. 2004.

[DING04] Ding, L., and Zhou, G. T., "Effects of Even-order Nonlinear Terms on Power Amplifier Modeling and Predistortion Linearization", *IEEE Trans. on Vehicular Technology*, vol.53, no.1, pp. 156-162, Jan. 2004.

[DVB08] DVB, "About DVB". [Online] http://www.dvb.org/technology/standards/, [cited on 15th Sep. 2008].

[DVBS08] DVB, "System Specifications for Satellite services to Handheld devices (SH) below 3 GHz". [Online] http://www.dvb.org/technology/standards/index.xml, [cited on 16th Apr. 2008]

[ETRI07] ETRI-Unis Project, "Comparison between WCDMA and OFDM for satellite UMTS", *ETRI-UniS collaborative research project report*, Feb. 2007.

[ETSI04] ETSI TSG, "Satellite Earth Stations and Systems (SES); Satellite Component of UMTS/IMT-2000; Evaluation of the W-CDMA UTRA FDD as a Satellite Radio Interface", TR-102-058, v1.1.1, (2004-11).

[EVAN04] Evans, B.G., "Role of satellites in mobile-wireless systems", *IEEE International Symposium Personal, Indoor and Mobile Radio Communications, PIMRC'04*, vol.3, no.4, pp. 2055-2060, 5-8 Sep. 2004.

[EVAN05] Evans, B. et al., "Integration of satellite and terrestrial systems in future multimedia communications", *IEEE Trans. on Wireless Communications*, vol.12, no.5, pp. 72-80, Oct. 2005.

[EVAN07] Evans, B. G., and Thompson, P. T., "Aspects of Satellite Delivered Mobile TV (SDMB)", *Proc. Mobile and Wireless Communications Summit, 2007. 16th IST*, vol., no., pp.1-5, 1-5 Jul. 2007.

[EVAN99] Evans, B.G., "Satellite Communication Systems", *IEE Telecommunications Series, Institution of Engineering and Technology*, 3rd Revised Edition, 1999.

[FALC02] Falconer, D., Ariyavisitakul, S.L., Benyamin-Seeyar, A., and Eidson, B., "Frequency domain equalization for single-carrier broadband wireless systems", *IEEE Communications Magazine*, vol.40, no.4, pp.58-66, Apr. 2002.

[FAZE03] Fazel, K., and Kaiser, S., "Multi-Carrier and Spread Spectrum Systems", *John Wiley & Sons Ltd*, 2nd Edition, 2003.

[FLOC95] Le Floch, B., Alard, M., and Berrou, C., "Coded orthogonal frequency division multiplex [TV broadcasting]", *Proceedings of the IEEE*, vol.83, no.6, pp.982-996, Jun. 1995.

[GATH98] Gatherer, A., and Polley, M., "Controlling clipping probability in DMT transmission", *in Proc. Asilomar Conference on Signals, Systems, and Computers*, vol. 1, pp. 578–584, Nov. 1997.

[GHAD94] Ghaderi, M., Khumar, S., and Dodds, D.E., "Adaptive Predistortion lineariser using polynomial functions", *IET Proc. in Communications*, vol. 141, no. 2, pp. 49-55, Apr. 1994.

[GONZ95] A.Gonzalez, and S.J. Elliott, "Adaptive Minimization of the maximum error signal in an active control system", *IEEE Workshop on Applications of Signal Processing to Audio and Acoustics, ASSP'95*, Oct. 1995.

[GONZ98] Gonzalez, A., Albiol, A., and Elliott, S.J., "Minimization of the maximum error signal in active control", *IEEE Trans. on Speech and Audio Processing*, vol.6, no.3, pp.268-281, May 1998.

[HARA03] Shinsuke Hara, and Ramjee Prasad, "Multicarrier Techniques for 4G Mobile Communications", *Artech House*, 3rd Edition, 2003.

[HAYK96] Simon Haykin, "Adaptive Filter Theory", *Prentice-Hall, New Jersey*, 3rd Edition, 1996.

[HETZ91] Hetzel, S. A., Bateman, A., and McGeehan, J. P., "A LINC transmitter", *IEEE Vehicular Technology Conference, VTC'91*, vol. 44, pp. 133–137, Apr. 1991.

[HEUN04] Heung-Gyoon Ryu, Jae-Eun Lee, and Jin-Soo Park, "Dummy sequence insertion (DSI) for PAPR reduction in the OFDM communication system", *IEEE Trans. on Consumer Electronics* , vol.50, no.1, pp. 89-94, Feb. 2004.

[HEUN07] Heung-Gyoon Ryu, and Sang-Woo Kim, " PAPR Reduction using DFT Transform of the OFDM Signal for the High-Speed Satellite Communication", *25th AIAA International communications Satellite Systems conference, ICSSC'07,* pp. 324-329, Jun. 2007.

[HOLM02] Holma, H., and Toskala, A., "WCDMA for UMTS: Radio Access for Third Generation Mobile Communications", *John –Wiley & Sons Ltd.*, 3rd edition, 2002.

[HORL04] Horlin, J. Tubbax, Van der Perre, L., and De Man, H., "A Single-Carrier – OFDM Comparison For Broadband Wireless Communications", *IEEE International conference on Acoustics, speech, and Signal Processing, ICASSP'04*, vol. 2, pp. 329-332, Montreal, May 2004.

[HUAN04] Ji-Huan He, "A Modified Newton-Raphson Method", *Journal on Communication in Numerical Methods in Engineering,* pp. 801-805, Jun. 2004.

[HUAN06] Huang, D., Leung, H., and Huang, X., "Experimental Evaluation of Predistortion Techniques for High-Power Amplifier", *IEEE Trans. on Instrumentation and Measurement,* vol.55, no.6, pp.2155-2164, Dec. 2006.

[HYUN03] Hyunchul Ku, and Kenney, J.S., "Behavioral modeling of nonlinear RF power amplifiers considering memory effects", *IEEE Trans. on Microwave Theory and Techniques*, vol.51, no.12, pp. 2495-2504, Dec. 2003.

[HYUN06a] Hyung G. Myung, Junsung Lim, and David J. Goodman, "Single carrier FDMA for uplink wireless transmission", *IEEE Vehicular Technology Magazine*, vol.1, no.3, pp.30-38, Sep. 2006.

[HYUN06b] Hyung G. Myung, Junsung Lim, and David J. Goodman, "Peak-To-Average Power Ratio of Single Carrier FDMA Signals with Pulse Shaping", *IEEE 17th International Symposium on Personal, Indoor and Mobile Radio Communications, PMIRC'06*, pp. 1-5, Sep. 2006

[JAAN02] Jaana Laiho, Achim Wacker, and Toma Novosad, "Radio Netwok Planning and Optimization for UMT", *John Wiley & Sons Ltd.*, 1st Edition, 2002.

[JAYA00] Jayalath, A.D.S., and Tellambura, C., "The use of interleaving to reduce the peak-to-average power ratio of an OFDM signal", *IEEE Global Telecommunications Conference, GLOBECOM '00*, vol.1, no.5, pp.82-86, Dec. 2000

[JAYA02] Jayalath, A., "OFDM for wireless broadband communications (peak power reduction, spectrum and coding)", PhD thesis, Monash University, Australia, May 2002.

[JENN99] Jennings, D., "A high efficiency RF transmitter using VCO-derived synthesis: CALLUM", *IEEE Trans. on Microwave Theory and Techniques*, vol. 47, no. 6, pp. 715–721, Jun. 1999.

[JEON97] Jeon, W. G.,et al., " An Adaptive Data Predistorter for Compensation of Nonlinear Distortion in OFDM system," *IEEE Trans. on Communications*, vol. 45, no. 10, pp. 1167-1171, Oct. 1997.

[JONE94] Jones, A.E., Wilkinson, T.A., and Barton, S.K., "Block coding scheme for reduction of peak to mean envelope power ratio of multicarrier transmission schemes", *IET Electronics Letters*, vol.30, no.25, pp.2098-2099, Dec. 1994.

[KARA04] Karaliopoulos, M., et al, "Satellite radio interface and radio resource management strategy for the delivery of multicast/broadcast services via an integrated satellite-terrestrial system", *IEEE Communications Magazine*, vol.42, no.9, pp. 108-117, Sep. 2004.

[KATZ01] Katz, A., "Linearization: reducing distortion in power amplifiers", *IEEE Microwave Magazine,* vol.2, no.4, pp.37-49, Dec. 2001.

[KENI02] Kenington, P.B., "Linearized transmitters: an enabling technology for software defined radio", *IEEE Communications Magazine,* vol.40, no.2, pp.156-162, Feb 2002.

[KENN98] Kennington, P., "Methods linearize RF transmitters and power amplifier linearization techniques, Part 1", *Microw. RF Journal*, vol. 37, no. 13, pp. 102–116, Dec. 1998.

[KIMJ01] Kim, J., and Konstantinou, K., "Digital predistortion of wideband signals based on power amplifier model with memory", *IET Electronics Letters*, vol. 37, no. 23, pp. 1417–1418, Nov. 2001.

[KRON03] Krongold, B.S., and Jones, D.L., "PAR reduction in OFDM via active constellation extension", *IEEE Trans. on Broadcasting*, vol.49, no.3, pp. 258-268, Sep. 2003.

[KUMA85] Kumar, P.V., Scholtz, R.A., and Welch, L.R., "Generalized bent functions and their properties", *Journal of Combinatorial Theory*, volume A, no. 40, pp. 90–107, Apr. 1985.

[LAIH99] Lai, H., and Bar-Ness, Y., "Minimum distortion power polynomial model (MDP-PM) of nonlinear power amplifiers and its application on analog predistorters", *IEEE Vehicular Technology Conference, VTC'99*, vol.3, pp.1501-1505, Aug. 1999.

[LANG99] Langridge, E., "A power re-use technique for improved efficiency of outphasing microwave power amplifiers", *IEEE Trans. on Microwave Theory and Techniques*, vol. 47, no. 8, pp. 1467–1470, Aug. 1999.

[LEEK01] Lee, K.C., and Gardner, P., "Comparison of different adaptation algorithms for adaptive digital predistortion based on EDGE standard", *IEEE International Microwave Symposium Digest, MTT-S'01*, vol.2, pp.1353-1356, May 2001.

[LEVI66] Levitin, E.S., and Polyak, B.T., "Constrained minimization methods", *USSR computational Mathematics and Mathematical Physics*, vol. 6, pp. 1-50, 1966.

[LING00] Hui-Ling Lou, Fernandez-Getino Garcia, M.J., and Weerackody, V., "FEC scheme for a TDM-OFDM based satellite radio broadcasting system", *IEEE Trans. On Broadcasting,* vol.46, no.1, pp.60-67, Mar. 2000.

[LIUW99] Liu, W., Lau, J., and Cheng, R.S., "Considerations on applying OFDM in a highly efficient power amplifier", *IEEE Transactions on Circuits and Systems II: Analog and Digital Signal Processing,* vol.46, no.11, pp.1329-1336, Nov. 1999.

[LOUV03] Louveaux, J., Vandendorpe, L., and Sartenaer, T., "Cyclic prefixed single carrier and multicarrier transmission: bit rate comparison", *IEEE Comm. Letters*, vol.7, no.4, pp. 180-182, Apr. 2003.

[MAES06] MAESTRO, "MAESTRO FP6 EU Project". [Online] http://www.ist-maestro.dyndns.org, [cited on 13th Mar. 2006].

[MALK07] Malkin, M., Chan-Soo Hwang, and Cioffi, J.M., "Reducing Insufficient-Cyclic-Prefix Distortion Using Tone Reservation", *IEEE Global Telecommunications Conference, GLOBECOM '07*, pp.2889-2893, 26-30 Nov. 2007.

[MATO02] Matolak, D.W., et al, "Recent progress in deployment and standardization of geostationary mobile satellite systems", *Proceddings of Military Communications*, MILCOMM'02, vol.1, pp. 173-177, 7-10 Oct. 2002.

[MBCO08] MBCO, "Mobile Broadcasting Corporation (MBCO) in Japan". [Online] http://www.mbco.co.jp/english, [cited on 23rd Mar. 2008].

[MOBI08] Mobile in Korea, "The Number of S-DMB Subscribers is increasing since June of 2008". [Online] http://www.mobileinkorea.com/entry/2008082701, [cited on 11th Oct. 2008].

[MODI06] MODIS, "MODIS FP5 EU Project ". [Online] http://www.ist-modis.org, [cited on 18th Mar. 2006].

[MOHA04] Mohamed K. Nazami, "Fundamental of Power Amplifier Linearization using Digital Pre-Distortion", *Journal on High Frequency Design,* pp. 54-59, Sep. 2004.

[MORR03] Morris, K., and Kennington, P., "Power Amplifier Linearization Using Pre-distortion Techniques", *IET Colloquium on RF and Microwave Components for Communication Systems*, Bradford, UK, vol. 6, pp. 1-6, Apr. 2003.

[MULL97] Muller, S.H, and Huber,J.B., "OFDM with reduced peak-to-average power ratio by optimum combination of partial transmit sequences", *IET Electronics Letters*, vol. 33, no. 5, pp. 368-369, Feb. 1997.

[MUQU02] Muquet, B., Zhengdao Wang, Giannakis, G.B., de Courville, M., and Duhamel, P., "Cyclic prefixing or zero padding for wireless multicarrier transmissions?", *IEEE Trans. on Communications*, vol.50, no.12, pp. 2136-2148, Dec. 2002.

[NAGA89] Nagata, Y., "Linear Amplification technique for Digital Mobile Communications", *IEEE Vehicular Technology Conference, VTC'99*, pp. 159-164, May 1989.

[NARE04] Narenthiran, K., Karaliopoulos, M., Evans, B.G., et al., "S-UMTS access network for broadcast and multicast service delivery: the SATIN approach", *International Journal of Sat. Comm. and Networking*, vol. 22, no. 1, pp. 87-111, Jan.-Feb. 2004.

[NELS93] Nelson, P.A., and Elliott, S.J., "Active Control of Sound", *Academic Press Ltd.*, 1st Edition, 1993.

[NGUY03] Nguyen, T.M., Yoh, J., Lee, C.H., Tran, H.T., and Johnson, D.M., "Modeling of HPA and HPA linearization through a predistorter: Global Broadcasting Service applications", *IEEE Trans. on Broadcasting,* , vol.49, no.2, pp. 132-141, Jun. 2003.

[PANC05] Pancaldi, F., and Vitetta, G.M., "Block channel equalization in the frequency domain", *IEEE Trans. on Communications*, vol.53, no.3, pp. 463-471, Mar. 2005.

[PARK00] Park, H.M., et al., "A Predistortion Linearizer Using Envelope-Feedback Technique with Simplified Carrier Cancellation Scheme for Class-A and Class-AB Power Amplifiers", *IEEE Trans. on Microwave Theory and Techniques*, vol. 48, no. 6, pp. 1221-1225, Jun. 2000.

[PETR84] Petrovic, V., "Reduction of intermodulation distortion by means of modulation feedback", *Proc. IEEE Colloq. Intermodulation—Causes, Effects and Mitigation*, pp. 811–818, Apr. 1984.

[PIPI05] Pipilos, S., et al., "A Transmitter IC for TETRA Systems Based on Cartesian Feedback Loop Linearization Technique", *IEEE Journal of Solid-State Circuits*, vol. 40, no. 3, pp. 707-718, Mar. 2005.

[POPO92] Popovic, B.M., "Generalized Chirp-like Polyphase Sequences with Optimal Correlation Properties", *IEEE Trans. on Information Theory*, vol. 38, pp. 1406-1409, Jul. 1992.

[PROA95] Proakis, J.G., "Digital communications", *McGraw-Hill series in electrical engineering. Communications and signal processing, New York: McGraw-Hill*, 3rd ed., 1995.

[QIUJ05] Qiu, J.X., Abe, D.K., Antonsen, T.M., Jr., Danly, B.G., Levush, B., and Myers, R.E., "Linearizability of TWTAs using predistortion techniques", *IEEE Trans. on Electron Devices* , vol.52, no.5, pp. 718-727, May 2005.

[QIUJ05] Qiu, J. X., et al., "Linearizability of TWTAs Using Predistortion Techniques", *IEEE Trans. on Electron Devices*, vol. 52, no. 5, pp. 718-727, May 2005.

[QUAC93] Quach, L.D., and Stapleton, S., "A postdistortion receiver for mobile communications", *IEEE Trans. Vehicular Technology*, vol. 42, no. 4, pp. 604 – 616, Nov. 1993.

[RAMJ00] Van Nee, R., and Prasad, R., "OFDM for Wireless Multimedia Communications", *Norwood, MA: Artech House,* 2nd Edition, 2000.

[ROHL99] Rohling, M., May, T., Bruninghaus, K., and Grunheid, R., "Broad-band OFDM radio transmission for multimedia applications", *Proceedings of the IEEE*, vol.87, no.10, pp.1778-1789, Oct. 1999.

[SANG07] Sang-Jin Lee, SangWoon Lee, Kyung-Won Kim, and Jong-Soo Seo, "Personal and Mobile Satellite DMB Services in Korea", *IEEE Trans. on Broadcasting*, vol.53, no.1, pp.179-187, Mar. 2007.

[SANT98] Santella, G., and Mazzenga, F., "A hybrid analytical-simulation procedure for performance evaluation in M-QAM-OFDM schemes in presence of nonlinear distortions", *IEEE Trans. on Vehicular Technology*, vol.47, no.1, pp.142-151, Feb. 1998.

[SARI95] Sari, H., Karam, G., and Jeanclaude, I., "Transmission techniques for digital terrestrial TV broadcasting", *IEEE Communications Magazine*, vol.33, no.2, pp.100-109, Feb. 1995.

[SATI06] SATIN, "SATIN FP5 EU Project". [Online] http://www.ist-satin.org, [cited on 11th Mar. 2006].

[SAYE03] Ali. H. Sayed, "Fundamentals of Adaptive Filtering", *A John-Wiley & Sons inc. publications*, 1st Edition, 2003.

[SEUN05] Seung Hee Han, and Jae Hong Lee, "An overview of peak-to-average power ratio reduction techniques for multicarrier transmission", *IEEE Trans. on Wireless Communications*, vol.12, no.2, pp. 56-65, Apr. 2005.

[SEVE02] Severijns, T., De Win W., Dieudonne, M., Karaliopoulos, M., Narenthiran, K., and Evans, B.G., "The Intermediate Module Concept within the SATIN Proposal for the S-UMTS AirInterface", *Proc. IST Mobile Summit'02*, 17-19 Jun. 2002.

[STAP92] Stapleton, S.P., and Costescu, F.C., "An adaptive Predistorter for a Power Amplifier Based on Adjacent Channel Emissions", *IEEE Trans. on Vehicular Technology*, vol. 41, no. 1, pp. 49-56, Feb. 1992.

[TAAG99] Taaghol, P., Evans, B.G., Buracchini, E., De Gaudinaro, G., Joon Ho Lee, and Chung Gu Kang, "Satellite UMTS/IMT2000 W-CDMA air interfaces", *IEEE Communications Magazine*, vol.37, no.9, pp.116-126, Sep. 1999.

[TELL01] Tellambura, C., "Computation of the continuous-time PAR of an OFDM signal with BPSK subcarriers", *IEEE Comm. Letters*, vol.5, no.5, pp.185-187, May 2001.

[TELL99] Tellado-Mourelo, J., "Peak to average power reduction for multicarrier modulation", PhD thesis, Stanford University, USA, Sep. 1999.

[THUR08] Thurya, "About Thurya services". [Online] http://www.thuraya.com/content/high-speed-data-services.html, [cited on 24th Mar. 2008].

[WATT05] Wattanasuwakull, T., and Benjapolakul, W., "PAPR Reduction for OFDM Transmission by using a method of Tone Reservation and Tone Injection", *Fifth International Conference on Information, Communications and Signal Processing, ICSP'05*, pp. 273-277, 06-09 Dec. 2005.

[WOOY07] Woo, Y. Y., Kim, J., Yi, J., Hong, S., Kim, I., Moon, J., and Kim, B., "Adaptive Digital Feedback Predistortion Technique for Linearizing Power Amplifiers", *IEEE Trans. on Microwave Theory and Techniques*, vol.55, no.5, pp.932-940, May 2007.

[XIAO98] Xiaodong Li, and Cimini, L.J., Jr., "Effects of clipping and filtering on the performance of OFDM", *IEEE Comm. Letters*, vol.2, no.5, pp.131-133, May 1998.

[YANG02] Yang, Y., Woo, Y.Y., and Kim, B., "New predistortion linearizer using low-frequency even-order intermodulation components", *IEEE Trans. on Microwave Theory and Techniques*, vol. 50, no. 2, pp. 446–452, Feb. 2002.

[YANG06] Yang Wen, Wei Huang, and Zhongpei Zhang, "CAZAC sequence and its application in LTE random access", *IEEE Information Theory Workshop, ITW '06,* pp.544-547, 22-26 Oct. 2006

[YIYA00] Yi, J., Yang, Y., Park, M., Kang, W., and Kim, B., "Analog predistortion linearizer for high-power RF amplifiers", *IEEE Trans. on Microwave Theory and Techniques*, vol. 48, no. 12, pp. 2709–2713, Dec. 2000.

[YUGA05] Yugang Zhou, McLane, P.J., and Chun Loo, "Performance of predistorted APK Modulation for one- and two-link nonlinear power amplifier Satellite communication channels", *IEEE Trans. on Vehicular Technology* , vol.54, no.2, pp. 629-638, Mar. 2005.

[ZHEN00] Zhendao Wang, and Giannakis, G.B., "Wireless multicarrier communications", *IEEE Signal Processing Magazine*, vol.17, no.3, pp.29-48, May 2000.

[ZHOU01] Zhou, S., and Giannakis, G.B., "Space-time coding with maximum diversity gains over frequency-selective fading channels", *IEEE Signal Processing Letters*, vol.8, no.10, pp.269-272, Oct. 2001.